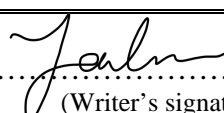## University of Stavanger

**Faculty of Science and Technology**

# MASTER'S THESIS

| Study program/ Specialization:<br><br>MSc in Offshore Technology /<br>Marine and Subsea Technology | Spring semester, 2018<br><br>Open / ~~Restricted~~ access |
|---|---|
| Writer:<br>    Marek Jan Janocha | ……………………………………………<br>(Writer's signature) |

Programme coordinator:
        Prof. Muk Chen Ong
Supervisor:
        Prof. Muk Chen Ong

Thesis title:

        CFD Simulations of Vortex-Induced Vibrations of a Subsea
        Pipeline Near a Horizontal Plane Wall

Credits (ECTS):    30

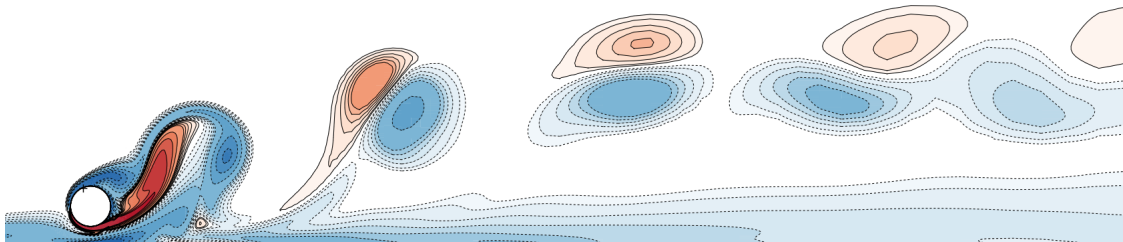| Key words:<br><br>vortex shedding, laminar flow, turbulent flow, near-wall, CFD, URANS, OpenFOAM, vortex induced vibration, circular cylinder, piggyback | Pages:      143<br><br>+ enclosure:    24<br><br>Stavanger, June 29, 2018<br>Date/year |
|---|---|

# CFD SIMULATIONS
# OF VORTEX-INDUCED VIBRATIONS
# OF A SUBSEA PIPELINE NEAR
# A HORIZONTAL PLANE WALL

**Author:**
**Marek Jan Janocha**

**Supervisor:**
**Prof. Muk Chen Ong**
University of Stavanger

*To my Family*

# ABSTRACT

Subsea pipelines, when exposed to free spans, can experience vortex-induced vibrations. This phenomenon was described as a resonance condition occurring when the vortex shedding frequency and the natural frequency of a structure approach common oscillation frequency. Fatigue life of the pipeline can be adversely affected by a high amplitude oscillations attributed to the vortex-induced vibrations. A numerical study has been performed on the effects of wall proximity on the vortex shedding of an elastically mounted circular cylinder. In addition, the study was extended to investigate the influence of a second cylinder with a smaller diameter rigidly coupled with the large cylinder. Such configurations can be regarded as a model of a subsea pipeline or, in case of coupled cylinders, a subsea piggyback pipeline in a free span situation. A series of two dimensional, numerical studies using open source CFD code OPENFOAM has been performed. Simulations were performed in two flow regimes, a laminar vortex street regime at Reynolds number $Re = 200$ and an upper transition regime at $Re = 3.6 \times 10^6$. A range of reduced velocities covering a frequency lock-in phenomenon was investigated. Hydrodynamic forces and response amplitudes were mapped with respect to the reduced velocity. Furthermore, a study of the phase differences between the hydrodynamic forces and cylinder displacements was conducted. The motions of the cylinder were recorded and presented on the trajectory plots. The frequency components of hydrodynamic forces and displacements were analyzed with the FFT algorithm in the frequency domain. In order to gain insight into the effects of the shear layers interaction in the area around the oscillating cylinder, flow visualizations of the numerical simulations were analyzed.

# ACKNOWLEDGMENTS

M. J. Janocha

*Stavanger, Norway*
*June, 2018*

# Contents

# LIST OF FIGURES

# LIST OF TABLES

# ACRONYMS

CF          Cross Flow

CFD         Computational Fluid Dynamics

CV          Control Volume

CWT         Continuous Wavelet Transform

DNS         Direct Numerical Simulation

DoF         Degree-of-Freedom

FEM         Finite Element Method

FFT         Fast Furrier Transform

FVM         Finite Volume Method

IL          In Line

LES         Large Eddy Simulation

PIV         Iarticle Image Velocimetry

RMS         Root-Mean-Squared

TrW         Transition in Wake

URANS       Unsteady Reynolds-Averaged Navier-Stokes

VIV         Vortex-Induced Vibrations

# SYMBOLS

ROMAN SYMBOLS

$A$    Amplitude of vibration / control surface

$c$    Damping coefficient

$C_F$    Skin friction coefficient

$C_p$    Pressure coefficient

$C_D$    Drag coefficient

$C_L$    Lift coefficient

$Co$    Courant number

$D$    Diameter / characteristic length

$e$    Gap distance

$F_D$    Drag force

$F_L$    Lift force

$f_n$   Natural frequency of a system

$f_{osc}$   Frequency of oscillation

$f_{st}$   Vortex shedding frequency of a body at rest

$f_{vac}$   Natural frequency measured in vacuum

$k$   Spring stiffness

$m$   Mass

$m^*$   Mass ratio

$m_a$   Added mass

$p$   Pressure

$Re$   Reynolds number

$St$   Strouhal number

$U_\infty$   Free-stream flow velocity

$U_r$   Reduced velocity

$u$   Velocity $x$-component

$V$   Control volume

$v$   Velocity $y$-component

$w$   Velocity $z$-component

$x$   Distance in streamwise direction

$y$   Distance in crossflow direction

$z$   Distance in spanwise direction

GREEK SYMBOLS

$\delta$   Boundary layer thickness

$\mu$    Dynamic viscosity

$\nu$    Kinematic viscosity

$\phi$    General unknown variable / phase difference

$\rho$    Material density

$\tau$    Shear stress / dimensionless time

$\zeta$    Damping factor

# CHAPTER 1

# INTRODUCTION

## 1.1  Background and Motivation

Study of the flow patterns around cylindrical structures is relevant in a variety of engineering applications. In the offshore industry, many structures can be represented by such geometry. Subsea pipelines are one of the most notable examples. It is estimated that more than 45.000 kilometers of pipelines have been installed in the North Sea since 1966.

From an economic and environmental point of view, subsea pipelines represent an important asset with high safety and reliability requirements imposed by the regulators. Reynolds number characteristic for flow around pipes at the sea bottom is typically of $\mathcal{O}(10^4) - \mathcal{O}(10^7)$ covering subcritical to transcritical flow regimes. When exposed to fluid flow, free pipeline spans are subjected to dynamic motions induced by currents and/or waves, referred to as vortex-induced vibrations (VIV), which can cause fatigue related failure (Fig. 1.1). Another consequence of VIV is the drag amplification effect which results in enlarged static displacements and tensile forces. It is therefore desirable to de-

velop a better understanding of the coupled dynamics of free span pipelines undergoing vibrations in the vicinity of a seabed.
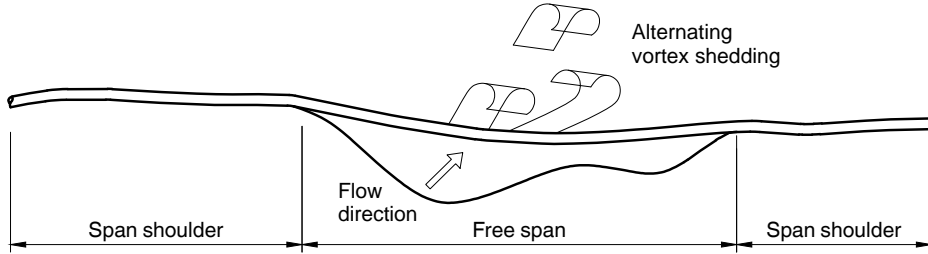


**Figure 1.1:** Free spanning subsea pipeline (DNV GL, 2017).

In this thesis, numerical simulations are used to study the motion of cylindrical structures undergoing vortex-induced vibrations. A numerical approach offers several benefits. Most importantly it allows performing parametric studies where among a large number of influencing parameters one of them can be varied while the others are kept constant. This provides the ability to discern the functional dependencies governing the inherently complex near-wall VIV physics. The second benefit of numerical studies is the ability to go beyond the limitations of experimental facilities, which are often limited with respect to the maximum Reynolds number possible to achieve.

## 1.2 Problem Definition and Objectives of the Thesis

The problem of a free-span along the pipeline can be modeled by the configuration in which flow is past an elastically mounted circular cylinder with two degree-of-freedom (2-DoF) in proximity to a stationary plane wall. Example of such problem can be seen in Fig. 1.2. Research methodology is based on the numerical study of the flow by using an open source finite volume method (FVM) code Open Field Operation And Manipulation (Weller et al., 2008).

It is a well established Computational Fluid Dynamics (CFD) code used by both academic and commercial organizations. The scope of the thesis is focused on two major studies. In the first part, the focus is on the flow around cylindrical structures at low Reynolds number. The second part is concerned with the upper transition flow regime. Two-dimensional models of the pipeline cross sections are investigated at $Re = 200$ in the first part and at $Re = 3.6 \times 10^6$ in the second part respectively. The results obtained from
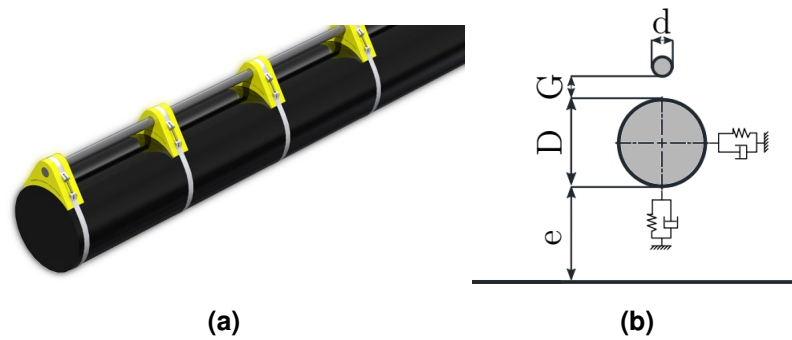
**Figure 1.2:** Example of a piggyback pipeline (a) (Subenesol.co.uk, 2018) and 2D model generalization (b).

CFD study are validated against other numerical and experimental studies. The main objectives established in the present thesis apply to both parts and are listed as follows:

**Research objective:** The formation and development of vortices around an oscillating cylinder in near-wall configuration and their interaction with the bottom boundary layer shall be investigated.

**Research objective:** The effects of different geometric configurations (including a single cylinder and different arrangements of two coupled cylinders with uneven diameters) on the flow characteristics shall be investigated.

**Research questions:** What are the key parameters governing the VIV in the near-wall configuration? What are the interactions between identified parameters? How suitable are tools used in the present study for practical design tasks concerning subsea pipelines?

## 1.3   Outline of the Thesis

Structure of the Thesis was established in the following way:

- Chapter 2: Flow around Circular Cylinder and Fluid-Structure Interaction introduces the fundamental theory of viscous flows, classification of flow regimes with respect to Reynolds number and classification of vortex shedding modes. The concepts of turbulence, boundary layers and, flow separation are briefly treated. Vortex shedding, dynamic equations of motion and vortex-induced vibrations theories are reviewed.

- Chapter 3: Computational Fluid Dynamics presents general concepts of CFD and Finite Volume Method. Fundamental governing equations and numerical method used are explained. Description of the OPENFOAM code used for the simulations is provided together with a short discussion on the selected solution methods.

- Chapter 4: Two degree-of-freedom near wall VIV in laminar vortex street regime describes the process of a model creation and set up used in the numerical simulations of 2DoF cylinder near a horizontal plane wall at Re = 200.

- Chapter 5: Vortex-induced vibrations of two rigid cylinders with uneven diameters near the horizontal plane wall at low Reynolds number. This chapter contains the paper draft which will be submitted to the Journal of Fluids and Structures. Presented study investigates the effects of different configurations of rigidly coupled cylinders with uneven diameters on VIV in the vicinity of a plane wall at Re = 200.

- Chapter 6: Two degree-of-freedom near wall VIV in upper transition regime describes the convergence studies and validation of a numerical model based on URANS approach to study the VIV at Re = $3.6 \times 10^6$.

- Chapter 7: Conclusionsand recommendations for future work.

## 1.4  Previous Work

The effect of vortex-induced vibration was known since the ancient times when it was first observed that wind can excite a taut wire of an Aeolian harp. The work of Henri Bénard and Theodore von Kármán in the beginning of 20th century resulted in a discovery of the vortex street formation and it's relation to the periodicity of the cylinder's wake. The wake of a cylindrical structure exhibits a large variety of complex phenomena stemming from the diverse instabilities in the transition regions. Flow around cylinders is well researched area of fluid dynamics and is covered by many comprehensive positions in the literature such as: Sarpkaya (2010), Sumer and Fredsøe (2006), Zdravkovich (1997). Extensive review on the flow induced vibrations was given in Blevins (1990) and Nakamura (2016).

*Experimental Studies.*   The effect of a plane wall on a flow around horizontally placed cylinders was investigated experimentally by numerous authors. Most existing studies have focused on the transverse VIV of the cylinder with one degree of freedom due to the larger amplitude in the transverse direction than that in the streamwise direction. One of the first published studies were those by Feng (1968) and Anand and Tørum (1985).

In his work Feng (1968) investigated cylinder's vibrations in air flow while Anand and Tørum (1985) focused on the behavior of the cylinder in the water flow. In both cases, Feng (1968) and Anand and Tørum (1985) demonstrated the vortex shedding frequency lock-in. Experiments conducted by Bearman and Zdravkovich (1978) investigated the effect of gap ratio ($e/D$ where $e$ is the gap distance and $D$ is the cylinder diameter) on the vortex shedding in the Reynolds number regime between $Re = 2.5 \times 10^4$ and $Re = 4.8 \times 10^4$. Their results indicate that for a stationary cylinder vortex shedding is suppressed if $e/D < 0.3$ thus vibrations cease at low gap ratios. Tsahalis and Jones (1981) performed model testing in a wave tank, tracking the response of the center of the pipe with an optical tracking system. It was observed that the proximity of the boundary plane reduced the maximum amplitude of vibration and the onset of VIV was shifted to higher velocities than without the boundary presence. Fredsøe et al. (1987) investigated the cross-flow vibration of cylinders near a rigid wall. They concluded that for the range of reduced velocities $3 < U_r < 8$ and $0 < e/D < 1$ the transverse vibrating frequency is noticeably larger than the frequency of vortex shedding from a stationary cylinder. More recently Yang et al. (2009) measured the vortex shedding frequency and mode by the method of hot film velocimetry and hydrogen bubbles. Researchers investigated the influence of reduced velocity, mass ratio, gap ratio and stability parameter on the amplitude and frequency of the cylinder vibrations. The results from the parametric study were summarized as follows: with decreasing mass ratio, the width of the lock-in ranges in terms of $U_r$ and the frequency ratio ($f/f_n$) become larger; with increasing gap-to-diameter ratio ($e/D$), the amplitude ratio ($A/D$) gets larger but frequency ratio ($f/f_n$) has a slight variation for the case of larger values of $e/D$. Wang et al. (2013) investigated flow around a neutrally buoyant cylinder with a mass ratio $m^* = 0.1$ and a low damping ratio $\zeta = 0.0173$. Experiment covered range of Reynolds number $3 \times 10^4 \le Re \le 1.3 \times 10^4$ and reduced velocity $1.53 \le U_r \le 6.6$. In contrast to the case of a stationary cylinder where vortex shedding was suppressed at a gap ratio $e/D < 0.3$ the elastically mounted cylinder was found to vibrate even at the smallest gap ratio $e/D = 0.05$. In the study by Hsieh et al. (2016), the velocity field was measured using a high-resolution particle image velocimetry (PIV) system. Vibration amplitude and oscillation frequency for different $U_r$, mean velocity field, turbulence characteristics, vortex behavior, gap flow velocity, and normal/shear stresses on the boundary were measured. The particle image velocimetry was also used by He et al. (2017) to investigate the vibrating cylinder at Re = 1072 and gap ratio range $e/D = (0 - 3.0)$. In both studies, the flow statistics and vortex dynamics revealed a strong dependence on the gap ratio. When the cylinder approaches the wall ($e/D < 2.0$) the wake becomes more asymmetric and a boundary layer separation occur on the wall downstream of the cylinder. The critical gap ratio was identified to be at

about $e/D = 0.25$, below that value the vortex shedding is irregular. For lower gap ratio is was found that only the upper shear layer can shed vortices.

*Numerical Studies.*   A rapid development of numerical methods and increasing computational power led to a dynamic growth of the number of published numerical studies. Following review covers some recent, relevant developments in the field. The near-wall cylinder in the turbulent regime was subject of numerical investigations by Ong et al. (2010) at $Re = 3.6 \times 10^6$. The k$-\epsilon$ model was used to study the effects of a gap to diameter ratio, Reynolds number, seabed roughness and boundary layer thickness $\delta$. One of the findings of this study was that the drag coefficient ($C_D$) increases as $e/D$ increases for small $e/D$, reaching a maximum value before decreasing to approach a constant value. The mean pressure coefficient ($C_p$) around the cylinder was studied and development of an asymmetry for small gap ratio ($e/D = 0.1$) was reported resulting in net positive upward lift. The effect disappears for large gap ratios and $C_p$ becomes symmetric. Rao et al. (2013) investigated numerically the flow past a stationary cylinder at different heights above a no-slip plane ranging from very small gap case $e/D = 0.005$ to freestream condition. They identified critical $Re$ in each of the simulated cases where the transition from steady two-dimensional flow to three-dimensional flow occurs. The behavior of the vortical wake created by a cylinder placed in the boundary layer flow was studied using URANS approach by Harichandan and Roy (2012). Two dimensional model was resolved using FVM solver at $Re = 100$ and $Re = 200$ respectively. Authors of the study describe the "vortex-wrapping" phenomena as the shear layer from the top and bottom cylinder surface curl up destabilizing the shear layer on the plane wall downstream of the cylinder. The vortex shedding frequency for wall proximity flows was found to be higher than for the unconfined flows. The flow past tandem of cylinders placed near a plane wall was investigated by Tang et al. (2015). Numerical simulations using two-dimensional Navier-Stokes equations were solved with a three-step finite element method at a low Reynolds number of $Re = 200$. Various gap ratios ($e/D$) and pitch lengths ($L/D$ where $L$ is the distance between the cylinder's centers) were considered. The mean drag coefficient of the upstream cylinder was found to be larger than that of the downstream cylinder for the same combination of $e/D$ and $L/D$. They noticed that change in the vortex shedding modes led to a significant increase in the RMS values of drag and lift coefficients. D'Souza et al. (2016) studied the dynamics of the flow of two cylinders along a moving plane wall at $Re = 200$. The interaction with the wall boundary layer was thus removed and the focus of the study was on the influence of the wall proximity effects and the wake dynamics. The study revealed an early transition from the reattachment to co-shedding behavior. Specifically at $Re = 200$ for $e/D = 0.5$ the

combined wake interference and wall proximity effects lead to a parallel double-row of vortices for the tandem cylinders. Turbulent flow dynamics was the main objective of the study of the flow around one cylinder (Abrahamsen Prsič et al. (2016)) and two cylinders (Li et al. (2018)) in the vicinity of a horizontal plane wall. In both studies, Large Eddy Simulations (LES) with Smagorinsky subgrid scale model was used to accurately capture the turbulence effect at $Re = 13.100$. Abrahamsen Prsič et al. (2016) investigated the effect of the incoming boundary layer profile by comparing the uniform inlet flow profile with two logarithmic boundary layer profiles $\delta = 0.48D$ and $\delta = 1.6D$. The importance of boundary layer thickness is manifested by decreasing RMS lift coefficient as the cylinder becomes immersed in the boundary layer. In Li et al. (2018) six sets of simulations were performed at $e/D = 0.1, 0.3$ and $0.5$ and pitch length $L/D = 2$ and $5$. The wall proximity demonstrated a decreasing effect on the mean drag coefficient of the upstream cylinder. The effects of the cylinder pitch length were manifested in the formation of cavity-like flow between the cylinders, with re-circulation zone being the most pronounced at $L/D = 2$ and $e/D = 0.1$. Both studies conclude that 3D LES simulations with subgrid scale modeling offer clear improvements over the 2D RANS approach, more accurately capturing details of the turbulent flow and associated forces.

Relatively small number of studies focuses on the freely vibrating cylinder in a proximity of a horizontal wall. In Tham et al. (2015) a 2-DoF cylinder close to the plane wall was simulated using Petrov-Galerkin FEM formulation. Gap ratio ranging from $0.5D$ to $10D$ and reduced velocities $U_r$ from 2 to 10 were analyzed at $Re = 100$. Tham et al. (2015) explored the origin of the increased streamwise oscillation of a freely vibrating cylinder near-wall as compared to the isolated case. For gap ratios lower than $e/D = 0.60$ additional branch in amplitude response was identified, namely upper branch in addition to the initial and lower branches. The effect of enhanced streamwise oscillation was explained based on the phase difference curves revealing positive net power transfer for gap ratios lower than $e/D = 0.9$. Study of Chung (2016) focused on a 1-DoF vibrating cylinder with low mass ratio and zero damping. The outcome of the numerical study at $Re = 100$ showed that cylinder vibration in the lock-in zone is controlled by either the Strouhal frequency or the natural frequency of the structure in a fluid. Strong dependence on the gap ratio and reduced velocity was experienced. The case of an impact with the wall was also investigated and has been proved to cause no change in the amplitude and frequency of cylinder vibration. A comprehensive study of the vortex-induced vibrations of a single cylinder freely vibrating in the proximity of the plane wall was presented in Li et al. (2016). Both 2D and 3D simulations were performed using a Petrov-Galerkin finite element formulation. Wall proximity effects were studied in the laminar flow regime at $Re = 200$ in a series of 2D simulations. Reasons for the enhanced

streamwise oscillations were explained in detail. The wall proximity effect was revealed to contribute to the reduction of streamwise vibration frequency by half. Streamwise frequency lock-in combined with positive net energy transfer was identified as the main mechanism behind large streamwise oscillation amplitude. The 2D simulations were supplemented by 3D simulations at $Re = 1000$ aimed at capturing the three-dimensional effects and assessing accuracy and validity of the 2D results. Over predictions of force coefficients in 2D simulations were revealed when the Reynolds number is higher than $Re = 200$.

## 1.5  Summary

The literature review presents the broad overview of the previous and current research focused on the VIV of elastically mounted cylinders. Large base of experimental and numerical work exists for the case of the freestream flow. Relatively small number of published research is focused on the near-wall effect in conjunction with the 2-DoF VIV. Furthermore, most of the published studies are investigating moderate to high Reynolds number flows. The validity of 2D simulations for low Reynolds number flows is confirmed in the available literature, on the other hand, the applicability of 2D URANS at very high Reynolds numbers has been explored only to a limited degree. It appears that further investigating the effects of wall proximity on vortex shedding mechanisms using numerical simulations at low Reynolds number could offer additional insight beyond the available literature. In the view of a very limited number of studies in the upper transition regime additional study focused on very high Reynolds flow provides an opportunity for gaining better understanding of the VIV physics.

# References

Abrahamsen Prsič, M., M. C. Ong, B. Pettersen, and D. Myrhaug (2016). Large eddy simulations of flow around a circular cylinder close to a flat seabed. *Marine Structures 46*, 127 – 148.

Anand, N. M. and A. Tørum (1985). Free span vibrations of submarine pipelines in steady flows-effect of free-stream turbulence on mean drag coefficients. *Journal of Energy Resources Technology 107*(4), 415 – 420.

Bearman, P. and M. Zdravkovich (1978). Flow around a circular cylinder near a plane boundary. *Journal of Fluid Mechanics 89*, 33 – 47.

Blevins, R. D. (1990). *Flow-Induced Vibration*. Van Nostrand Reinhold.

Chung, M.-H. (2016). Transverse vortex-induced vibration of spring-supported circular cylinder translating near a plane wall. *European Journal of Mechanics - B/Fluids 55*(Part 1), 88 – 103.

DNV GL (2017, June). Free Spanning Pipelines - Recommended Practice. Standard, DNV GL, Oslo, Norway.

D'Souza, J. E., R. K. Jaiman, and C. K. Mak (2016). Dynamics of tandem cylinders in the vicinity of a plane moving wall. *Computers & Fluids 124*(Supplement C), 117 – 135.

Feng, C. C. (1968). *The measurement of vortex induced effects in flow past stationary and oscillating circular and D-section cylinders*. Ph. D. thesis, University of British Columbia.

Fredsøe, J., B. Sumer, J. Andersen, and A. E. Hansen (1987). Transverse vibrations of a cylinder very close to a plane wall. *Journal of Offshore Mechanics and Arctic Engineering 109*, 52 – 60.

Harichandan, A. B. and A. Roy (2012). Numerical investigation of flow past single and tandem cylindrical bodies in the vicinity of a plane wall. *Journal of Fluids and Structures 33*(Supplement C), 19 – 43.

He, G.-S., J.-J. Wang, C. Pan, L.-H. Feng, Q. Gao, and A. Rinoshika (2017). Vortex dynamics for flow over a circular cylinder in proximity to a wall. *Journal of Fluid Mechanics 812*, 698 – 720.

Hsieh, S.-C., Y. M. Low, and Y.-M. Chiew (2016). Flow characteristics around a circular cylinder subjected to vortex-induced vibration near a plane boundary. *Journal of Fluids and Structures 65*(Supplement C), 257 – 277.

Li, Z., M. Abrahamsen Prsič, M. Ong, and B. Khoo (2018). Large eddy simulations of flow around two circular cylinders in tandem in the vicinity of a plane wall at small gap ratios. *Journal of Fluids and Structures 76*, 251 – 271.

Li, Z., W. Yao, K. Yang, R. K. Jaiman, and B. C. Khoo (2016). On the vortex-induced oscillations of a freely vibrating cylinder in the vicinity of a stationary plane wall. *Journal of Fluids and Structures 65*, 495 – 526.

Nakamura, T. (2016). *Flow-Induced Vibrations: Classifications and Lessons from Practical Experiences*. Elsevier Science & Technology.

Ong, M. C., T. Utnes, L. E. Holmedal, D. Myrhaug, and B. Pettersen (2010). Numerical simulation of flow around a circular cylinder close to a flat seabed at high Reynolds numbers using a k-$\epsilon$ model. *Coastal Engineering 57*(10), 931 – 947.

Rao, A., M. Thompson, T. Leweke, and K. Hourigan (2013). The flow past a circular cylinder translating at different heights above a wall. *Journal of Fluids and Structures 41*, 9 – 21.

Sarpkaya, T. S. (2010). *Wave Forces on Offshore Structures*. Cambridge University Press.

Subenesol.co.uk (2018). Piggyback clamps. http://http://www.subenesol.co.uk/. Accessed: 2018-04-30.

Sumer, B. M. and J. Fredsøe (2006). *Hydrodynamics around cylindrical strucures*. World Scientific.

Tang, G., C.-Q. Chen, M. Zhao, and L. Lu (2015). Numerical simulation of flow past twin near-wall circular cylinders in tandem arrangement at low Reynolds number. *Water Science and Engineering 8*(4), 315 – 325.

Tham, D. M. Y., P. S. Gurugubelli, Z. Li, and R. K. Jaiman (2015). Freely vibrating circular cylinder in the vicinity of a stationary wall. *Journal of Fluids and Structures 59*, 103 – 128.

Tsahalis, D. and T. W. Jones (1981). Vortex-induced vibrations of a flexible cylinder near a plane boundary in steady flow. *Journal of Energy Resources Technology 101*, 206 – 213.

Wang, X. K., Z. Hao, and S. K. Tan (2013). Vortex-induced vibrations of a neutrally buoyant circular cylinder near a plane wall. *Journal of Fluids and Structures 39*(Supplement C), 188 – 204.

Weller, H., G. Tabor, H. Jasak, and C. Fureby (2008). A tensorial approach to computational continuum mechanics using object-oriented techniques. *Computers in Physics 12*.

Yang, B., F. Gao, D.-S. Jeng, and Y. Wu (2009). Experimental study of vortex-induced vibrations of a cylinder near a rigid plane boundary in steady flow. *Acta Mechanica Sinica 25*(1), 51 – 63.

Zdravkovich, M. M. (1997). *Flow Around Circular Cylinders: Volume I: Fundamentals*. OUP Oxford.

**CHAPTER 2**

---

# FLOW AROUND CIRCULAR CYLINDER AND VORTEX-INDUCED VIBRATION

---

The present chapter provides a theoretical background of viscous fluid flow around a circular cylinder and basic concepts of vortex-induced vibration.

## 2.1 Flow Around Immersed Cylinders

Bodies immersed in a fluid stream are characterized by viscous effects (*shear* and *no-slip*) occurring near the body surface and in the wake. Such flows can be classified as boundary layer flows. Boundary layer growth and flow separation are defined by fluid forces on a microscopic level (Blevins, 1990). The flow around the circular cylinder disturbed by its presence can be divided into four regions proposed by Zdravkovich (1997), as shown in Fig. 2.1:

1. Region of retarded flow. Local time-averaged velocity, $u$, in this region is smaller than the freestream velocity $U_\infty$.

2. Boundary layer attached to the surface of the cylinder. The thickness of the boundary layers $\delta$ is very small compared with diameter $D$, therefore high-velocity gradient normal to the cylinder surface is present and shear stress effects are significant.

3. Two sideways regions where the flow is accelerated ($u > U_\infty$) and displaced.

4. Wide downstream region of separated flow: wake, where $u < U_\infty$.
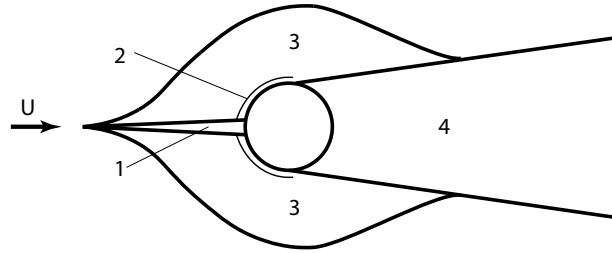


**Figure 2.1:** Regions of disturbed flow around circular cylinder, (Zdravkovich, 1997, p.4).

Reynolds number governs the ratio of inertial force to the viscous force and is expressed as:

$$Re = \frac{UD}{\nu} \tag{2.1}$$

where $\nu$ is the kinematic viscosity, $U$ is the flow velocity and $D$ is the characteristic diameter. As the Reynolds number increases from zero the flow characteristics change considerably. Sumer and Fredsøe (2006) gave a concise summary of the flow regimes of a circular cylinder in steady current. Their classification is presented in Table 2.1.

### 2.1.1   Flow Regimes

Flows with a very small $Re < 5$ are characterized by a lack of separation (*creeping flows*). At about $5 < Re < 40$ separation occurs in the form of a pair of vortices behind the cylinder. Increasing $Re$ further up leads to the phenomenon of vortex shedding which first appears at $Re = 40$. The vortices are shed alternating from each side of the cylinder with a frequency called vortex-shedding frequency, denoted $f_{st}$. The vortex street formed behind the body remains laminar in the range $40 < Re < 200$ and shedding can be treated as two-dimensional due to small variation in the spanwise direction (Sumer and Fredsøe, 2006). Three-dimensional effects become significant after the transition to turbulence occurs in the wake ($200 < Re < 300$). At $Re > 300$ the flow is characterized by the completely turbulent wake and 3D effects become significant in
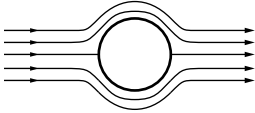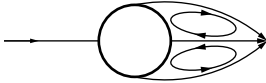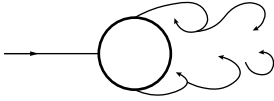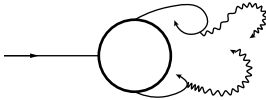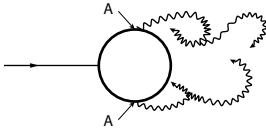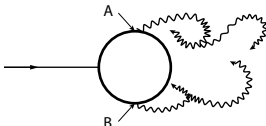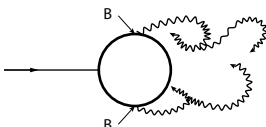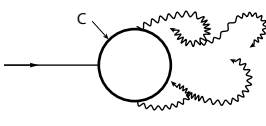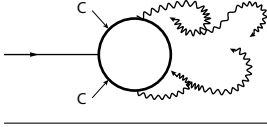
this regime. The range between $300 < Re < 3 \times 10^5$ is called the subcritical regime. Boundary layer around the cylinder is laminar in this wide range of Reynolds numbers. Lower transition regime covers approximately, $3 \times 10^5 < Re < 3.5 \times 10^5$, and separation occurs in the cylinder boundary layer at one side of the cylinder leading to an asymmetric mean lift. The supercritical regime, $3.5 \times 10^5 < Re < 1.5 \times 10^6$, is characterized by a turbulent boundary layer separation at both sides of the cylinder with transition point located between the stagnation point and separation point. In the upper transition regime, $1.5 \times 10^6 < Re < 4 \times 10^6$, fully turbulent transition develops at one side of the cylinder. After exceeding $Re > 4.5 \times 10^6$, the boundary layer around the cylinder is fully turbulent and such flow regime is called the transcritical regime.

## 2.2  Turbulence

According to Batchelor (2000) turbulent flow is a pattern of fluid motion characterized by chaotic changes in pressure and flow velocity. Turbulence has inherent features which can be listed as follows:

1. Turbulent flows are characteized by random velocity fluctuations with a wide range of length and time scales.

2. The large-scale eddying motions are strongly influenced by the geometry of the flow. In other words the boundary conditions govern the transport and mixing within the flow. The behavior of the small-scale motions can be predicted by a rate at which they receive the energy from the large scale motions in a cascading way. The smallest lenght scales are affected by the viscosity of the fluid.

3. Random nature of the fluctuations requires statistical methods to analyze it.

4. Turbulent flows are characterized by a large Reynolds number in the sense that the inertia forces dominate the viscosity effects in the flow.

5. Turbulent flows are always dissipative. This means that they lose energy and decay. Ultimately the smallest eddies dissipate into heat through the molecular viscosity.

6. Turbulent flows are characterized by enhanced diffusivity. Turbulent diffusion is much greater than that of a laminar flow (molecular diffusivity). The highly diffusive turbulence causes rapid mixing and increased rates of mass, momentum, and heat transfer.

7. Turbulent flow is highly vortical, meaning that it is rotational and characterized by high levels of fluctuating vorticity. The vorticity vector is defined as the curl of the

**Table 2.1:** Flow regimes around circular cylinder (Sumer and Fredsøe, 2006, p.2).

| | |
|---|---|
| | No separation<br>Creeping flow<br>Re < 5 |
| | Fixed pair of symmetric vortices<br>5 < Re < 40 |
| | Laminar vortex street<br>40 < Re < 200 |
| | Transition to turbulence in wake<br>200 < Re < 300 |
| | Wake completely turbulent<br>A: Laminar boundary layer separation<br>$300 < \text{Re} < 3.5 \times 10^5$ |
| | A: Laminar boundary layer separation<br>B: Turbulent boundary layer separation<br>Boundary layer still laminar<br>$3 \times 10^5 < \text{Re} < 3.5 \times 10^5$ |
| | B: Turbulent boundary layer separation<br>Boundary layer partly laminar partly turbulent<br>$3.5 \times 10^5 < \text{Re} < 1.5 \times 10^6$ |
| | C: Boundary layer completely turbulent at one side<br>$1.5 \times 10^6 < \text{Re} < 4 \times 10^6$ |
| | C: Boundary layer completely turbulent at both sides<br>$\text{Re} > 4 \times 10^6$ |

velocity vector:

$$\vec{\omega} = \nabla \times \vec{U} = \left( \frac{\partial w}{\partial y} - \frac{\partial v}{\partial z}, \frac{\partial u}{\partial z} - \frac{\partial w}{\partial x}, \frac{\partial v}{\partial x} - \frac{\partial u}{\partial y}, \right) \tag{2.2}$$

Vorticity is a measure of rotational effects, being equal to twice the local angular velocity of a fluid particle. Flow is irrotational if the vorticity is equal to zero.

8. Turbulence is inherently three-dimensional. The term two-dimensional turbulence is only used to describe the simplified case where the flow is restricted to two dimensions. Vortex stretching is the phenomenon responsible for the continuous three dimensional deformation of the primary vortices.

9. Turbulence is a continuum phenomenon and is governed by the equations of fluid mechanics. Even the smallest turbulent length scales are much larger than the molecular length.

## 2.3   Boundary Layer Concept

### 2.3.1   Laminar Boundary Layer

In the range of applicability of continuum mechanics, the flow of a real fluid has two distinct characteristics. Namely, the *no-slip* condition meaning that, at a solid surface, the velocity of a fluid relative to the surface is zero and the condition of no discontinuity of velocity (Ward-Smith, 2005). Based on those assumptions it is possible to derive the velocity profile expression in the region near a solid surface as depicted in Fig. 2.2. Equations for the laminar boundary layer were derived from Navier-Stokes equations by
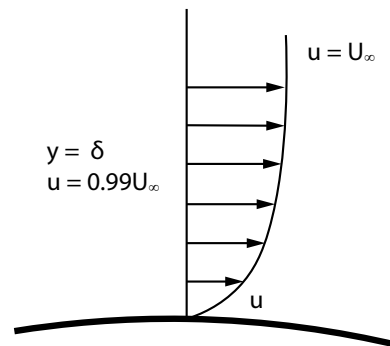


**Figure 2.2:** Velocity profile in a boundary layer (Schetz and Bowersox, 2011, p.3).

Prandtl (1904) and for a steady, two-dimensional flow they take form (White, 2006):

$$\frac{\partial u}{\partial x} + \frac{\partial v}{\partial y} = 0 \tag{2.3}$$

$$u\frac{\partial u}{\partial x} + v\frac{\partial u}{\partial y} = U\frac{dU}{dx} + \nu\frac{\partial^2 u}{\partial y^2} \tag{2.4}$$

where $U = u(x, \infty)$ is the freestream velocity, $u$ is the horizontal velocity component and $v$ is vertical the velocity component. Solution to this system of parabolic partial differential equations can be obtained numerically. In case of a laminar flow past a plate,

analytical solution was found by Blasius (1908) by using a similarity transformation. Thickness of a boundary layer was customarily taken as the distance from the solid surface at which the velocity reaches the 99% of velocity in the main stream $U_\infty$. Blasius solution can be expressed in terms of the boundary layer thickness (White, 2011):

$$\delta_{99\%} \approx \frac{5.0\,x}{\sqrt{Re_x}} \tag{2.5}$$

where $\delta$ is the boundary layer thickness, $x$ is the distance along the plate and $Re_x = \rho U x/\mu$ is the local Reynolds number. Blasius expression was derived and holds true in the situation with zero pressure gradient. Occurrence of flow separation and effects of pressure gradient are discussed in the next section.

### 2.3.1.1   Separation Point.

Adverse pressure gradient effect is the main reason behind the separation of the flow. The momentum loss near the wall in the boundary layer of a flow moving against increasing pressure gradient leads to the backflow at the wall. Bernouilli equation links pressure gradient to the edge velocity $U_\infty(x)$, so for an increasing pressure the velocity decreases:

$$u\frac{du}{ds} = -\frac{1}{\rho}\frac{dp}{ds} \tag{2.6}$$

If the pressure varies in the direction of a flow it can greatly affect the behavior of the fluid. In case of a flow over the curved surface with curvature large compared to the boundary layer thickness the velocity profile forms as shown in Fig. 2.3. Second
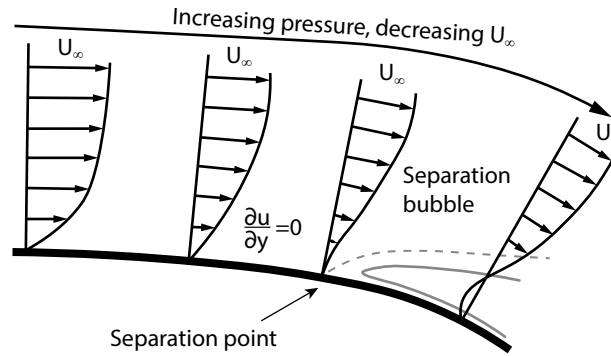


**Figure 2.3:** Separation of a boundary layer over curved surface (Schetz and Bowersox, 2011, p.24).

derivative of velocity $u$ at the wall can be used to explain the flow separation. From the momentum equation (Eq. 2.4) at the wall, where $u = v = 0$, we obtain:

$$\left.\frac{\partial\tau}{\partial y}\right|_{wall} = \left.\mu\frac{\partial^2 u}{\partial y^2}\right|_{wall} = -\rho U\frac{dU}{dx} = \frac{dp}{dx} \tag{2.7}$$

To ensure smooth transition with the freestream flow the velocity profile must have a negative curvature. The wall curvature has the sign of the pressure gradient. In case of an adverse pressure gradient the second derivative of velocity is positive at the wall but it must be negative at the outer layer ($y = \delta$) to merge with the freestream flow $U_\infty(x)$. It is therefore required that point of inflection exists at which the curvature changes signs from positive to negative. It should be noted that laminar flows separates easily in adverse gradients whereas turbulent boundary layer is more resistant due to increased wall friction and heat transfer.

### 2.3.2 Turbulent Boundary Layer

Situation of a flow over a flat plate with a uniform velocity profile is presented in Figure 2.4. The formation of a boundary layer can be separated into three distinct regions. The laminar region, the transition region and, the turbulent region. In a close proximity to the plate surface, the fluid particles are subject to no-slip condition and their velocity becomes zero resulting in the formation of a viscous sublayer. This results in the shear stress development in the thin fluid layer close to a plate. After some distance the flow becomes unstable and eddies are formed. This region is called a transition region. It should be noted that transition process is unsteady and is difficult to predict, even with modern CFD codes (Çengel and Cimbala, 2010, p. 558). Further downstream the plate, a turbulent boundary layer is formed. The viscous sublayer is characterized by very high
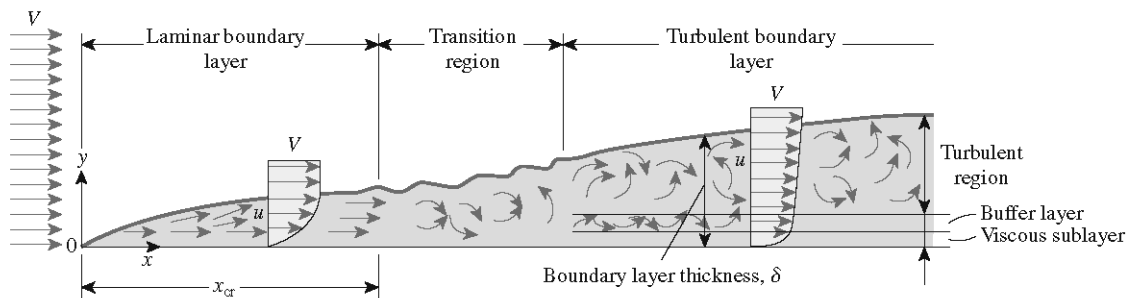


**Figure 2.4:** Formation of the laminar and turbulent boundary layer (Çengel and Cimbala, 2010, p.558).

turbulent energy production rate. It is estimated that in this region more than 30% of the total production and dissipation takes place (Cebeci and Cousteix, 2009). The turbulent boundary layer can be treated as a composite layer which is composed of an inner and outer region (Fig. 2.4). The inner layer is about the laminar boundary layer thickness and is further divided into a linear sublayer, buffer layer and, log-law region. The outer layer is about 85% of the total boundary layer thickness (Cebeci and Cousteix, 2009).

### 2.3.3  Plus Units

Plus units are non-dimensional variables used in turbulent boundary layer analysis. They are defined as:

$$y^+ = \frac{u_\tau r}{\nu}, \quad U^+ = \frac{U}{u_\tau}, \quad Re_\tau = \frac{u_\tau H}{\nu} \tag{2.8}$$

where $y^+$ is the non-dimensional distance from the wall, $U^+$ is the non-dimensional velocity and $Re_\tau$ is the Reynolds number based on shear velocity $u_\tau = \sqrt{\tau_w/\rho}$, $\tau_w$ is the shear stress at the wall and $H$ is the radius of the control volume.

### 2.3.4  Law-of-the-wall

The velocity profile of a fully turbulent boundary layer can be non-dimensionalized using the derived plus units. The curve shape in the inner layer close to the wall is common for all Reynolds numbers. This relation was first observed and described by von Kármán in 1930. Figure 2.5 shows the plot of the velocity distribution in the inner layer. This universal curve is referred to as the law-of-the-wall. The equations relating the velocity to the nondimensional distance from the wall can be derived for the linear sublayer and for the outer layer. Close to the wall the velocity varies linearly with the nondimensional wall distance:

$$U^+ = y^+ \tag{2.9}$$

Further away from the wall at a distance where the kinematic viscosity is negligible the velocity can be approximated by:

$$U^+ = \frac{1}{\kappa} \ln(y^+) + C^+ \tag{2.10}$$

where $\kappa$ is the von Kármán constant, usually equal to 0.41, $C^+$ is an integration constant, commonly taken as 5.1. Assuming the linear variation of $\tau_w$ with increasing $y$, the velocity distribution in the inner layer is a function of the wall shear stress $\tau_w$, kinematic viscosity $\nu$ and the distance from the wall $y$. The approximate range of the viscous sublayer is in the range of $0 < y^+ < 5$. The log-law region is defined at $30 < y^+$ where Eq. 2.9 is a good approximation of the velocity profile. A buffer region exists in the range of $5 < y^+ < 30$ where neither Eq. 2.10 nor Eq. 2.9 applies. This region is of particular importance in CFD simulations of turbulent flows using the wall function approach.
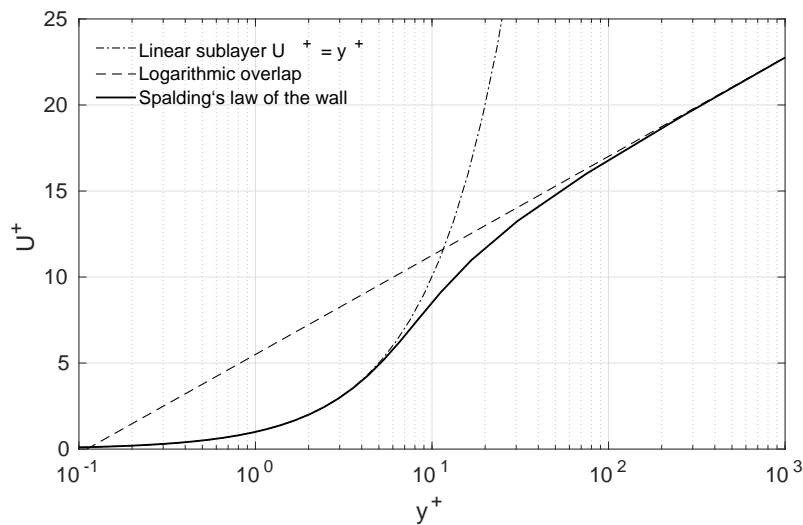
**Figure 2.5:** The inner layer of a turbulent boundary layer.

## 2.4   Vortex Shedding

Vortex shedding is a result of the basic instability which exists between the two free shear layers released from the separation points at each side of the cylinder into the downstream flow from the separation points. These free shear layers roll-up and feed vorticity and circulation into large discrete vortices which form alternately on opposite sides of the cylinder.

### 2.4.1   Mechanism of Vortex Shedding

Phenomenon of vortex-shedding is common for all flow regimes for $Re > 40$. Due to the reasons explained in the previous section the boundary layer over the cylinder surface will separate and shear layers will be formed. The separated boundary layer is characterized by high vorticity which is then subject of the shear layer roll up into the vortex with an identical sign. Vortices rotating in opposite direction are thus formed at both sides of the cylinder. These vortices are very sensitive to the disturbances in the flow and in consequence one of the formed vortices will become dominating and will draw the opposite vortex across the wake (Sumer and Fredsøe, 2006). The opposite sign of the vorticity carried by the drawn vortex leads to cut off of the dominating vortex from the boundary layer and formation of the free vortex. After the vortex is shed, it is convected downstream in the wake. The drawn vortex will now become dominant and will draw newly formed vortex on the opposite side. The whole cycle repeats on the opposite side of the cylinder. This leads to the cyclic shedding of the vortices behind the cylinder.
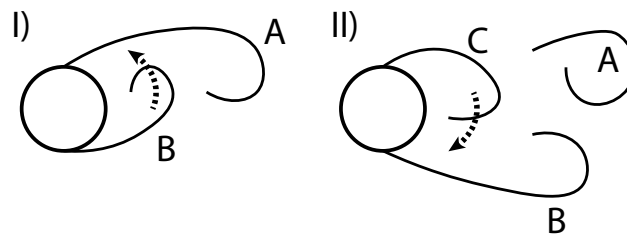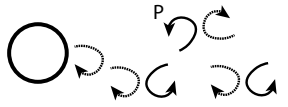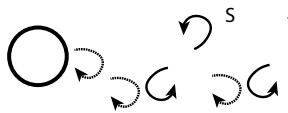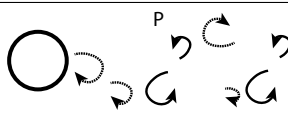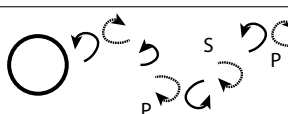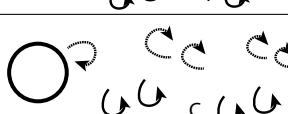
**Figure 2.6:** Vortex shedding mechanism (Sumer and Fredsøe, 2006, p.8).

## 2.4.2  Vortex Shedding Patterns

The vortex shedding can be characterized by the pattern in which the vortices are formed. A thorough review of the shedding patterns and proposed classification was given in Williamson and Roshko (1988), Williamson and Govardhan (2004), Jauvtis and Williamson (2004) and Morse and Williamson (2009). The symbols, patterns and corresponding examples of vorticity contours were given in Table 2.2. Short classification of the modes based on the text by Williamson and Govardhan (2004) can be summarized as follows:

- 2S mode is characterized by the alternate shedding of one vortex from each side of the cylinder.

- 2P mode is distinguished by pairs of vortices of the same vorticity sign thus two vortices are shed from each side during one cycle.

- P + S mode is formed by a pattern wherein each cycle a vortex pair and a single vortex are formed.

- 2Po mode is similar to 2P mode, but a secondary vortex in each pair is significantly smaller than the primary vortex.

- 2P + 2S mode is comprised of two vortex pairs, formed alternatively like in 2P mode but additional vortex appears in between.

- 2T mode can be recognized by a characteristic triplet of vortices formed in each half cycle. In each triplet, two vortices have the same sign and one vortex of opposite sign is formed.

- 2C mode is similar to 2T mode but a doublet of vortices is formed instead of a triplet. Both vortices have the same sign and full cycle comprises formation of four vortices, two on each side of the cylinder.

**Table 2.2:** Vortex shedding patterns (Williamson and Govardhan, 2004).



## 2.5  Hydrodynamic Forces

### 2.5.1  Forces on a Cylinder in Steady Current

Following discussion is based on Sumer and Fredsøe (2006). The total force acting on the surface of the cylinder in steady flow can be divided into two components, namely the pressure component and the viscous component. The forces acting in two directions: in-line (IL) and cross-flow (CF) can be found by integrating the orthogonal components of pressure and viscous forces along the cylinder surface. The total force acting in the IL direction is the mean drag $\overline{F_D}$ and is a sum of mean form drag $\overline{F_p}$ (due to the pressure) and mean friction drag $\overline{F_f}$ (due to the viscous forces). Force acting in the CF direction - mean lift force $\overline{F_L}$ - is defined in a similar way. In the case of a cylinder in the free stream flow, the $\overline{F_L}$ will be equal zero due to the symmetry of the flow, however, for $Re > 40$ the vortex shedding phenomenon occurs and instantaneous CF force on the cylinder will be non-zero.

Change of the pressure distribution over the cylinder surface during a shedding cycle was shown in Fig. 2.7. It is evident that due to the periodic change of the pressure distribution the force components will also exhibit the periodic variation. Due to vortex
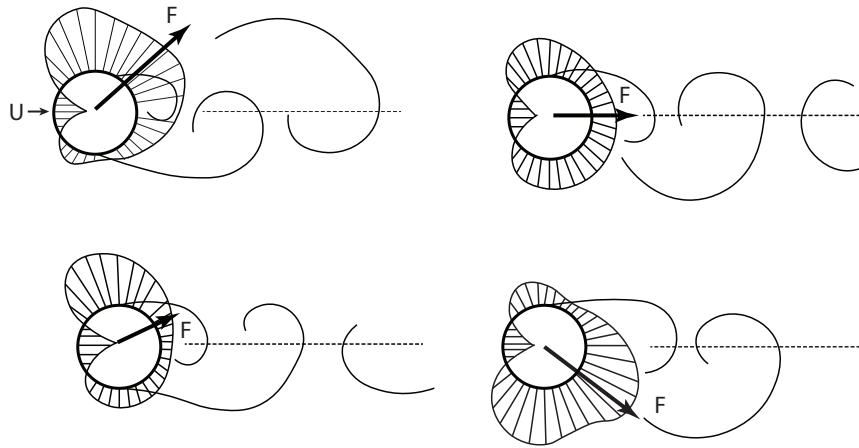


**Figure 2.7:** Development of pressure distribution and force during vortex shedding cycle (Sumer and Fredsøe, 2006, p.38).

shedding the velocity of the flow around the cylinder will change periodically at the top and bottom surface. When a vortex is shed at the lower edge of the cylinder the upward lift is developed. The velocity will be higher on the lower edge and the pressure at the bottom will then be larger than at the top according to Bernoulli's equation. This induces the force which will be directed upwards. After the other vortex is developed at the opposite side, the situation is inverse and result is a force directed downwards. Each complete vortex shedding cycle comprises the effects of a complementary pair of vortices. Cylinder with low structural damping properties will be thus forced to vibrate in the CF and to a lesser extent in the IL directions.

### 2.5.2   Drag and Lift Coefficients

The dimensionless drag coefficient ($C_D$) for a smooth cylinder is a function of $Re$ and is expressed as:

$$C_D = \frac{\overline{F_D}}{\frac{1}{2}\rho U^2 A} \tag{2.11}$$

The lift coefficient is defined as:

$$C_L = \frac{\overline{F_L}}{\frac{1}{2}\rho U^2 A} \tag{2.12}$$

where: $\overline{F_L}$ is the mean lift force, $\overline{F_D}$ is the mean drag force, $\rho$ is the density of a fluid, $U$ is the flow velocity and $A$ is the projected area perpendicular to the incoming flow. The denominator in both expressions is the product of the dynamic pressure of the undisturbed flow and the specified projected area. Therefore as a ratio of two forces the drag and lift coefficients are the same for two dynamically similar flows.

### 2.5.3   Pressure Coefficient and Skin-friction Coefficient

The pressure coefficient gives the ratio of static pressure to dynamic pressure and is expressed as:

$$C_p = \frac{p - p_\infty}{\frac{1}{2}\rho U_\infty^2} \tag{2.13}$$

where $p$ is the static pressure at the evaluated point, $p_\infty$ is the static pressure in the freestream, $\rho$ is the density of a fluid and $U_\infty$ is the freestream flow velocity. $C_p$ equal one indicates stagnation point as it corresponds to stagnation pressure. The dimensionless number that relates the wall shear stress to dynamic pressure is skin-friction coefficient, defined as:

$$C_f = \frac{\tau_w}{\frac{1}{2}\rho U_\infty^2} \tag{2.14}$$

where $\tau_w = \mu \frac{\partial u}{\partial y}$ is the local wall shear stress. An approximate point of separation can be found at the location where $C_f = 0$ indicating that $\tau_w$ changes sign from positive to negative.

## 2.6   Dynamic Equations of Motion

### 2.6.1   Solutions of a Viscous Damped Vibration Equation

In case of a single DoF freely oscillating system the equation of motion in the form (Inman, 2013):

$$m\ddot{x}(t) + c\dot{x}(t) + kx(t) = 0 \tag{2.15}$$

where $m$ is the mass of the system, $c$ is the damping coefficient, $k$ is the spring stiffness, $x(t)$ is the displacement, $\dot{x}(t)$ denotes the velocity and $\ddot{x}(t)$ is the acceleration. To find the solution to Eq. (2.15) one can write the equation in the form:

$$(m\lambda^2 + c\lambda + k)ae^{\lambda t} = 0 \tag{2.16}$$

The term $ae^{\lambda t} \neq 0$ so that this reduces Eq. (2.16) to a characteristic equation which is quadratic equation of $\lambda$ variable:

$$m\lambda^2 + c\lambda + k = 0 \tag{2.17}$$

Solving quadratic formula yields two solutions:

$$\lambda_{1,2} = -\frac{c}{2m} \pm \frac{1}{2m}\sqrt{c^2 - 4km} \tag{2.18}$$

It can be shown that depending on the value of the discriminant, $c^2 - 4km$, the roots of Eq. (2.18) will be real or complex. As long as $m$, $c$, and $k$ are positive real numbers, $\lambda_1$ and $\lambda_2$ will be distinct negative real numbers if $c^2 - 4km > 0$. If the discriminant is negative, the roots will be a complex conjugate pair with a negative real part. If the discriminant is zero, the two roots $\lambda_1$ and $\lambda_2$ are equal negative real numbers. It is useful to define the critical damping coefficient $c_{cr}$ by:

$$c_{cr} = 2\,m\,\omega_n = 2\sqrt{km} \tag{2.19}$$

where: $\omega_n$ is the undamped natural frequency. The nondimensional number $\zeta$ called damping ratio can be defined as:

$$\zeta = \frac{c}{c_{cr}} = \frac{c}{2\sqrt{km}} \tag{2.20}$$

It can be shown that the nature of the roots and and hence the behavior of the solution, Eq. (2.15), depends upon the magnitude of damping. Underdamped motion occurs when $0 < \zeta < 1$ and discriminant in Eq. (2.18) is negative. Overdamped motion requires that $\zeta > 1$, and critically damped motions, as follows from Eq. (2.20), when $\zeta = 1$.

### 2.6.2  Dynamics of 2-Dof Systems in Fluid Flow

The equations of motion of the two-degree-of-freedom dynamic system can be given in a following form:

$$m\ddot{x}(t) + c\dot{x}(t) + kx(t) = F_x(t) \tag{2.21}$$

$$m\ddot{y}(t) + c\dot{y}(t) + ky(t) = F_y(t) \tag{2.22}$$

where $m$ is the total mass of the system including hydrodynamic added mass, $c_x, c_y$ are damping coefficients in $x$ direction and $y$ direction respectively, $k_x, k_y$ denote the spring stiffness in $x$ direction and $y$ direction respectively, $x,\dot{x},\ddot{x}$ is the displacement, velocity and acceleration in $x$ direction, $y,\dot{y},\ddot{y}$ is the displacement, velocity and acceleration in $y$

direction, $F_x$ is the force induced by vortex shedding acting in $x$ direction and $F_y$ denotes the force induced by vortex shedding acting in $y$ direction.

For a vibrating system, a feed-back between the motion of the structure, and the hydrodynamic forces exists. According to Sumer and Fredsøe (2006) the major problem encountered in the mathematical and numerical treatment of vibrations is the correct representation of the exciting force $F(t)$. The solution can be obtained by using a simplified harmonic models like van der Pol's wake-oscilator model or semi empirical frequency domain methods. Second approach which is employed in this study is based on obtaining the $F(t)$ directly from the solution of Navier-Stokes equations. The equations of motion Eq. (2.21) are then coupled with the flow equations and the whole system is solved numerically. Navier-Stokes equations and more detailed discussion of the solution procedure are given in Chapter 3.

## 2.7    Vortex-Induced Vibrations

Elastically mounted cylinder placed in a flow characterized by a Reynolds number higher than $Re > 40$ will be subject to vortex shedding. The oscillating hydrodynamic forces may then induce the vibrations of the cylinder, called the vortex-induced vibrations. In the most synthetic form, the VIV phenomenon can be regarded as a feedback between the body motion and vortex motion with many parameters influencing this interaction. It is useful to define properly different frequencies used in the description of the vortex-induced-vibrations. We can list them as follows:

- $f_{vac} = \frac{1}{2\pi}\sqrt{\frac{k}{m}}$ - natural frequency of a structure measured in vacuum;

- $f_n = \frac{1}{2\pi}\sqrt{\frac{k}{m+m_a}}$ - natural frequency of a system (e.g. cylinder in air, in still water, in steady current in water);

- $f_{st}$ - vortex shedding frequency (called also Strouhal frequency) of a body at rest;

- $f_{vs}$ - vortex shedding frequency of a body in motion;

- $f_{osc}$ - oscillation frequency.

### 2.7.1    Influencing Parameters

The vortex-induced vibrations are governed by several influencing parameters which can be divided into three main groups: flow parameters, structural parameters and,

interaction parameters. A full overview of the influencing parameters and their effect on the VIV will be given in subsequent paragraphs. According to Sarpkaya (2004) the nondimensional Strouhal number emerges as the most robust one.

### 2.7.2  Strouhal Number

Strouhal number is the dimensionless proportionality constant given as the ratio between the predominant frequency of vortex shedding and the diameter of cylinder:

$$St = \frac{f_{st}D}{U} \tag{2.23}$$

where $f_{st}$ is the frequency of vortex shedding, $D$ is the diameter of the cylinder and $U$ is the flow velocity. The Strouhal number is a function of Reynolds number. Figure 2.8 presents $St$ change in relation to $Re$. From Figure 2.8 it can be seen that at $Re = 40$ the Strouhal number is approximately equal to 0.1 and increases gradually to 0.2 at $Re = 300$. It remains approximately constant in the subcritical range and experiences a sudden increase in the critical range ($Re = 3 - 3.5 \times 10^5$). The reason behind the jump in $St$ value is the transition to fully turbulent boundary layer and relocation of the separation points further downstream. The consequence of this is a higher frequency of vortex shedding as the vortices formed in the cylinder's shear layers can interact with each other at a faster rate.
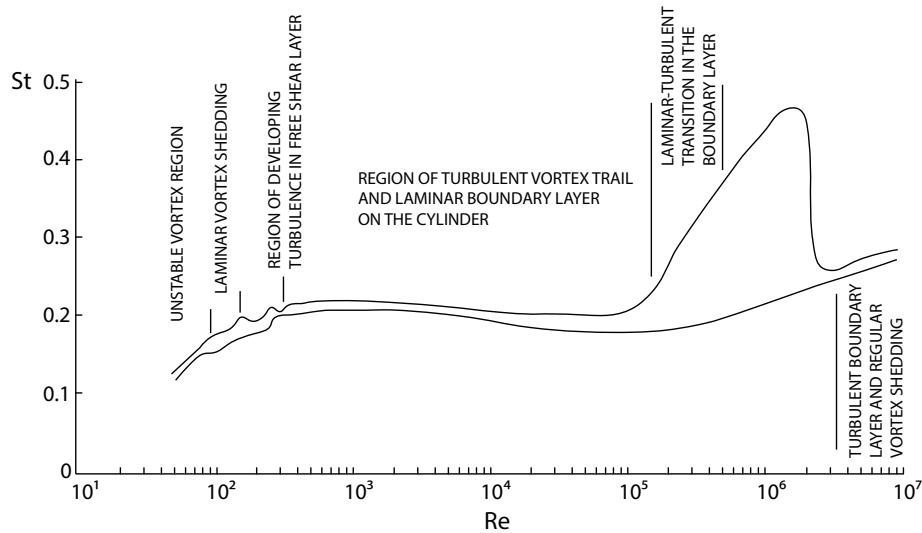


**Figure 2.8:** Strouhal - Reynolds number relationship for circular cylinders by Lienhard (1966), figure reproduced from (Sarpkaya, 2010, p. 53).

### 2.7.3  Mass Ratio

The ratio of the cylinder mass per unit length to the mass of a fluid it displaces is called the mass ratio:

$$m^* = \frac{m}{\rho \pi \frac{D^2}{4} L} \tag{2.24}$$

The mass ratio expresses the relative importance of the buoyancy and added mass effects on the body and can be regarded as a measure of the susceptibility of a structure to flow-induced vibrations. Low mass ratio structures demonstrate a wider range of synchronization in terms of reduced velocity at which the resonance occurs.

### 2.7.4  Reduced Velocity

The length of the path of a body vibrating in the fluid can be expressed as a ratio of flow velocity to the vibration frequency $U/f_n$. When normalized by the characteristic dimension of the structure ($D$ in case of a cylinder) the dimensionless reduced velocity is given:

$$U_r = \frac{U}{f_n D} \tag{2.25}$$

### 2.7.5  Added Mass

Unsteady flow around the submerged body (due to fluid acceleration or body acceleration) will result in the additional force exerted on the body which can be attributed to the disturbance of the surrounding fluid. Therefore, in the case of a structure vibrating in fluid, the equation of motion Eq. (2.21) has to be modified to account for this additional force. This force is proportional to the relative acceleration between the body and the fluid. The added mass force opposes the motion of the body, thus modified equation of motion can be then expressed as:

$$m\ddot{x} + c\dot{x} + kx = F_x - m_a \ddot{x} \tag{2.26}$$

where $m_a$ is the hydrodynamic added mass. Rearranging the terms the equation of motion becomes:

$$(m + m_a)\ddot{x} + c\dot{x} + kx = F_x \tag{2.27}$$

It is evident that the added mass will affect the natural frequency of the system, thus the new natural frequency can be found as:

$$\omega_n = \sqrt{\frac{k}{m}} = \sqrt{\frac{k}{m + m_a}} \tag{2.28}$$

The added mass is strongly dependent on the non-dimensional oscillation frequency, $\hat{f} = \frac{f_{osc}D}{U}$ and the amplitude ratio, $\frac{A}{D}$. This causes the natural frequency to change, which means it is possible to have a resonance over a range of excitation frequencies, or flow velocities.

### 2.7.6   Frequency Lock-in

Numerous experiments have shown that a cylinder with low material damping $\zeta$ and proper reduced mass $m^*$ can be excited by the vortices it sheds if it is elastically mounted and exposed to a steady uniform flow (Sarpkaya, 2004). When the vortex shedding frequency $f_{vs}$ and natural frequency of the system $f_n$ approach common frequency the cylinder will start to experience vortex-induced vibrations at oscillation frequency $f_{osc}$. Following that the $f_{vs}$ locks onto the $f_{osc}$ for a certain range of reduced velocity. Within the lock-in range, the structure experiences large amplitude oscillations as shown in Fig. 2.10. Figure 2.9 presents the results of an experiment by Anand and Tørum (1985) with flexibly mounted cylinder in steady current. The lock-in phenomenon can be observed,
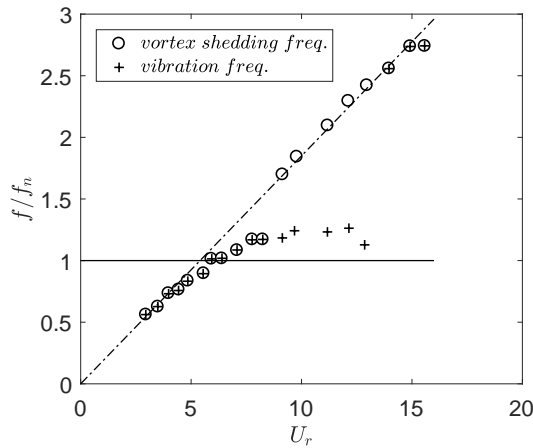


**Figure 2.9:** Experimental vortex shedding frequencies and oscillation frequencies of submerged cylinder by Anand and Tørum (1985), figure reproduced from (Sumer and Fredsøe, 2006, p. 359).

starting approximately at $U_r = 4$. Increasing reduced velocity further it can be noted that $f_{osc}$ departs from following the Strouhal relation. Due to the motion of the cylinder, the vortices are forced to interact at a frequency close to the oscillation frequency rather than

the Strouhal frequency. Furthermore, the added mass is frequency dependent and thus the natural frequency of the oscillating system will deviate from the natural frequency in still water. The oscillation frequency increases monotonously with $U_r$. For a cylinder vibrating in steady current $f_{osc}$ becomes a compromise between $f_n$ and $f_{vs}$. The VIV phenomenon is self-limiting in nature. The reason for this behavior lies in the energy balance between the hydrodynamic forcing and fluid damping. The response amplitude and flow velocity govern this process. When the $A/D$ is small the vortex shedding provides positive net energy transfer from the fluid to the structure, which in turn, lead to the increase of the oscillation amplitude. At a certain point, the equilibrium is reached and the structure is in the lock-in region. When the reduced velocity exceeds certain limit either due to the increased flow velocity or due to the increase of the amplitude of oscillation the vortices are shed before the cylinder reaches $A_{max}/D$. The vortex shedding $f_{vs}$ falls out of synchronization with the oscillation frequency $f_{osc}$, as an outcome the lift force opposing the transverse motion of the cylinder is developed. The net energy balance is then negative and lock-in is terminated.
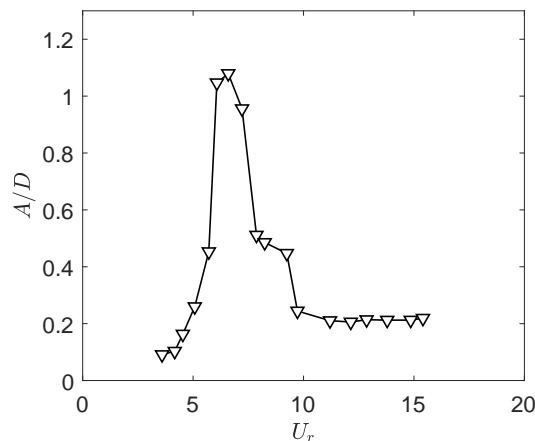


**Figure 2.10:** Cross-flow response of a flexibly-mounted circular cylinder subject to steady current, in water by Anand and Tørum (1985), figure reproduced from (Sumer and Fredsøe, 2006, p. 359).

### 2.7.7  Response Amplitude

The amplitudes of vibration in the lock-in region are not the same for each velocity. The amplitude curve splits into three distinct branches for low mass damping systems. Figure 2.11 shows how the amplitudes vary over a range of reduced velocities. The switch between initial and upper branch is hysteretic, while the switch between upper and lower branch is intermittent. These switches are attributed to a change in phase
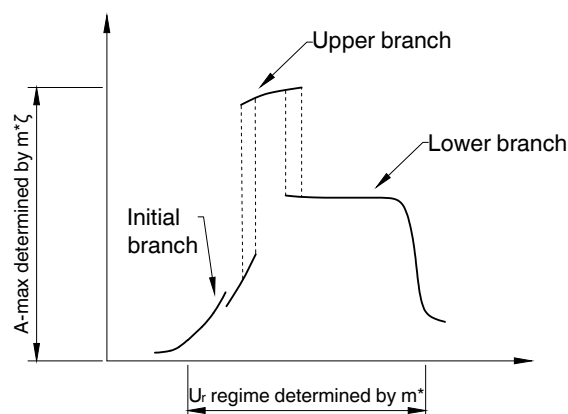
**Figure 2.11:** Overview diagram of a low mass-damping type response (Williamson and Govardhan, 2004, p. 426).

between the exciting force and the motion of the cylinder. This phase difference also influences how cross-flow and in-line vibrations interact.

### 2.7.8   Effect of Wall Proximity

The proximity of a boundary affects the flow around the cylinder in multiple ways, altering the magnitude of hydrodynamic forces. The dependency on additional influencing parameters beyond Reynolds number is manifested. Gap to diameter ratio $e/D$ and relative boundary layer thickness $\delta/D$ play an important role. According to Sumer and Fredsøe (2006), when a cylinder is placed near a plane wall, a number of changes occur in the flow around the cylinder. These changes are summarized as follows:

- When the gap-ratio ($e/D$) is smaller than 0.3, the vortex shedding will be suppressed. In the contact regime $e/D = 0$ periodic shedding is not found resulting in a completely random wake.

- The stagnation point will move to a lower angular position as seen in Fig. 2.13, which is caused by the asymmetry of the pressure distribution.

- The angular position of the separation point (denoted as S in Fig. 2.13) will change. The separation point at the free-stream side of the cylinder will move upstream and that at the wall side moves downstream.

- The suction is larger on the free-stream side of the cylinder than on the wall-side of the cylinder as seen in Fig. 2.12. This results in non zero mean lift force.
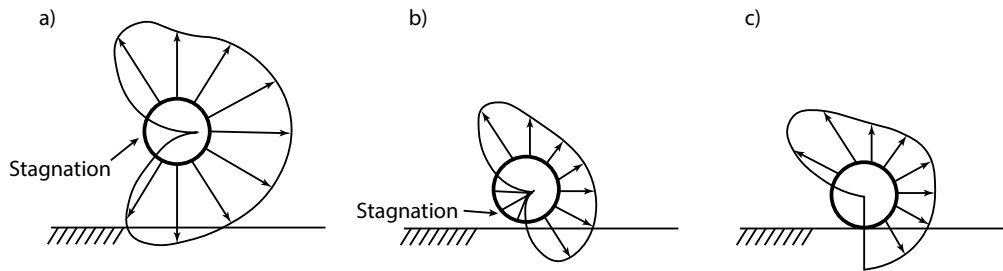
**Figure 2.12:** Changes in pressure distribution and stagnation point - cylinder placed in a proximity of a wall (Sumer and Fredsøe, 2006, p. 58).

According to Sumer and Fredsøe (2006), the drag coefficient decreases with decreasing gap ratio near wall. This remark is consistent with the pressure distribution that we see in Fig. 2.12 where the pressure in horizontal direction is getting smaller as the gap ratio decreases. The mean flow around the near-wall cylinder is not symmetric, therefore a
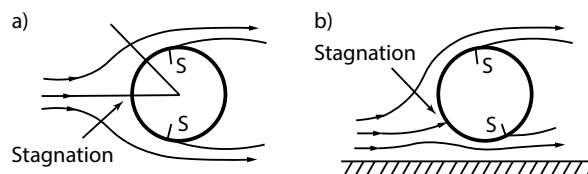


**Figure 2.13:** Streamlines and stagnation point around the cylinder in freestream and near-wall configuration (Sumer and Fredsøe, 2006, p. 21).

non-zero mean lift must exist. This is a major difference when compared to the case of a free cylinder where the mean lift coefficient is always zero. Sumer and Fredsøe (2006) explained that while the lift is fairly small for moderately small gap ratios (e/D = 0.2 - 0.3), it increases as the gap ratio is decreased.

## 2.8  Summary

A brief theory review of hydrodynamics and vibration of circular cylinders is outlined in the present chapter. From the discussion follows that the vortex-induced vibrations are governed by a number of parameters. One of the most important parameter is the Reynolds number which greatly affects the boundary layer and vortex shedding physics. The Strouhal-Reynolds relationship relates the nondimensional shedding frequency with the flow parameters. Nevertheless additional factors like a surface roughness can have large effect on the Strouhal number, in particular at very high Reynolds numbers. The

structural dynamics plays equally important role. As pointed out by Williamson and Govardhan (2004) the mass-damping parameter is the key parameter influencing the response of a structure. Characteristic response branches can be associated with the value of mass-damping. The width of the synchronization range increases with decreasing mass ratio. This relation is important for marine structures due to the high density of the fluid. The disturbance of the flow field can have a significant influence on the hydrodynamic forces acting on the cylinder as demonstrated by the proximity of the wall effects.

# References

Anand, N. M. and A. Tørum (1985). Free span vibrations of submarine pipelines in steady flows-effect of free-stream turbulence on mean drag coefficients. *Journal of Energy Resources Technology 107*(4), 415 – 420.

Batchelor, G. K. (2000). *An introduction to fluid dynamics*. Cambridge University Press.

Blevins, R. D. (1990). *Flow-Induced Vibration*. Van Nostrand Reinhold.

Cebeci, T. and J. Cousteix (2009). *Modeling and Computation of Boundary-Layer Flows: Laminar, Turbulent and Transitional Boundary Layers in Incompressible and Compressible Flows*. Springer.

Çengel, Y. A. and J. M. Cimbala (2010). *Fluid Mechanics: Fundamentals and Applications*. McGraw-Hill Higher Education.

Inman, D. (2013). *Engineering Vibrations, International Edition*. Pearson Education Limited.

Sarpkaya, T. S. (2004). A critical review of the intrinsic nature of vortex-induced vibrations. *Journal of Fluids and Structures 19*(4), 389 – 447.

Sarpkaya, T. S. (2010). *Wave Forces on Offshore Structures*. Cambridge University Press.

Schetz, J. A. and R. D. W. Bowersox (2011). *Boundary Layer Analysis*. American Institute of Aeronautics and Astronautics.

Sumer, B. M. and J. Fredsøe (2006). *Hydrodynamics around cylindrical strucures*. World Scientific.

Ward-Smith, J. (2005). *Mechanics of Fluids, Eighth Edition*. Taylor & Francis.

White, F. M. (2006). *Viscous Fluid Flow*. McGraw-Hill Higher Education.

White, F. M. (2011). *Fluid Mechanics*. McGraw Hill Higher Education.

Williamson, C. H. K. and R. Govardhan (2004). Vortex-induced vibrations. *Annual Review of Fluid Mechanics 36*(1), 413 – 455.

Zdravkovich, M. M. (1997). *Flow Around Circular Cylinders: Volume I: Fundamentals*. OUP Oxford.

# CHAPTER 3

# COMPUTATIONAL FLUID DYNAMICS

General concepts of Computational Fluid Dynamics and Finite Volume Method are presented in the present chapter. A brief description of the OPENFOAM code used for the simulations is given. Theory of the Finite Volume discretization outlined in this chapter is based on the texts of Cebeci et al. (2009), Ferziger and Perić (2012) and Versteeg and Malalasekera (2007).

## 3.1 Introduction

Decreasing cost of computing power is the main driver of the rapid development of numerical methods in fluid dynamics. Due to the complexity of the fluid motion and high computational cost, use of CFD was originally limited to research applications and major projects in the aerospace industry. Increase in affordability enabled employment of CFD as a design tool in many engineering applications. Presently the computer simulations are regarded as a third main scientific method, next to experimental development and mathematical theory, effectively bridging the gap between them. Types of simulated flows vary greatly in terms of complexity, size of the problem, level of required accuracy and physical properties of interest (e.g. compressibility or heat transfer). Direct

solution (DNS - Direct Numerical Simulation) of Navier-Stokes equations, which govern the motion of a Newtonian viscous fluid is in most cases prohibitively expensive, therefore numerous approximate methods were developed in the field of CFD. The choice of the appropriate method is crucial for maintaining the balance between computational efficiency and accuracy.

## 3.2  OpenFOAM

OPENFOAM is an object-oriented C++ framework that can be used to build numerical solvers for problems in continuum mechanics using a finite volume approach (Moukalled et al., 2015). The software is organized as a set of applications and libraries without proprietary graphical user interface (GUI). Setting up and running simulation tasks is carried out using the appropriate text files and terminal commands. The OPENFOAM simulation case is a file directory containing configuration files, mesh information and file subdirectories used to store the simulation data.

```
Case Directory
 📁 0
    📁 p
    📁 pointDisplacement
    📁 U
 📁 constant
    📁 polyMesh
       📁 boundary
       📁 ...
    📁 dynamicMeshDict
    📁 turbulenceProperties
 📁 system
    📁 controlDict
    📁 fvSchemes
    📁 fvSolution
    📁 ...
```
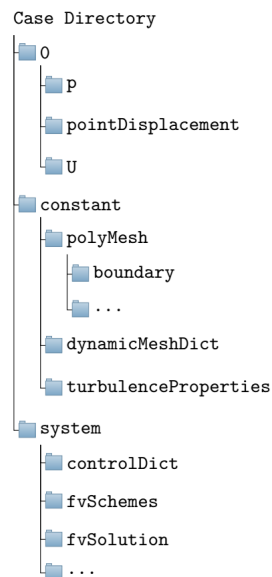
**Figure 3.1:** Simulation case directory structure.

### 3.2.1  Case Directory Structure

The case structure in present work is shown in Fig. 3.1. Directory 0 contains initial and boundary conditions for the resolved scalar and vector fields, namely pressure field p,

velocity field `U` and the mesh morphing `pointDisplacement`. Directory `constant` stores the mesh data in the `polyMesh` folder, where the settings of the boundary conditions are specified, `dynamicMeshDict` is a control file for mesh motion solver used to morph the mesh around the moving body (cylinder). `turbulenceProperties` define the turbulence model settings if turbulence modeling is used. In the `system` directory numerical solvers (`fvSolution`) and discretization schemes (`fvSchemes`) are defined. Time step and runtime variables are defined in the `controlDict`, database controls I/O are also specified in this file.

## 3.3  Governing Equations

Navier-Stokes equations for an incompressible, viscous, three-dimensional flow form the governing equations of considered flow problem and are given in differential form as:

- Continuity equation

$$\frac{\partial u}{\partial x} + \frac{\partial v}{\partial y} + \frac{\partial w}{\partial z} = 0 \tag{3.1}$$

- $x$-component of the momentum equation

$$\frac{Du}{Dt} = -\frac{1}{\rho}\frac{\partial p}{\partial x} + \nu\nabla^2 u + f_x \tag{3.2}$$

- $y$-component of the momentum equation

$$\frac{Dv}{Dt} = -\frac{1}{\rho}\frac{\partial p}{\partial y} + \nu\nabla^2 v + f_y \tag{3.3}$$

- $z$-component of the momentum equation

$$\frac{Dw}{Dt} = -\frac{1}{\rho}\frac{\partial p}{\partial z} + \nu\nabla^2 w + f_z \tag{3.4}$$

where total derivative is given as:

$$\frac{D}{Dt} = \frac{\partial}{\partial t} + u\frac{\partial}{\partial x} + v\frac{\partial}{\partial y} + w\frac{\partial}{\partial z} = \frac{\partial}{\partial t} + \boldsymbol{u} \cdot \nabla \tag{3.5}$$

Finite volume method is based on a discretization of the integral forms of the conservation equations. The generic form of the conservation integral equation is given in the

form:

$$\frac{\partial}{\partial t} \iiint\limits_{V} \phi \, dV + \iint\limits_{A} \vec{F} \cdot d\vec{A} = \iiint\limits_{V} V_V \, dV + \iint\limits_{A} V_A \, dA \qquad (3.6)$$

where $A$ is the control surface, $V$ is the control volume, $\phi$ is the general unknown variable, $V_A$ is the possible sources of $\phi$ on the control surface, $V_V$ is the possible sources of $\phi$ inside control volume and $\vec{F}$ is the flux associated with $\phi$. When applied to physical space divided into a discrete network of cells integral formulation provides mass and momentum conservation at the discrete level.

## 3.4   The Finite Volume Method

The following section presents the principles of the Finite Volume Method. At the core of the method lies discretization. Term discretization is used to describe a process of transforming one or more partial differential equations into a system of algebraic equations. When dealing with an unsteady flow problem, three distinct steps can be identified:

- Spatial discretization based on splitting the space domain into a set of control volumes (CV's) thus forming a computational mesh.

- Temporal discretization required in transient problems. The time domain is divided into a finite number of time steps.

- Equation discretization applied to the governing equations of the problem. It allows obtaining a system of algebraic equations in terms of discrete quantities defined at specific locations in the computational mesh which can be solved iteratively.

### 3.4.1   Spatial Discretisation

The most fundamental element of the spatial discretization is a finite control volume. Figure 3.2 shows an example of a control volume. In most generalized form the idea of discretization can be expressed by the equation:

$$\int\limits_{V_P} (x - x_P) dV = 0 \qquad (3.7)$$

where $P$ is the centroid of the CV, $V_P$ is the volume of the CV, $N$ is the centroid of a neighboring CV, $f$ is the center of the face. Point $P$ is named a computational node and is the locus at which the variables values are calculated. Arrangement in which the
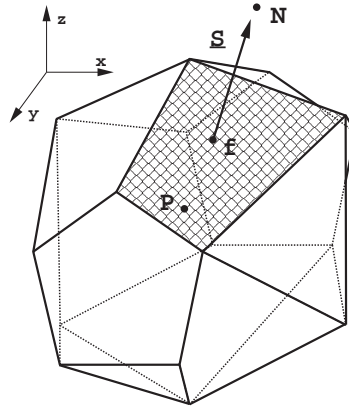
**Figure 3.2:** Control Volume example (Jasak, 1996).

control volume centroid is used to store the calculated values of all variables is called collocated grid. This solution was implemented in OPENFOAM. Each of the faces of the CV is flat and is shared, at most, with only one neighboring CV. Faces which do not have neighbors are boundary faces. Two main classes of computational meshes (grids), showed in Fig. 3.3, can be defined (Versteeg and Malalasekera, 2007):

- Structured meshes. In this type of mesh grid points are located at the intersection of coordinate lines. Interior grid points have a fixed number of neighboring grid points.

- Unstructured meshes are characterized by control volumes of any shape and no implicit structure of coordinate lines required.

OPENFOAM is capable of handling both structured and unstructured grids. While structured mesh cells can be represented by a set of integers such as $i$, $j$ specifying the location of vertices of a cell, the unstructured mesh cells must be numbered individually in a certain order. The consequence is higher memory requirement and more computation time required. A major benefit of the unstructured grids stems from their suitability for complex geometries and relative ease of local mesh refinement. Interpolation is used to express values of the variables at the CV surface calculated from the stored in collocated arrangement nodal values. OPENFOAM offers flexibility to choose different interpolation schemes for field values. Most commonly used interpolation scheme which was also used in present study is linear interpolation. For a scalar variable $\phi$ which can represent pressure or velocity component the expression for interpolation can be written:

$$\phi_f = f_x \phi_P + (1 - f_x)\phi_N \tag{3.8}$$
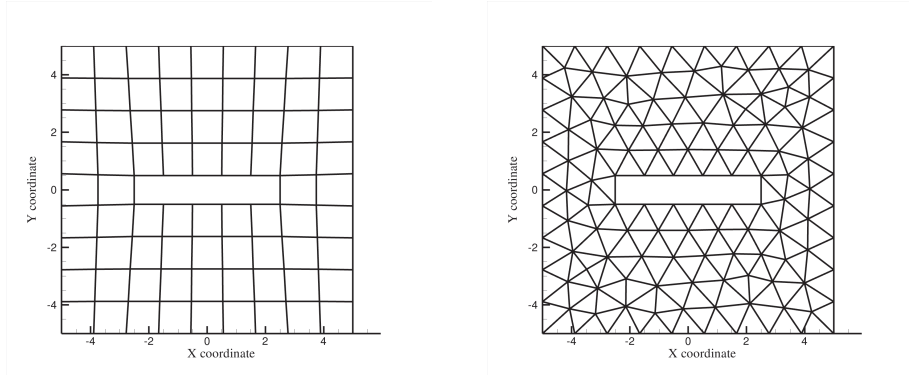
**Figure 3.3:** Structured (left) and unstructured (right) mesh examples (Ferziger and Perić, 2012).

where $f_x$ is a linear interpolation factor defined as:

$$f_x = \frac{|x_f - x_N|}{|x_f - x_N| + |x_f - x_P|}$$

(3.9)

This method is second order accurate.

### 3.4.2 Temporal Discretisation

Unsteady flows are parabolic in time thus time-stepping methods can be used to advance transient solution step-by-step. Similar to the interpolation schemes, OPENFOAM offers several time discretisation schemes. Euler implicit method is selected in the present work. This scheme expresses the face-values in terms of the new time-level cell values, and can be written in the form:

$$\phi_f = f_x \phi_P^n + (1 - f_x)\phi_N^n$$

(3.10)

where $f_x$ is the linear interpolation factor, ratio of the distance from centroids to the face center.

$$\boldsymbol{S} \cdot (\nabla\phi)_f = |\boldsymbol{\Delta}|\frac{\phi_N^n - \phi_P^n}{|\boldsymbol{x}|} + \boldsymbol{k} \cdot (\nabla\phi)_f$$

(3.11)

where $\boldsymbol{S}$ is the surface normal vector and $\boldsymbol{k}$ is the orthogonal to the normal surface vector $\boldsymbol{S}$. This method is first order accurate but unlike Euler explicit scheme allows for higher Courant number to satisfy stability of the solution. Courant number represents the portion of a cell that the flow will transverse due to advection effect in one time step and can be defined as:

$$Co = \frac{\Delta t|U|}{\Delta x}$$

(3.12)

where $\Delta t$ is the maximum time step, $\Delta x$ is the cell size in the direction of the velocity and $U$ is the magnitude of the velocity at considered location.

### 3.4.3 Equation Discretisation

The integral form of the conservation equation shown in Eq. (3.6) is a starting point of the FVM discretisation of continuity and momentum equations. The continuity equation in incompressible form can be thus discretised as follows:

$$\int_{V_P} \nabla \cdot (\boldsymbol{u}) dV = 0 \tag{3.13}$$

Which after apllying Green's theorem becomes:

$$\int_{A_P} \boldsymbol{u} \cdot \boldsymbol{n} \, dA = 0 \tag{3.14}$$

where $A_P$ is the surface of the control volume $V_P$, $\boldsymbol{n}$ is the vector normal to the surface $A_P$ and $\boldsymbol{u}$ is the velocity vector. Since the finite volume $V_P$ has $N$ discrete faces, each with area $A_n$, the equation can be written in the flowing form:

$$\sum_{n=1}^{N} \int_{A_n} \boldsymbol{U} \cdot \boldsymbol{n} \, dA = \sum_{n=1}^{N} \widetilde{U}_n A_n = 0 \tag{3.15}$$

where $\boldsymbol{U} = \boldsymbol{u} \cdot \boldsymbol{n}$ is the velocity component normal to face $N$, $\widetilde{U}$ is the face averaged value of $\boldsymbol{U}$, $N$ is the number of discrete faces of CV. This expression gives the finite-volume discretized continuity equation. The momentum equation consisting temporal term $\frac{\partial u}{\partial t}$, convection term $\nabla \cdot (\boldsymbol{uu})$ and diffusion term $\nabla \cdot (\nu \nabla \boldsymbol{u})$. Applying integral Eq. (3.6) the momentum equation becomes:

$$\int_{V_P} \frac{\partial \boldsymbol{u}}{\partial t} dV + \int_{V_P} \nabla \cdot (\boldsymbol{uu}) dV - \int_{V_P} \nabla \cdot (\nu \nabla \boldsymbol{u}) dV = \int_{V_P} \frac{\nabla p}{\rho} dV \tag{3.16}$$

Convection and diffusion terms can be then discretised using Gauss theorem, similarly to previously presented continuity equation discretisation. Additional details on the disceretisation procedure and correction schemes can be found in Versteeg and Malalasekera (2007), Ferziger and Perić (2012) and OpenFOAM-UserGuide (2017).

### 3.4.4 Pressure - Velocity Coupling

Solver used in all present simulations is a `PimpleDyMFoam` solver implemented in OPEN-FOAM. It is an unsteady solver for incompressible Navier-Stokes equations, using a PIMPLE algorithm for pressure coupling solution. The PIMPLE algorithm is a combination of a SIMPLE (semi-implicit method for pressure-linked equations) and a PISO (pressure-implicit split-operator) algorithms. The governing equations are solved in this method using standard pressure-velocity coupling composed of momentum predictor, pressure

solver, and momentum corrector. Flowchart of the PIMPLE solution procedure was shown in Fig. 3.4. The solution of the PISO algorithm can be summarized in three main steps:

1. Momentum predictor is used to solve the momentum equation based on the pressure field from the previous time-step.

2. Approximated solution of the pressure field is obtained.

3. Velocity is corrected explicitly based on the estimation of the pressure field from step 2.
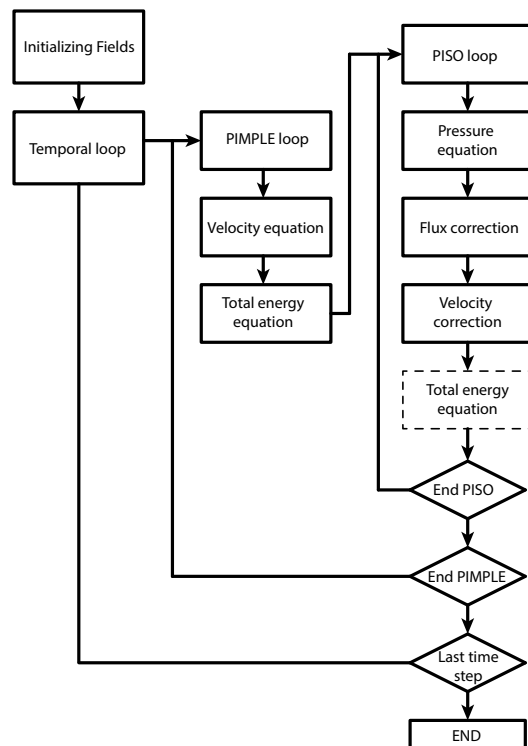


**Figure 3.4:** Flowchart of PIMPLE algorithm.

In the `pimpleDyMFoam` algorithm, PISO can be repeated for multiple iterations at each time step. This process is referred to as the PIMPLE loop. By using under-relaxation technique the PIMPLE loop allows to use higher Courant number, thus larger timesteps as compared to pure PISO algorithm which is strictly limited to $Co < 1$ criterion for stability.

## 3.5  Turbulence Modeling

The Navier-Stokes equations account for all length and time scales of the motions of
the fluid. Turbulent flows consists of continuous spectrum of scales ranging from largest
to smallest. The largest scales are governed by the geometry of the flow domain. The
smallest scales were first described by Kolmogorov who defined them as:

$$\eta = \left(\frac{\nu^3}{\epsilon}\right)^{1/4} \tag{3.17}$$

$$\tau = \left(\frac{\nu}{\epsilon}\right)^{1/2} \tag{3.18}$$

These two scales depend on the molecular properties of the fluid: the viscosity $\nu$ and the
dissipation rate $\epsilon$. The Kolmogorov scales become smaller with an increasing Reynolds
number, therefore increasing the range of scales in the fluid motion. It can be shown
that the cost of solving the full Navier-Stokes equations numerically grows proportion-
ally to $Re^3$ (Wilcox, 2004). Therefore, even for a relatively low Reynolds number flows
the capacity of modern computers can be exceeded easily. The result was development
of different approaches to resolve turbulence numerically. Direct Numerical Simulation
resolves all the length scales that are present in the turbulent flow. In the Large Eddy
Simulation concept the smallest eddies are not resolved. This method originally pro-
posed by Smagorinsky assumes spatial filtering of the turbulent length scales using a
low-pass filter. Different approach was proposed by Reynolds who is the aouthor of the
Reynolds decomposition. The main idea behind Reynolds decomposition is to separate
the mean and fluctuating components of the velocity and pressure:

$$\widetilde{U}_i = U_i + u'_i \tag{3.19}$$

$$\widetilde{p} = P + p' \tag{3.20}$$

where $\widetilde{U}_i$ is the instantaneous velocity, $U_i$ is the mean part of $\widetilde{U}_i$ and $u'_i$ is the fluctuating
part of $\widetilde{U}_i$; $\widetilde{p}$ is the instantaneous pressure, $P$ and $p'$ are the mean and the fluctuating part
of $\widetilde{p}$ respectively. Substitution of the separated mean and fluctuating parts into Navier-
Stokes equations Eq. (3.1-3.3) results in the Reynolds-averaged equations of continuity
and momentum conservation, given by (Wilcox, 2004):

$$\frac{\partial U_i}{\partial x_i} = 0, \tag{3.21}$$

$$\frac{\partial U_i}{\partial t} + U_j \frac{\partial U_i}{\partial x_j} = -\frac{1}{\rho}\left(\frac{\partial P}{\partial x_i}\right) + \nu \frac{\partial^2 U_i}{\partial x_j^2} - \frac{\partial \overline{u'_i u'_j}}{\partial x_j}, \tag{3.22}$$

where $i, j = 1, 2$; $x_1, x_2$ are streamwise and wall-normal directions accordingly; $U_1, U_2$ are the mean flow velocity components corresponding to directions $x_1$ and $x_2$; $\overline{u'_i u'_j}$ denotes Reynolds stress tensor; $\rho$ is the density of the fluid; $P$ is the dynamic pressure. The specific Reynolds stress tensor is expressed as:

$$\overline{u'_i u'_j} = \tau_{ij} = \nu_t \left( \frac{\partial U_i}{\partial x_j} + \frac{\partial U_j}{\partial x_i} \right) - \frac{2}{3} k \delta_{ij}, \tag{3.23}$$

where $\nu_t$ is the turbulent viscosity; $k$ is the turbulent kinetic energy and $\delta_{ij}$ is the Kronecker's delta. To solve the resulting system of equations additional assumptions have to be made concerning the uknown quantities (turbulence closure problem). Numerous RANS turbulence models exist ranging from the simplest zero equation algebraic models up to Reynolds Stress Transport Models which introduce five additional transport equations.

### 3.5.1 $k - \omega$ SST Turbulence Model

The shear stress transport (SST) $k - \omega$ turbulence model by Menter (1994) is used in the present study. The $k - \omega$ SST model has been proved to perform well in predicting flows characterized by the adverse pressure gradients (see eg. Zhang (2017), Robertson et al. (2015)). The model is constructed upon an empirical approach combining Wilcox' standard $k - \omega$ model and classic $k - \epsilon$ model. Transport equations for specific dissipation rate $\omega$ and turbulent kinetic energy $k$ are given by:

$$\frac{Dk}{Dt} = \tau_{ij} \frac{\partial u_i}{\partial x_j} - \beta^* k \omega + \frac{\partial}{\partial x_j} \left[ (\nu + \sigma_k \nu_t) \frac{\partial k}{\partial x_j} \right] \tag{3.24}$$

$$\frac{D\omega}{Dt} = \frac{\gamma}{\nu_t} \tau_{ij} \frac{\partial u_i}{\partial x_j} - \beta \omega^2 + \frac{\partial}{\partial x_j} \left[ (\nu + \sigma_k \nu_t) \frac{\partial \omega}{\partial x_j} \right] + 2(1 - F_1) \frac{\sigma_{\omega 2}}{\omega} \frac{\partial k}{\partial x_j} \frac{\partial \omega}{\partial x_j} \tag{3.25}$$

where: standard model coefficients are given in Table 3.1, and turbulent viscosity $\nu_t$ is defined as:

$$\nu_t = \frac{a_1 k}{\max(a_1 \omega, \Omega F_2)}, \tag{3.26}$$

where $a_1 = 0.31$, $\Omega = \sqrt{2 W_{ij} W{ij}}$ is the vorticity magnitude, with

$$W_{ij} = \frac{1}{2} \left( \frac{\partial u_i}{\partial x_j} - \frac{\partial u_j}{\partial x_i} \right), \tag{3.27}$$

$F_1$ and $F_2$ are blending functions introduced to smoothly switch between the two formulations ($k - \omega$ near to the wall and $k - \epsilon$ in the far field) and the corresponding variables

**Table 3.1:** Constant values used in the $k - \omega$ SST model.

| $\phi$ | $\sigma_k$ | $\sigma_w$ | $\beta$ | $\beta^*$ | $\gamma$ |
|--------|-----------|-----------|---------|-----------|----------|
| $\phi_1$ | 0.85 | 0.5 | 0.075 | 0.09 | $\beta/\beta^* - \sigma_k\kappa^2/\sqrt{\beta^*}$ |
| $\phi_2$ | 1.0 | 0.856 | 0.0828 | 0.09 | |

value. They are defined accordingly by

$$F_1 = \tanh(arg_1^4) \tag{3.28}$$

$$F_2 = \tanh(arg_2^2) \tag{3.29}$$

$$arg_1 = \min\left[\max\left(\frac{\sqrt{k}}{\beta^*\omega d_w}, \frac{500\nu}{d_w^2\omega}\right), \frac{4\rho\sigma_{\omega_2}k}{CD_{k\omega}d_w^2}\right] \tag{3.30}$$

$$arg_2 = \max\left(2\frac{\sqrt{k}}{\beta^*\omega d_w}, \frac{500\nu}{d^2\omega}\right) \tag{3.31}$$

The $CD_{k\omega}$ is the positive value of the cross-diffusion given by

$$CD_{k\omega} = \max\left(2\rho\sigma_{\omega_2}\frac{1}{\omega}\frac{\partial k}{\partial x_j}\frac{\partial \omega}{\partial x_j}, 10^{-20}\right) \tag{3.32}$$

In $arg_1$, the first argument is the ratio between the turbulence length scale and the distance to the nearest wall. The second argument forces $F_1$ to be 1 in the viscous sub-layer whereas the third one ensures that the solution remains insensitive to the freestream. All arguments vanish far from the wall. In this way, $F_1$ is equal to one in the viscous and logarithmic layers: the original $k - \omega$ is activated in theses regions. As the wall distance increases, the transformed $k - \epsilon$ is progressively activated as $F_1$ goes to 0.

# References

Cebeci, T., J. P. Shao, F. Kafyeke, and E. Laurendeau (2009). *Computational Fluid Dynamics for Engineers: From Panel to Navier-Stokes Methods with Computer Programs*. Springer.

Ferziger, J. H. and M. Perić (2012). *Computational Methods for Fluid Dynamics*. Springer Science & Business Media.

Jasak, H. (1996). *Error Analysis and Estimation for Finite Volume Method with Applications to Fluid Flow*. Ph. D. thesis, Imperial College, University of London.

Menter, F. (1994). Two-equation eddy-viscosity turbulence models for engineering applications. *AIAA Journal 32*, 1598 – 1605.

Moukalled, F., L. Mangani, and M. Darwish (2015). *The Finite Volume Method in Computational Fluid Dynamics: An Advanced Introduction with OpenFOAM® and Matlab*. Springer.

OpenFOAM-UserGuide (2017, 7). *OpenFOAM - The Open Source CFD Toolbox - User's Guide* (5.0 ed.). United Kingdom: OpenCFD Ltd.

Robertson, E., V. Choudhury, S. Bhushan, and D. Keith Walters (2015, 10). Validation of openfoam numerical methods and turbulence models for incompressible bluff body flows. *Computers & Fluids 123*, 122 – 145.

Versteeg, H. K. and W. Malalasekera (2007). *An Introduction to Computational Fluid Dynamics: The Finite Volume Method*. Pearson Education.

Wilcox, D. (2004). *Turbulence Modeling for CFD*. DCW Industries.

Zhang, D. (2017). Comparison of various turbulence models for unsteady flow around a finite circular cylinder at Re = 20000. *Journal of Physics: Conference Series 910*(1), 12 − 27.

**CHAPTER 4**

# TWO DEGREE-OF-FREEDOM NEAR WALL VIV IN LAMINAR VORTEX STREET REGIME

This chapter presents the process of a model creation and set up used in the numerical simulations of a 2DoF cylinder near a horizontal plane wall at $Re = 200$. This includes the convergence studies in terms of mesh density and time step sensitivity. A set of 2D simulations is carried out at different reduced velocities in order to study the frequency lock-in of an oscillating cylinder. The hydrodynamic forces and amplitude responses are characterized as a function of reduced velocity and compared with other numerical studies. The frequency spectrum analysis of the force coefficients and the displacement time histories is carried out by means of FFT. The flow fields are compared in three distinct cases of pre-lock-in regime ($U_r = 3$), lock-in regime ($U_r = 5$) and post lock-in regime ($U_r = 8$). Vorticity contours at selected time instances are used to visualize the vortex shedding modes.

## 4.1  Pre-processing

The pre-processing is carried out in two steps. Firstly the structured 3D mesh with one cell thickness is generated. Meshing is done using GMSH, which is a mesh generation program with built-in pre- and post-processing utility (Geuzaine and Remacle, 2009).

The software is distributed under GNU General Public License. Because of the included CAD engine combined with the scripting capabilities of the software, it is relatively easy to generate structured meshes with a high degree of control over the cell distribution. Mesh sensitivity study and details of the mesh generation settings are given in section 4.3. The second step of the pre-processing involves defining the boundary conditions and control parameters in the simulation case files. Summary of all prescribed boundary conditions is given in section 4.2.

## 4.2  Model Description

The computational domain is established as a rectangular box, the boundary conditions imposed in all simulations are shown in Fig. 4.1. The size of the whole computational domain is $40D \times 20D$, where $D$ is the cylinder diameter. In the crossflow direction, it extends from the rigid wall where $e$ is the gap distance between the wall and the cylinder up to $20D$. Setting domain width to $20D$ results in a blockage equal to 5% which does not affect the flow around the cylinder as discussed in Navrose and Mittal (2013). The
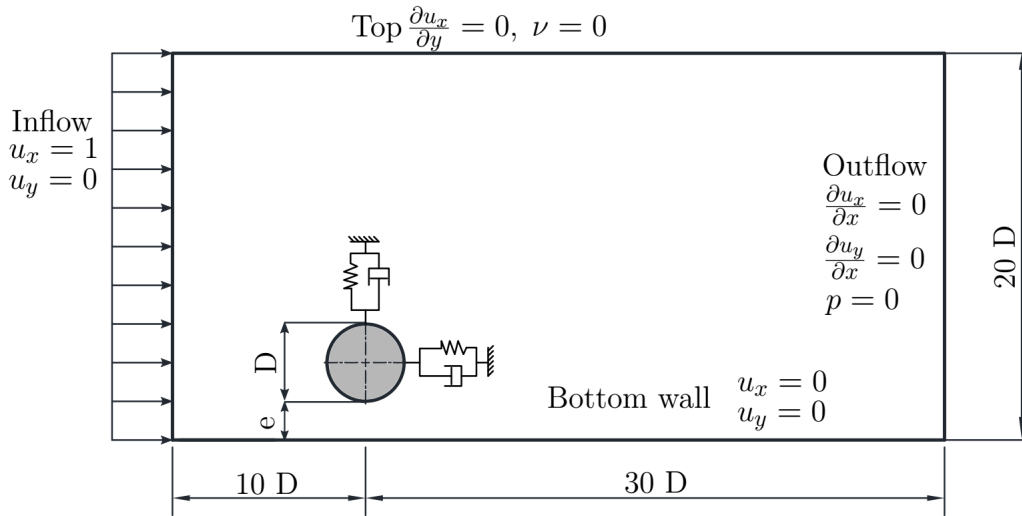


**Figure 4.1:** Schematic of a computational domain and imposed boundary conditions.

upstream distance extends $10D$ from the cylinder center and downstream distance is set to $30D$. Similar boundary locations were used in earlier works in Prasanth and Mittal (2008), Jaiman et al. (2016) Navrose and Mittal (2013), and has been proven to be sufficient to eliminate the far field effects on the flow upstream and downstream of the cylinder. It is therefore believed that in the present study, the domain boundaries have

negligible influence on the flow close to the cylinder. The boundary conditions are kept constant throughout the study.

1. At the inlet uniform velocity field in $x$-direction is imposed: $u_x = 1$;

2. At the outlet, the pressure is set to constant value: $p = 0$, and the normal gradient of the velocity is set to zero: $\frac{\partial u_x}{\partial x} = \frac{\partial u_y}{\partial x} = 0$;

3. Bottom of the domain and cylinder surface are defined as a no-slip condition: $u_x = u_y = 0$;

4. The upper boundary is defined as a symmetry boundary condition. Here the normal gradients of the velocity components are set to zero and convective flux of fluid is zero resulting in zero shear stress and non-zero normal stress: $\frac{\partial u_x}{\partial y} = 0$, $\nu = 0$.

The cylinder is modeled as an elastically mounted by springs and dampers and allowed to vibrate freely in both transverse ($y$-axis) and streamwise ($x$-axis) directions. Spring stiffness is assumed to be linear and homogeneous in both $x$- and $y$-directions thus the ratio of $f_{nx}$ to $f_{ny}$ is equal to 1. Fixed mass ratio of the cylinder, $m^* = 10$ is used in all simulations. By adjusting the spring stiffness it is possible to set the $U_r$ which is governed by the $f_n$ of the cylinder. Damping ratio $\zeta$ in all simulations is set to zero.

## 4.3   Convergence Studies

A grid and time step independence studies are carried out in this section. The domain is discretized using a structured hexahedral mesh. The mesh topology is presented in Fig. 4.2. Cell distribution parameters are summarized in Table 4.1. The cell size is refined in the high gradient regions and a coarser grid is used in the far-field regions to decrease the computational effort. The simulations are performed for a circular cylinder of $m^* = 10$ with 2-DoF at $Re = 200$, $e/D = 0.9$ and $U_r = 5$. It is expected that for the selected reduced velocity and gap ratio, high vibration amplitudes are achieved. The large amplitude response is desired when estimating the numerical discretization errors. To asses the dependency of the numerical results on the mesh density, three meshes are generated with different densities. The summary of the meshes used is given in Table 4.2. In the refinement of the grid, a constant refinement factor is used to ensure the geometric similarity of the grid cells. Figure 4.3, and Figure 4.4 present details of the generated mesh B. Representative hydrodynamic force coefficients and responses of the cylinder undergoing free vibrations are used to asses the convergence. The `forceCoeffs`
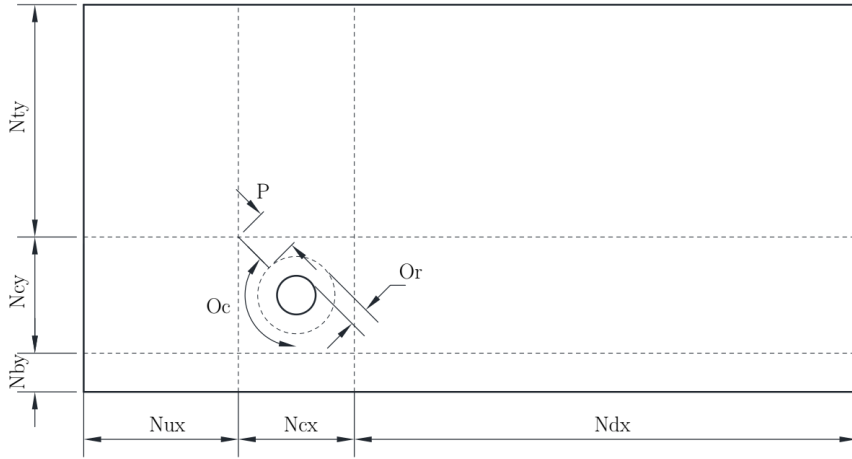
**Figure 4.2:** Mesh topology schematic.
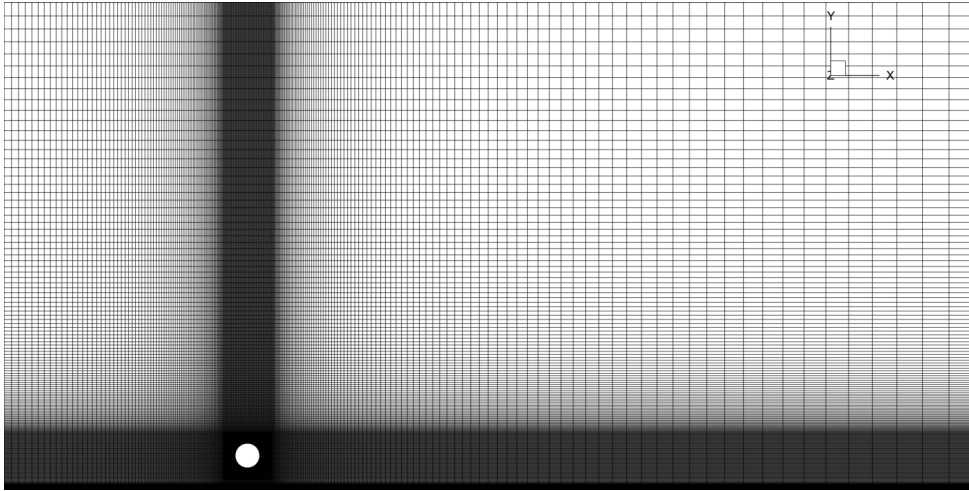


**Figure 4.3:** Mesh B: complete domain view.

function object implemented in OPENFOAM is used to extract the hydrodynamic forces and moments coefficient data for defined cylinder surface. The lift force ($F_L$) and drag force ($F_D$) calculated for the cylinder are normalized by the dynamic pressure and area ($0.5\rho U^2 D$) to obtain the lift ($C_L$) and drag ($C_D$) coefficients, respectively. The mean drag coefficient and mean lift coefficient are defined and calculated as follows:

$$\overline{C_L} = \frac{1}{n} \sum_{i=1}^{n} C_{L,i} \tag{4.1}$$

$$\overline{C_D} = \frac{1}{n} \sum_{i=1}^{n} C_{D,i} \tag{4.2}$$

**(a)** Refinement box around the cylinder.



**(b)** Details of the mesh near the cylinder wall.
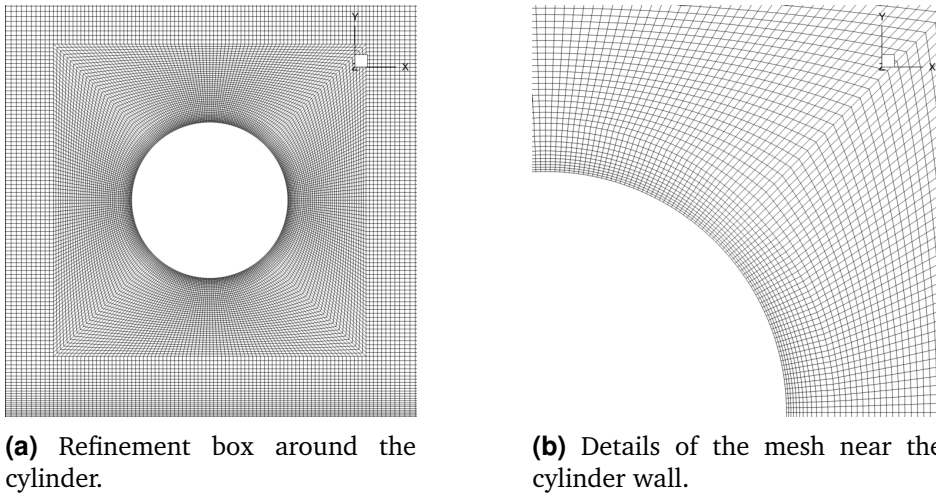
**Figure 4.4:** Enlarged views of the mesh B details.

**Table 4.1:** Mesh topology - cell distribution parameters.

| Parameter | Description | Refinement factor |
|-----------|-------------|-------------------|
| Nux | Cell distribution in x-direction upstream | 1.03 |
| Ncx | Cell distribution in x-direction cylinder zone | 1.00 |
| Ndx | Cell distribution in x-direction downstream | 1.03 |
| Nby | Cell distribution in y-direction bottom | 1.05 |
| Ncy | Cell distribution in y-direction cylinder zone | 1.00 |
| Nty | Cell distribution in y-direction top | 1.03 |
| Oc | Circumferential cell distribution around cylinder | 1.00 |
| Or | Radial cell distribution around cylinder | 1.10 |
| P | Diagonal cell distribution in cylinder box | 1.01 |

**Table 4.2:** Cell distribution of meshes used in the convergence study.

| | Number of elements | | | | | | | | | |
|------|-----|-----|-----|-----|-----|-----|-----|----|----|-----------------|
| Mesh | Nux | Ncx | Ndx | Nby | Ncy | Nty | Oc | Or | P | Total Cell Count |
| A | 60 | 60 | 80 | 20 | 60 | 80 | 240 | 10 | 25 | 36 800 |
| B | 80 | 80 | 120 | 25 | 80 | 120 | 320 | 12 | 30 | 70 040 |
| C | 100 | 100 | 140 | 30 | 100 | 140 | 400 | 15 | 35 | 101 800 |

Root-mean-square values of drag coefficient and lift coefficient are calculated using expressions:

$$C_L^{rms} = \sqrt{\frac{1}{n}\sum_{i=1}^{n}(C_{L,i} - \overline{C_L})^2} \tag{4.3}$$

$$C_D^{rms} = \sqrt{\frac{1}{n}\sum_{i=1}^{n}(C_{D,i} - \overline{C_D})^2} \tag{4.4}$$

The maximum vertical and root-mean-square horizontal vibration amplitudes are given as:

$$\frac{(A_y)_{max}}{D} = \frac{1}{2}\frac{|(A_y)_{max} - (A_y)_{min}|}{D} \tag{4.5}$$

$$\frac{(A_x)_{rms}}{D} = \frac{\sqrt{\frac{1}{n}\sum_{i=1}^{n}(A_{x,i} - \overline{A_x})^2}}{D} \tag{4.6}$$

The simulations are performed with a time step $\Delta t = 0.002$ for a total duration of $\tau = 500$, where $\tau$, is non-dimensionalised time given by:

$$\tau = tU/D \tag{4.7}$$

Results of the mesh convergence study are summarized in Table 4.3. With mesh C being the reference, the differences between results obtained on mesh A and mesh B and those obtained on mesh C are calculated and % difference is given in the brackets. Convergence plots of $\overline{C}_D$ and $C_L^{rms}$ are presented in Figure 4.5. The differences between the results for the two finer meshes, mesh B and mesh C are approximately within 1% except for $(A_x)_{rms}$ which differs by 1.5% from the finest mesh results. Considering the computational efficiency and assuming acceptable difference in the value of $(A_x)_{rms}$, mesh B is then selected as the mesh to perform further simulations. Time step independence

**Table 4.3:** Mesh convergence study results.

| | Parameter | | | |
|---|---|---|---|---|
| **Mesh** | $\overline{C}_D$ | $C_L^{rms}$ | $(A_y)_{max}/D$ | $(A_x)_{rms}/D$ |
| A | 1.9646 (1.21%) | 0.0976 (3.58%) | 0.4573 (1.98%) | 0.0743 (4.31%) |
| B | 1.9477 (0.36%) | 0.0943 (0.21%) | 0.4516 (0.75%) | 0.0722 (1.52%) |
| C | 1.9407 (-) | 0.0941 (-) | 0.4482 (-) | 0.0711 (-) |
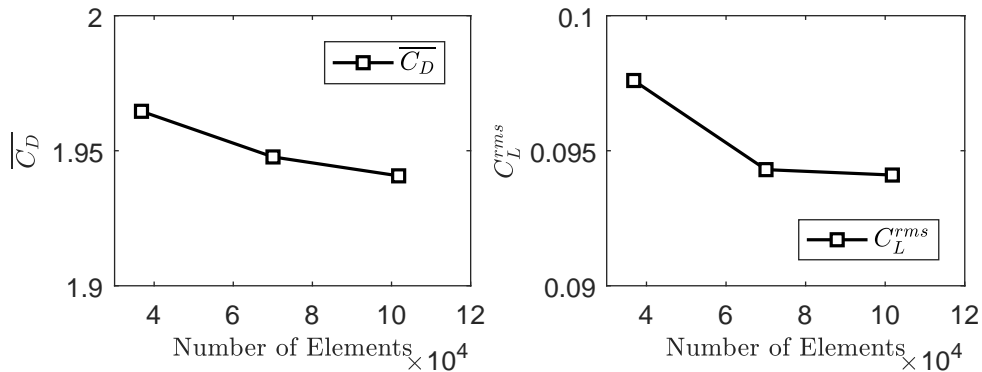


**Figure 4.5:** Mesh density convergence plots of $\overline{C}_D$ and $C_L^{rms}$.

**Table 4.4:** Time step independence study results.

| | Parameter | | | |
|---|---|---|---|---|
| **Time step** | $\overline{C}_D$ | $C_L^{rms}$ | $(A_y)_{max}/D$ | $(A_x)_{rms}/D$ |
| $\Delta t = 0.001$ | 1.9765 (-) | 0.0959 (-) | 0.4541 (-) | 0.0714 (-) |
| $\Delta t = 0.002$ | 1.9477 (-1.48%) | 0.0943 (-1.69%) | 0.4516 (-0.55%) | 0.0722 (1.1%) |
| $\Delta t = 0.003$ | 1.9927 (5.25%) | 0.0844 (-13.63%) | 0.4012 (-13.18%) | 0.0834 (14.39%) |

study is summarized in Table 4.4. Time step $\Delta t = 0.001$ is taken as the reference, the differences between results obtained in simulations with $\Delta t = 0.002$ and $\Delta t = 0.003$ are calculated and % difference is given in the brackets. Convergence plots of $\overline{C}_D$ and $C_L^{rms}$ are presented in Figure 4.6. It is shown in Table 4.4 that differences between the results are approximately 1.5% apart for the $\Delta t = 0.001$ and $\Delta t = 0.002$. Considering the computational efficiency, $\Delta t = 0.002$ is then selected as the time step to perform further simulations. Additional study is carried out to investigate the effects of the domain size.
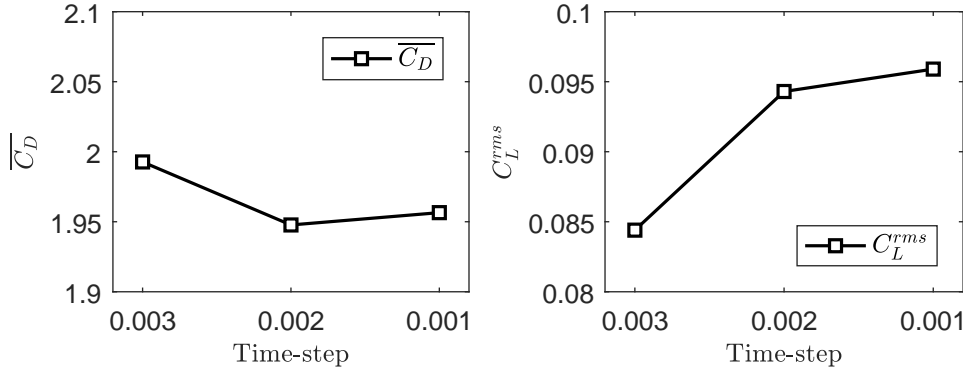


**Figure 4.6:** Time step convergence plots of $\overline{C}_D$ and $C_L^{rms}$.

In case D01 the size of the downstream distance ($L_{DD}$) is increased from 30D to 50D. In case D02 the width of the domain ($W$) is increased from 20D to 40D. The results compared to reference case ($\Delta t = 0.002$, mesh B) with relative error are given in Table 4.5. In both cases, the effects of the domain size are relatively small, with more pronounced

**Table 4.5:** Influence of the domain size.

| | | | | Parameter | | | |
|---|---|---|---|---|---|---|---|
| **Mesh** | Domain size | $W$ | $L_{DD}$ | $\overline{C}_D$ | $C_L^{rms}$ | $(A_y)_{max}/D$ | $(A_x)_{rms}/D$ |
| B | $20 \times 40$ | 20 | 30 | 1.9477 (-) | 0.0943 (-) | 0.4516 (-) | 0.0722 (-) |
| D01 | $20 \times 60$ | 20 | 50 | 1.9508 (0.16%) | 0.0953 (1.05%) | 0.4522 (0.13%) | 0.0715 (-0.98%) |
| D02 | $40 \times 40$ | 40 | 30 | 1.9423 (-0.28%) | 0.0956 (1.36%) | 0.4523 (0.15%) | 0.0730 (1.09%) |

influence on the root-mean-square lift coefficient value and root-mean-square stream-wise amplitude. In case D02 the $C_L^{rms}$ is 1.36% higher than in the reference case but the $(A_y)_{max}/D$ differs only by 0.15%. It can be concluded that the domain size suggested in

Li et al. (2016) is appropriate to accurately capture the wake dynamics and have a small influence on the flow around the cylinder. Based on the convergence study results a set of simulation cases is prepared with mesh B and time step set to $\Delta t = 0.002$ in order to investigate the VIV of the flexibly mounted cylinder over the range of reduced velocities. The summary of simulation cases used in the study is given in Table 4.6.

**Table 4.6:** List of simulation cases used in the study.

| Case | | | Parameter | | |
| --- | --- | --- | --- | --- | --- |
| | Mesh | $\Delta t$ | $Re$ | $U_r$ | $m^*$ |
| B09UR3 | B | 0.002 | 200 | 3.00 | 10 |
| B09UR3_2 | B | 0.002 | 200 | 3.20 | 10 |
| B09UR3_4 | B | 0.002 | 200 | 3.40 | 10 |
| B09UR3_6 | B | 0.002 | 200 | 3.60 | 10 |
| B09UR3_8 | B | 0.002 | 200 | 3.80 | 10 |
| B09UR3_9 | B | 0.002 | 200 | 3.90 | 10 |
| B09UR4 | B | 0.002 | 200 | 4.00 | 10 |
| B09UR4_1 | B | 0.002 | 200 | 4.10 | 10 |
| B09UR4_2 | B | 0.002 | 200 | 4.20 | 10 |
| B09UR4_3 | B | 0.002 | 200 | 4.30 | 10 |
| B09UR4_4 | B | 0.002 | 200 | 4.40 | 10 |
| B09UR4_6 | B | 0.002 | 200 | 4.60 | 10 |
| B09UR5 | B | 0.002 | 200 | 5.00 | 10 |
| B09UR5_2 | B | 0.002 | 200 | 5.20 | 10 |
| B09UR5_4 | B | 0.002 | 200 | 5.40 | 10 |
| B09UR5_6 | B | 0.002 | 200 | 5.60 | 10 |
| B09UR5_8 | B | 0.002 | 200 | 5.80 | 10 |
| B09UR5_9 | B | 0.002 | 200 | 5.90 | 10 |
| B09UR6 | B | 0.002 | 200 | 6.00 | 10 |
| B09UR6_1 | B | 0.002 | 200 | 6.10 | 10 |
| B09UR6_2 | B | 0.002 | 200 | 6.20 | 10 |
| B09UR6_5 | B | 0.002 | 200 | 6.50 | 10 |
| B09UR7 | B | 0.002 | 200 | 7.00 | 10 |
| B09UR8 | B | 0.002 | 200 | 8.00 | 10 |

## 4.4    Results and Discussion

In this section, the results and the discussion on VIV of the single cylinder in a vicinity of a horizontal plane wall are presented. In subsection 4.4.1. mean flow features are shown in the considered range of reduced velocities. Subsection 4.4.2. presents the vibration responses. In subsections 4.4.3 and 4.4.4. the phase diagrams and frequency response curves are presented respectively. Motion trajectories analysis is outlined in subsection 4.4.5. followed by the detailed analysis of the flow structures using vorticity contours

at selected $U_r$ presented in subsection 4.4.6. Interaction of the vibrating cylinder with the plane wall boundary layer is explained. The vibration frequency characteristics and vortex shedding modes are given in subsections 4.4.7 and 4.4.8 respectively.

### 4.4.1  Hydrodynamic Forces

Mean lift coefficient $\overline{C_L}$, mean drag coefficient $\overline{C_D}$ , root-mean-square lift coefficient $C_L{}^{rms}$ and root-mean-square drag coefficient $C_D{}^{rms}$ are extracted and calculated in each simulation case from the dimensionless time range $\tau = tU/D = 250-500$. The exception were cases in reduced velocity range from $U_r = 3.8$ to $U_r = 4.2$, where it was found that longer simulation time is required to develop statistically steady vibration pattern, thus simulated time was extended to $\tau = 1000$. Results are validated against data from the study by Li et al. (2018) who conducted 2D simulations of an elastically mounted cylinder near a horizontal plane wall at $Re = 200$. The isolated cylinder VIV simulation results at $Re = 200$ are from the study by Li et al. (2016). Results from Li et al. (2016) are used as a reference to identify the differences between the near-wall VIV characteristics and free stream VIV. It is evident from the Fig. 4.7(a) that the mean lift coefficient in the near-wall configuration is non zero as opposed to free stream case where $\overline{C_L}$ is close to zero. This is the result of the broken symmetry in the wake caused by the wall presence. There is a significant increase in $\overline{C_L}$ in the lock-in regime which can be identified between $3.5 \leq U_r \leq 6$ in the Fig. 4.7(a). The peak of $\overline{C_L}$ occurs at reduced velocity $U_r = 3.9$. The peak in $\overline{C_L}$ is correlated with the peak in transverse vibration amplitude which has been presented in Fig. 4.9(a). It is apparent that both mean and root-mean-square values of drag and lift coefficients are in excellent agreement with data from Li et al. (2018) with a small discrepancy in the peak values of mean lift coefficient $\overline{C_L}$ and peak in $C_L{}^{rms}$. Peak in $C_L{}^{rms}$ occurs at $U_r = 3.9$ and is slightly smaller when compared to the results from Li et al. (2018). The difference can be attributed to highly sensitive nature of the cylinder oscillations in that regime. It was observed that in some instances the cylinder oscillation was transitioning to the different pattern if simulation time was extended long enough. This situation is depicted in Fig. 4.8, it can be observed that from apparently steady state between $\tau = 400$ and $\tau = 500$ the oscillations transition to more chaotic pattern and beating oscillations appear after approximately $\tau = 500$.

Both mean and root-mean-square values of drag coefficient are lower than in the isolated cylinder counterpart. This effect is in agreement with the remarks of Zdravkovich (1997) and Sumer and Fredsøe (2006) which were outlined in Chapter 2.
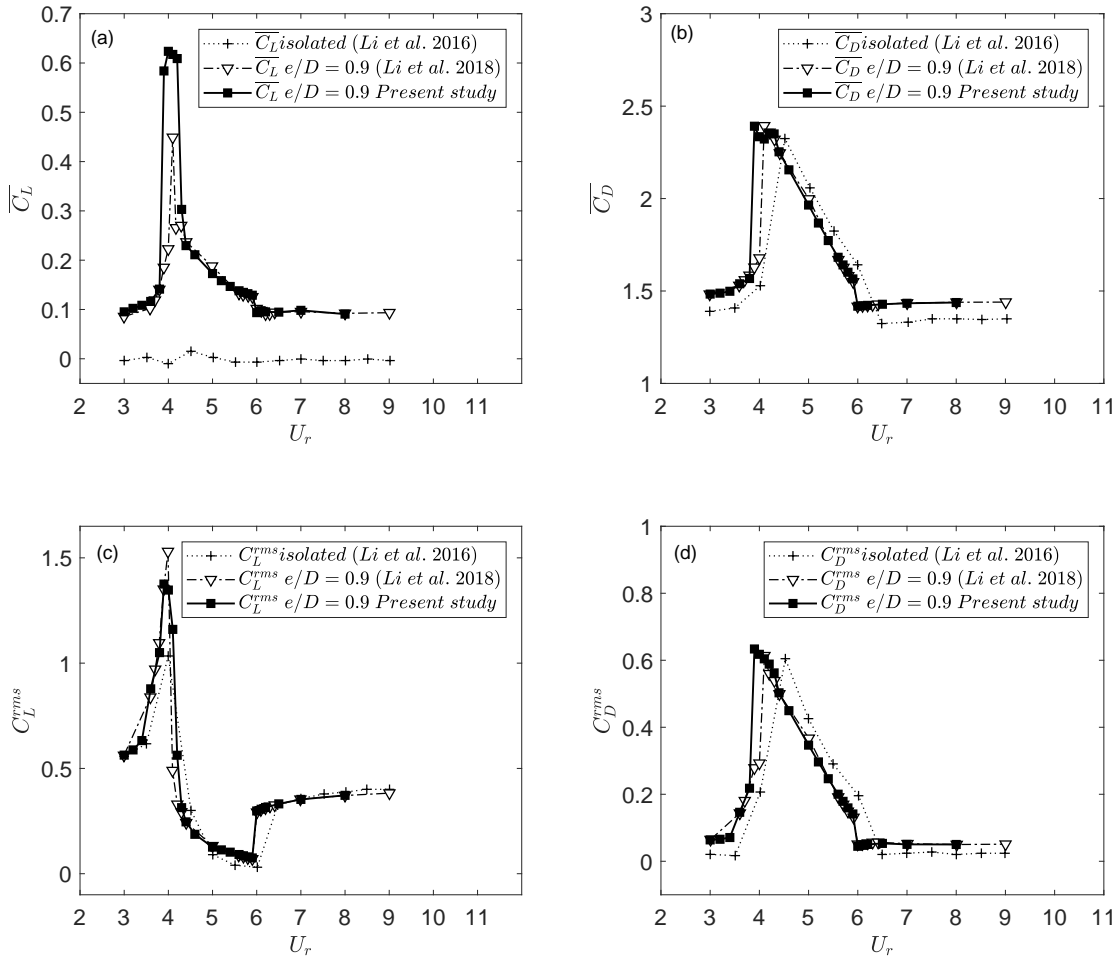
**Figure 4.7:** Force coefficients as a function of $U_r$ at $Re = 200$, mean lift coefficient $\overline{C_L}$, mean drag coefficient $\overline{C_D}$, root-mean-square lift coefficient $C_L{}^{rms}$, root-mean-square drag coefficient $C_D{}^{rms}$.

### 4.4.2  Response Amplitudes

Figure 4.9 presents the normalized displacements in transverse direction $A_{Y,max}/D$ and root-mean-square normalized displacement in streamwise direction $A_{X,rms}/D$. Both transverse and streamwise amplitude response values display good agreement with the results obtained by Li et al. (2018). The slight differences appear in the transition to lock-in regime which occurs at reduced velocity $U_r = 3.8$ as opposed to $U_r = 4.0$ in the reference study. The reason is explained in subsection 4.4.2 and can be attributed to the duration of the simulation and resolution of $U_r$ which is higher in the present study. The distinct difference between the freestream cylinder oscillations and the near-wall configuration case is the correlation of $\overline{C_D}$ and streamwise displacement. The change in $\overline{C_D}$ and $C_D{}^{rms}$ with respect to $U_r$ is similar in the near-wall and in the freely vibrat-
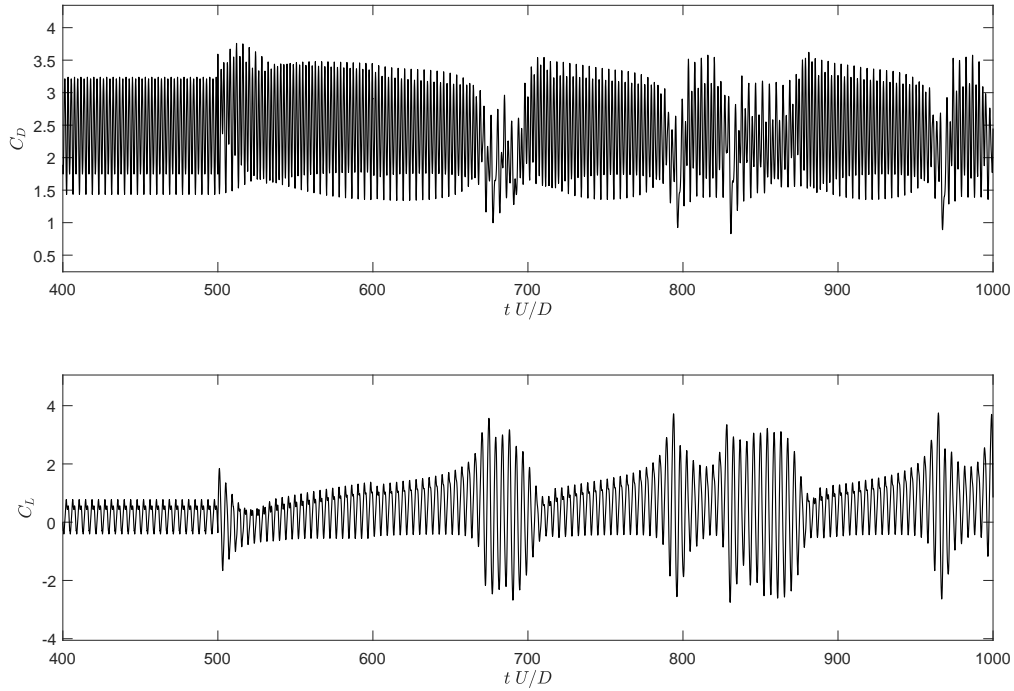
**Figure 4.8:** Time history of drag (top) and lift (bottom) coefficients of a vibrating cylinder at $U_r = 4.1$ and $Re = 200$.
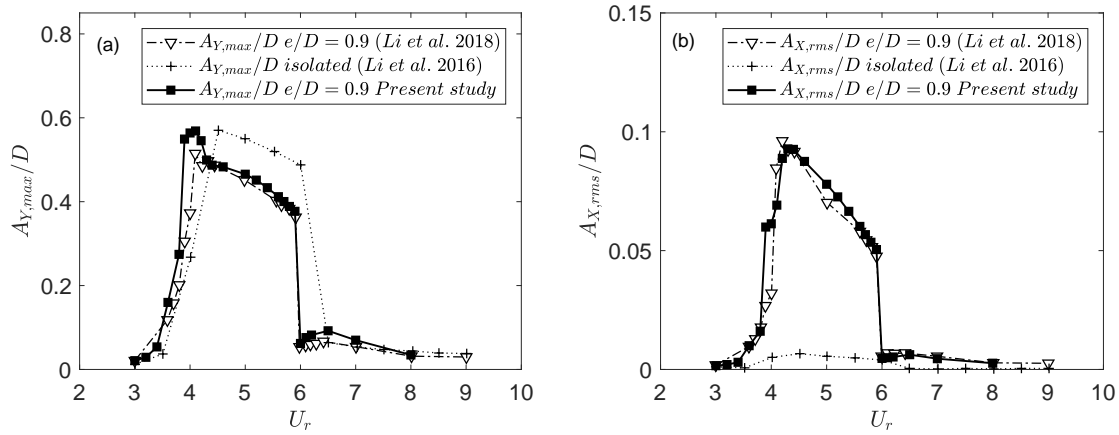


**Figure 4.9:** Normalized peak transverse displacement $A_{Y,max}/D$ and root-mean-square streamwise displacement $A_{X,rms}/D$ as a function of $U_r$ at $Re = 200$.

ing cylinder configurations but the $A_{X,rms}/D$ is strongly enhanced in the near-wall case. From the Fig. 4.9 the lock-in regime can be identified to start approximately at $U_r = 3.5$ and extend to $U_r = 6.0$, after that the response of the cylinder displacement is greatly decreased. According to Williamson and Govardhan (2004) a low mass-damping cylinder will exhibit two branches in the displacement response plot: the initial branch and the lower branch. The initial branch is characterized by an increase in the oscillation

amplitude, typical for the beginning of the lock-in phenomenon. Here the peak value of the transverse displacement $A_{Y,max}/D = 0.58$ is reached at $U_r = 4$. The lower branch is characterized by a gradual decrease of the response amplitude which then drops down rapidly in the desynchronization regime. This behavior is clearly visible in Fig. 4.9(a) where the initial branch can be identified between $3.5 \leq U_r \leq 4.2$ at the onset of synchronization and lower branch ranging from $U_r = 4.2$ to $U_r = 6.0$ with gradual decrease of $A/D$. In contrast to high $Re$ number flows, there is no upper branch as seen in 2.10 with a characteristic peak of displacement amplitudes. Lack of the upper branch was described in the study of Prasanth and Mittal (2008) who focused on the low $Re$ number regime and reported an absence of hysteretic behavior and intermittent switching between the oscillation amplitudes in the lock-in regime of $U_r$. Comparing the freestream cylinder VIV characteristics with the near-wall VIV the $A_{Y,max}/D$ response is slightly lower in the near wall case but overall response is similar in both isolated and near-wall arrangements. The streamwise response is on the other hand radically different. Figure 4.9(b) shows that the $A_{X,rms}/D$ is greatly affected by the wall proximity. Findings of the analysis of averaged forces and response amplitudes are thus as follows: the wall presence greatly influences the streamwise response but has little effect on the streamwise force, the wall presence has little effect on the transverse response while largely enhancing the transverse force. To explain this behavior it is useful to study the phase diagrams of the force-displacement relation in the streamwise and transverse directions.

### 4.4.3   Phase Difference of Forces and Responses

The phase difference between transverse displacement and lift force $\phi C_L - Y$ and streamwise displacement and drag force $\phi C_D - X$ as a function of $U_r$ has been shown in Fig. 4.10. Investigation of the phase relations can give important insight about the origins of enhanced streamwise response caused by the wall proximity. The phase angle can be associated with the direction of the energy transfer in the system: when the phase angle between the exciting force and the response amplitude is close to $0°$ the net energy transfer is positive. In the present study, it means that the energy is transferred from the fluid to the structure. When the phase angle is close to $180°$ an opposite situation takes place and the energy is dissipated by the fluid. Looking at Fig. 4.10 one can spot that $\phi C_L - Y$ is approximately equal to $0°$ in pre-lock-in regime extending to the onset of the lock-in ($3 \leq U_r \leq 4$), namely in the initial branch. The phase switches then suddenly to $180°$ at $U_r = 5.5$ corresponding to the transition from the initial branch to the lower branch. $\phi C_D - X$ shows the more gradual transition from an in-phase state in the pre-lock-in regime to out of phase state in the lower branch. According to Blackburn and

Henderson (1999) proposed hypothesis explaining this sudden change in phase angle in the case of a transversely oscillated cylinder is connected to the vorticity production mechanisms. Cylinder vibrations at different reduced velocities are characterized by a different balance between the pressure gradient vorticity production mechanism and motion-induced vorticity production mechanism. In both $\phi C_D - X$ and $\phi C_L - Y$ relations the phase switch is observed between $U_r = 5.0$ when the oscillation amplitude is still high and $U_r = 6.0$ where the vibration amplitude decays and cylinder leaves the lock-in regime. This implies that not only the energy transfer governs the motion of the cylinder but the frequency lock-in appears to be the main driver of the high amplitude oscillations.
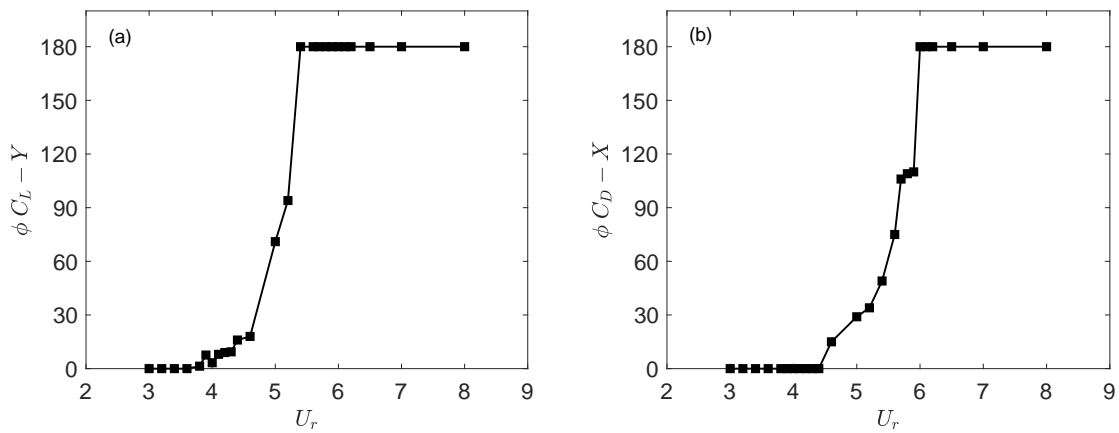


**Figure 4.10:** Phase difference between transverse displacement and lift force $\phi C_L - Y$ and streamwise displacement and drag force $\phi C_D - X$ as a function of $U_r$ at $Re = 200$.

### 4.4.4 Frequency Response

The relation between frequency ratios of vibration frequencies and natural frequency of the cylinder and $U_r$ is shown in Fig. 4.11(a) and (b). Figure 4.11(c) shows the ratio of the transverse vibration frequency to the streamwise vibration frequency in the range of investigated $U_r$. A characteristic feature of VIV is that of the lock-in phenomenon, where the vortex shedding frequency diverges from Strouhal's relationship (vortex shedding frequency of a stationary cylinder) and becomes equal or close to the cylinder's natural frequency. In Fig. 4.11(a) and (b) it is clearly visible that in the range of reduced velocities ($3.5 \leq U_r \leq 6$) the lock-in occurs, both transverse and streamwise oscillation frequencies depart from following the Strouhal's relation (marked as dotted line for $St = 0.21$) and become close to natural frequency of the system. As discussed in Chapter 2 the relation is not perfectly aligned to unity but increases monotonically because

of the frequency-dependent added mass. The ratio of the streamwise to the transverse frequencies is on the other hand almost perfectly equal to unity. This is a significant departure from the behaviour of the freestream VIV of 2DoF cylinder which is characterized by a frequency of vibration in the streamwise direction equal twice the frequency of the vibration in the transverse direction. This leads to the conclusion that not only
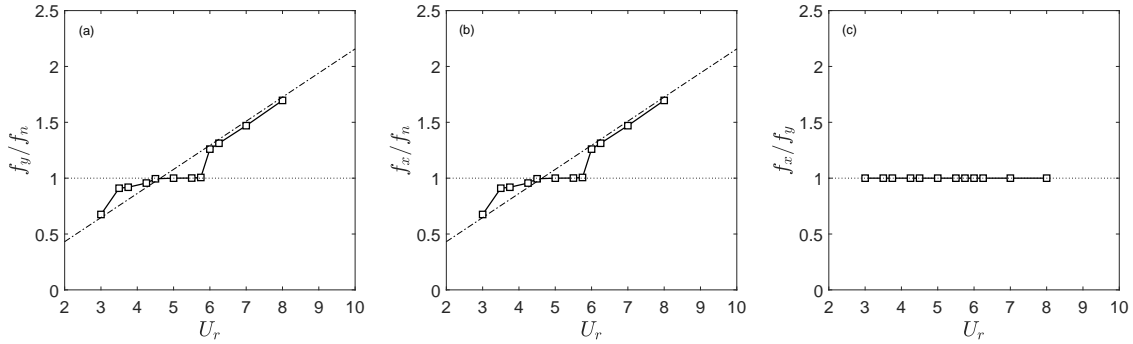


**Figure 4.11:** Vibration frequency response in transverse $f_y/f_n$, streamwise $f_y/f_n$ and ratio of streamwise vibration frequency to transverse vibration frequency $f_x/f_y$ as a function of $U_r$ at $Re = 200$.

the transverse oscillations are in the lock-in but also the streamwise oscillations are in resonance with the vortex shedding. This leads to the largely enhanced response in the streamwsie direction experienced by the cylinder placed close to the horizontal plane wall. The motion trajectory plots are helpful in understanding the nature and pattern of the near-wall VIV.

### 4.4.5   Motion Trajectories

The $XY$-trajectory of a freely vibrating cylinder in cross-flow is well known from the published studies figure of eight. The trajectories obtained from the simulations at different $U_r$ are plotted in Fig. 4.12(a) - (l). The shape of a skewed oval is in line with the experimental observations by (Zdravkovich, 1997) and other numerical studies focused on low $Re$ regime (similar oval trajectories were reported by Li et al. (2016) and Tham et al. (2015)). A characteristic effect which should be mentioned here is the more chaotic nature of the trajectories at $3.8 \leq U_r \leq 4.1$, and $U_r = 6.5$. According to Li et al. (2016) the cylinder vibration mode transitions from the wake mode (weak interaction) to a combined wake and structure mode (strong interaction) across the critical value of $U_r$ between the pre-lock-in and lock-in. The mode switching mechanism is the source of instabilities in the cylinder trajectories.
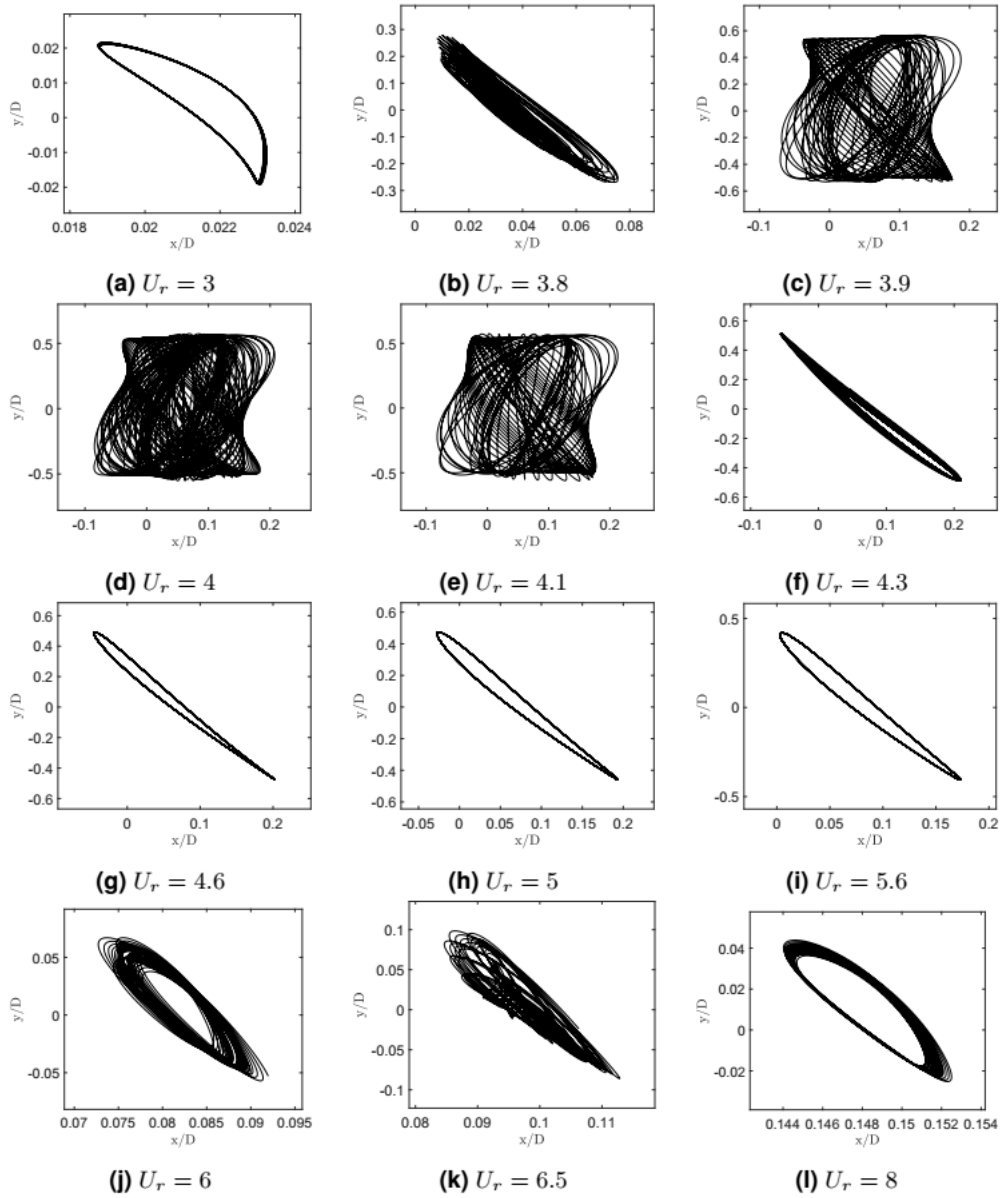
**Figure 4.12:** Trajectories of near-wall cylinder ($e/D = 0.9$) for different reduced velocities $U_r$ at $Re = 200$.

## 4.4.6  Flow Field Characteristics

To explain the reason for the lower streamwise oscillation frequency and phenomena underlying the streamwise near-wall VIV it is useful to visualize the flow fields around the cylinder. For better understanding of different vortex shedding modes characteristic for pre-lock-in, lock-in and post-lock-in conditions the plots of $z$-vorticity were taken at three different reduced velocities: $U_r = 3$ (4.13), $U_r = 5$ (4.14) and $U_r = 8$ (4.15).

The time instances of the snapshots were selected corresponding to the maximum and minimum values of the force coefficients and displacement amplitudes.



**(a)** Time histories of $C_D$, $C_L$, $X/D$ and $Y/D$



**(b)** $tU/D = 502$



**(c)** $tU/D = 502.5$



**(d)** $tU/D = 504.5$

**Z Vorticity:**   -1 -0.9 -0.8 -0.7 -0.6 -0.5 -0.4 -0.3 -0.2 -0.1 0.1 0.2 0.3 0.4 0.5 0.6 0.7 0.8 0.9 1

**Figure 4.13:** Time histories of $C_D$, $C_L$, $X/D$ and $Y/D$ and evolution of vorticity contours for near-wall cylinder ($e/D = 0.9$) at $U_r = 3$ and $Re = 200$.

### 4.4.6.1  *Pre-lock-in, $U_r$ = 3.*  Figure 4.13 represents time histories of $C_D$, $C_L$, $X/D$ and $Y/D$ and vorticity contour plots at corresponding time instances. Both drag and lift force are in phase with transverse and streamwise displacements respectively as indicated by 4.10(a). The neutral position of the cylinder's center is marked with a cross. It can be seen that the displacement of the cylinder is very small since it barely changes position with the reference to the marker at dimensionless time instance $\tau = 502$ which corresponds to the maximum streamwise displacement (in positive $x$-axis direction) and at the same time the minimum transverse position. This is consistent with the observations made in Fig. 4.7 and Fig. 4.9 since the cylinder is still in the pre-lock-in regime and there is no resonance leading to the big amplitudes of vibration. The mechanism of the

**(a)** Time histories of $C_D$, $C_L$, $X/D$ and $Y/D$

**(b)** $tU/D = 502$

**(c)** $tU/D = 502.5$

**(d)** $tU/D = 504.2$

**(e)** $tU/D = 504.9$

Z Vorticity: -1 -0.9 -0.8 -0.7 -0.6 -0.5 -0.4 -0.3 -0.2 -0.1 0.1 0.2 0.3 0.4 0.5 0.6 0.7 0.8 0.9 1
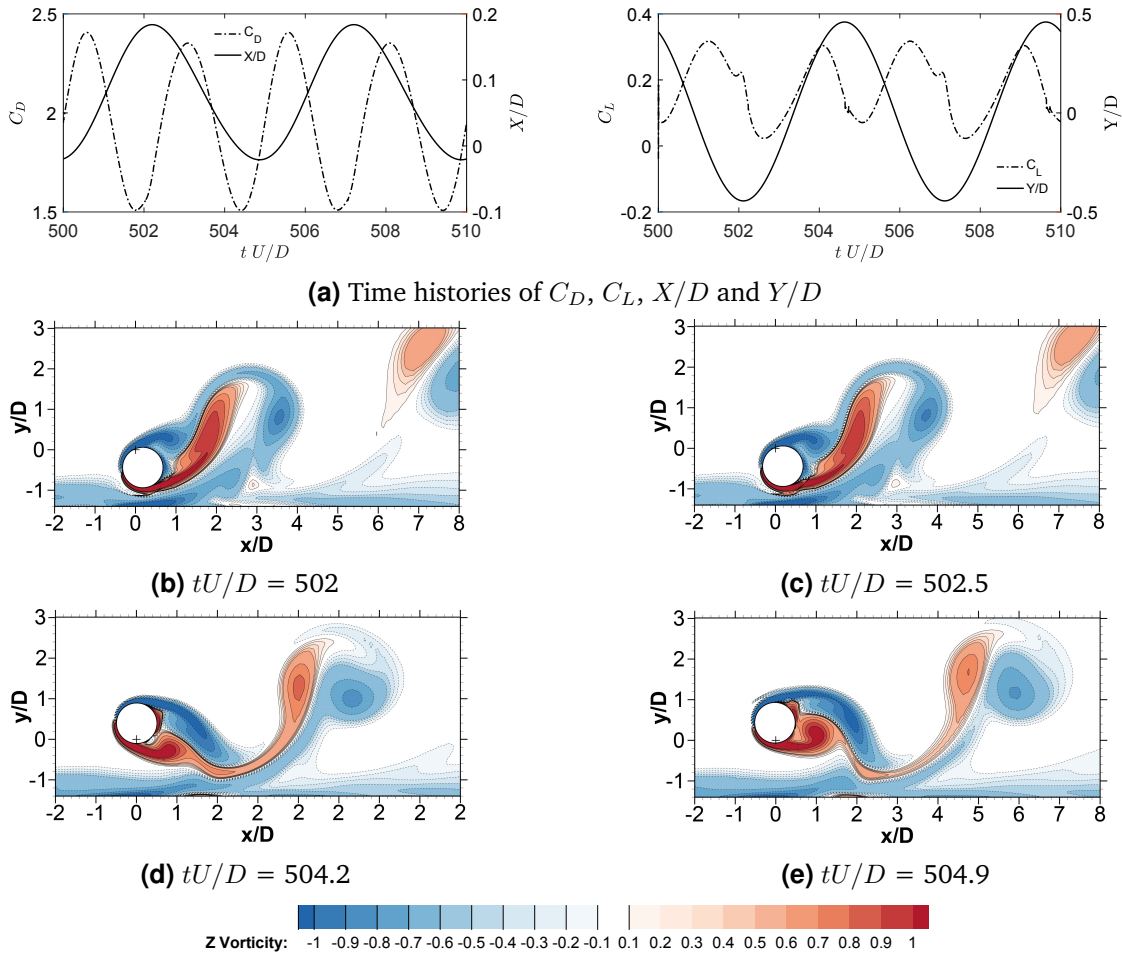
**Figure 4.14:** Time histories of $C_D$, $C_L$, $X/D$ and $Y/D$ and evolution of vorticity contours for near-wall cylinder ($e/D = 0.9$) at $U_r = 5$ and $Re = 200$.

bottom shear layer rollup can be observed. The anti-clockwise vortex shed from the bottom surface of the cylinder (B) forces the boundary layer to rollup. In Fig. 4.13 (d) the clockwise vortex shed from the upper cylinder surface (A) shows coalescent interaction with the clockwise vortex shed from the bottom boundary layer (C). This interaction reinforces the clockwise vortices shed from the top surface of the cylinder and weakens the anticlockwise vortices shed from the bottom surface of the cylinder. In accordance with observations of Li et al. (2016) the suppression of the counter-clockwise vortices shed from the bottom of the cylinder is the reason for matched vibration frequencies in streamwise and transverse directions. This, in turn, leads to streamwise frequency lock-in and is the root cause of the significantly increased streamwise oscillations.

#### 4.4.6.2 *Lock-in, $U_r$ = 5.*   A representative case for the lock-in regime is the simulated case at $U_r = 5$, where large amplitudes of vibrations are reported. Figure 4.14 presents

**(a)** Time histories of $C_D$, $C_L$, $X/D$ and $Y/D$



**(b)** $tU/D = 502.4$



**(c)** $tU/D = 502.7$



**(d)** $tU/D = 504.7$



**(e)** $tU/D = 505.1$

Z Vorticity: -1 -0.9 -0.8 -0.7 -0.6 -0.5 -0.4 -0.3 -0.2 -0.1 0.1 0.2 0.3 0.4 0.5 0.6 0.7 0.8 0.9 1
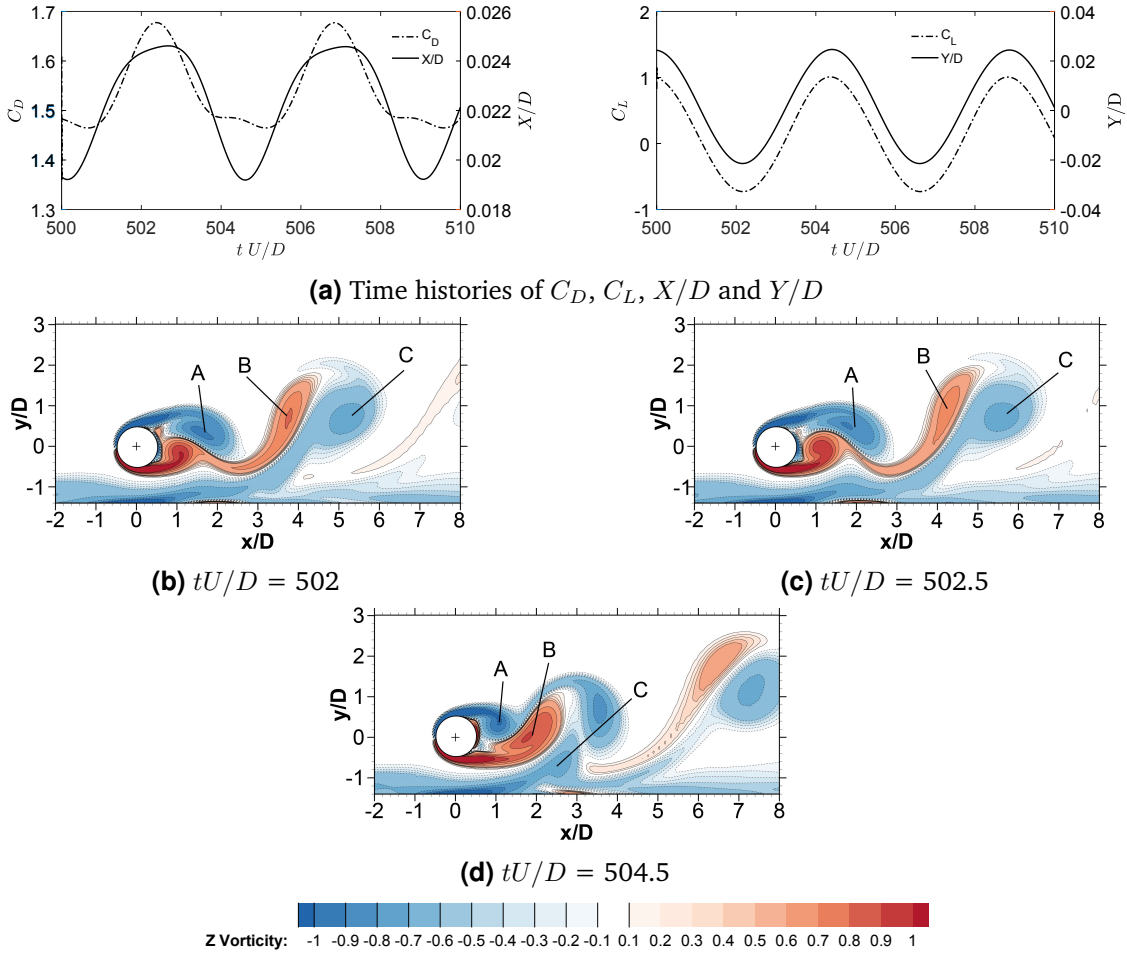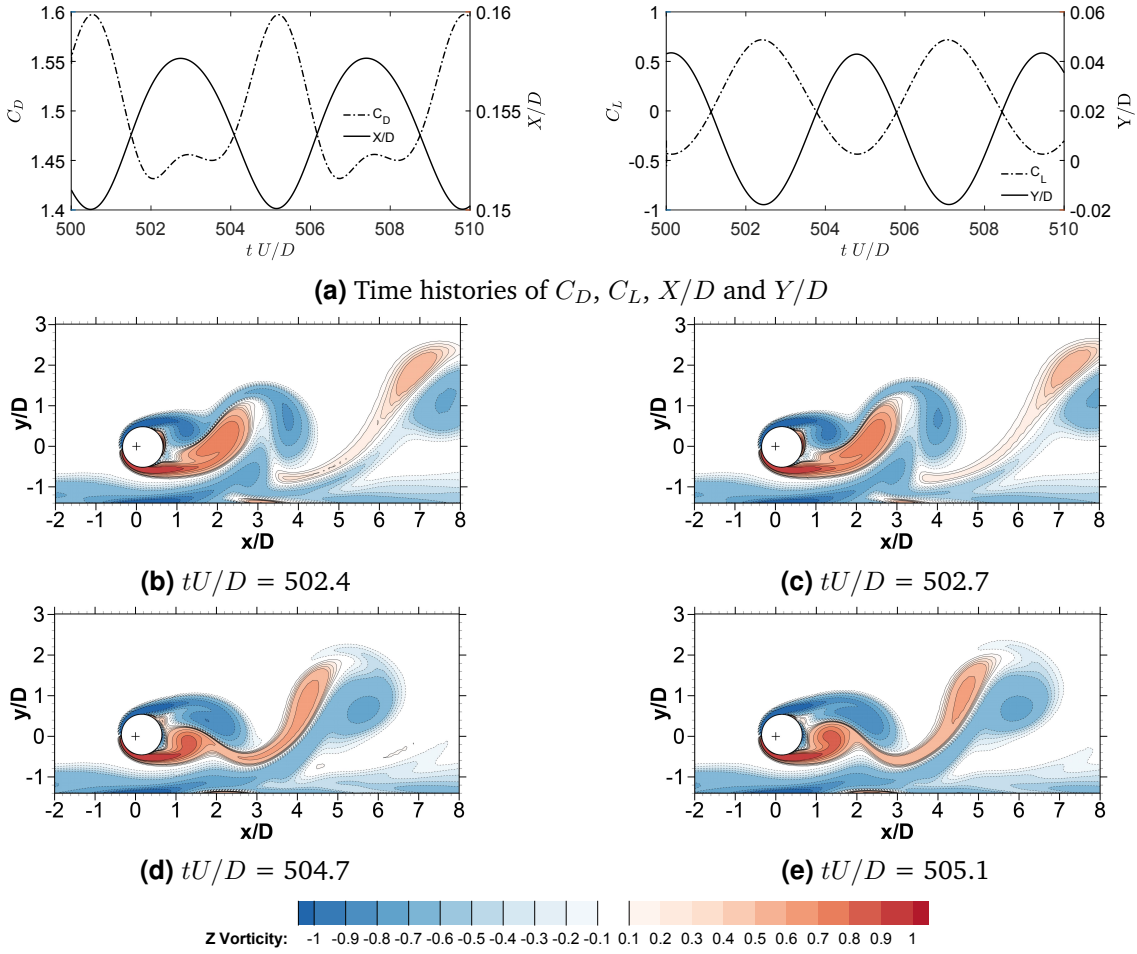
**Figure 4.15:** Time histories of $C_D$, $C_L$, $X/D$ and $Y/D$ and evolution of vorticity contours for near-wall cylinder ($e/D = 0.9$) at $U_r = 8$ and $Re = 200$.

the time histories of $C_D$, $C_L$, $X/D$ and $Y/D$ and the vorticity contour plots at corresponding time instances. From the time history of $C_L$ (Fig. 4.14 (a)) it can be seen that relatively small lift coefficient values correspond to large transverse displacements. Similarly to the pre-lock-in case, here the bottom layer roll-up effect is present as well. Because of the large cylinder displacements in the transverse direction, the coalescent interaction between the clockwise vortices shed from the top of the cylinder and clockwise vortices rolled-up by negative vorticity shed from the bottom of the cylinder is more pronounced. The reason for that is the larger displacement in the transverse direction cause the cylinder to submerge deeper into the bottom boundary layer. The cylinder's wake is much wider at $Ur = 5$ than $U_r = 3$.

**4.4.6.3  Post Lock-in, $U_r = 8$.**  Figure 4.15 represents time histories of $C_D$, $C_L$, $X/D$ and $Y/D$ and vorticity contour plots for post-lock-in case at $U_r = 8$. It can be clearly seen

from the time history (Fig.4.15 (a)) that the force coefficients are now in an out of phase relation with the displacements. The amplitudes of oscillations are small, similar to the situation discussed in the pre-lock-in case. The bottom shear layer roll-up is present and the interaction of vortices shed from the cylinder is analogous to the pre-lock-in case, thus the wake formed at $U_r = 8$ is of similar width to that observed at $U_r = 3$.

### 4.4.7  Vibration Frequency Characteristics

Fast Fourier Transform analysis is used to compute the frequency power spectra of the hydrodynamic forces $C_D$, $C_L$, as well as of the displacement time histories $Y/D$, $X/D$ in dimensionless period $\tau = 250 - 500$ ($\tau = 600 - 1000$ in cases at $3.8 \leq U_r \leq 4.2$). Results of the calculations covering all analyzed reduced velocities can be found in the Appendix A. Selected representative cases will be discussed here.

In the pre-lock-in regime, the displacements are characterized by a single-mode response, and the vibration amplitudes are small. This situation can be seen in Fig. 4.16. The drag force has a second super-harmonic at a frequency twice that of the dominating excitation frequency. The dominant frequencies of the drag and the lift force are coinciding and are equal to approximately 0.21 Hz. In the synchronization regime, the $U_r$ reaches a critical value at which the cylinder enters the lock-in regime. In accordance with the lock-in regime of $U_r$ identified by inspection of Fig. 4.9 the transition occurs at $U_r = 3.8$. The characteristic beating phenomenon is encountered in the hydrodynamic forces and displacements time series. The most distinguishable are the fluctuations in the drag force followed by the streamwise oscillations. Due to the presence of many harmonics



**Figure 4.16:** Power spectral analysis for transverse vibration and lift (right), streamwise vibration and drag (left) at $e/D = 0.9$, $U_r = 3$, $Re = 200$.

in the signal, the FFT picture cannot identify the single dominating frequency and the

**Figure 4.17:** Power spectral analysis for transverse vibration and lift (right), streamwise vibration and drag (left) at $e/D = 0.9$, $U_r = 3.8$, $Re = 200$.

characteristic scattered image is produced (Fig. 4.17). This implies that many concurrent exciting frequencies exist, this is the effect of switching between different vorticity production mechanisms. In the lock-in regime, the time traces display stable quasi-steady behavior. Looking at reduced velocities between $U_r = 4.3$ and $U_r = 5.6$ following conclusions can be drawn. The dominating vibration frequency in the streamwise direction coincides with the dominating vibration frequency in the transverse direction and decreases monotonically with increasing $U_r$. Both, drag and lift force have dominating frequency of approximately twice the frequency of the cylinder vibrations. The streamwise displacement amplitude decreases slightly with increasing $U_r$ while the transverse displacement amplitude decrease is more pronounced as $U_r$ is increased. The transition from the lock-in regime to the post-lock-in regime at $U_r = 6.5$ (Fig. 4.18) is marked with the beating phenomenon. The oscillations of the hydrodynamic forces and displacements are less chaotic during transition from the lock-in to the post-lock-in than when the transition to the lock-in occurs. In the post-lock-in regime, the power spectra pictures are similar to the pre-lock-in regime. In Figure 4.19 at $U_r = 8$ the dominating frequencies of the lift and drag forces coincide with the dominating frequencies of respective displacements but similarly to $U_r = 3$ the amplitudes are very small.

## 4.4.8  Vortex Shedding Modes

Figure 4.20 and Figure 4.21 presents the wake development at selected reduced velocities. Snapshots were taken at the minimum transverse displacement position and approximately around the same nondimensional time $\tau = 495$. Referring to the discussion on the flow field characteristics given in Section 4.4.6, the proximity of the wall has significant implications on the behavior of the wake. Specifically the break-down of the
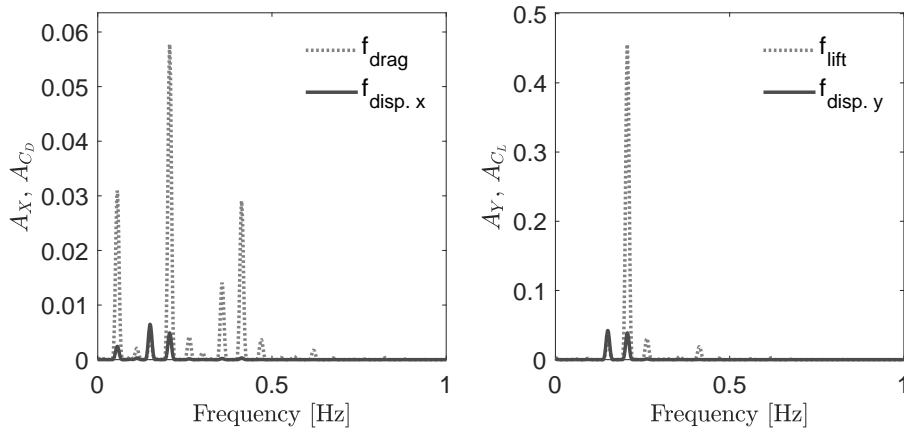
**Figure 4.18:** Power spectral analysis for transverse vibration and lift (right), stream-wise vibration and drag (left) at $e/D = 0.9$, $U_r = 6.5$, $Re = 200$.
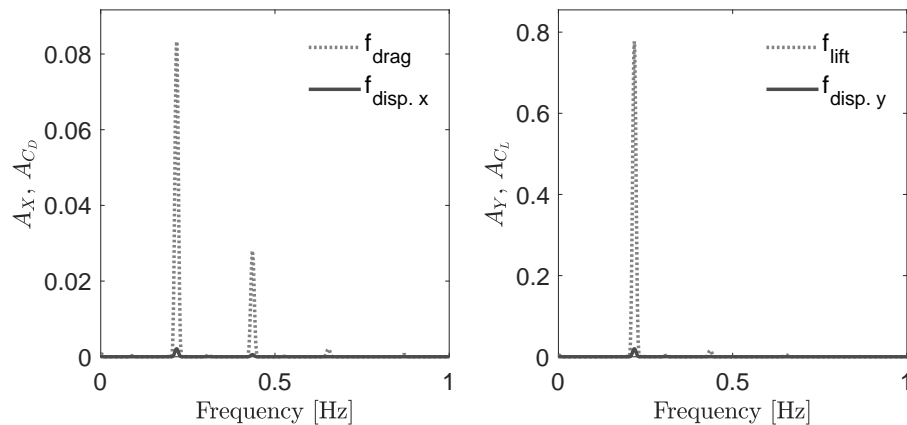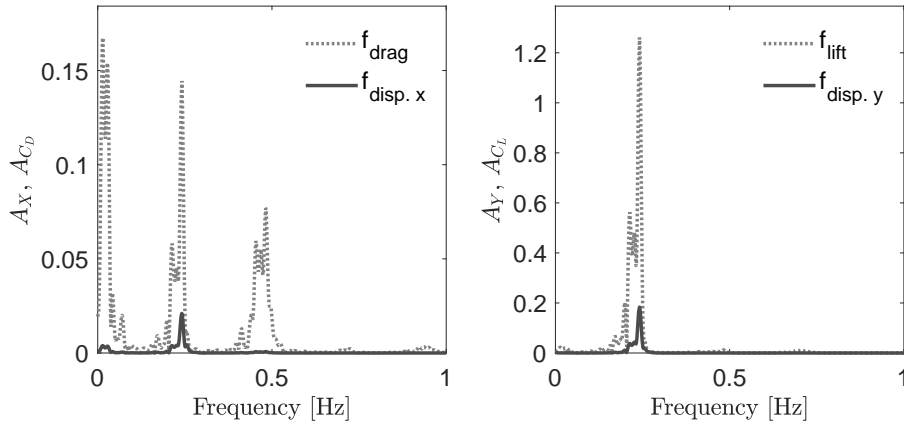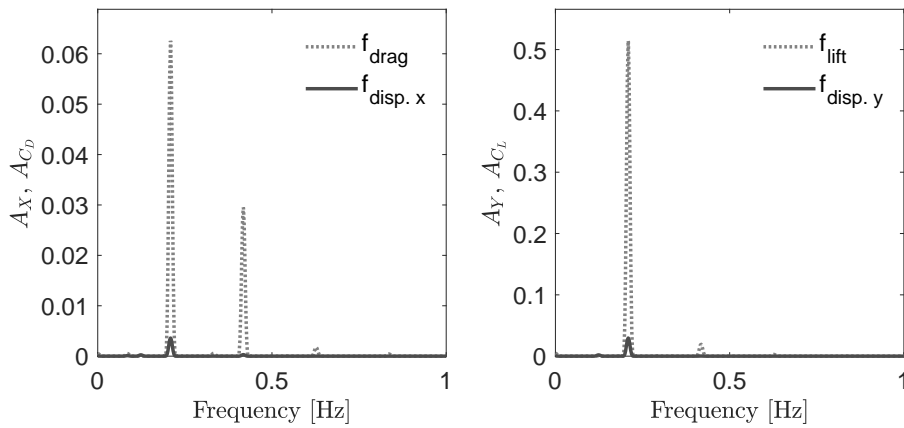


**Figure 4.19:** Power spectral analysis for transverse vibration and lift (right), stream-wise vibration and drag (left) at $e/D = 0.9$, $U_r = 8$, $Re = 200$.

symmetry in the flow and the bottom shear layer roll-up. The suppression of the bottom vortex shedding is closely connected to the asymmetry in the development of the vortices on both sides of the cylinder. The strength of the clockwise vortices is enhanced by the coalescence with the clockwise vortices developed from the bottom boundary layer roll-up. The anticlockwise vortices shed from the bottom of the cylinder are on the other hand weaker due to the interaction with the bottom boundary layer. In all analyzed cases the vortex shedding pattern represents the 2S mode. It should be noted that in the pre-lock-in regime as well as in the post-lock-in regime counterclockwise vortices are slightly weaker than in the lock-in regime.

**(a)** $U_r = 3.0$

**(b)** $U_r = 3.9$

**(c)** $U_r = 4.3$

**Z Vorticity:**    -1  -0.9 -0.8 -0.7 -0.6 -0.5 -0.4 -0.3 -0.2 -0.1 0.1  0.2  0.3  0.4  0.5  0.6  0.7  0.8  0.9  1
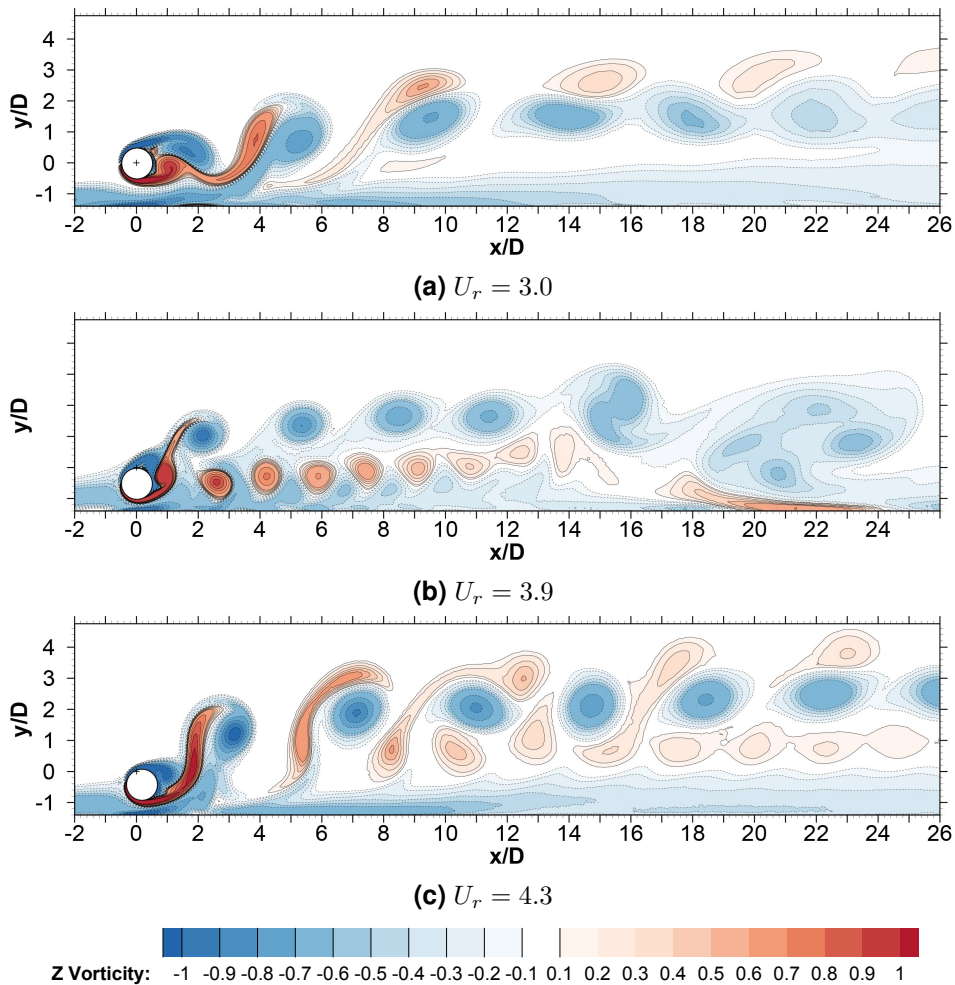
**Figure 4.20:** Vortex shedding modes at selcted $U_r$ for near-wall cylinder ($e/D = 0.9$; $Re = 200$).

## 4.5  Summary

A series of numerical simulations in laminar ($Re = 200$) regime is performed to study the flow around a freely oscillating cylinder in the proximity of a plane wall. All numerical solutions are obtained by using incompressible Finite Volume Code OPENFOAM. Range of reduced velocities from $U_r = 3$ to $U_r = 8$ is investigated, at a gap ratio of $e/D = 0.9$. Hydrodynamic forces and response amplitudes are mapped with respect to the investigated reduced velocities. Furthermore, a study of phase differences between the drag force and the streamwise displacement and the lift force and the transverse displacement is conducted. The motions of the cylinder are recorded and displayed on the trajectory plots, Fast Fourier Transform is used to analyze the frequency components

**(a)** $U_r = 5.0$

**(b)** $U_r = 6.0$

**(c)** $U_r = 7.0$

**(d)** $U_r = 8.0$

**Z Vorticity:** -1 -0.9 -0.8 -0.7 -0.6 -0.5 -0.4 -0.3 -0.2 -0.1 0.1 0.2 0.3 0.4 0.5 0.6 0.7 0.8 0.9 1
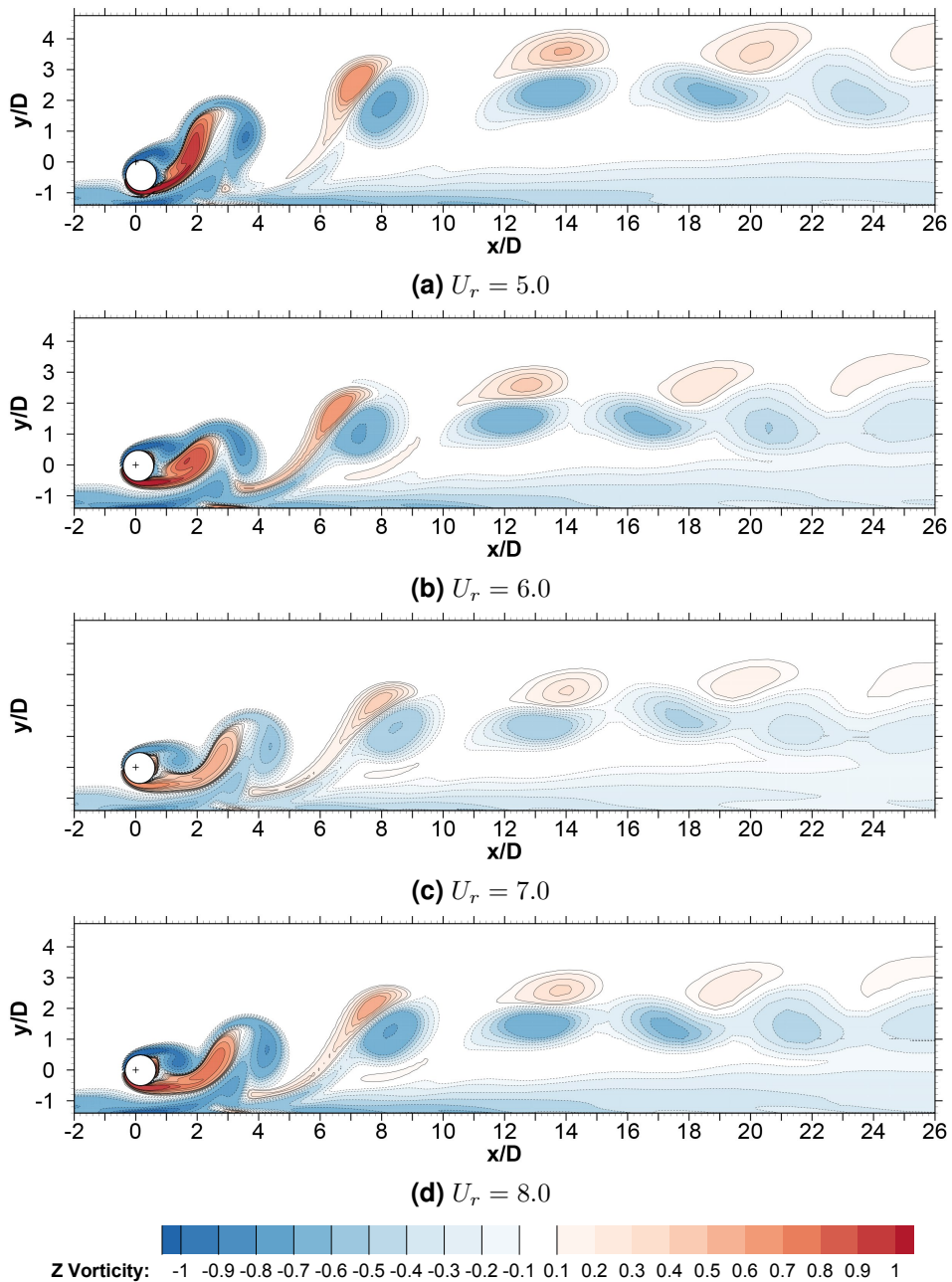
**Figure 4.21:** Vortex shedding modes at selcted $U_r$ for near-wall cylinder ($e/D = 0.9$; $Re = 200$).

of hydrodynamic forces and displacements. Vorticity fields are analyzed to study the effects of the shear layers interaction in the area around the oscillating cylinder. Based on the observations presented in this chapter following conclusions can be drawn from the study:

1. The results are supportive to the suggestion that the wall proximity enlarges the mean lift force but the influence on the mean drag force is minimal.

2. Proximity of the wall strongly enhances the streamwise response of a cylinder. Analysis of the phase relations between the drag force and the streamwise displacement revealed two distinct phases in the lock-in regime. The phase of the positive net energy transfer from the fluid to the structure and the phase of the negative energy transfer when the energy is dissipated by the fluid. The first phase is found to coincide with the pre-lock-in regime and the initial branch of the lock-in. The second phase is identified in the lower branch of the lock-in regime.

3. Study of the vortex shedding mechanism shows that the bottom shear layer vorticity counteracts the vortices shed from the bottom surface of the cylinder leading to the asymmetry of the wake. This, in turn, reduces the streamwise oscillation frequency by half. It is the reason for the streamwise frequency lock-in, thus both transverse and streamwise vibration frequencies are simultaneously in resonance with hydrodynamic forcing.

4. Vortex shedding patterns in the investigated $U_r$ range show the 2S shedding pattern. The width of the wake and strength of the counterclockwise vortices are affected by the vibration amplitude with wider wake and stronger counter-clockwise vortices occurring in the lock-in regime.

5. In the lock-in transition regime, the beating oscillations of the hydrodynamic forces and vibration response are found. More pronounced, chaotic patterns occur at $U_r = 3.75$ in the transition from pre-lock-in to lock-in. Oscillations of the hydrodynamic forces and vibration responses are more organized when the cylinder exits the lock-in regime.

# References

Blackburn, H. M. and R. D. Henderson (1999). A study of two-dimensional flow past an oscillating cylinder. *Journal of Fluid Mechanics 385*, 255 – 286.

Geuzaine, C. and J. F. Remacle (2009). Gmsh: a three-dimensional finite element mesh generator with built-in pre- and post-processing facilities. *International Journal for Numerical Methods in Engineering 79*(11), 1309 – 1331.

Jaiman, R. K., M. Z. Guan, and T. P. Miyanawala (2016). Partitioned iterative and dynamic subgrid-scale methods for freely vibrating square-section structures at subcritical Reynolds number. *Computers & Fluids 133*(Supplement C), 68 – 89.

Li, Z., R. C. Mysa, R. K. Jaiman, and B. C. Khoo (2018). Freely vibrating circular cylinder in the vicinity of fully developed scour holes at low Reynolds numbers. *Computers & Fluids 163*, 97 – 120.

Li, Z., W. Yao, K. Yang, R. K. Jaiman, and B. C. Khoo (2016). On the vortex-induced oscillations of a freely vibrating cylinder in the vicinity of a stationary plane wall. *Journal of Fluids and Structures 65*, 495 – 526.

Navrose, N. and S. Mittal (2013). Free vibrations of a cylinder: 3d computations at Re = 1000. *Journal of Fluids and Structures 41*, 109 – 118.

Prasanth, T. K. and S. Mittal (2008). Vortex-induced vibrations of a circular cylinder at low Reynolds numbers. *Journal of Fluid Mechanics 594*, 463 -âĂŞ 491.

Sumer, B. M. and J. Fredsøe (2006). *Hydrodynamics around cylindrical strucures*. World Scientific.

Tham, D. M. Y., P. S. Gurugubelli, Z. Li, and R. K. Jaiman (2015). Freely vibrating circular cylinder in the vicinity of a stationary wall. *Journal of Fluids and Structures 59*, 103 – 128.

Williamson, C. H. K. and R. Govardhan (2004). Vortex-induced vibrations. *Annual Review of Fluid Mechanics 36*(1), 413 – 455.

Zdravkovich, M. M. (1997). *Flow Around Circular Cylinders: Volume I: Fundamentals*. OUP Oxford.

**CHAPTER 5**

# PAPER I: VORTEX-INDUCED VIBRATIONS OF TWO RIGID CYLINDERS WITH UNEVEN DIAMETERS NEAR THE HORIZONTAL PLANE WALL AT LOW REYNOLDS NUMBER

This chapter contains the paper draft which will be submitted to the Journal of Fluids and Structures. Results and discussions contained in this study can be treated as an extension of the work presented in Chapter 4. In particular, the scope of the study is extended to investigate the effects of different configurations of rigidly coupled cylinders with uneven diameters on VIV in the vicinity of a plane wall. One example of an engineering application of such model are subsea flowlines in a "piggyback" configuration, where a small diameter pipeline is rigidly attached to a larger diameter pipeline. In current guidelines a common practice is to use an equivalent hydrodynamic diameter (DNV GL, 2017) and consider the most critical cross-section orientation in the calculations. The results of the present analysis indicate however that the position of the small cylinder can have a fundamental impact on the VIV response of the coupled system. It is therefore desireable to gain additional insight on the complex flow physics involved in such flows which can translate to more accurate and robust design practices.

# Vortex-induced vibrations of two cylinders with uneven diameters near the horizontal plane wall at low Reynolds number

**Marek Jan Janocha[1] , Muk Chen Ong[1]\*,  Zhong Li[2]**

[1]Department of Mechanical and Structural Engineering and Materials Science, University of Stavanger, Stavanger 4036, Norway

[2]NUS Graduate School for Integrative Sciences and Engineering, National University of Singapore, 28 Medical Drive, Singapore 117456, Singapore

A numerical study is performed on the vortex-induced vibrations of two rigidly coupled cylinders of uneven diameters placed in the proximity of the plane wall. The two cylinders are elastically supported and free to vibrate in two degree-of-freedom. The Reynolds number is kept constant at $Re = 200$. Different position angles of the small cylinder are systematically studied. The effects on the vibration amplitudes and hydrodynamic forces are analyzed. The flow structures around the cylinders are investigated to explain the variations in observed structural responses. At selected gap ratio ($e/D = 0.9$) the bottom boundary effects are found to significantly affect the behavior of the structure. The suppression of the vortex shedding from the bottom surface of the large cylinder is observed, leading to streamwise vibration lock-in. The cross-flow vibration amplitude of the coupled cylinders is found enhanced in the widest range of reduced velocities ($U_r$), among analyzed configurations, when the small cylinder is located downstream of the large cylinder ($\alpha = 0°$). When located side by side ($\alpha = 90°$) the effect of the small cylinder is manifested by increased mean drag and change in the direction of the mean lift force to negative (directed towards the wall). In case of the small cylinder located upstream of the large cylinder ($\alpha = 180°$) reduced vibration response and narrower lock-in range is identified compared with the single cylinder and other analyzed coupled cylinders configurations.

**Key words:** vortex-induced vibrations, piggyback, lock-in, vortex shedding

\*  Email address for correspondence: muk.c.ong@uis.no

2

## 1. Introduction

Vortex-induced vibrations (VIV) of elastically supported structures is an area of interest for many practical engineering applications. One major group of structures, often subject to VIV, are offshore subsea pipelines. Due to various economic and engineering reasons it is a common practice to install subsea pipelines in bundles where, in the most frequent arrangement, the main pipe is accompanied by a smaller pipe attached to it at certain intervals via clamps or blocks. Physically this system can be modeled as two rigidly coupled cylinders interacting with an incoming flow and experiencing vibrations in two degrees of freedom (2DoF). It is known that oscillatory forces caused by vortex shedding can negatively affect the pipeline stability and its fatigue life. Therefore, the investigation of the influence of the presence and positioning of the secondary cylinder has significant practical implications.

Flow around cylinders is well researched area of fluid dynamics and is covered by many comprehensive positions in the literature, most prominently by Sarpkaya (2010), Sumer & Fredsøe (2006) and Zdravkovich (1997). Large and continuously expanding body of research is related to the study of VIV. However, majority of the studies are focused on the free flow in isolated cylinder configuration.

Near wall effects were investigated experimentally by numerous authors. Most existing studies have focused on the transverse VIV of the cylinder with one degree of freedom due to the larger amplitude in the transverse direction than that in the streamwise direction. Experiments conducted by Bearman & Zdravkovich (1978) investigated the effect of gap ratio ($e/D$ where $D$ is the diameter of the cylinder and $e$ is the distance between the bottom of the cylinder and the wall) on the vortex shedding in the Reynolds number regime varying form $2.5 \times 10^4$ to $4.8 \times 10^4$. Their results indicate that for a stationary cylinder vortex shedding is suppressed if $e/D < 0.3$, thus vibrations cease at low gap ratios. More recently Yang *et al.* (2009) measured the vortex shedding frequencies and modes by the method of hot film velocimetry. The results from the parametric study showed that with decreasing mass ratio ($m^*$), the width of the lock-in range in terms of reduced velocity ($U_r$) and the frequency ratio ( $f/f_n$ ) becomes larger. It was shown that with increasing $e/D$, the amplitude ratio ($A/D$) gets larger up to a critical value of $e/D = 0.5$. PIV measurements by Wang & Tan (2008) at $Re = 1.2 \times 10^4$ confirmed the strong influence of the boundary proximity for small and intermediate gap ratios on the wake development but revealed relatively small sensitivity of Strouhal number and convection velocity to change with respect to change of $e/D$. Wang *et al.* (2013) investigated flow around a neutrally buoyant cylinder with a mass ratio $m^* = 1.0$ and a low damping ratio $\zeta = 0.0173$. Experiment covered range of Reynolds numbers from $Re = 3 \times 10^4$ to $Re = 1.3 \times 10^4$ and reduced velocities from $U_r = 1.53$ to $U_r = 6.6$. In contrast to the case of a stationary cylinder where vortex shedding was suppressed at a gap ratio $e/D < 0.3$ the elastically mounted cylinder was found to vibrate even at the smallest gap ratio $e/D = 0.05$.

Comprehensive numerical studies of the vortex-induced vibrations of a single cylinder freely vibrating in the proximity of the plane wall were carried out by Tham *et al.* (2015), Li *et al.* (2016) and Li *et al.* (2017). Li *et al.* (2016) performed both 2D and 3D simulations using a Petrov-Galerkin finite element formulation. Wall proximity effects were studied in the laminar flow regime at $Re = 200$ in a series of 2D simulations. The wall proximity effects were discussed in terms of streamwise vibration frequency. They investigated the mechanism of wake vortices interaction with the bottom boundary layer. In particular the suppression of the counter-clockwise vortices shed from the bottom of the cylinder proved to be a reason of the streamwise vibration frequency reduction. Li *et al.* (2017) performed 3D simulations at $Re = 1000$ to capture the three dimensional flow effects and assess accuracy and validity of the 2D simulations reported in Li *et al.* (2016). The numerical results reported by Li *et al.* (2017) show that for $Re > 200$ the 3D effects become significant and use of 2D approach in this regime can lead to over predictions of hydrodynamic forces.

Relatively few experimental studies focused on the VIV response of the piggyback pipelines exist up to date. Experiments conducted by Kalghatgi & Sayer (1997) covering the Reynolds number range from $Re = 9 \times 10^4$ to $Re = 3 \times 10^5$, revealed that drag coefficient is significantly increased by the presence of a piggyback pipeline in side by side arrangement. It was also noticed that direction of the lift force is dependent on the $Re$, with dominantly negative mean lift coefficient values in the subcritical regime and positive values of mean lift coefficient in the critical regime. Zang *et al.* (2013) used PIV system to visualize flow around piggyback pipeline with $Re$ ranging from $1.5 \times 10^4$ to $4 \times 10^4$. The vortex shedding characterized by swirling strength was found to be highly sensitive to changes in $G/D$ (where $G$ denotes distance between the small cylinder and the large cylinder) and $e/D$. Zang & Gao (2014) studied the effects of configuration parameters on the VIV suppression in $Re$ numbers from $1.8 \times 10^4$ to $6 \times 10^4$. Besides different diameter ratios $d/D$ ($d$ is the small cylinder diameter, $D$ is the large cylinder diameter), gap ratios $e/D$ and spacing $G/D$, the position angle $\alpha$ of the piggyback pipeline was studied. Here $\alpha$ is defined as the angle position of the small cylinder measured from the center line of the upstream surface of the large cylinder. The maximum lift force was reported for $\alpha = 90°$ and $G/D = 0.25$. When $\alpha = 0°$, the lock-in range of reduced velocity was widest among the analyzed positions. Zhao *et al.* (2007) conducted a series of numerical studies focusing on the flow around piggyback pipelines. In Zhao *et al.* (2007) different values of gap ratio and spacing were studied for a stationary piggyback pipeline in stacked configuration near the seabed. Four shedding modes were identified at $Re = 2 \times 10^4$, governed by the gap and spacing ratios. Zhao & Yan (2013) conducted simulations of an elastically mounted piggyback pipeline in free flow configuration at Reynolds number $Re = 250$. They reported that in comparison to a single cylinder case the lock-in regime in terms of reduced velocity is significantly widened for the small cylinder with $\alpha = 0°$, $22.5°$, $90°$, and $112.5°$. Yang *et al.* (2013) studied flow characteristics of a piggyback pipeline in

4

oscillatory flow at different Keulegan-Carpenter ($KC$) numbers, ranging from $KC = 4$ to $KC = 24$. The influence of the small cylinder was identified to be a function of the spacing $G/D$. The piggyback cylinder was found to disrupt the symmetry of the vortex shedding leading to an increase in the lift force. This effect was reported to be the most pronounced when $KC = 4$.

In this paper, two-dimensional numerical simulations are carried out to investigate the effects on VIV of two cylinders with uneven diameters in different arrangement close to a horizontal plane wall. To the authors' knowledge there is no published numerical study on investigating VIV response of a two rigid cylinders with uneven diameters in the vicinity of a horizontal plane wall in low Reynolds number regime.

The rest of the paper is organized as follows. In Section 2, the governing equations and the numerical model used in the present study are outlined. Section 3, presents the problem description, verification of used numerical meshes and time step selection. The numerical model is also compared with the results from other similar published studies. In Section 4, simulations are performed with different placements of the smaller cylinder and reduced velocities. Diameter ratio $d/D = 0.2$, gap ratio $e/D = 0.9$ and dimensionless cylinder spacing $G/D = 0.1$ is kept constant in all simulations. The effects of a cylinders configuration and plane boundary on VIV of the structure are discussed. Finally, conclusions are presented in Section 5.

## 2. Governing equations and numerical method

### 2.1. *Flow equations*

Incompressible Newtonian fluid flow considered in this work is governed by the Navier-Stokes equations. In an arbitrary Lagrangian Eulerian frame they are expressed as follows:

$$\nabla \cdot \boldsymbol{u} = 0, \tag{2.1}$$

$$\frac{\partial \boldsymbol{u}}{\partial t} + \nabla \cdot ((\boldsymbol{u} - \boldsymbol{w})\boldsymbol{u}) = -\nabla \cdot p + \nabla \cdot (\nu \nabla \boldsymbol{u}), \tag{2.2}$$

where $\boldsymbol{u}$ is the flow velocity vector, $\boldsymbol{w}$ is the moving mesh velocity vector, $p$ represents pressure, $\nu$ is the kinematic viscosity.

### 2.2. *Structure equation*

In the present study we consider elastically supported rigidly coupled cylinders experiencing VIV as shown in figure 1. Flow direction is parallel to the horizontal plane wall. The dynamic behavior of the two rigid, coupled cylinders with uneven diameters vibrating with 2DoF is modeled via a mass-spring-damper system as follows:

$$\frac{\partial^2 x}{\partial t^2} + 4\pi\zeta\frac{\partial x}{\partial t} + 4\pi^2 x = \frac{2}{\pi}\frac{U_r^2 C_D}{m^*(1 + d/D)} \tag{2.3}$$

$$\frac{\partial^2 y}{\partial t^2} + 4\pi\zeta\frac{\partial y}{\partial t} + 4\pi^2 y = \frac{2}{\pi}\frac{U_r^2 C_L}{m^*(1 + d/D)} \tag{2.4}$$
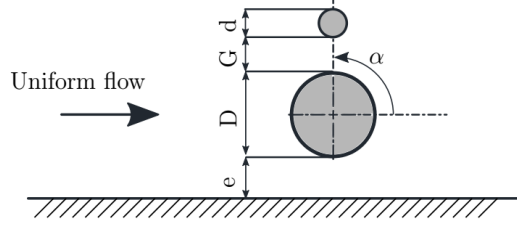
5



Figure 1: Schematic of a problem definition: flow induced vibrations of a two rigidly coupled cylinders with uneven diameters near a horizontal plane wall.

where $x$ and $y$ denote the in-line and transverse displacements respectively, $\zeta$ is the structural damping ratio, and $m^*$ is the mass ratio, given as:

$$m^* = \frac{m}{m_d}, \quad \zeta = \frac{c}{2\sqrt{km}}, \tag{2.5}$$

where $m$ is the mass of the cylinders, $m_d$ is the mass of displaced fluid, $k$ is the structural stiffness and $c$ is the structural damping. The reduced velocity, $U_r$ is defined as $U_r = U_\infty/(f_n D)$, where $f_n$ is the structural natural frequency, $U_\infty$ is free stream flow velocity. $C_D$ and $C_L$ are the drag and lift coefficients, respectively, computed by:

$$C_D = \frac{1}{\frac{1}{2} U_\infty^2 \rho DL} \int_\Gamma \left[ \left( -p\boldsymbol{I} + \mu \left( \nabla \boldsymbol{u} + (\nabla \boldsymbol{u})^T \right) \right) \cdot \boldsymbol{n} \right] \cdot \boldsymbol{n_x} \, d\Gamma \tag{2.6}$$

$$C_L = \frac{1}{\frac{1}{2} U_\infty^2 \rho DL} \int_\Gamma \left[ \left( -p\boldsymbol{I} + \mu \left( \nabla \boldsymbol{u} + (\nabla \boldsymbol{u})^T \right) \right) \cdot \boldsymbol{n} \right] \cdot \boldsymbol{n_y} \, d\Gamma \tag{2.7}$$

where $\Gamma$ is the cylinders surface area, $\rho$ is the fluid density, $L$ represents spanwise dimension of the cylinder, $\boldsymbol{n}$ is the unit vector normal to the cylinders surface, $\boldsymbol{I}$ is the identity tensor. The fluid forces $F_x$ and $F_y$ acting in streamwise and transverse directions are obtained by solving the flow Eqns. 2.1 and 2.2 coupled with structural Eqns. 2.3 and 2.4. The temporal integration of the dynamic equations is performed numerically using Newmark - $\beta$ algortihm.

## 3. Problem description

Problem definition sketch is presented in Figure 1. In the present study a piggyback configuration of two cylinders with uneven diameters is investigated in a series of simulations. The flow configuration considered consists of a uniform fluid stream with velocity $U_\infty$, density $\rho$ and viscosity $\mu$. According to Leontini et al. (2007) the wake of an oscillating cylinder in a uniform cross flow remains two dimensional for $Re < 260$ which is significantly higher than that of a stationary isolated cylinder at $Re < 180$. Due to the oscillatory movement the correlation length in the spanwise direction is increased. It is therefore expected that for $Re = 200$ the vortical structures remain effectively
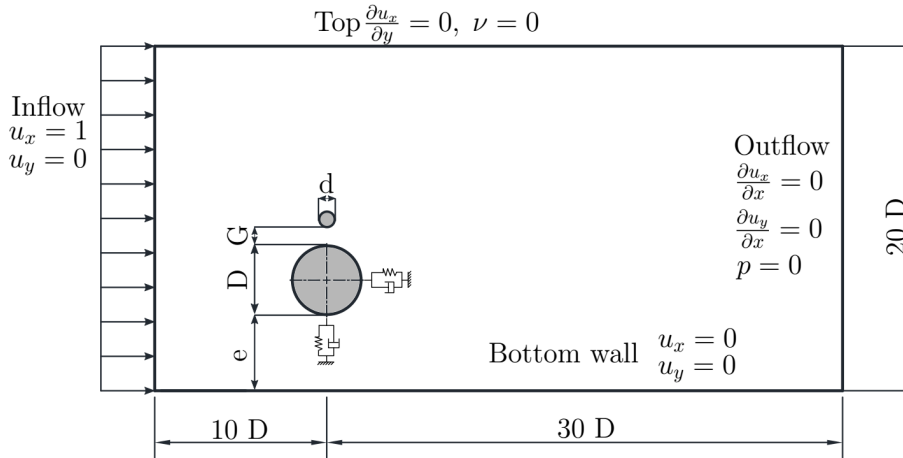
6



Figure 2: Schematic of a computational domain and imposed boundary conditions. Dimensions are given in terms of large cylinder diameter $D$.

two dimensional and 2D simulations give realistic approximation of the flow problem. Reynolds number based on the free stream velocity $U_\infty$ and diameter of the larger cylinder $D$ is kept constant at $Re = 200$ which corresponds to $Re = 40$ based on the diameter of the smaller cylinder $d$. This allows to investigate the effects of vortex shedding from the smaller cylinder as the critical value of Reynolds number at which vortex shedding occurs is satisfied. The reduced mass of the two cylinders system coupled together is set to $m^*$ = 10. The cylinders are rigidly coupled and mounted on elastic supports free to undergo transverse and streamwise vibrations. To encourage large amplitude of displacement, the damping coefficient $\zeta$ is set to zero. The springs in both transverse and in-line directions are assumed to be linear and homogeneous $k = k_x = k_y$. The effect of reduced velocity $U_r$ is investigated in the range from $U_r = 3.0$ to $U_r = 9.0$ with increments of 1, for $\alpha = 90°$ and $\alpha = 180°$ configurations. For the case of $\alpha = 0°$ the $U_r$ range is extended and spans from $U_r = 3.0$ to $U_r = 12.0$ in order to capture the extended lock-in regime. The value of $U_r$ is changed by changing the structural natural frequency. This is done by adjusting the spring stiffness as described by:

$$f_n = \frac{1}{2\pi}\sqrt{\frac{k}{m}} \tag{3.1}$$

The diameter ratio between two cylinders is set to $d/D = 0.2$ reflecting typical value encountered in the subsea piggyback pipelines. This diameter ratio was previously considered in the studies by Yang $et\ al.$ (2013) and Zhao & Yan (2013).

### 3.1. Computational domain and boundary conditions

The present computational domain is established as a rectangular box, and the boundary conditions imposed in all simulations are shown in Fig. 2. The center of the large

7

cylinder is the origin of the coordinate system. The size of the whole computational domain is $40D \times 20D$. In the crossflow direction, it extends from the rigid wall at the bottom up to $20D$. Setting domain width to $20D$ results in blockage equal to 5% which does not affect significantly the flow around cylinder as suggested in Navrose & Mittal (2013). The upstream distance extends $10D$ from the cylinder center and downstream distance is set to $30D$. Similar boundary locations were used in earlier works by Li *et al.* (2016), Navrose & Mittal (2013), Prasanth & Mittal (2008) and has been proven to be sufficient to eliminate the far field effects on the flow upstream and downstream of the cylinder. It is believed that the selected domain boundaries have negligible influence on the flow close to the cylinder in the present study. Surface of both of the cylinders is assumed to be smooth, where no slip boundary is applied: $u_x = 0$, $u_y = 0$ where $u_x$ is the velocity component in $x$-direction and $u_y$ is the velocity component in the $y$-direction. The location of the moving boundary is calculated at each time step. At the inlet Dirichlet conditions are imposed: $u_x = 1$, $u_y = 0$. Bottom wall is specified as a no slip boundary: $u_x = 0$, $u_y = 0$. The top boundary is prescribed with the normal component of the velocity and component of stress vector along the boundary equal to zero: $\frac{\partial u_x}{\partial y} = 0$, $\nu = 0$. At the outlet, the pressure and the normal gradients of the velocities are set to zero: $\frac{\partial u_x}{\partial x} = 0$, $\frac{\partial u_y}{\partial x} = 0$, $p = 0$.

### 3.2. *Grid and timestep convergence studies and code verification*

Hybrid meshes composed of hexahedra and prisms are used. Figure 3 shows a typical mesh of the computational domain for the $\alpha = 90°$ case. Meshes for other configurations are similar. Details of the mesh near the cylinder surfaces are shown in Fig. 4. The mesh topology can be divided into three regions: structured prism layers around the cylinders surfaces, unstructured mesh in the box bounding cylinders and structured background mesh. Mesh around cylinders can be defined using parameters $N_{ik}$, $N_{jk}$ which corresponds to the number of grid points in circumferential and radial directions respectively. Subscript $k = 1$ corresponds to the large cylinder and $k = 2$ corresponds to the small cylinder. Total number of cells in the domain is denoted $N_t$. The bounding box around the cylinder and the background mesh are refined to capture the flow features close to the cylinder and in the wake. Further away from the bounding box and wake refinement region the mesh is gradually coarsened to decrease the computational cost. Two sets of three meshes were prepared for the grid convergence study, one for $\alpha = 0°$ configuration and one for $\alpha = 90°$ configuration. The number of cells $N_{ik}$, $N_{jk}$ and $N_t$ for each case is summarized in Table 1. In order to ensure the mesh independence, computations are performed with three different meshes (a coarse mesh $M1$, a medium mesh $M2$, and a fine mesh $M3$) for two different cylinders configurations $\alpha = 0°$ and $\alpha = 90°$, at $Re = 200$ and reduced velocity $Ur = 5$. At $Ur = 5$ large oscillation amplitudes are expected facilitating comparison of hydrodynamic parameters obtained from the simulations. The time step corresponding to the mesh resolution is set as $\Delta t = 0.002$. Representative hydrodynamic

8

| | Large cylinder | | Small cylinder | | |
| Mesh | $N_{i1}$ | $N_{j1}$ | $N_{i2}$ | $N_{j2}$ | $N_t$ |
|---|---|---|---|---|---|
| $M1_{\alpha=90}$ | 160 | 8 | 80 | 6 | 19758 |
| $M2_{\alpha=90}$ | 320 | 10 | 120 | 8 | 44615 |
| $M3_{\alpha=90}$ | 400 | 16 | 160 | 12 | 79662 |
| $M1_{\alpha=0}$ | 160 | 8 | 80 | 6 | 19758 |
| $M2_{\alpha=0}$ | 320 | 10 | 120 | 8 | 44615 |
| $M3_{\alpha=0}$ | 400 | 16 | 160 | 12 | 79662 |

Table 1: Summary of cell distribution in the structured block around cylinders for different meshes used in the convergence study.
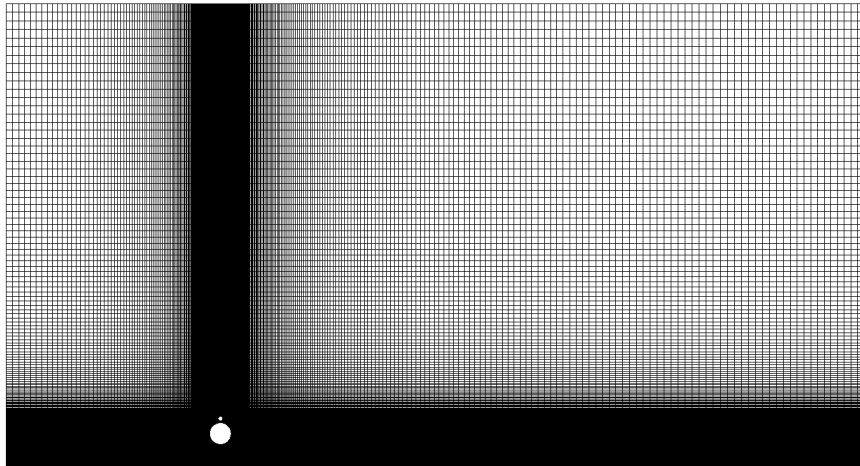


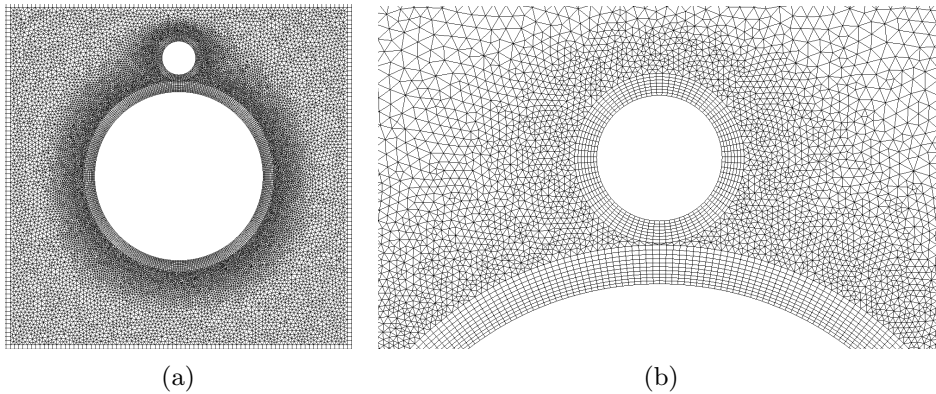Figure 3: A typical computational mesh with 44615 elements: computational domain view.



(a)                                          (b)

Figure 4: Mesh details: Close up view of the mesh around the cylinders (a). Details of the mesh near the cylinders surface (b).

9

force coefficients and cylinder responses undergoing free vibrations are used to asses the convergence. The mean drag coefficient and mean lift coefficient are defined and calculated as follows:

$$\overline{C}_L = \frac{1}{n} \sum_{i=1}^{n} C_{L,i} \tag{3.2}$$

$$\overline{C}_D = \frac{1}{n} \sum_{i=1}^{n} C_{D,i} \tag{3.3}$$

Root-mean-square values of drag coefficient and lift coefficient are calculated using expressions:

$$C_L^{rms} = \sqrt{\frac{1}{n} \sum_{i=1}^{n} (C_{L,i} - \overline{C}_L)^2} \tag{3.4}$$

$$C_D^{rms} = \sqrt{\frac{1}{n} \sum_{i=1}^{n} (C_{D,i} - \overline{C}_D)^2} \tag{3.5}$$

The maximum vertical and root-mean-square horizontal amplitudes are given as:

$$\frac{(A_y)_{max}}{D} = \frac{1}{2} \frac{|(A_y)_{max} - (A_y)_{min}|}{D} \tag{3.6}$$

$$\frac{(A_x)_{rms}}{D} = \frac{\sqrt{\frac{1}{n} \sum_{i=1}^{n} (A_{x,i} - \overline{A}_x)^2}}{D} \tag{3.7}$$

The simulations are performed with time-step $\Delta t = 0.002$ for total duration of $\tau = 500$, where $\tau$, is non-dimensionalised time given by:

$$\tau = tU/D \tag{3.8}$$

The mesh parameters and corresponding representative hydrodynamic quantities obtained from convergence study are given in Table 2, along with the percentage changes. The differences between the results of solutions obtained on mesh M2 and mesh M3 are approximately within 1.5%. By considering the computational cost, meshes with density similar to M2 are used for other simulations in the present study. Simulations are performed using two different values of the time step in order to study the influence of temporal resolution on the flow parameters. Quantified results of the time step study are shown in Table 3. The difference in calculated mean drag coefficient using time step $\Delta t = 0.001$ compared to the timestep $\Delta t = 0.002$ is on both meshes smaller than 0.5%. Root-mean-square lift coefficient values are slightly more sensitive to the timestep value and differ by approximately 1% between $\Delta t = 0.001$ and $\Delta t = 0.002$. The maximum transverse vibration amplitude is more sensitive to the timestep value change in the $\alpha = 90°$ configuration and is approximately 1.3% lower when smaller timestep is used. In the $\alpha = 90°$ configuration this difference is smaller and is equal to 0.35% when smaller timestep is used. The Strouhal number appears to be insensitive to the timestep change in

10

| Mesh parameters: | | | Hydrodynamic parameters: | | | |
|---|---|---|---|---|---|---|
| Mesh variant | Mesh density | Cell count | $\overline{C}_D$ | $C_L^{rms}$ | $St$ | $Ay_{max}$ |
| $M1_{\alpha=0}$ | Coarse | 19758 | 1.734 | 0.7532 | 0.190 | 0.5124 |
| $M2_{\alpha=0}$ | Normal | 44615 | 1.722 (0.69%) | 0.7489 (0.57%) | 0.190 (0%) | 0.5066 (1.13%) |
| $M3_{\alpha=0}$ | Fine | 79662 | 1.712 (0.58%) | 0.7442 (0.62%) | 0.190 (0%) | 0.4992 (1.46%) |
| $M1_{\alpha=90}$ | Coarse | 19758 | 2.886 | 0.4403 | 0.21 | 0.4669 |
| $M2_{\alpha=90}$ | Normal | 44615 | 2.874 (0.41%) | 0.4421 (0.41%) | 0.21 (0%) | 0.4589 (1.71%) |
| $M3_{\alpha=90}$ | Fine | 79662 | 2.854 (0.69%) | 0.4431 (0.22%) | 0.21 (0%) | 0.4519 (1.52%) |

Table 2: Flow past 2DoF cylinder near plane wall at $Re = 200$: effects of mesh resolution. Other parameters of the simulations: $\Delta t = 0.002$.

| Mesh parameters: | | | Hydrodynamic parameters: | | | |
|---|---|---|---|---|---|---|
| Mesh variant | Time step | Cell count | $\overline{C}_D$ | $C_L^{rms}$ | $St$ | $Ay_{max}$ |
| $M2_{\alpha=0}$ | $\Delta t = 0.002$ | 44615 | 1.722 | 0.7489 | 0.190 | 0.5066 |
| $M2_{\alpha=0}$ | $\Delta t = 0.001$ | 44615 | 1.724 (0.12%) | 0.7416 (0.97%) | 0.190 (0%) | 0.5047 (0.35%) |
| $M2_{\alpha=90}$ | $\Delta t = 0.002$ | 44615 | 2.874 | 0.4421 | 0.21 | 0.4589 |
| $M2_{\alpha=90}$ | $\Delta t = 0.001$ | 44615 | 2.860 (0.47%) | 0.4369 (1.19%) | 0.21 (0%) | 0.4527 (1.35%) |

Table 3: Flow past 2DoF cylinder near plane wall at $Re = 200$: effects of time-step. Other parameters of the simulations: Mesh M2.

the investigated range. Considering the computational effort and small differences in the calculated representative hydrodynamic quantities the timestep $\Delta t = 0.002$ is selected for other simulations in the present study. In the summary of the convergence studies the mesh M2 with the timestep $\Delta t = 0.002$ is considered to provide the best balance of accuracy and computational efficiency.

Accuracy of selected numerical technique is assessed by comparison with the study by Li *et al.* (2018) for the flow past a 2DoF single cylinder in a proximity of the plane wall. Li *et al.* (2018) performed 2D simulations at $Re = 200$ using a rectangular domain with the cylinder located at a distance of $10D$ from the inlet where the uniform flow was specified and $30D$ from the outlet of the domain. The width of the domain was set to $20D$. Mesh of a near-wall single cylinder used in the comparison study is qualitatively similar to the mesh M2 shown in Fig. 3. The results of normalized maximum transverse displacement $A_{Y,max}/D$ and root-mean-square normalized streamwise displacement $A_{X,rms}/D$ are in a good agreement with the results reported by Li *et al.* (2018) shown in Fig. 5. Similarly values of mean drag coefficient $\overline{C}_D$ and root-mean-square lift coefficient $C_L^{rms}$ presented in Fig. 6 reach fairly good match compared with Li *et al.* (2018). It appears that the present numerical approach is suitable for studying the VIV of a two cylinders with uneven diameters in the vicinity of a horizontal plane wall.
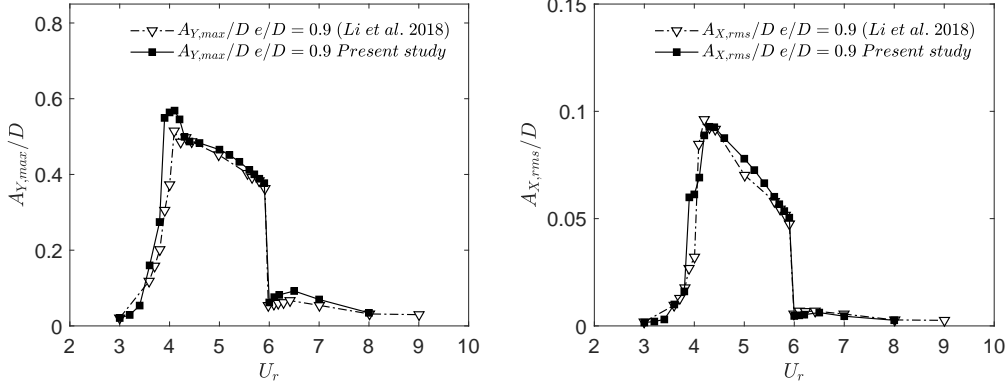
Figure 5: Validation study: Non-dimensional maximum amplitude of cross flow vibration $A_{Y,max}/D$ and non-dimensional root-mean-square in-line displacement $A_{X,rms}/D$ against reduced velocity at $Re = 200$.
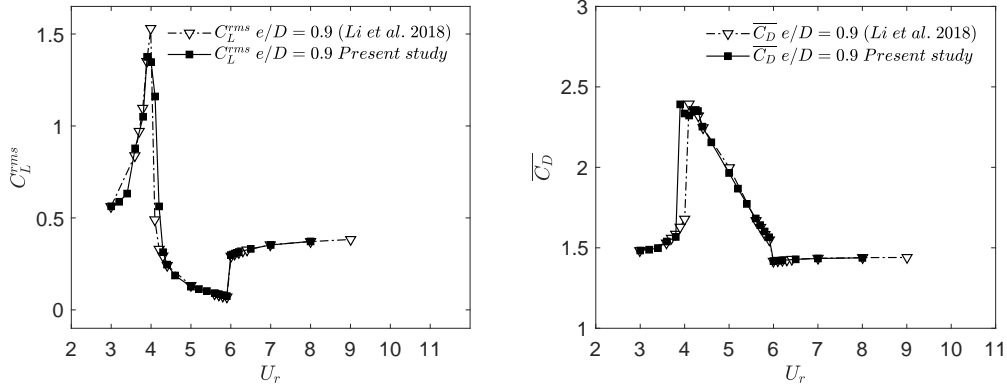


Figure 6: Validation study: Mean lift coefficient $\overline{C}_L$ and mean drag coefficient $\overline{C}_D$ against reduced velocity at $Re = 200$.

## 4. Results and Discussion

Each simulation is carried out for $\tau = 500$ in order to obtain sufficiently long period of repetitive vibration pattern. Normalized maximum displacement in $y$-direction ($A_{Y,max}/D$) and normalized root-mean-square displacement in $x$-direction ($A_{X,rms}/D$), mean lift coefficient ($\overline{C}_L$), mean drag coefficient ($\overline{C}_D$), root-mean-squared lift coefficient ($C_L^{rms}$) and root-mean-squared drag coefficient ($C_D^{rms}$) are extracted and calculated in each simulation case from a dimensionless time range $\tau = (250 - 500)$, ensuring that at least 20 cycles of vertex shedding are covered.

### 4.1. *Analysis of the amplitude response*

Figure 7 presents the normalized displacements in transverse direction $A_{Y,max}/D$ and root-mean-squared normalized displacement in streamwise direction $A_{X,rms}/D$. The lock-in range can be easily identified in all analyzed cases. The present shape of the prdeicted response curves is typical for low mass ratio and low $Re$ vortex-
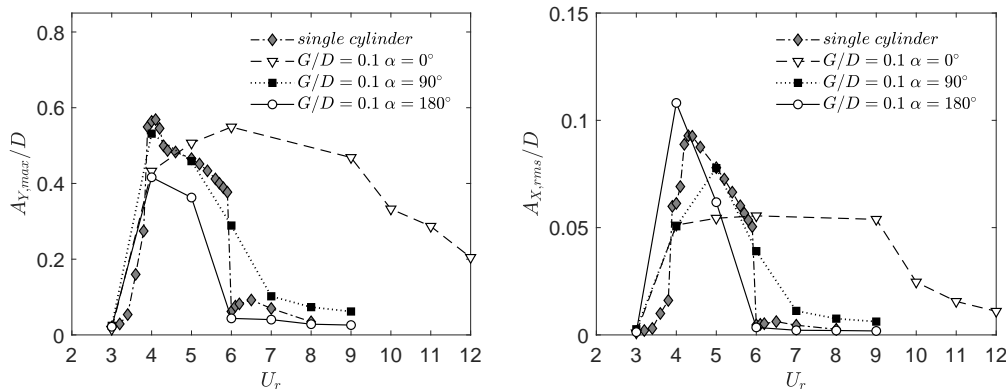
12



Figure 7: Non-dimensional maximum amplitude of cross flow vibration $A_{Y,max}/D$ and non-dimensional root-mean-square in-line displacement $A_{X,rms}/D$ against reduced velocity at $Re = 200$.

induced vibrations as reported in Williamson & Govardhan (2004). Two branches can be distinguished in the lock-in at the low Reynolds number and the low mass ratio. The initial branch where the amplitude reaches its highest value is characterized by the phase angle ($\phi_{C_L-Y}$) between the hydrodynamic lift force coefficient and the transverse displacement close to $0°$ and lower branch with decaying amplitude of vibration is characterized by $\phi_{C_L-Y}$ close to $180°$. The maximum amplitude observed in simulations is close to $0.6D$ which is a typical value encountered in other studies on VIV with similar settings. In the $\alpha = 90°$ configuration the lock-in range is approximately the same as in the single cylinder case, covering approximately values of reduced velocity $4 \leqslant U_r \leqslant 6$. The peak transverse amplitude in $\alpha = 90°$ configuration is very close to the maximum transverse amplitude of the single cylinder. The streamwise normalized root-mean-square vibration amplitude is however smaller than that of the single cylinder. In case of the tandem arrangement with the small cylinder placed upstream of the large cylinder ($\alpha = 180°$) the transverse response is generally smaller but the streamwise response is markedly larger with a peak in $A_{X,rms}/D$ occurring at $U_r = 4$. The lock-in range is narrower than the critical values identified in the single cylinder case and the case of $\alpha = 90°$ and is expected between $4 \leqslant U_r \leqslant 5$. The most evident influence on the amplitude response as compared to the single cylinder case is exhibited in the $\alpha = 0°$ case. The lock-in range in this case is significantly extended to $4 \leqslant U_r \leqslant 12$. The peak occurrence of the peak in $A_{Y,max}/D$ is shifted to $U_r = 6$ with slightly lower magnitude than the peak value observed in the single cylinder case. The $A_{X,rms}/D$ exhibits similar extended range but the peak magnitude is approximately 50% smaller than that of the single cylinder case.

13

## 4.2. *Hydrodynamic coefficients*

For the single cylinder oscillating near wall, the mean lift coefficient, as opposed to free stream case, is non zero due to the break of symmetry in the wake caused by the wall presence. There is a significant increase in $\overline{C}_L$ in the lock-in region with a peak at reduced velocity $U_r = 4$ which can be seen in Fig. 8. The peak in $\overline{C}_L$ is correlated with the peak in cross-flow vibration amplitude which was discussed in the amplitude response. It is apparent that the position angle of the small cylinder has a strong influence on the mean lift coefficient. In the $\alpha = 0°$ arrangement $\overline{C}_L$ is noticeably lower than in single cylinder case with the peak value shifted to $U_r = 5$. In the $\alpha = 180°$ configuration the $\overline{C}_L$ is close to 0.1 for all investigated $U_r$ values. For stacked arrangement ($\alpha = 90°$) the $\overline{C}_L$ values are negative in all $U_r$ investigated except for the $U_r = 4$ which coincides with the peak in the amplitude response. In this case mean lift coefficient is positive with a value close to 0.1. It is worth to note that the direction of the lift force in the $\alpha = 90°$ is dependent on the $Re$. Negative values in the present study are in line with the findings of Kalghatgi & Sayer (1997) who reported negative values of $\overline{C}_L$ in the subcritical regime and positive values of $\overline{C}_L$ in the critical regime. Mean drag coefficient is elevated in the synchronization range in all analyzed cases. The highest value of the drag coefficient is obtained in the stacked arrangement ($\alpha = 90°$) with a peak value occurring at $U_r = 5$. When the small cylinder is placed upstream of the large cylinder the mean drag coefficient values are lower outside the lock-in regime than in the single cylinder configuration. When $\alpha = 0°$ the system behaves like a streamlined body. When the oscillations reach a peak value at $U_r = 4$, the $\overline{C}_D$ is close to that of a peak value for the single cylinder case. When the small cylinder is placed downstream the $\overline{C}_D$ is markedly lower in the lock-in range ($4 \leqslant U_r \leqslant 6$) with a peak occurring at $U_r = 4$ which is approximately 50% of the values noted in the single cylinder and the $\alpha = 180°$ cases. Figure 9 shows variation in the $C_L^{rms}$ and the $C_D^{rms}$. The peak values for the single cylinder case, the $\alpha = 90°$ case and the $\alpha = 0°$ case occur at $U_r = 4$. The peak value for the $\alpha = 90°$ case is substantially higher. There is also a sharp drop in the $C_L^{rms}$ observed in this configuration, after the transition from the initial branch to lower branch of the lock-in. Similar drop is also noted in the single cylinder configuration. The $\alpha = 0°$ case displays more gradual decrease in $C_L^{rms}$ with increasing $U_r$. No major fluctuations in $C_L^{rms}$ are spotted when the small cylinder is located upstream of the large cylinder. In contrast $C_D^{rms}$ peak value in this configuration is close to a peak value obtained in the single cylinder case. Similar to $C_L^{rms}$ behavior, $C_D^{rms}$ in the $\alpha = 0°$ case is characterized by a lower peak value than in the single cylinder configuration and extended decay range of the $C_D^{rms}$ .

## 4.3. *Analysis of vibration frequency*

Figure 10 and Figure 11 present the ratio of the transverse vibration frequency $f$ and the natural frequency $f_N$ of the stystem. Reference lines corresponding to the Strouhal's relation and a horizontal line at a frequency ratio $f/f_N = 1$ are given in Fig. 10 and
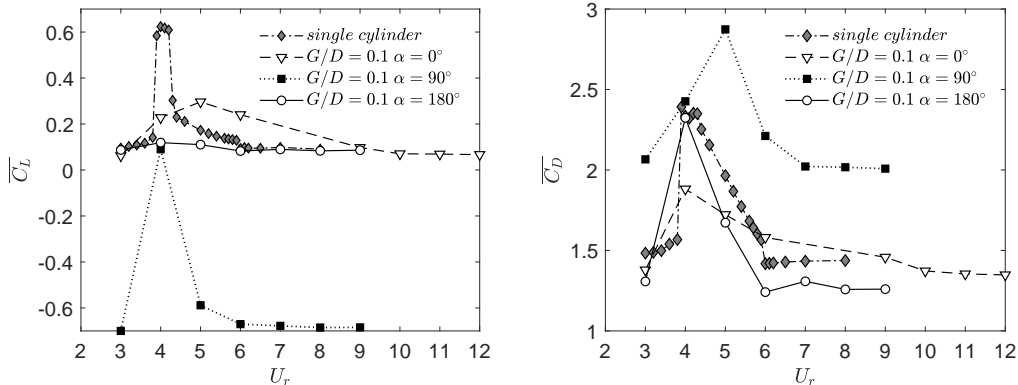
14



Figure 8: Mean lift coefficient $\overline{C}_L$ and mean drag coefficient $\overline{C}_D$ against reduced velocity at $Re = 200$.
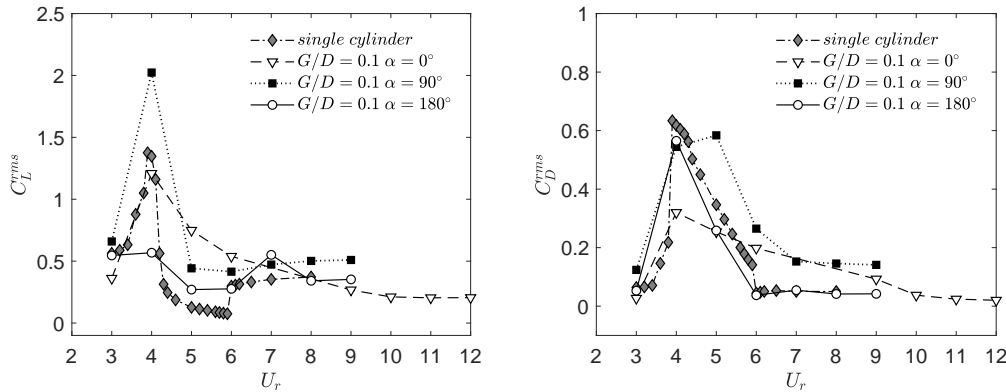


Figure 9: Root-mean-square lift coefficient $C_L^{rms}$ and root-mean-square drag coefficient $C_D^{rms}$ against reduced velocity at $Re = 200$.

Fig. 11 for better interpretation of the results. Figures 10 and 11 show that the lock-in phenomenon is easy to discern by inspecting the behavior of the frequency ratio, which in the synchronization range diverges from following the Strouhal's relationship and tends towards the unity. In Fig. 10(a) for the single cylinder configuration it is clearly visible that the lock-in occurs when $3.8 \leqslant U_r \leqslant 6$. Figure 10(b) shows the frequency characteristic for the $\alpha = 0°$ case. The extended lock-in range is evidently spanning from $U_r = 4$ to $U_r = 12$, this is in accordance with the observations made in the response analysis. When the small cylinder is placed upstream of the large cylinder the lock-in range is narrowing and after the desynchronization the frequency of a structural vibration falls back to following the Strouhal's relation. This can be clearly seen in Fig. 11(b). In the $\alpha = 90°$ case with the small cylinder directly above the large cylinder (see Fig.11(a)) the Strouhal number is slightly lower ($St = 0.19$) than that in the single cylinder case, the $\alpha = 0°$ case and the $\alpha = 180°$ case, which is equal to $St = 0.21$ respectively. The reason of the Strouhal number reduction in the $\alpha = 90°$ configuration is twoflod. Firstly the presence of the small cylinder increases the transverse dimension of the system.

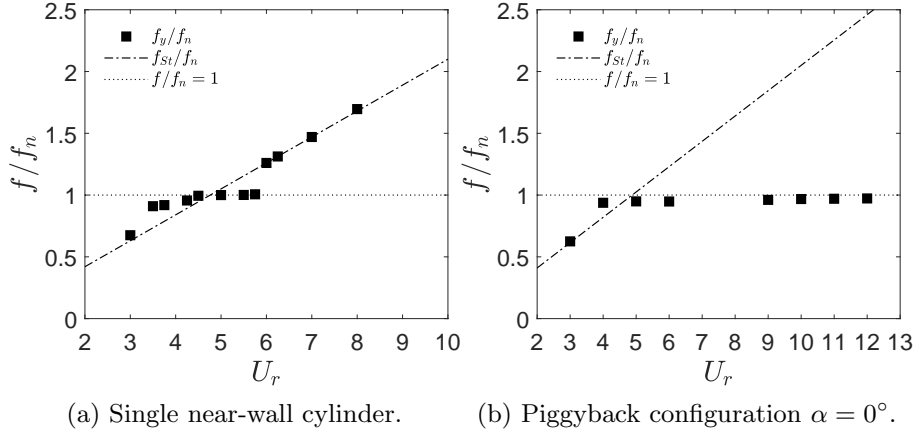(a) Single near-wall cylinder.     (b) Piggyback configuration $\alpha = 0°$.

Figure 10: Response frequencies as a function of reduced velocity $U_r$ at $Re = 200$.



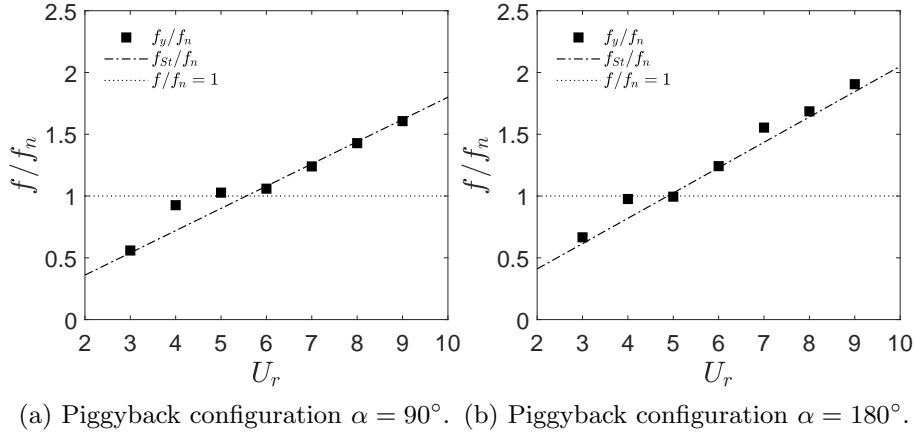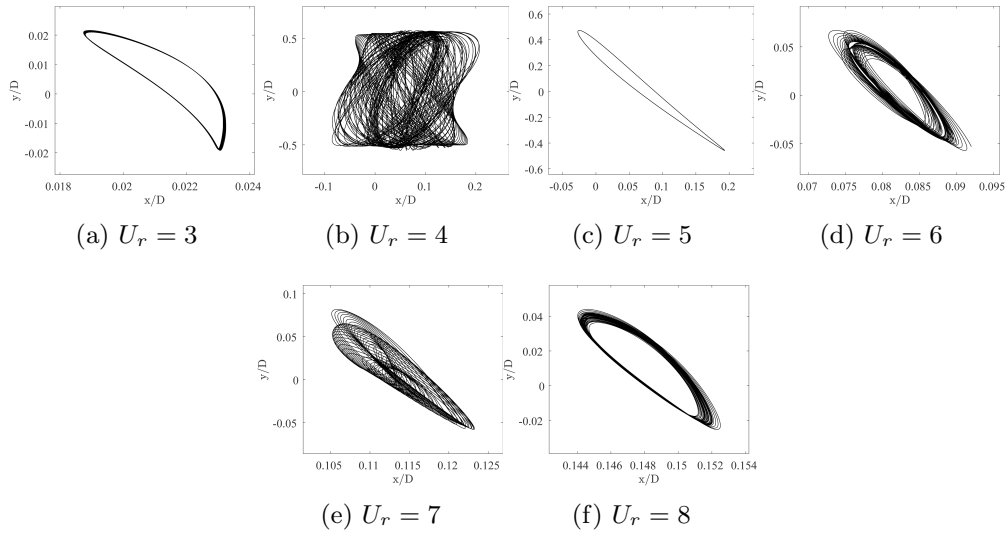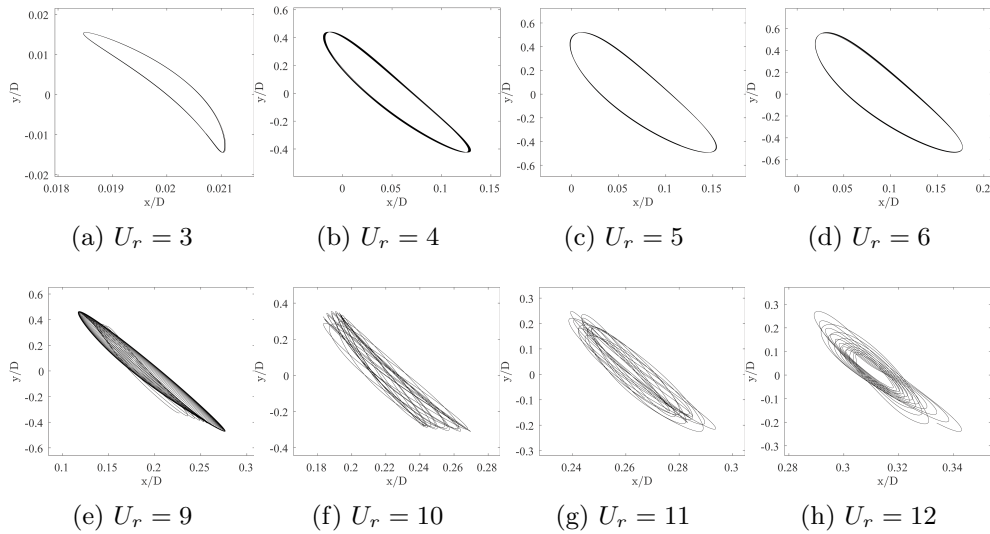(a) Piggyback configuration $\alpha = 90°$. (b) Piggyback configuration $\alpha = 180°$.

Figure 11: Response frequencies as a function of reduced velocity $U_r$ at $Re = 200$.

Secondly it is influenced by the gap flow between the small and the large cylinders which is interacting with the wake delaying the vortex formation.

### 4.4. *Motion trajectories*

The $X - Y$ trajectories extracted from the simulation time $\tau = 250 - 500$ are shown in Fig. 12 - 15. In the near wall placement the "figure eight" oscillation pattern , known from an isolated cylinder vibration studies, is replaced by a skewed oval trajectory. The shape of the skewed oval was also reported by Li *et al.* (2016) and Tham *et al.* (2015). The reason of a change in the vibration trajectory is the suppression of the counter-clockwise vortices shed from the bottom of the cylinder which are interacting with the horizontal plane wall boundary layer. This suppression mechanism is in turn the cause of the stream-wise frequency lock-in and large amplification of the streamwise response. Both the single cylinder case and the investigated coupled configurations exhibit similar regular oscillation pattern. It is observed that the trajectories in the single cylinder case

16



Figure 12: $X - Y$ trajectories: single near-wall cylinder at $Re = 200$.



Figure 13: $X - Y$ trajectories: Piggyback configuration $\alpha = 0°$ at $Re = 200$.

vibration captured at $U_r = 4$, $U_r = 6.5$ and the $\alpha = 0°$ case at $U_r = 10 - 12$ are more chaotic than in other ivestigated $U_r$. The chaotic fluctuations in the cylinder trajectories can be attributed to the shedding mode switching mechanism as mentioned by Li *et al.* (2016). Across the critical value of $U_r$ between the pre-lock-in and lock-in, the cylinder vibration mode transitions from the wake mode (weak interaction) to a combined wake and structure mode (strong interaction). This results in a chaotic vibration pattern. Less pronounced instabilities occur during densynchronization when switching back to the weak interaction occurs.

(a) $U_r = 3$ (b) $U_r = 4$ (c) $U_r = 5$ (d) $U_r = 6$

(e) $U_r = 7$ (f) $U_r = 8$ (g) $U_r = 9$
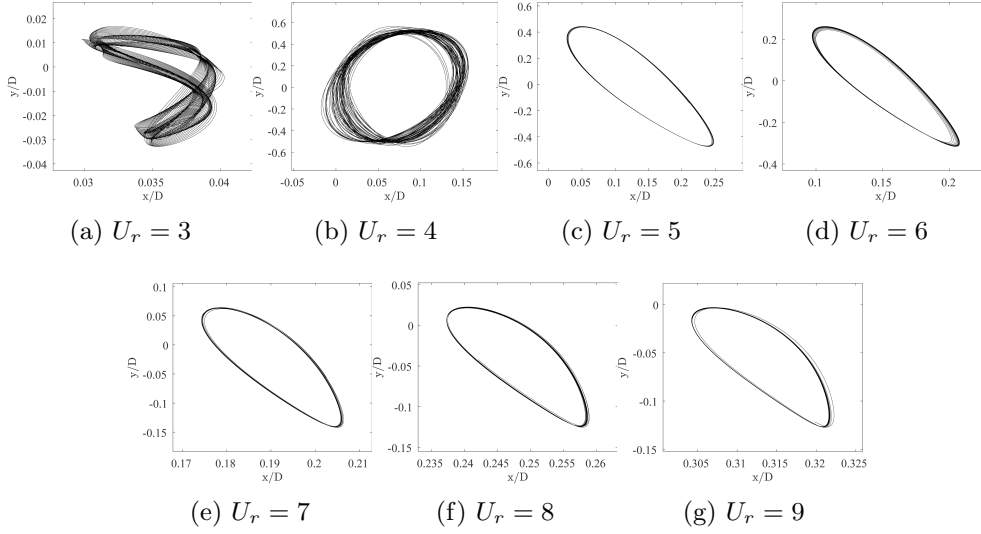
Figure 14: $X - Y$ trajectories: Piggyback configuration $\alpha = 90°$ at $Re = 200$.



(a) $U_r = 3$ (b) $U_r = 4$ (c) $U_r = 5$ (d) $U_r = 6$

(e) $U_r = 7$ (f) $U_r = 8$ (g) $U_r = 9$
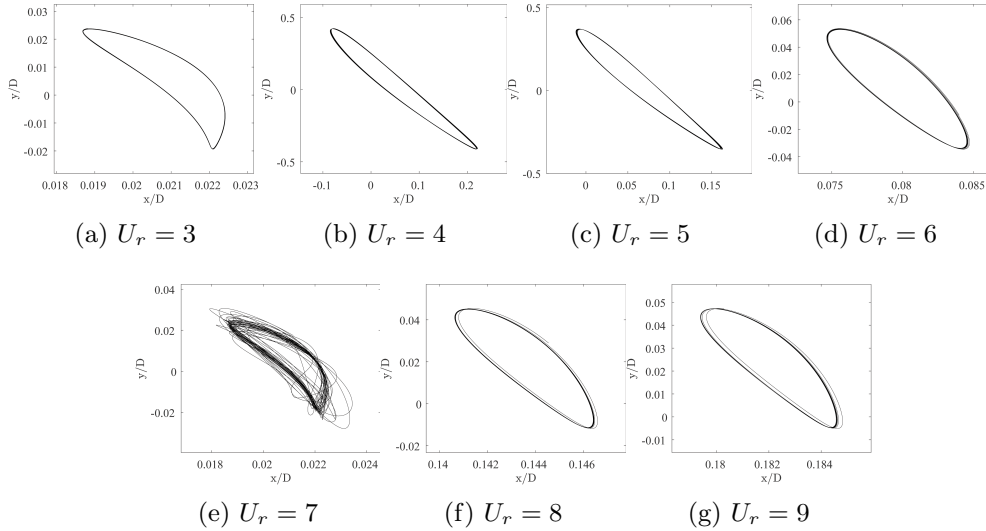
Figure 15: $X - Y$ trajectories: Piggyback configuration $\alpha = 180°$ at $Re = 200$.

### 4.5. *Phase differences*

Phase difference between the hydrodynamic force and the corresponding displacement response can be associated with the direction of the energy transfer in the system. Figure 16 shows the phase portraits of the cylinder transverse displacement $Y/D$ against the lift coefficient $C_L$ for the investigated range of reduced velocities. Trace position in the first and third quadrant is indicative of an in-phase relation between the displacement and the hydrodynamic force. As the phase portrait transitions to the second and fourth quadrant this relation becomes out of phase. Comparing the phase portraits with the response plots (Fig. 7) one can relate the shift in the phase from 0° to 180° with the shift
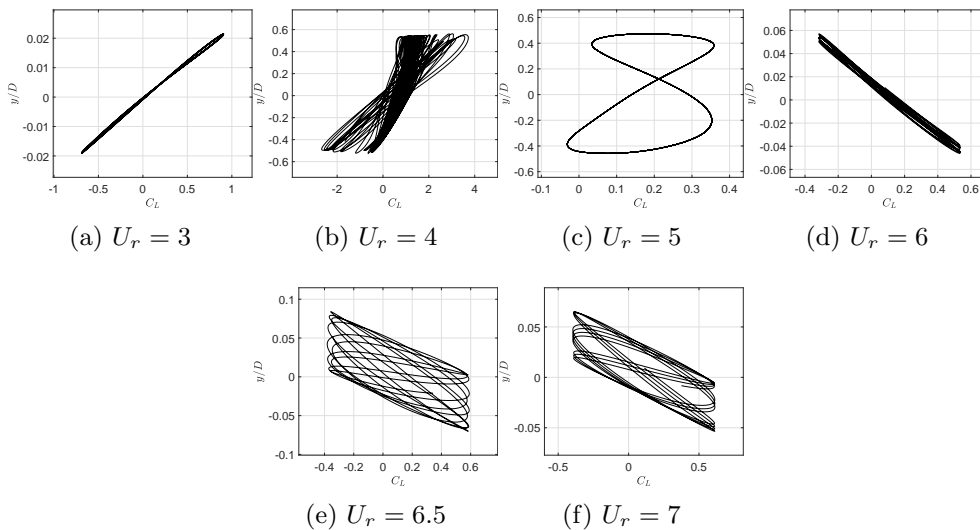
18



(a) $U_r = 3$      (b) $U_r = 4$      (c) $U_r = 5$      (d) $U_r = 6$

(e) $U_r = 6.5$      (f) $U_r = 7$

Figure 16: Phase pictures of $C_L$ and cross-flow displacement $Y/D$ of a single near-wall cylinder.

from the initial to the lower branch of the lock-in regime. Looking at the phase picture of the $\alpha = 90°$ case (Fig. 18) it stands out that $\phi_{C_L - Y}$ is approximately equal to $0°$ in pre-lock-in state extending to the onset of the lock-in (Fig. 18(a) and Fig. 18(b)). The phase switches then suddenly to $180°$ at $U_r = 5$ (Fig. 18(c)) corresponding to transition from the initial branch to the lower branch. The vibration amplitude is still enhanced in the lower branch despite the fact that the energy is dissipated by the fluid after the phase switch. Interesting phenomenon can be identified in the $\alpha = 180°$ case which is shown in Fig. 19. After the phase switch and desynchronization which takes place at $U_r = 6$ the lift force and the transverse displacement switch back to in-phase state again at $U_r = 7$. Zhao & Yan (2013) found that for lower mass ratio $m^* = 2$ systems this effect can lead to multi-lock-in with two distinct peaks in the response curve. In the present study however, for the $\alpha = 180°$ configuration with the mass ratio $m^* = 10$ the response is not enhanced significantly.

### 4.6. *Frequency characteristics*

Time histories covering dimensionless time $\tau = 450 - 500$ of the transverse and stream-wise displacements and hydrodynamic coefficients at representative reduced velocities are displayed for each position angle and for the single cylinder configuration in Fig. 20 - Fig. 23. Fast Fourier Transform (FFT) analysis is used to compute the frequency power spectra of the hydrodynamic forces $C_D$, $C_L$, and the displacement time histories $Y/D$, $X/D$ in dimensionless period $\tau = 250 - 500$. The transverse and stream-wise vibration frequencies in all considered cases coincide, which is in accordance with the observed images of the oval motion trajectories. The single exception is the $\alpha = 90°$ case at $U_r = 3$. In this instance the streamwise displacement frequency is twice the transverse
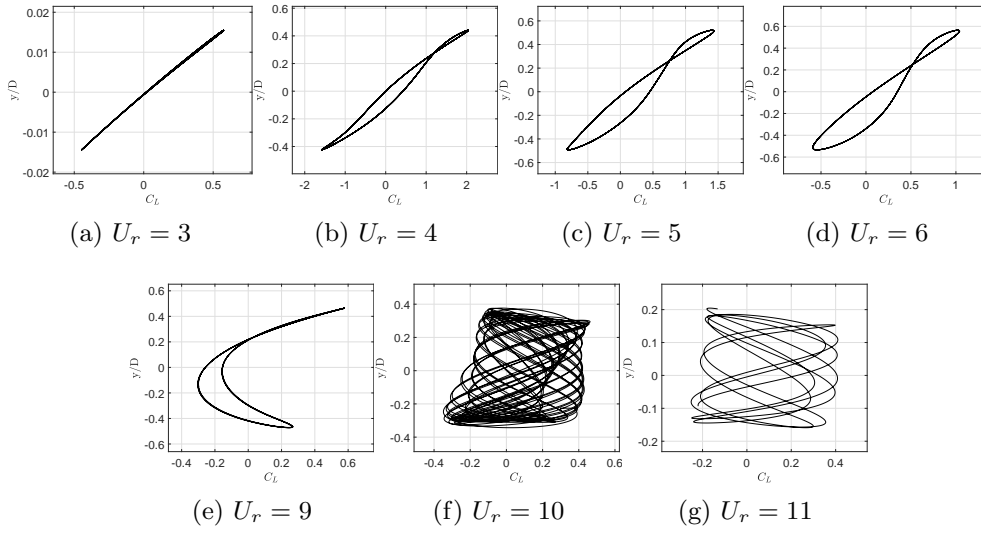
Figure 17: Phase pictures of $C_L$ and cross-flow displacement $Y/D$ of a piggyback configuration $\alpha = 0°$.
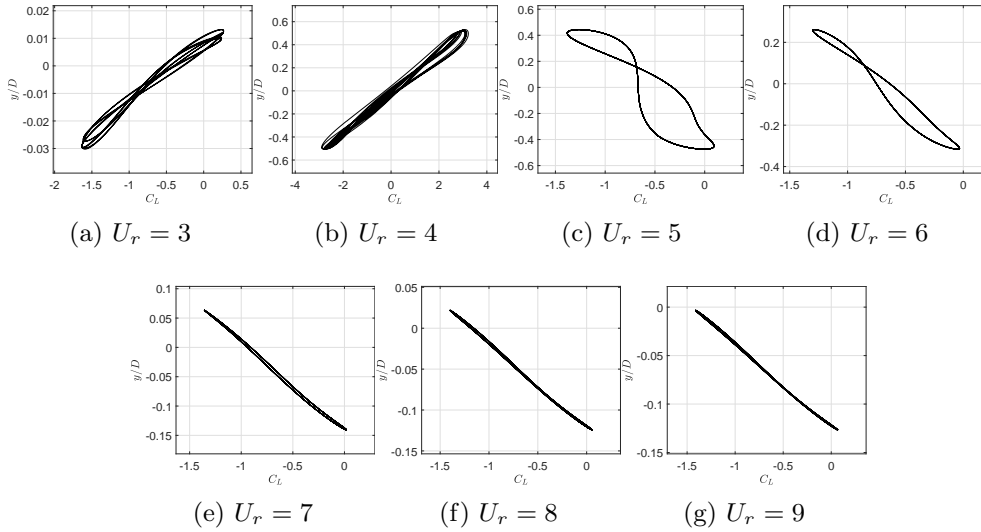


Figure 18: Phase pictures of $C_L$ and cross-flow displacement $Y/D$ of a piggyback configuration $\alpha = 90°$.

vibration frequency resulting in the trajectory similar to that of the single isolated cylinder. Pre-lock-in range and the initial branch of the lock-in can be characterized by a single dominant frequency in the temporal response of the lift force. At the onset of the lock-in the shedding frequency is tuned in to the natural frequency of the system. This behavior can be observed at $U_r = 4$ in all considered cases (Fig. 20(b), Fig. 21(b), Fig. 22(b), Fig. 23(b)). The drag force temporal response in the initial branch in the single cylinder case and in the $\alpha = 0°$ and $\alpha = 180°$ configurations is characterized
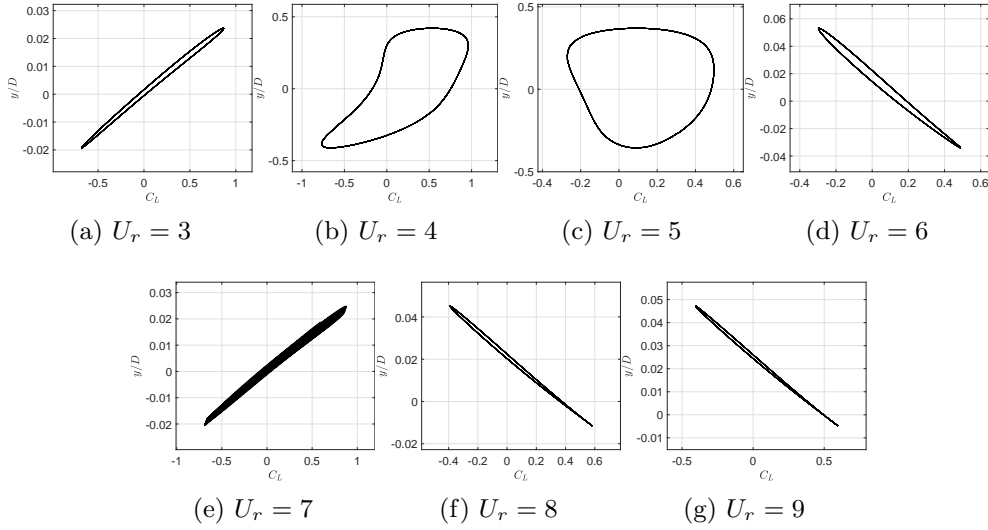
20



Figure 19: Phase pictures of $C_L$ and cross-flow displacement $Y/D$ of a piggyback configuration $\alpha = 180°$.

by a dominant frequency at second harmonic corresponding to twice the frequency of a transverse displacement. In the $\alpha = 90°$ configuration there are multiple harmonics in the temporal response of the drag force with dominant frequency synchronized with the stream-wise vibration frequency. In the lower branch the second harmonic contribution in the temporal response of the lift force becomes enhanced. This can be observed in the spectra of the single cylinder case (Fig. 20(c)), in the $\alpha = 90°$ case (Fig. 22(c)) and in the $\alpha = 0°$ case (Fig. 21 (e),(f)). After the desynchronization the dominant frequencies of the vibration response become the same as the hydrodynamic forces frequencies. The beating vibration is found in the single cylinder case at the onset of the initial branch of the lock-in at $U_r = 4$ (Fig. 20(b)) and during the desynchronization at $U_r = 6.5$ (Fig. 20(e)). In the $\alpha = 0°$ case the beating oscillations are found at $U_r = 10$ and $U_r = 11$ (Figure 21(f)). The chaotic fluctuations of the hydrodynamic forces are the outcome of a change in the balance between two different vorticity production mechanisms, namely between the pressure gradient and motion-induced vorticity production. For the other investigated reduced velocities the vibration time history is regular.

## 4.7. Analysis of vortex shedding

In order to elucidate the qualitative differences in the time histories of the hydrodynamic forces and the structural responses between different position angles the flow features are analyzed. Vorticity and pressure contours at selected time instants ($\tau = 490 - 500$) and reduced velocities $U_r$ are used for that purpose. First the influence of the bottom boundary layer is discussed based on the flow field around the single cylinder in the initial branch of the lock-in regime at $U_r = 4$. This situation is shown in Fig. 24. Presented vorticity and pressure contours correspond to the time instants when the
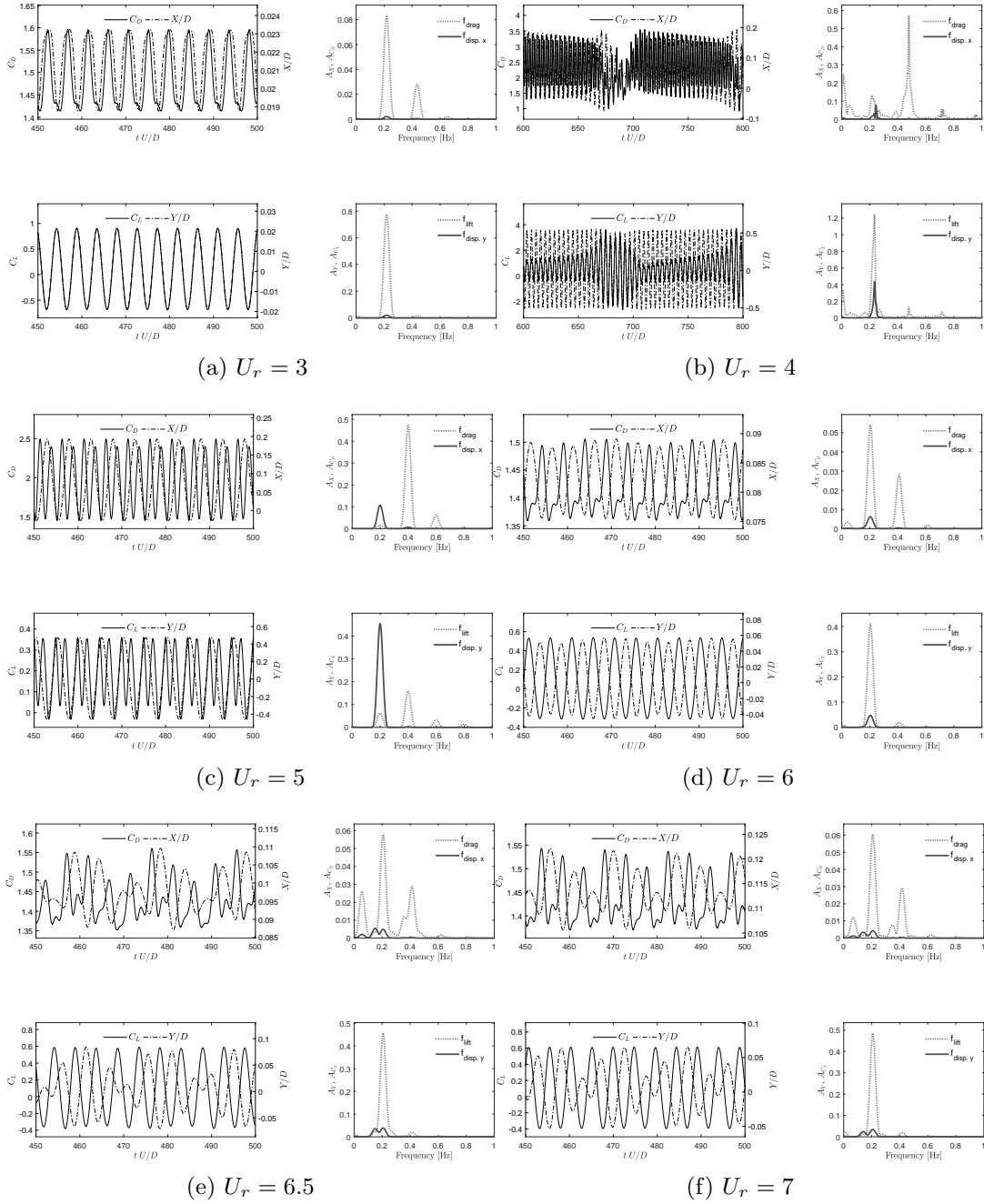
Figure 20: Temporal variations of cross-flow displacement ($Y/D$), streamwise displacement ($X/D$), lift coefficient ($C_L$) and drag coefficient ($C_D$) with corresponding FFT spectra at selected reduced velocities $U_r$. Single cylinder at $Re = 200$.

amplitudes of the forces and displacements are the largest. The cross marker indicates the initial location of the cylinder center. It is evident that the proximity of the horizontal wall significantly affects the vortex shedding of the cylinder by breaking the symmetry of the wake. Both drag and lift forces are in phase with the transverse and stream-wise
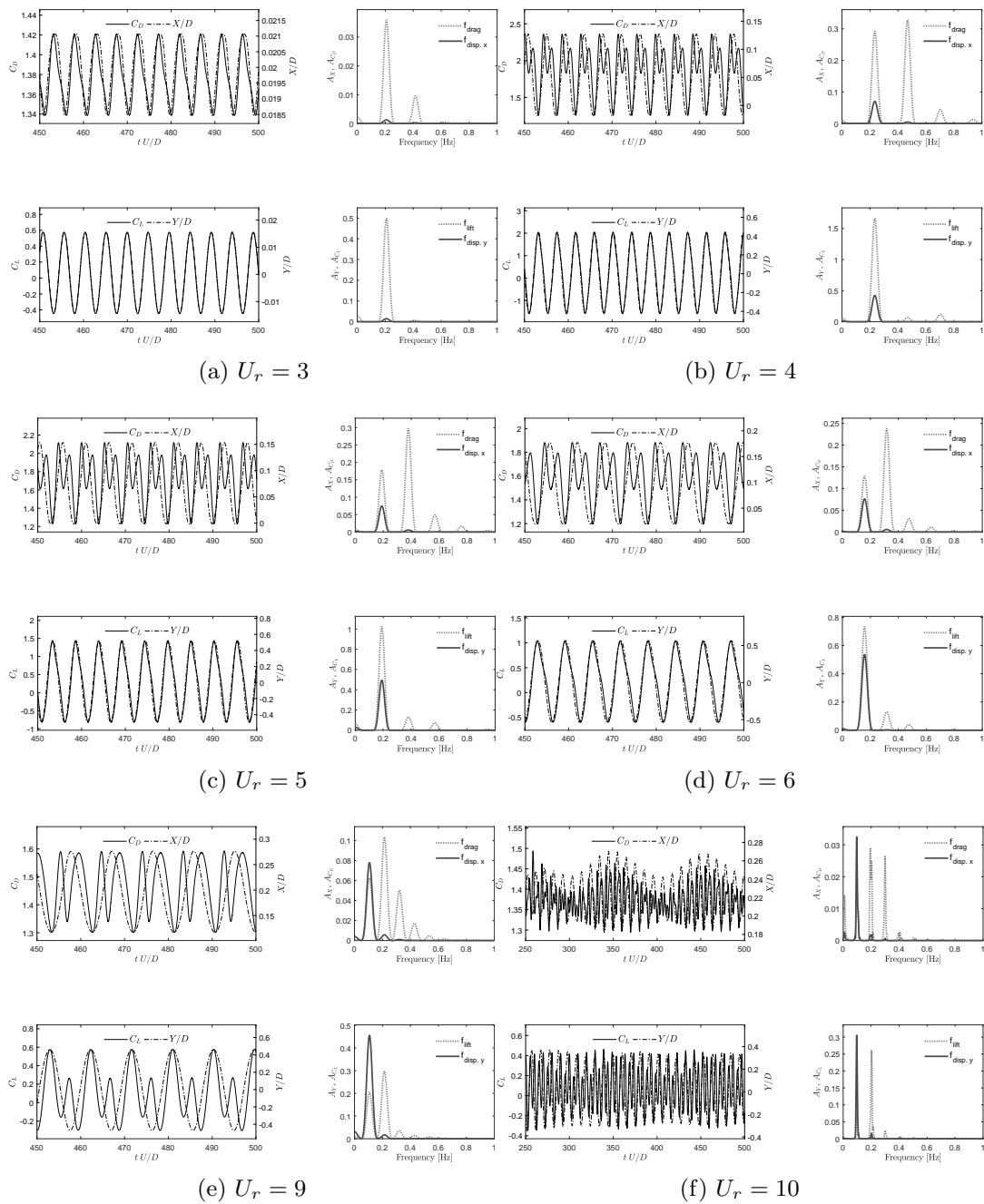
22



(a) $U_r = 3$                     (b) $U_r = 4$

(c) $U_r = 5$                     (d) $U_r = 6$

(e) $U_r = 9$                     (f) $U_r = 10$

Figure 21: Temporal variations of cross-flow displacement $(Y/D)$, streamwise displacement $(X/D)$, lift coefficient $(C_L)$ and drag coefficient $(C_D)$ with corresponding FFT spectra at selected reduced velocities $U_r$. Piggyback configuration $\alpha = 0°$ at $Re = 200$.

displacements in this instance as indicated by the time history plot in Fig. 24(a). The net energy transfer from the fluid to the structure is positive, resulting in a large amplitude of transverse vibration. The mechanism of the bottom shear layer roll up can be observed
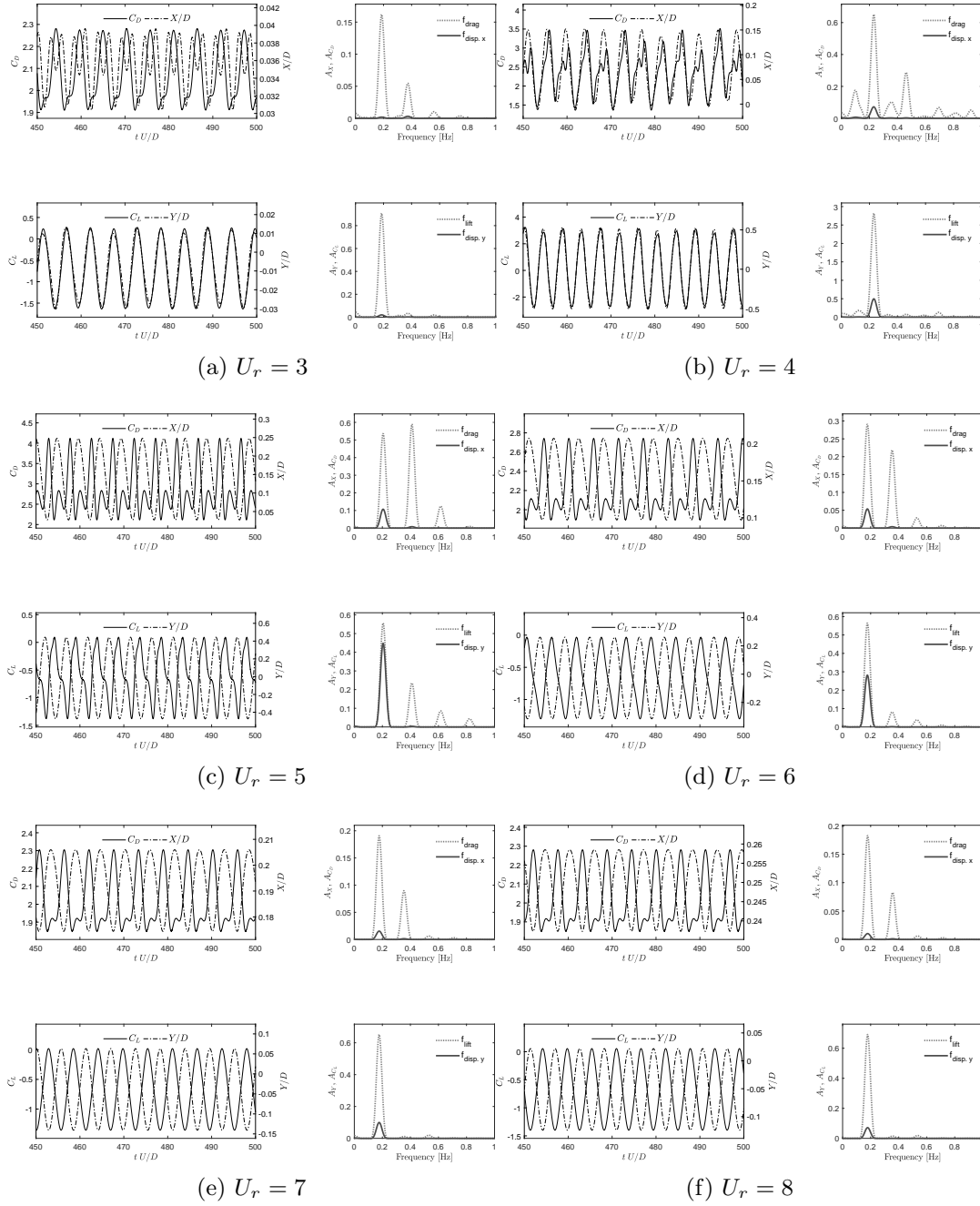
(a) $U_r = 3$        (b) $U_r = 4$

(c) $U_r = 5$        (d) $U_r = 6$

(e) $U_r = 7$        (f) $U_r = 8$

Figure 22: Temporal variations of cross-flow displacement $(Y/D)$, streamwise displacement $(X/D)$, lift coefficient $(C_L)$ and drag coefficient $(C_D)$ with corresponding FFT spectra at selected reduced velocities $U_r$. Piggyback configuration $\alpha = 90°$ at $Re = 200$.

in the sequence of vorticity snapshots (Fig. 24(b),(d),(f),(h)). The anti-clockwise vortex shed from the bottom surface of the cylinder (B1) forces the boundary layer to roll-up (C1). In Fig. 24(b) the clockwise vortex shed from the upper cylinder surface (A1) is
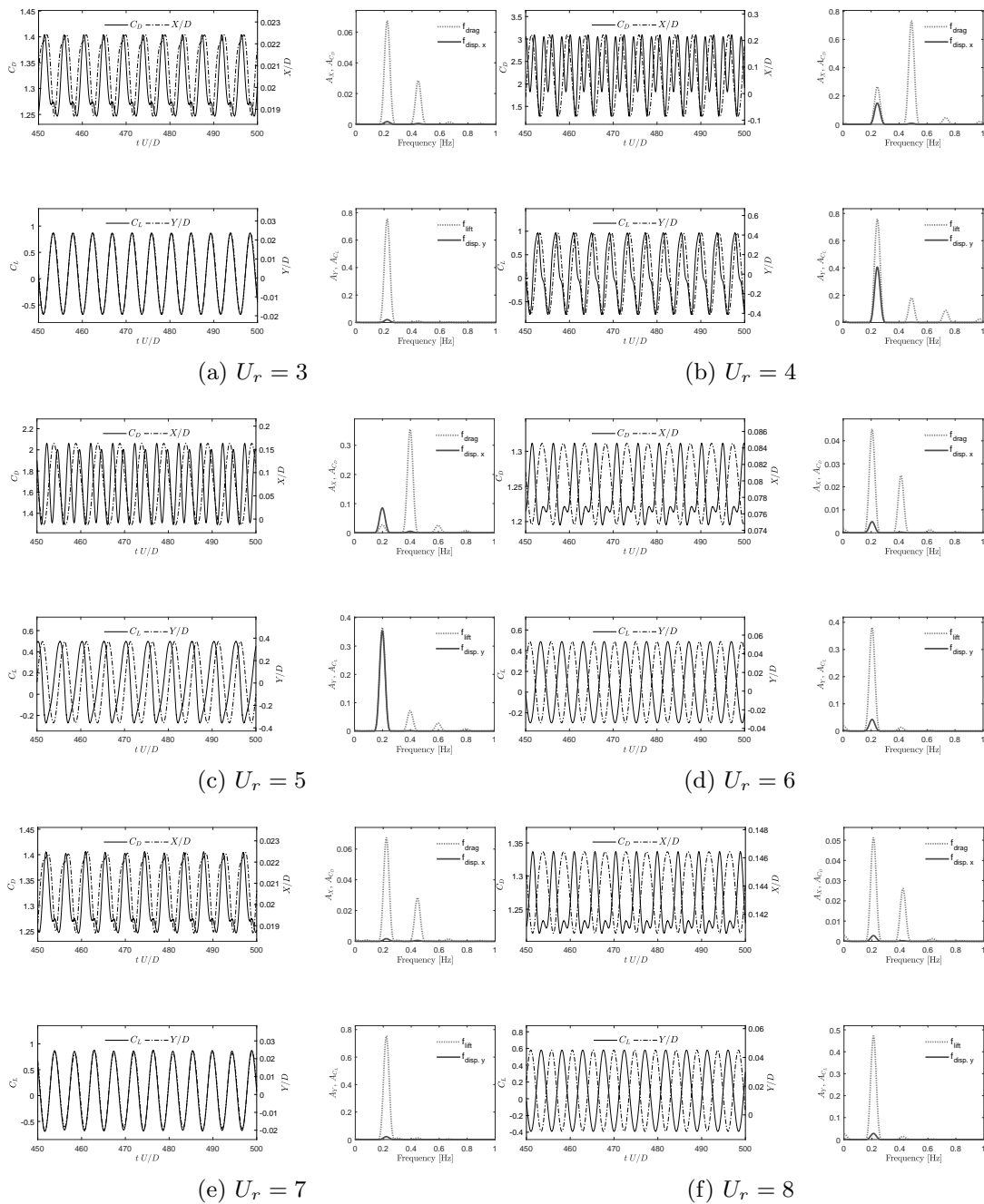
24



Figure 23: Temporal variations of cross-flow displacement $(Y/D)$, streamwise displacement $(X/D)$, lift coefficient $(C_L)$ and drag coefficient $(C_D)$ with corresponding FFT spectra at selected reduced velocities $U_r$. Piggyback configuration $\alpha = 180°$ at $Re = 200$.

coalescing with the clockwise vortex formed from the rolled-up bottom wall boundary layer (C1). This interaction reinforces the clockwise vortices shed from the top surface of the cylinder and weakens the anticlockwise vortices shed from the bottom surface of the

25

cylinder. The suppression of the counter-clockwise vortices shed from the bottom of the cylinder is the reason of matched vibration frequencies in the streamwise and transverse directions. This in turn leads to a streamwise frequency lock-in and is the root cause of a significantly increased streamwise oscillations. Large amplitude of vibration further amplifies this mechanism by immersing the cylinder deeper in the bottom wall boundary layer (Fig. 24(b)).

In Fig. 25 the $\alpha = 90°$ configuration with the small cylinder placed on top of the large cylinder is investigated at $U_r = 4$. The mean drag coefficient is significantly increased due to the increased area exposed to the incoming flow. The biggest difference between the single cylinder configuration and analyzed side by side configuration is unveiled in the lift coefficient characteristics. It is believed that the variation of the $\overline{C}_L$ and the $C_L^{rms}$ stems from the interaction of vortex shedding from the large and from the small cylinder. Figures 25(b) - (g) show development of the wake with the distinct flow features caused by the presence of the small cylinder. The variation in the lift and drag forces is closely related to the evolution of the vortical structures near the large cylinder body. The anti-clockwise vortex shed from the bottom of the large cylinder (B4) is interacting with the bottom boundary layer resulting in the boundary layer roll-up (C2). This mechanism is analogous to the one presented in the single cylinder case. However, presence of the small cylinder introduces another anti-clockwise vorticity (B2) which is amalgamating with the the anti-clockwise vortical structure generated at the back of the large cylinder (B3) (Fig. 25(a) and (b)). It is then deflected upwards delaying the interaction between the shear layers separating from the both sides of the coupled cylinders (A2) and (B4). This is the reason of a lower dominant frequency of the drag force identified in the spectral analysis (Fig. 22(b)).

Figure 26 shows the flow fields at selected time instants of the oscillation cycle for the $\alpha = 90°$ configuration at $U_r = 5$. The structure is in a lower branch of the lock-in regime and the the lift force and the transverse displacement are in this case out of phase. The near-wake structure shown in Fig. 25 is clearly different than that for the $U_r = 4$. It can be characterized by markedly wider vortex street. The wake is qualitatively similar to that of the single cylinder at $U_r = 4$. Large difference in the pressure field between flows at $U_r = 4$ and $U_r = 5$ is clearly visible. Explanation of the significant drop in the mean lift coefficient value can be found by analyzing pressure filed development during the shedding cycle. The large negative pressure zone (P1) is developed on the back side of the large cylinder. The reason is the anti-clockwise vortex shed from the bottom of the large cylinder (B4) which stays attached to the back side of the large cylinder for a longer time (Fig. 26(b)) compared to the case at $U_r = 4$ (Fig. 25(b)).

Figure 27 presents the time histories of the displacements, hydrodynamic coefficients and flow features of the single cylinder at $U_r = 6$. The structural vibration is outside of the lock-in regime. The lift force is $180°$ out of phase with the transverse displacement and the vibration amplitude is very small. In Fig. 28 the $\alpha = 0°$ configuration flow fields and
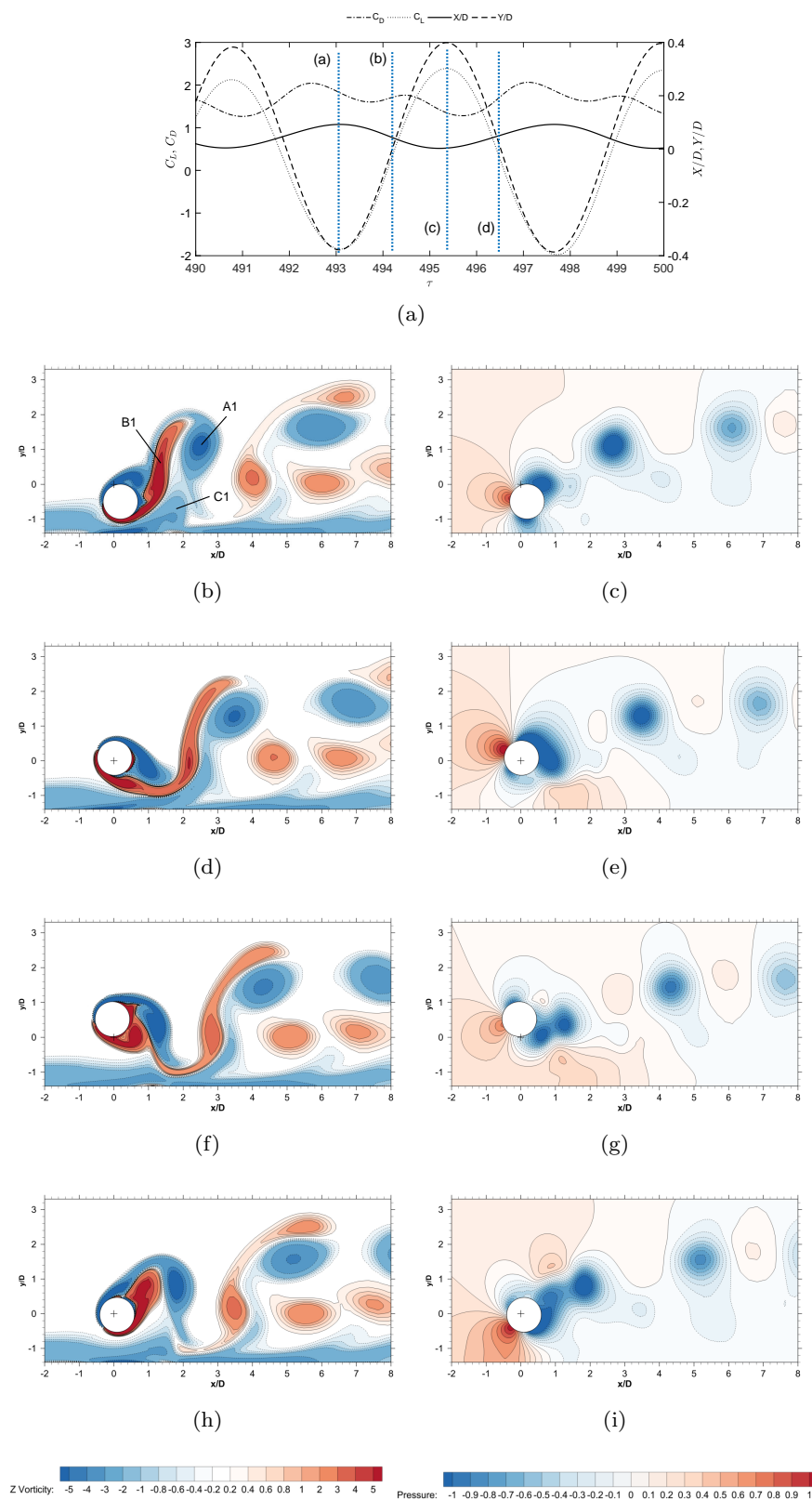
26



(a)



Figure 24: Time histories of displacements $Y/D$, $X/D$ and hydrodynamic coefficients $C_L$, $C_D$. Vorticity contours (left column) and pressure contours (right column) at selected time instances (b)-(i). Single cylinder at $U_r = 4$, $Re = 200$.
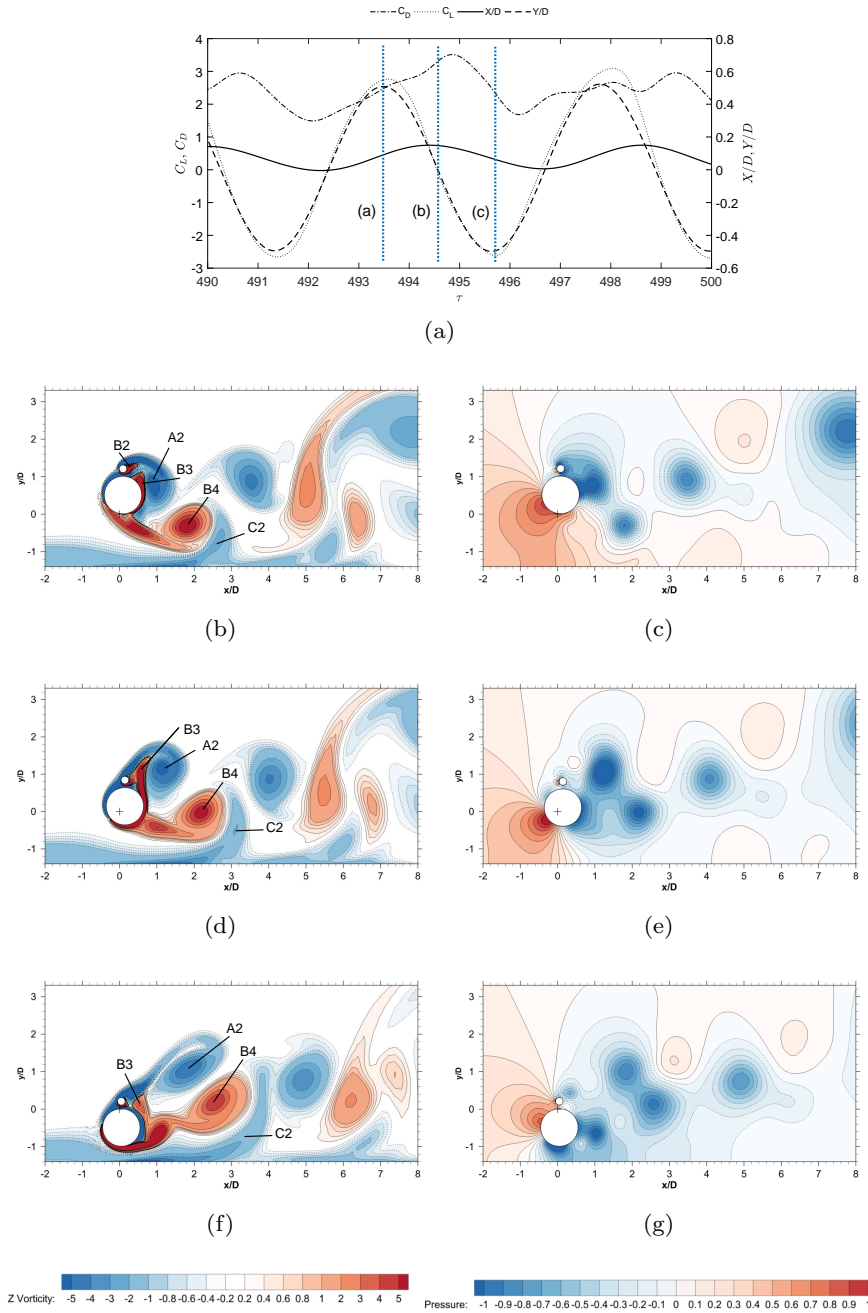
Figure 25: Time histories of displacements $Y/D$, $X/D$ and hydrodynamic coefficients $C_L$, $C_D$. Vorticity contours (left column) and pressure contours (right column) at selected time instances (b)-(c). Piggyback configuration $\alpha = 90°$ at $U_r = 4$, $Re = 200$.

time histories at $U_r = 6$ are shown. Transverse displacement amplitude is markedly larger than that at $U_r = 6$ in the single cylinder case, indicating frequency lock-in. Placement of the small cylinder downstream the large cylinder widens the reduced velocity lock-in regime significantly. This behavior can be attributed to the increase in the vortex formation length. This in turn leads to the shift in phase between the lift force and the
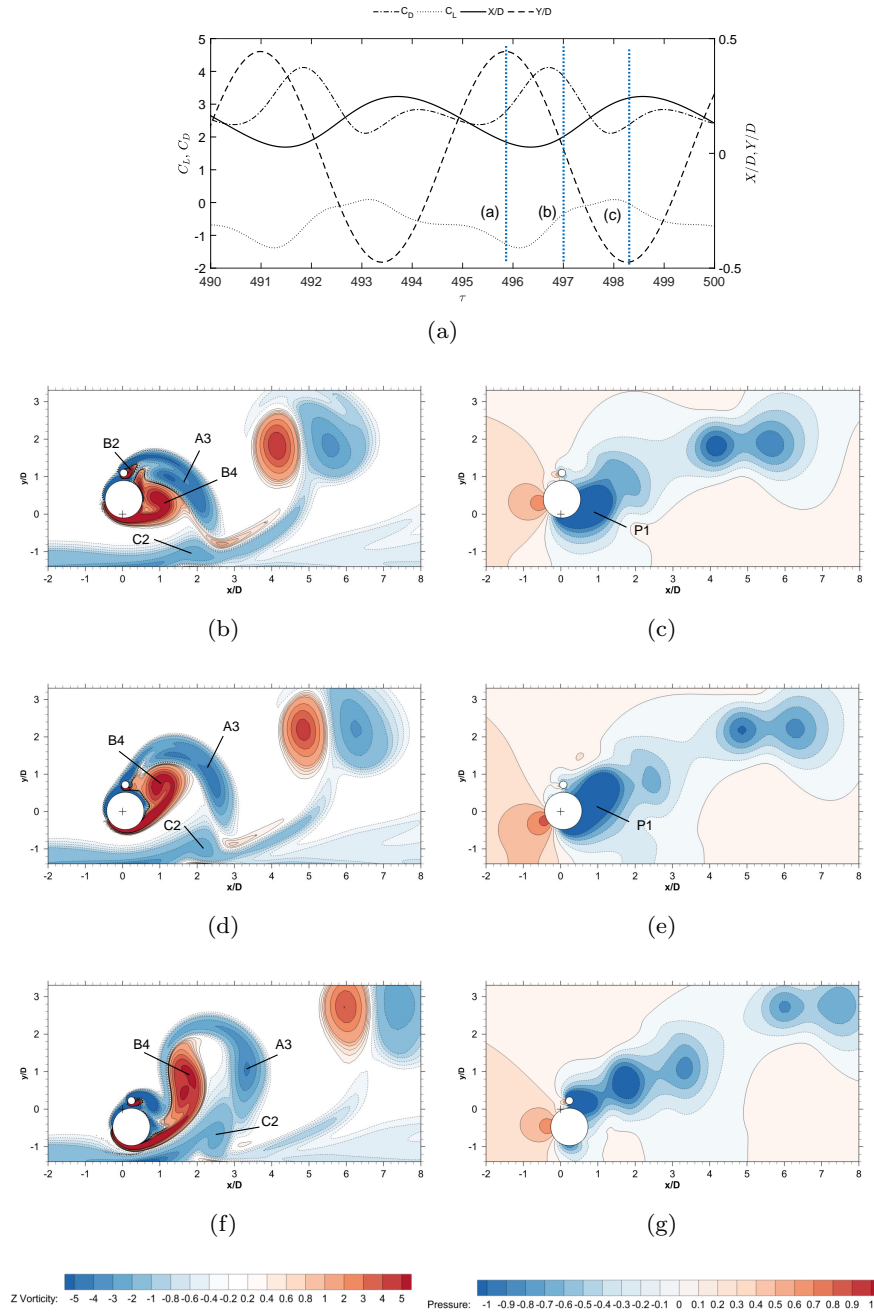
28



(a)



(b)

(c)

(d)

(e)

(f)

(g)

Z Vorticity: -5 -4 -3 -2 -1 -0.8 -0.6 -0.4 -0.2 0.2 0.4 0.6 0.8 1 2 3 4 5

Pressure: -1 -0.9 -0.8 -0.7 -0.6 -0.5 -0.4 -0.3 -0.2 -0.1 0 0.1 0.2 0.3 0.4 0.5 0.6 0.7 0.8 0.9 1

Figure 26: Time histories of displacements $Y/D$, $X/D$ and hydrodynamic coefficients $C_L$, $C_D$. Vorticity contours (left column) and pressure contours (right column) at selected time instances (b)-(g). Piggyback configuration $\alpha = 90°$ at $U_r = 5$, $Re = 200$.

streamwise vibration thus the positive net energy transfer from the fluid to the structure is maintained over wider range of reduced velocities exciting large amplitude oscillations.
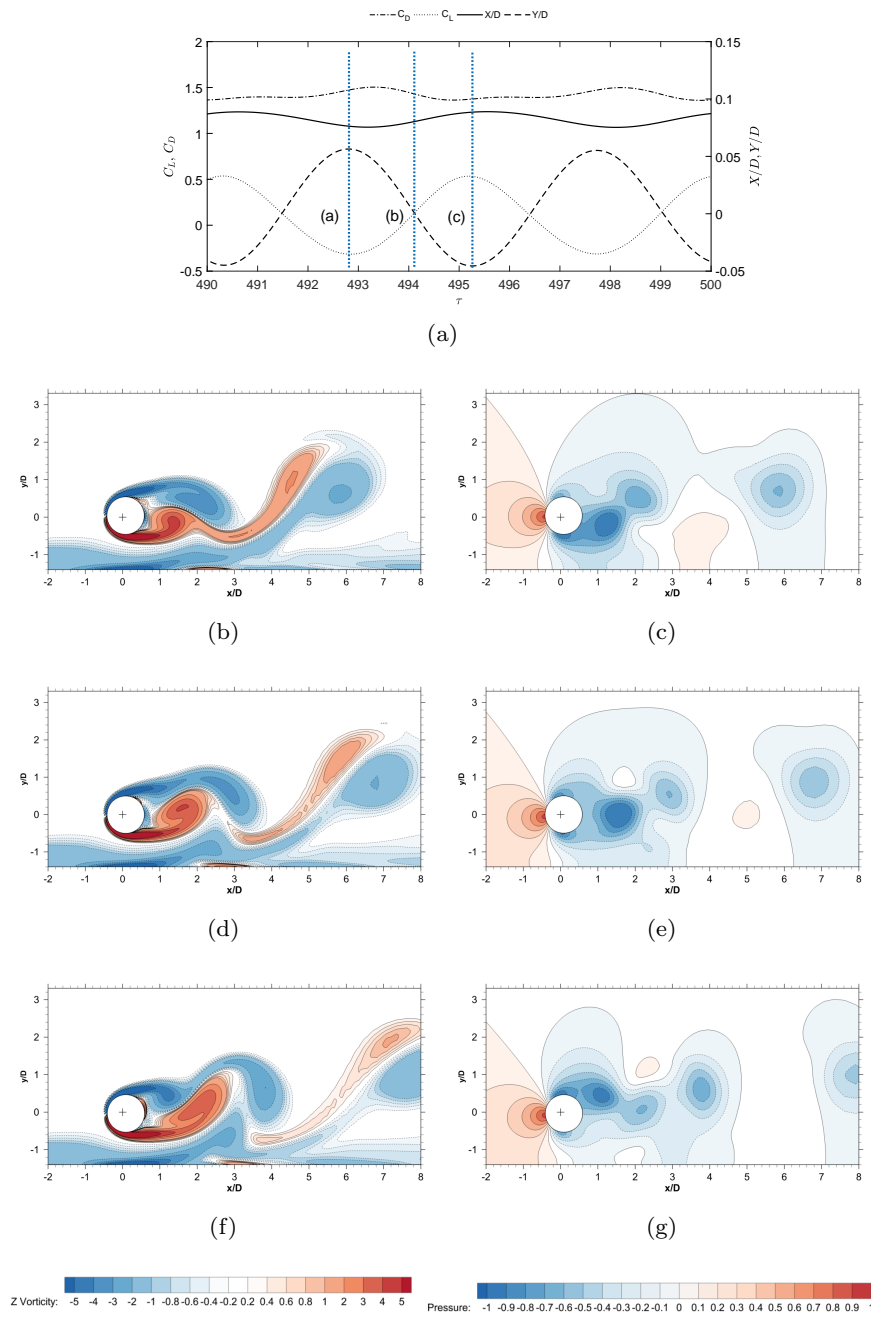
Figure 27: Time histories of displacements $Y/D$, $X/D$ and hydrodynamic coefficients $C_L$, $C_D$. Vorticity contours (left column) and pressure contours (right column) at selected time instances (b)-(g). Single cylinder at $U_r = 6$, $Re = 200$.
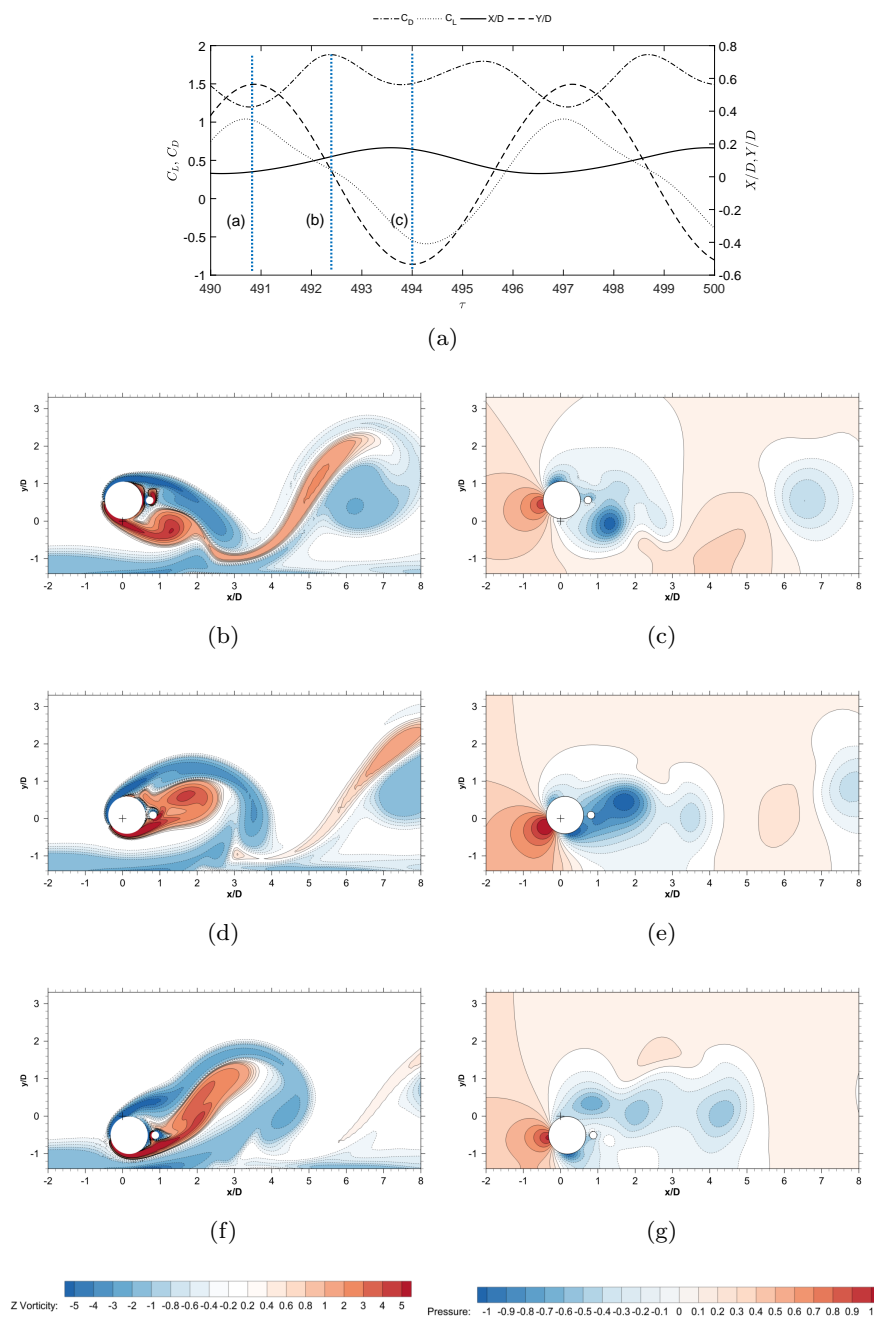
30



(a)



(b)



(c)



(d)



(e)



(f)



(g)

Z Vorticity: -5 -4 -3 -2 -1 -0.8 -0.6 -0.4 -0.2 0.2 0.4 0.6 0.8 1 2 3 4 5

Pressure: -1 -0.9 -0.8 -0.7 -0.6 -0.5 -0.4 -0.3 -0.2 -0.1 0 0.1 0.2 0.3 0.4 0.5 0.6 0.7 0.8 0.9 1

Figure 28: Time histories of displacements $Y/D$, $X/D$ and hydrodynamic coefficients $C_L$, $C_D$. Vorticity contours (left column) and pressure contours (right column) at selected time instances (b)-(c). Piggyback configuration $\alpha = 0°$ at $U_r = 6$, $Re = 200$.

## 5. Concluding remarks

Two-dimensional numerical study of vortex-induced vibrations of two circular cylinders with uneven diameters at a low Reynolds number of $Re = 200$ near a horizontal plane wall is carried out. Constant mass ratio $m^* = 10$, gap ratio $e/D = 0.9$ and spacing ratio between the cylinders $G/D = 0.1$ is maintained. The study is focused on the influence of the position angle of the small cylinder on the lock-in regime. Position of the small cylinder is varied between the three angles relative to the main cylinder center line ($\alpha = 0°$, $\alpha = 90°$, $\alpha = 180°$). The cylinders diameter ratio $d/D$ is set to a typical value encountered in the offshore subsea piggyback flow-lines $d/D = 0.2$. The conclusions drawn from the study are summarized as follows:

(i) The wall proximity effect is similar in both the single cylinder and the investigated coupled cylinders arrangements. At a selected gap ratio $e/D = 0.9$ in all investigated cases the bottom boundary layer roll-up is responsible for the suppression of the vortex shedding from the bottom surface of the large cylinder. This suppression mechanism leads to the reduction of the streamwise vibration frequency by half and largely enhances streamwise oscillation amplitude. Observed vibration patterns are in the form of the skewed oval.

(ii) The response of the coupled cylinders is widened significantly compared to the single cylinder configuration when the small cylinder is located downstream of the large cylinder. The lock-in regime when the $\alpha = 0°$ is identified in the range of $4 \leqslant U_r \leqslant 12$. The mechanism of the increased vortex formation length and the delay in the phase switch between the lift force and transverse displacement are induced in this configuration. On the contrary, placing the small cylinder upstream of the large cylinder is an effective way of reducing the structural response. In the $\alpha = 180°$ configuration the lock in range is the smallest among all analyzed arrangements. Upstream interference due to the small cylinder presence results in the weaker interaction between the shear layers shed from the two sides of the large cylinder. When located at $\alpha = 90°$ the effect of the small cylinder is manifested by an increased mean drag and switch in the direction of the lift force. Except at the peak vibration value of $U_r = 4$ the force acting on the pipeline is directed towards the horizontal plane wall. Analysis in the frequency domain using FFT shows that in the initial branch of the lock-in dominating frequencies of hydrodynamic coefficients are close to the natural frequency of the system. When the phase switch occurs beating oscillations are reported and the harmonic content of the displacement signal is enhanced by superharmonics at double and triple the fundamental excitation frequency.

### Acknowledgments

32

REFERENCES

BEARMAN, P. & ZDRAVKOVICH, M. 1978 Flow around a circular cylinder near a plane boundary. *Journal of Fluid Mechanics* **89**, 33 – 47.

KALGHATGI, S.G. & SAYER, P.G. 1997 Hydrodynamic forces on piggyback pipeline configurations. *Journal of Waterway, Port, Coastal & Ocean Engineering* **123** (1), 16.

LI, Z., JAIMAN, R.K. & KHOO, B.C. 2017 Coupled dynamics of vortex-induced vibration and stationary wall at low reynolds number. *Physics of Fluids* **29** (9), 093601.

LI, Z., MYSA, R.C., JAIMAN, R.K. & KHOO, B.C. 2018 Freely vibrating circular cylinder in the vicinity of fully developed scour holes at low reynolds numbers. *Computers & Fluids* .

LI, Z., YAO, W., YANG, K., JAIMAN, R.K. & KHOO, B.C. 2016 On the vortex-induced oscillations of a freely vibrating cylinder in the vicinity of a stationary plane wall. *Journal of Fluids and Structures* **65**, 495 – 526.

NAVROSE, N. & MITTAL, S. 2013 Free vibrations of a cylinder: 3d computations at re = 1000. *Journal of Fluids and Structures* **41**, 109 – 118.

PRASANTH, T. K. & MITTAL, S. 2008 Vortex-induced vibrations of a circular cylinder at low reynolds numbers. *Journal of Fluid Mechanics* **594**, 463 – 491.

SARPKAYA, T.S. 2010 *Wave Forces on Offshore Structures*. Cambridge University Press.

SUMER, B.M. & FREDSØE, J. 2006 *Hydrodynamics around cylindrical strucures*. World Scientific.

THAM, D.M.Y., GURUGUBELLI, P.S., LI, Z. & JAIMAN, R.K. 2015 Freely vibrating circular cylinder in the vicinity of a stationary wall. *Journal of Fluids and Structures* **59**, 103 – 128.

WANG, X.K., HAO, Z. & TAN, S.K. 2013 Vortex-induced vibrations of a neutrally buoyant circular cylinder near a plane wall. *Journal of Fluids and Structures* **39** (Supplement C), 188 – 204.

WANG, X.K. & TAN, S.K. 2008 Near-wake flow characteristics of a circular cylinder close to a wall. *Journal of Fluids and Structures* **24** (5), 605 – 627.

WILLIAMSON, C.H.K. & GOVARDHAN, R. 2004 Vortex-induced vibrations. *Annual Review of Fluid Mechanics* **36** (1), 413 – 455.

YANG, B., GAO, F., JENG, D.-S. & WU, Y. 2009 Experimental study of vortex-induced vibrations of a cylinder near a rigid plane boundary in steady flow. *Acta Mechanica Sinica* **25** (1), 51 – 63.

YANG, K., CHENG, L., AN, H., BASSOM, A.P. & ZHAO, M. 2013 The effect of a piggyback cylinder on the flow characteristics in oscillatory flow. *Ocean Engineering* **62**, 45 – 55.

ZANG, Z.P. & GAO, F.P. 2014 Steady current induced vibration of near-bed piggyback pipelines: Configuration effects on viv suppression. *Applied Ocean Research* **46**, 62 – 69.

ZANG, Z.P., GAO, F.P. & CUI, J.S. 2013 Physical modeling and swirling strength analysis of vortex shedding from near-bed piggyback pipelines. *Applied Ocean Research* **40**, 50 – 59.

ZDRAVKOVICH, M.M. 1997 *Flow Around Circular Cylinders: Volume I: Fundamentals*. OUP Oxford.

ZHAO, M., CHENG, L. & TENG, B. 2007 Numerical modeling of flow and hydrodynamic forces around a piggyback pipeline near the seabed. *Journal of Waterway, Port, Coastal, and Ocean Engineering* **133** (4), 286 – 295.

ZHAO, M. & YAN, G. 2013 Numerical simulation of vortex-induced vibration of two circular cylinders of different diameters at low reynolds number. *Physics of Fluids* **25** (8), 083601.

# CHAPTER 6

# TWO DEGREE-OF-FREEDOM NEAR WALL VIV IN UPPER TRANSITION REGIME

The present chapter describes the convergence studies and validation of a numerical model based on URANS approach to study the VIV in the upper transition regime. The turbulence closure used in the simulations is the k-$\omega$ SST model by Menter (1994) available in OPENFOAM. The numerical model is then used to study the flow around a single cylinder and three different configurations of two coupled cylinders with uneven diameters at a gap ratio $e/D = 2$ near the horizontal plane wall. A discussion on the observed response amplitudes, hydrodynamic forces and, flow features is given.

## 6.1 Computational Domain and Boundary Conditions

Problem definition sketch is presented in Fig. 6.1. In the present study, a rectangular computational domain is established with dimensions of $30D$ by $10D$. The cylinder center is located at a distance of $10D$ from the inflow and $20D$ from the outflow. The upper boundary is located at a distance $8.5D$ from the cylinder center, the bottom wall is located $1.5D$ from the cylinder center. Therefore, the gap-to-diameter ratio ($e/D$) is equal to one. The boundary layer thickness $\delta$ of the inflow is expressed in terms of the nondimensional boundary layer to diameter ratio ($\delta/D$) and is set to $\delta/D = 0.48$. The

domain settings which were previously used in Ong et al. (2010) and Ong et al. (2012), are considered to be sufficient to eliminate the far field effects associated with the inflow, outflow and top boundaries proximity.
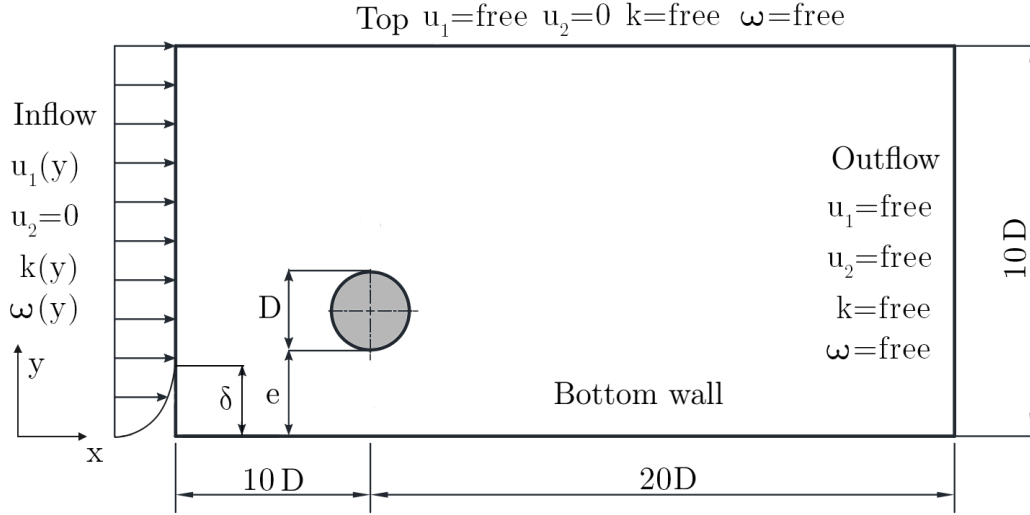


**Figure 6.1:** Schematic of a computational domain and imposed boundary conditions. Dimensions are given in terms of large cylinder diameter $D$.

1. The boundary layer flow profile is specified at the inlet using following expressions for $u$, $k$, and $\omega$:

$$u_1(y) = \min\left[\frac{u_*}{\kappa}\ln\left(\frac{y}{z_w}\right), U_\infty\right] \tag{6.1}$$

$$u_2(y) = 0 \tag{6.2}$$

$$k(y) = \max\left[C_\mu^{-1/2}\left(1 - \frac{y}{\delta}\right)^2 u_*^2, 0.0001U_\infty^2\right] \tag{6.3}$$

$$\omega(y) = \max\frac{k(y)^{1/2}}{\beta*^{1/4}\ell(y)} \tag{6.4}$$

$$\ell(y) = \min\left[\kappa y\left(1 + 3.5\frac{y}{\delta}\right)^{-1}, C_\mu\delta\right] \tag{6.5}$$

where $y$ is the wall-normal direction starting from the bottom as illustrated in Fig. 6.1; $\ell$ is the estimated turbulent length scale; $C_\mu = 0.09$ is the model constant; $\kappa = 0.41$ is the von Kármán constant; $u_*$ is the friction velocity expressed as

$$u_* = \frac{\kappa U_\infty}{\ln\left(\frac{\delta}{z_w}\right)} \tag{6.6}$$

$U_\infty$ denotes the free stream velocity; $z_w = 1 \times 10^{-6}$ m is the imposed seabed roughness.

2. At the outlet of the domain $u$, $k$ and $\omega$ are prescribed with "zero gradient" condition, meaning that convective fluxes and normal stresses are set to zero. The reference pressure $p = 0$ is set along the boundary.

3. The top boundary is prescribed with the "symmetry" boundary condition which sets the normal component of $u$, $k$ and $\omega$ to zero.

4. On the bottom and on the cylinder wall a "no slip" condition is imposed with $u_1 = 0$ and $u_2 = 0$. Standard wall functions are applied for $k$ and $\omega$

$$k = \frac{u_*^2}{\sqrt{C_\mu}} \tag{6.7}$$

$$\omega = \frac{\sqrt{k}}{C_\mu^{1/4} \kappa h_p} \tag{6.8}$$

where $h_p$ is the radial distance from the wall to the first cell center. The friction velocity $u_*$ in equation 6.8 is evaluated using log law expression

$$\frac{u_{tan}}{u_*} = \frac{1}{\kappa} \ln\left(\frac{h_p}{z_w}\right) \tag{6.9}$$

where $u_{tan}$ is the flow velocity tangential to the wall.

The Reynolds number based on the free stream velocity $U_\infty$, diameter of the larger cylinder $D$ and kinematic viscosity $\nu$ is kept constant at $Re = 3.6 \times 10^6$.

### 6.1.1 Convergence Studies

Structured meshes composed of hexahedral cells are used. Figure 6.2 shows typical mesh of the computational domain with 76364 cells. Mesh around the cylinders can be defined using parameters $N_c$ and $N_r$ which corresponds to the number of grid points in circumferential and radial directions around the cylinder surface respectively. $N_b$ denotes the number of grid points in the radial direction in the refinement box around the cylinder as shown in the close-up view in Fig. 6.2. A total number of cells in the domain is denoted $N_t$. The bounding box around the cylinder and the background mesh are refined to capture the flow features close to the cylinder and in the cylinder's wake. Further away the background mesh is coarsened to decrease the computational cost. The convergence studies are carried out in two steps. In the first step, a series of simulations of a single cylinder with a fixed position above the horizontal plane wall is carried out. The results

are used to assess the required grid density and time step and the effects of the mesh motion on the results are excluded. The main aim is to establish appropriate mesh spacing in the near-wall regions where the wall function modeling is used. The results from the static mesh study are also used to validate the computational setup used against other published experiments and simulations in upper transition regime. Mesh density is then reevaluated to account for the effects of the mesh motion. Time step sensitivity is carried out based on the desired maximum Courant number. Adjustable time step capability of the PIMPLE solver is engaged for that purpose. This approach is selected due to the mesh deformation which is a consequence of the motion solver. In case of large displacements there are mesh regions where the cell size can vary considerably compared to the initial state, therefore the Courant number is also affected. Compared to the fixed time step the adjustable time step approach is more suitable to study the effects of the temporal discretization in a class of problems involving mesh movement and was previously employed by Wen and Qiu (2017). Two sets of four meshes are prepared for the grid convergence study. In the first set, the parameter studied is the height of the first cell layer. The overall mesh density is kept constant here with cell count equal 76364 (mesh M3). Second mesh set is used to study the effect of mesh density. It contains four meshes where grid cell count of the meshes is varied using constant refinement factor preserving geometric similarity. Parameters of the meshes used are summarized in Table 6.1. The time step used in grid convergence study with a fixed cylinder position is kept constant at $\Delta t = 0.001 D/U_\infty$, ensuring that Courant number defined as $Co = U \Delta t / \Delta x$ is less than one. Firstly the effect of the distance to

**Table 6.1:** Summary of cell distribution parameters of the meshes used in the convergence study.

| Mesh | $N_c$ | $N_r$ | $N_b$ | $N_t$ |
|------|-------|-------|-------|-------|
| $M1$ | 180 | 30 | 20 | 18886 |
| $M2$ | 270 | 45 | 30 | 41754 |
| $M3$ | 320 | 60 | 40 | 76364 |
| $M4$ | 450 | 75 | 50 | 117648 |

**Table 6.2:** Convergence study: Static cylinder, effects of the first cell layer height. Other parameters of the simulations: $Re = 3.6 \times 10^6$, $e/D = 1$, Mesh M3.

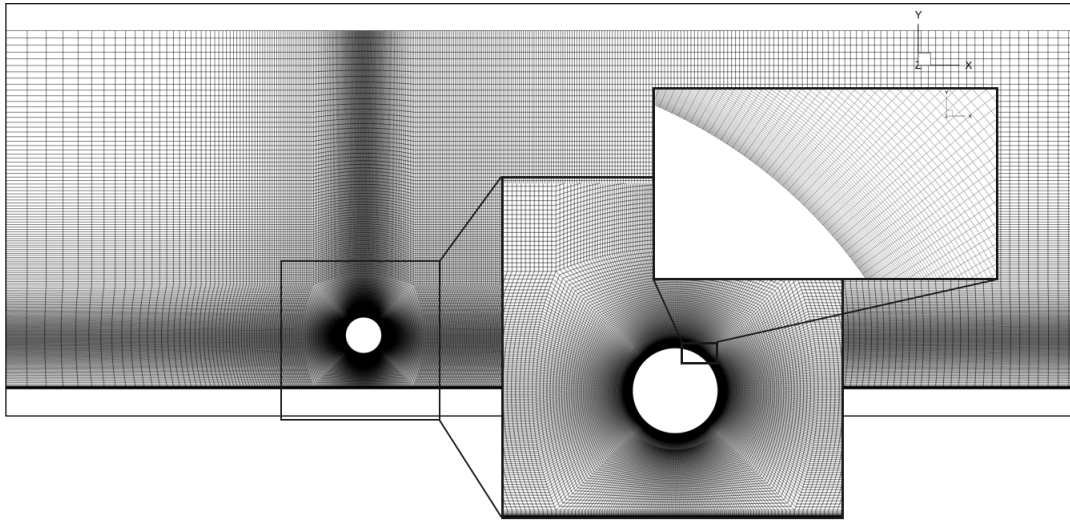| | Mesh parameters: | | Hydrodynamic parameters: | | | |
|------|------|------|------|------|------|------|
| Mesh | Time step | First cell height $\Delta y_1$ | $\overline{C}_D$ | $\overline{C}_L$ | max. $y^+$ | avg. $y^+$ |
| $M3A$ | $\Delta t = 0.001$ | 0.0007 D | 0.4778 (3.72%) | 0.0445 (9.21%) | 98.40 | 50.54 |
| $M3B$ | $\Delta t = 0.001$ | 0.0006 D | 0.4705 (2.23%) | 0.0425 (4.94%) | 84.85 | 43.73 |
| $M3C$ | $\Delta t = 0.001$ | 0.0005 D | 0.4610 (0.21%) | 0.0404 (0.00%) | 69.40 | 38.34 |
| $M3D$ | $\Delta t = 0.001$ | 0.0004 D | 0.4600 (-) | 0.0404 (-) | 56.86 | 29.65 |

**Figure 6.2:** Computational mesh details - mesh M3, 76364 cells.

the first cell center is evaluated. The results are presented in Table 6.2. The $y^+$ is defined here as $y^+ = h_p u_*/\nu$. Relative percentage change between consecutive simulations is given in the brackets. The difference in obtained results between the two smallest cell heights M3D $\Delta y_1 = 0.0004D$ and M3C $\Delta y_1 = 0.0005D$ is negligible and the maximum and average $y^+$ values are within the range appropriate for the wall function use. In the two other cases, a significant variation in the lift and drag forces is observed. Therefore the first cell height is established as $\Delta y_1 = 0.0005D$ and the first cell layer adjacent to the walls is kept constant in the following grid density study.

To evaluate the effect of the grid density, meshes with different cell count are compared. The mesh parameters and corresponding representative hydrodynamic quantities obtained from the convergence study are given in Table 6.3, along with the percentage changes between the consecutive simulations. The differences between the results of solutions obtained on mesh M3 and mesh M4 are in general smaller than 1%, similar results are obtained with mesh M2 with the exception of root-mean-square value of lift coefficient which is particularly sensitive to the mesh resolution. In that case, the difference between $C_L^{rms}$ on mesh M2 and mesh M3 is higher than 5%. On the coarsest mesh, the numerical results diverge by more than 5% as compared to mesh M2. Considering the computational cost the mesh M3 is selected to conduct the further study and is expected to be sufficiently accurate.

Results of the simulations with motion solver engaged are summarized in Table 6.4 and Table 6.5. The reduced velocity is set to $U_r = 6$ where a large amplitude of oscillation is expected. Gap ratio is extended from $e/D = 1$ to $e/D = 2$. This is done to prevent the

**Table 6.3:** Convergence study: Static cylinder, effects of the grid density. Other parameters of the simulations: $Re = 3.6 \times 10^6$, $e/D = 1$.

| | Mesh parameters: | | Hydrodynamic parameters: | | | |
|---|---|---|---|---|---|---|
| Mesh | Time step | Cell count | $\overline{C}_D$ | $\overline{C}_L$ | $C_L^{rms}$ | $St$ |
| $M1$ | $\Delta t = 0.001$ | 18886 | 0.4406 (-4.82%) | 0.0442 (9.28%) | 0.196 (14.29%) | 0.324 (-7.10%) |
| $M2$ | $\Delta t = 0.001$ | 41754 | 0.4624 (0.13%) | 0.0405 (0.99%) | 0.178 (5.62%) | 0.342 (-1.46%) |
| $M3$ | $\Delta t = 0.001$ | 76364 | 0.4610 (-0.17%) | 0.0404 (0.74%) | 0.169 (0.59%) | 0.347 (0.0%) |
| $M4$ | $\Delta t = 0.001$ | 117648 | 0.4618 (-) | 0.0401 (-) | 0.168 (-) | 0.347 (-) |

oscillating cylinder from hitting the horizontal wall at the bottom of the domain. One of the limitations of the mesh motion solver is the necessity to provide sufficient distance around the body where the mesh morphing algorithm is active. The large amplitude of motion requires large morphed mesh distance to accommodate the moving boundaries displacements. Time step is adjusted on every outer loop iteration of the PIMPLE solver and is constrained to a maximum value of Courant number $Co_{max} = 0.5$. Compared to the static simulations results it is apparent that simulations with the mesh motion solver are more sensitive with respect to the mesh density and quality. The results summarized in Table 6.4 seem to support the selection of the mesh M3 as sufficiently accurate for the present study. All of the investigated parameters differ less than 2% from the values obtained on the finest mesh M4. The largest differences occur in the $C_L^{rms}$ values. Results from the time step sensitivity study are presented in Table 6.5. Mesh M3 is used in the simulations, at $U_r = 6$. When the maximum Courant number is set higher than 1 the solution is not converging as indicated in Table 6.5. Discrepancies between the two finest settings at $Co_{max} = 0.25$ and $Co_{max} = 0.5$ are well below 1%. Based on the results from the convergence studies mesh M3 and time step restricted to $Co_{max} = 0.5$ are considered to give sufficient numerical accuracy.

**Table 6.4:** Convergence study: Vibrating cylinder, effects of the grid density. Other parameters of the simulations: $Re = 3.6 \times 10^6$, $e/D = 2$, $U_r = 6$.

| | Mesh parameters: | | Hydrodynamic parameters: | | | |
|---|---|---|---|---|---|---|
| Mesh | Time step | Cell count | $\overline{C}_D$ | $(A_y)_{max}/D$ | $C_L^{rms}$ | $St$ |
| $M1$ | $Co_{max} = 0.5$ | 18886 | 0.7642 (-6.7%) | 1.0732 (7.12%) | 0.3815 (16.12%) | 0.1508 (-6.14%) |
| $M2$ | $Co_{max} = 0.5$ | 41754 | 0.7983 (-2.53%) | 1.0245 (2.26%) | 0.3491 (6.26%) | 0.1577 (-1.83%) |
| $M3$ | $Co_{max} = 0.5$ | 76364 | 0.8098 (-1.15%) | 1.0115 (0.95%) | 0.3349 (1.89%) | 0.1605 (-0.12%) |
| $M4$ | $Co_{max} = 0.5$ | 117648 | 0.8191 (-) | 1.0018 (-) | 0.3289 (-) | 0.1606 (-) |

**Table 6.5:** Convergence study: Vibrating cylinder, effects of the time step. Other parameters of the simulations: $Re = 3.6 \times 10^6$, $e/D = 2$, $U_r = 6$.

| Mesh parameters: | | | Hydrodynamic parameters: | | | |
|---|---|---|---|---|---|---|
| Mesh | Time step | Cell count | $\overline{C}_D$ | $(A_y)_{max}/D$ | $C_L^{rms}$ | $St$ |
| $M3$ | $Co_{max} = 2$ | 76364 | not converged | not converged | not converged | not converged |
| $M3$ | $Co_{max} = 1$ | 76364 | 0.8661 (7.76%) | 1.0638 (5.64%) | 0.3128 (-7.21%) | 0.1664 (3.65%) |
| $M3$ | $Co_{max} = 0.5$ | 76364 | 0.8098 (0.75%) | 1.0115 (0.43%) | 0.3349 (-0.65%) | 0.1605 (0%) |
| $M3$ | $Co_{max} = 0.25$ | 76364 | 0.8037 (-) | 1.007 (-) | 0.3371 (-) | 0.1605 (-) |

### 6.1.2  Model Validation

The accuracy of the selected numerical technique is compared with the available experimental data and numerical studies in the upper transition regime. Due to the technical difficulties in the experimental setup and high computational demands in the numerical studies the availability of the reference data is relatively scarce compared to the lower Reynolds number flows. Comprehensive numerical study at $Re = 3.6 \times 10^6$ was carried out by Ong et al. (2010), who investigated flow around a near-wall cylinder in the upper transition regime. More recently Porteous et al. (2015) conducted benchmark simulations of flow around a cylinder at $Re = 1 - 3.6 \times 10^6$ using RANS and URANS models in OPENFOAM. In Ong et al. (2010) the standard $k - \epsilon$ turbulence model was used and finite element solver employed on the domain setup similar to the one in the present study. Summary of the mean drag coefficient, root-mean-square lift coefficient, Strouhal number and base pressure coefficient values are given in Table 6.6. The $\overline{C}_D$ values show very good agreement with the other numerical studies and fall well within the experimental results range. The $C_L^{rms}$, on the other hand, is higher than the value from the computations by Ong et al. (2010). The same tendency can be noted for the Strouhal number value, at $St = 0.347$ it falls at the upper limit of the uncertainty band of experimental data. The base pressure coefficient compares well with the reference data from Ong et al. (2010) and Porteous et al. (2015). The plot of pressure coefficient is shown in Fig. 6.3. It can be seen that the fit to experimental data by Achenbach (1968) is very good between $0° \leq \theta \leq 70°$, $k - \omega$ SST model tends to overpredict the $C_P$ value at $70° \leq \theta \leq 110°$ and underpredict at $110° \leq \theta \leq 180°$. It should be noted that in $110° \leq \theta \leq 180°$ range the fit to the results by Ong et al. (2010) is almost exact. In general, the agreement of the present computational model with the other published results can be viewed as satisfactory considering high uncertainty and scatter of the experimental data at very high Reynolds numbers.
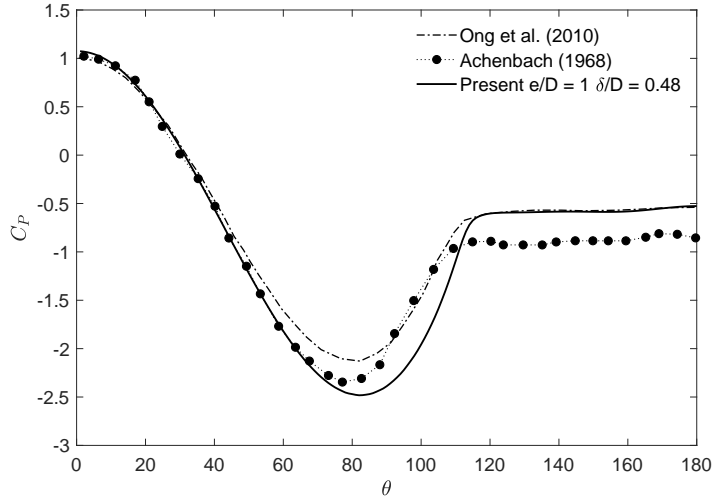
**Figure 6.3:** Mean pressure coefficient around the cylinder at $Re = 3.6 \times 10^6$; $\delta/D = 0.48$; $e/D = 1.0$.

**Table 6.6:** Experimental data and numerical results at $Re = 3.6 \times 10^6$.

| Study | Description | $\overline{C}_D$ | $C_L^{rms}$ | $St$ | $-C_{Pb}$ |
|---|---|---|---|---|---|
| Present study $e/D = 1.0$, $\delta/D = 0.48$ | $k - \omega$ SST URANS | 0.461 | 0.169 | 0.347 | 0.5268 |
| Ong et al. (2010) $e/D = 1.0$, $\delta/D = 0.48$ | $k - \epsilon$ URANS | 0.4608 | 0.0857 | 0.3052 | 0.5392 |
| Ong et al. (2009) isolated cylinder | $k - \epsilon$ URANS | 0.4573 | 0.0766 | 0.3052 | - |
| Catalano et al. (2003) Re $= 4.0 \times 10^6$ | URANS | 0.46 | - | - | - |
| Porteous et al. (2015) | $k - \omega$ SST URANS | 0.518 | - | - | 0.513 |
| Zdravkovich (1997) | Experiments | 0.36-0.75 | 0.06-0.14 | 0.17-0.29 | |
| Achenbach (1968) Re $= 0.5 - 5 \times 10^6$ | Experiments | 0.6-0.76 | - | - | 0.85 |
| Roshko (1961) Re $= 1 - 3.5 \times 10^6$ | Experiments | 0.3-0.7 | - | - | 0.62-0.85 |
| Schewe (1983) Re $= 1 - 5 \times 10^6$ | Experiments | 0.22-0.52 | - | - | - |
| Jones et al. (1969) Re $= 0.5 - 8 \times 10^6$ | Experiments | 0.15-0.54 | - | - | 0.53 - 0.63 |
| Schmidt (1966) Re $= 1 - 5 \times 10^6$ | Experiments | 0.18-0.53 | - | - | 0.35 - 0.60 |
| Shih et al. (1993) Re $= 0.3 - 8 \times 10^6$ | Experiments | 0.16-0.50 | - | - | 0.10 - 0.60 |

## 6.2   Results and Discussion

For each analyzed case the simulations are performed sufficiently long to ensure at least 30 periods of regular vibration if the vibration is regular and periodic. In case of irregular vibration, the duration of the simulations is extended to extract representative mean flow features. Meshes used in the simulations of coupled cylinders with uneven diameters have similar density and are qualitatively similar to the mesh M3 presented in the convergence studies. Similarly to the study presented in Chapter 5, three different angular positions of the small cylinder are investigated over the range of reduced velocities

$2 \leq U_r \leq 12$. The mass ratio is kept constant in all cases at $m^* = 10$. Structural damping ratio is set to zero $\zeta = 0$.

### 6.2.1   Response Amplitudes

Normalized displacements in transverse direction are shown in Fig. 6.4. Among the analyzed configurations the $\alpha = 0°$ configuration has the narrowest lock-in regime, approximately $2 < U_r < 6$ with a peak value $A_{Y,max}/D = 1.15$ at $U_r = 5$. The widest lock-in regime is observed when the small cylinder is placed upstream of the large cylinder at $\alpha = 180°$ and extends from $U_r = 2$ beyond $U_r = 12$ which was the limit of the present study. The peak value of $A_{Y,max}/D = 1.23$ is in this case reached at $U_r = 10$. This behavior is the opposite of the behavior observed in the low Reynolds regime presented in Chapter 5, where the widest lock-in regime occured in the $\alpha = 0°$ configuration and the narrowest lock-in regime occured in the $\alpha = 180°$ configuration. This phenomenon is confirmed by the experimental results by Zang and Gao (2014) who observed similar relation in high Reynolds flow at $Re = 3.8 \times 10^4$. In the side-by-side configuration $\alpha = 90°$ lock-in regime can be identified between $3 \leq U_r \leq 12$ with a peak $A_{Y,max}/D = 0.92$ occuring at $U_r = 6$. The single cylinder vibrations are in the locin regime at $3 \leq U_r \leq 7$ with a peak value $A_{Y,max}/D = 1.01$ identified at $U_r = 6$. Both the single cylinder and the $\alpha = 0°$ configurations show abrupt decrease in the response and very narrow desynchronization regime. The densynchronization in the $\alpha = 90°$ configuration is gradual and vibration amplitudes are decreasing monothonically between $U_r = 6$ and $U_r = 12$. The desynchronization in the $\alpha = 180°$ configuration is not captured in the present study due to lock-in regime exceeding the $U_r$ limits of the simulations.

The streamwise response in term of the root-mean-square streamwise displacement $A_{X,rms}/D$ is presented in Fig. 6.5. A characteristic feature of the streamwise response at $Re = 3.6 \times 10^6$ compared to the low Reynolds studies presented in Chapter 4 and Chapter 5 is that the streamwise lock-in regime is generally slightly shifted to the lower range of reduced velocities. The streamwise lock-in regimes in all analyzed configurations are considerably narrower than the corresponding transverse lock-in regimes. The peak values are also shifted towards lower $U_r$ compared to the corresponding peak values in the $A_{Y,max}/D$ response. The largest $A_{X,rms}/D$ response is experienced by the single cylinder and the $\alpha = 90°$ configuration. A peak value of $A_{X,rms}/D \approx 0.3$ is reached at $U_r = 4$ in both single cylinder and $\alpha = 90°$ configurations. The widest streamwise lock-in regime is observed when the small cylinder is placed upstream of the large cylinder $3 \leq U_r \leq 8$. In the $\alpha = 0°$ configuration the $A_{X,rms}/D$ response is very small compared to the other
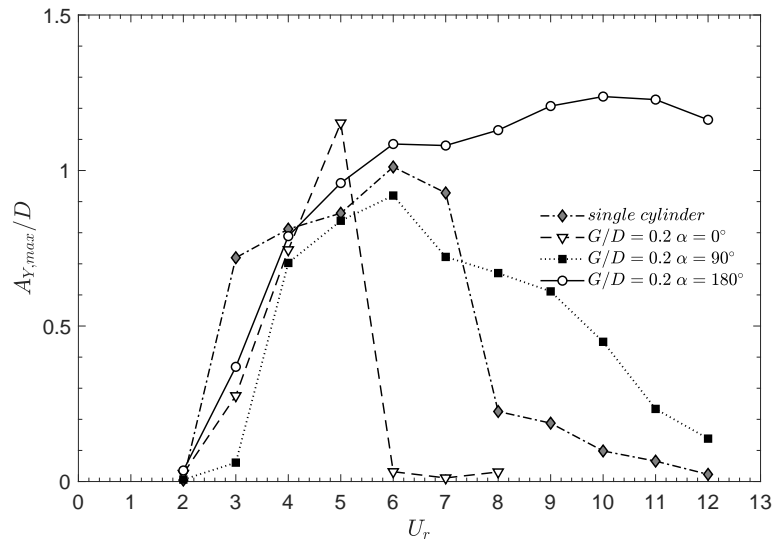
**Figure 6.4:** Non-dimensional maximum amplitude of transverse vibration $A_{Y,max}/D$ at $Re = 3.6 \times 10^6$ as a function of reduced velocity $U_r$.

considered configurations. Slight excitation can be spotted at $U_r = 4$ and $U_r = 5$ but there is no apparent peak present in the $A_{X,rms}/D$ response picture.
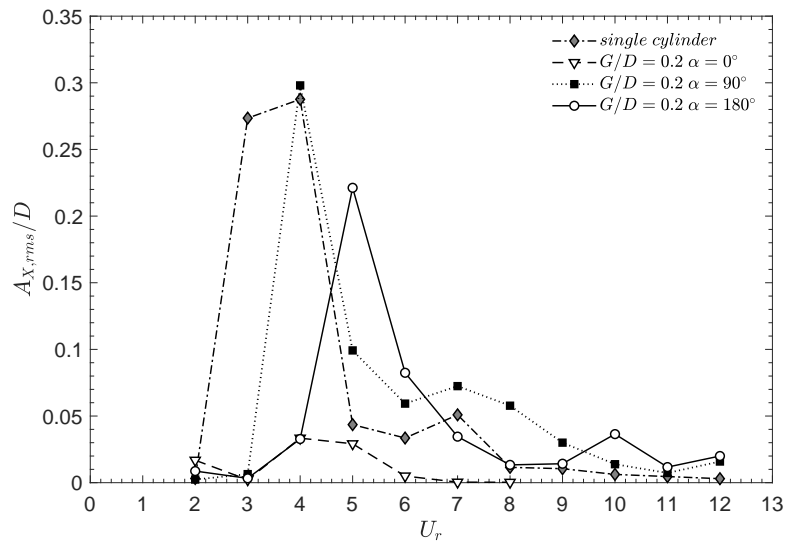


**Figure 6.5:** Non-dimensional root-mean-square amplitude of streamwise vibration $A_{X,rms}/D$ at $Re = 3.6 \times 10^6$ as a function of reduced velocity $U_r$.

### 6.2.2  Hydrodynamic Forces

Mean lift coefficient values against reduced velocity are shown in Fig. 6.6. A negative value indicates the force acting in the direction of the bottom wall. The dashed line representing $\overline{C}_L$ of a single stationary cylinder at $Re = 3.6 \times 10^6$ and $e/D = 1$ is given for comparison. The $\overline{C}_L$ pictures vary considerably depending on the configuration. In the single cylinder configuration, the mean lift coefficient is negative except in the initial branch of the lock-in regime corresponding to $3 \leq U_r \leq 4$ which can be seen in Fig. 6.6. The $\alpha = 180°$ configuration and the $\alpha = 0°$ configuration show similar $\overline{C}_L$ response curves but the peak values are considerably lower than in the single cylinder case. Outside of the initial branch, the $\overline{C}_L$ values in those configurations are approaching zero. Presence of the small cylinder at $\alpha = 90°$ angular position results in the dominantly negative $\overline{C}_L$, reported at all investigated $U_r$ except $U_r = 4$. The $\overline{C}_L$ value increases in the lock-in regime and at $U_r = 4$ becomes slightly positive. Figure 6.7 shows root-mean-
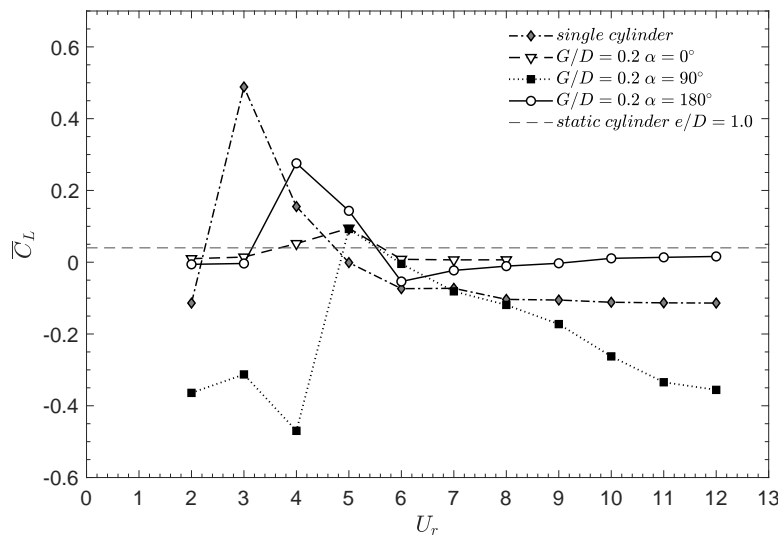


**Figure 6.6:** Mean lift coefficient $\overline{C_L}$ at $Re = 3.6 \times 10^6$ as a function of reduced velocity $U_r$.

square values of $C_L$. In the $\alpha = 0°$ configuration the $C_L^{rms}$ peak value is considerably higher than in the other considered configurations. The response curve shape in this case is coinciding with the $A_{Y,max}/D$ response curve with peak located at $U_r = 5$. After reaching the peak value, $C_L^{rms}$ drops to the value observed in the static cylinder case. The peak of $C_L^{rms}$ in the single cylinder configuration is located at $U_r = 3$ which is different than the peak of transverse response observed at $U_r = 6$. This indicates that other mechanism than lift force oscillations alone is responsible for the enhanced vibration amplitude. Similar observations can be made with respect to the $\alpha = 90°$ and the $\alpha =$

$180°$ configurations. Here the peak values are identified in both cases at $U_r = 4$. The
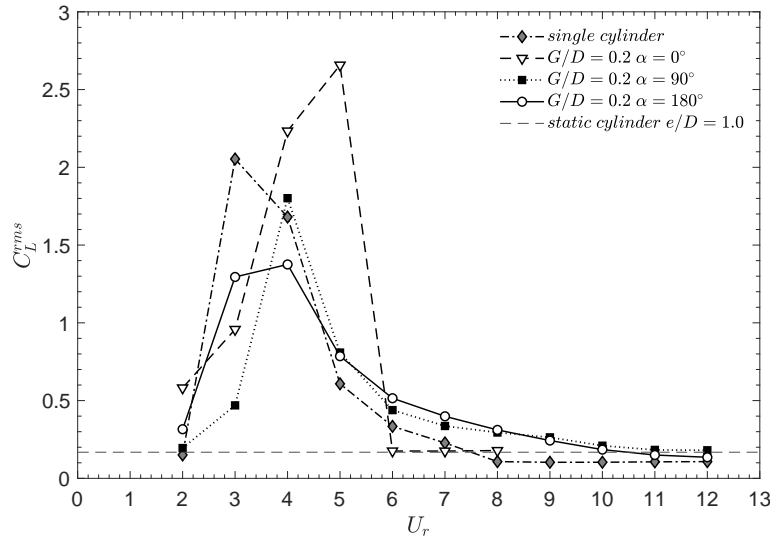


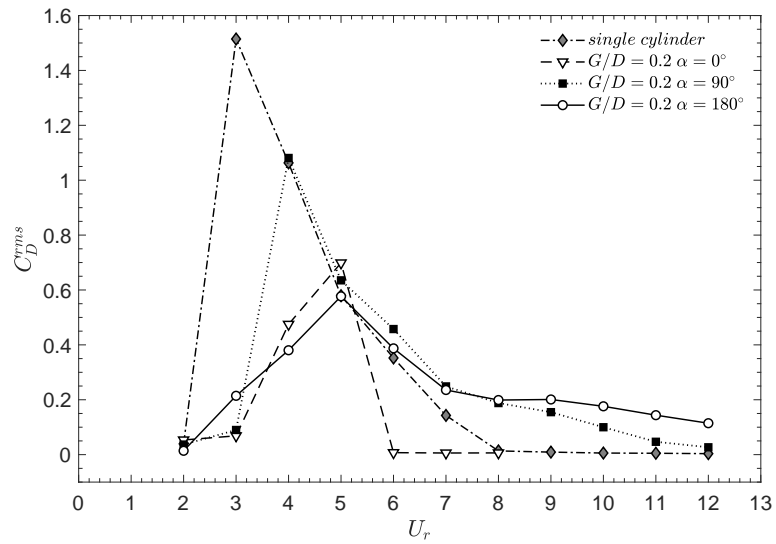**Figure 6.7:** Root-mean-square lift coefficient $C_L^{rms}$ at $Re = 3.6 \times 10^6$ as a function of reduced velocity $U_r$.

effect of the small cylinder presence on the mean drag force can be seen in Fig. 6.8. In the range of reduced velocities $3 \leq U_r \leq 4$ the mean drag coefficient in the single cylinder case is considerably higher than in the three investigated configurations of two coupled cylinders. Outside of this $U_r$ range the $\overline{C_D}$ is smaller than in the $\alpha = 0°$, $\alpha = 90°$ and $\alpha = 180°$ configurations. The lowest peak value of $\overline{C_D}$ is observed in the $\alpha = 0°$ configuration. Slightly higher peak value can be identified in the $\alpha = 90°$ configuration. Similar observations were made by Zang and Gao (2014) who reported decrease in the mean lift coefficient when tha small cylinder was placed at $\alpha = 0°$ and $\alpha = 180°$ positions. The root-mean-square values of $C_D$ can be seen in Fig. 6.9. The peak values in the $C_D^{rms}$ plot overlap with those identified for mean values in Fig. 6.8.

### 6.2.3 Phase Pictures and Motion Trajectories

In this subsection, the $X - Y$ trajectories and phase pictures of transverse displacement $Y/D$ against the lift coefficient $C_L$ are analyzed at selected reduced velocities. For the sake of completeness the results from all simulation cases in this study are assembled in the Appendix B. The phase difference between the hydrodynamic force and the corresponding displacement response can be associated with the direction of the energy transfer in the system. Trace position in the first and third quadrant is indicative of an in-phase relation between the displacement and the hydrodynamic force. As the phase portrait transitions to the second and fourth quadrant, this relation becomes out of phase.
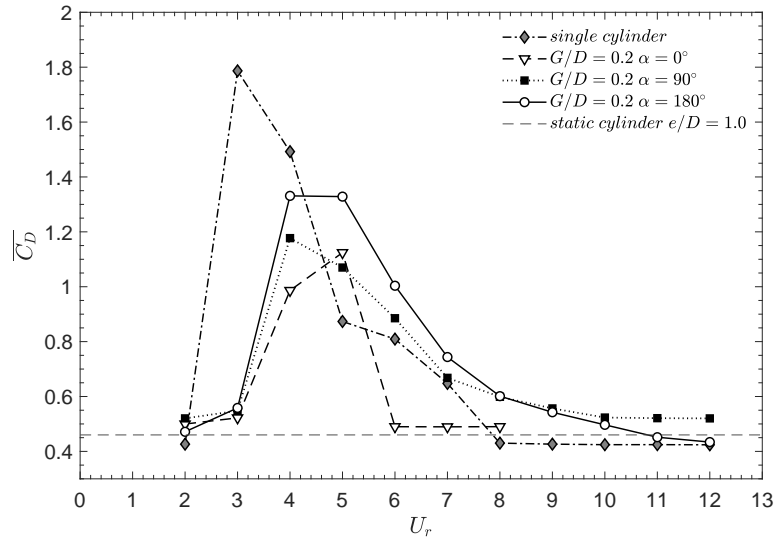
**Figure 6.8:** Mean drag coefficient $\overline{C_D}$ at $Re = 3.6 \times 10^6$ as a function of reduced velocity $U_r$.



**Figure 6.9:** Root-mean-square drag coefficient $C_D^{rms}$ at $Re = 3.6 \times 10^6$ as a function of reduced velocity $U_r$.

Figure 6.11 shows the phase picture ($\phi_{C_L-Y}$) of $C_L$ and $y/D$ and $X - Y$ trajectory of the single cylinder at $U_r = 6$. At this reduced velocity, the cylinder transverse oscillations



**(a)** $\phi_{C_L-Y}$ at $U_r = 6$      **(b)** Trajectory at $U_r = 6$
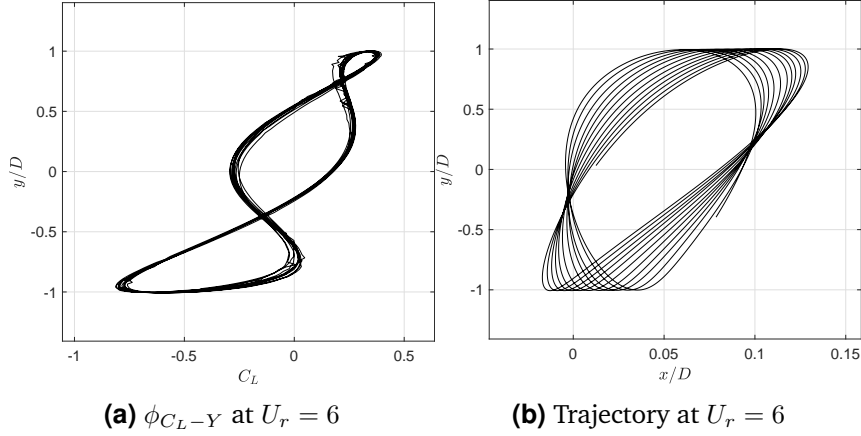
**Figure 6.11:** Phase picture ($\phi_{C_L-Y}$) of $C_L$ and $y/D$ and $X - Y$ trajectory; single cylinder; $e/D = 2.0$; $Re = 3.6 \times 10^6$; $U_r = 6$.

reach its peak amplitude. The trajectory pattern is in form of the skewed oval which is representative for the near-wall VIV of a single cylinder and was previously discussed in Chapter 4 and Chapter 5. The $\phi_{C_L-Y}$ trace lies in the first and third quadrant indicating that the lift force and the transverse displacement are in-phase. Vibration trajectories at other investigated $U_r$ show similar oval shape. In the configuration with the small cylinder located downstream of the large cylinder ($\alpha = 0°$) trajectories and phase portraits at $U_r = 4$ and $U_r = 5$ will be compared. Both analyzed cases correspond to the lock-in regime where the transverse oscillation amplitude is large. Figure 6.13 presents the $X - Y$-trajectory and $\phi_{C_L-Y}$ plots at $U_r = 4$. Similarly to the single cylinder case shown in Fig. 6.11(a) the phase plot indicate here (Fig. 6.13(a)) the in-phase relation between $C_L$ and $y/D$. The vibration trajectory is in the form of skewed oval (Fig. 6.13(b)). At $U_r = 5$ the trajectory shape switch from the oval shape to the figure eight shape as shown in Fig. 6.15(b). When the cylinders are placed in the $\alpha = 90°$ configuration the phase picture and $X - Y$ trajectory shown in Fig. 6.17 is similar to the plots obtained from the other investigated $U_r$. In all investigated cases of the $\alpha = 90°$ configuration the trajectories are very regular and less skewed compared to the other considered configurations. In the $\alpha = 180°$ configuration plots presented in Fig. 6.19 are representative for the range of reduced velocities $4 \leq U_r \leq 7$. This range can be associated with the initial branch of the lock-in regime. Between the $U_r = 7$ and $U_r = 8$ the vibration pattern changes from the skewed oval to the figure eight which can be seen in Fig. 6.21(b).

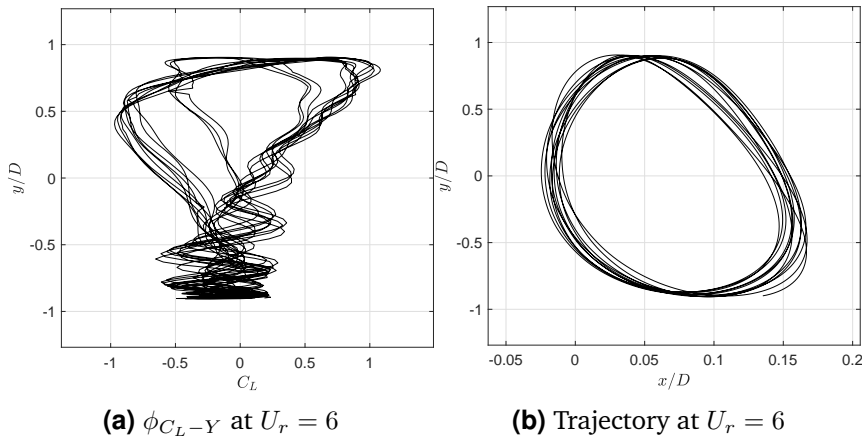**(a)** $\phi_{C_L-Y}$ at $U_r = 4$      **(b)** Trajectory at $U_r = 4$
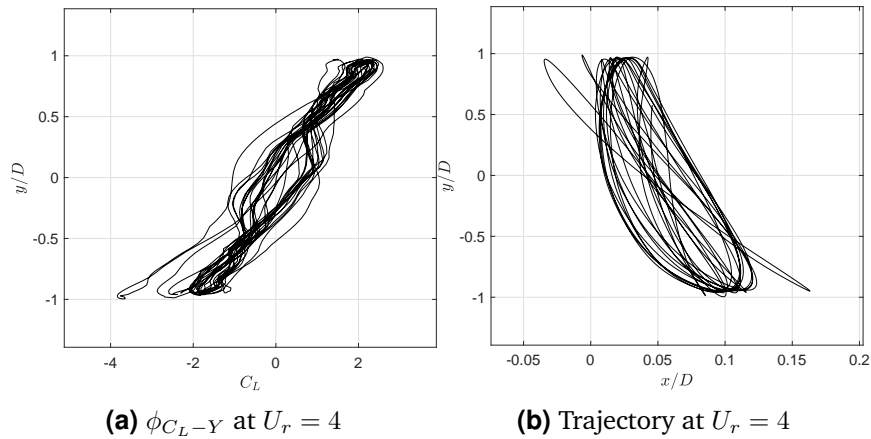
**Figure 6.13:** Phase picture ($\phi_{C_L-Y}$) of $C_L$ and $y/D$ and $X-Y$ trajectory; coupled cylinders $\alpha = 0°$; $e/D = 2.0$; $Re = 3.6 \times 10^6$; $U_r = 4$.
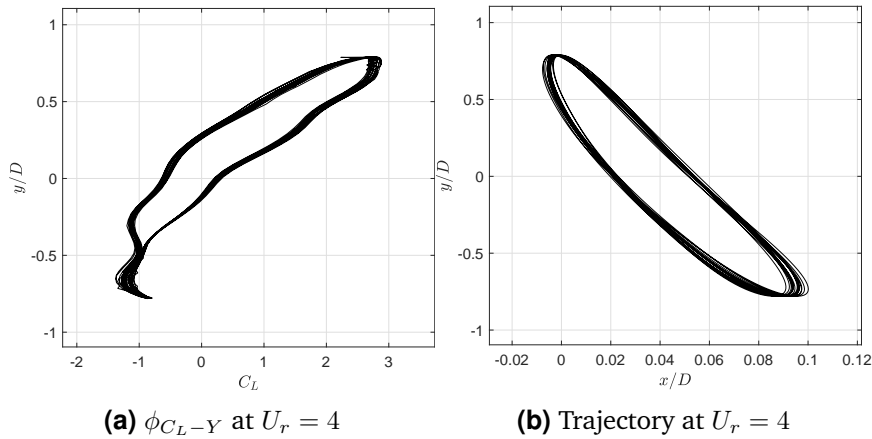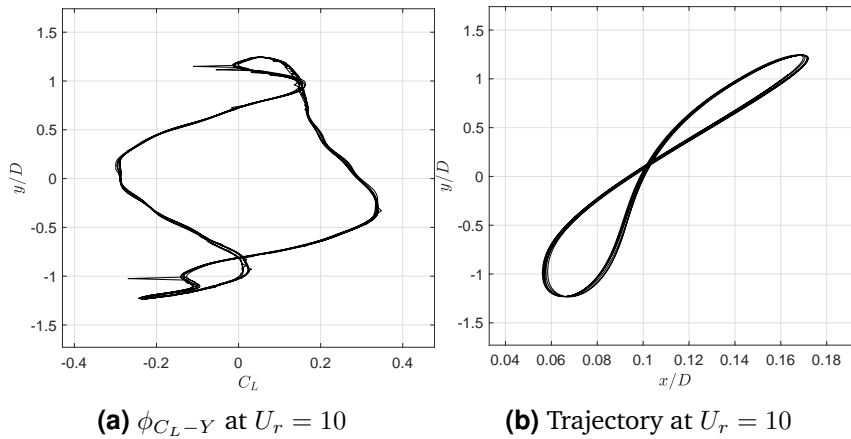


**(a)** $\phi_{C_L-Y}$ at $U_r = 5$      **(b)** Trajectory at $U_r = 5$
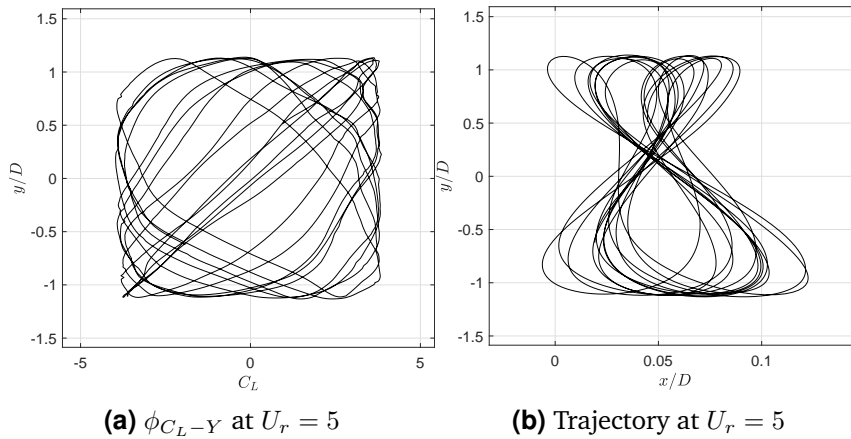
**Figure 6.15:** Phase picture ($\phi_{C_L-Y}$) of $C_L$ and $y/D$ and $X-Y$ trajectory; coupled cylinders $\alpha = 0°$; $e/D = 2.0$; $Re = 3.6 \times 10^6$; $U_r = 5$.

### 6.2.4   Flow Field Charactersitics

Vorticity and pressure contours at reduced velocities $U_r$ corresponding to the largest transverse amplitude response are used to study the flow field characteristics of analyzed cylinder configurations. The cross marker indicates the initial location of the cylinder center. Figure 6.23 shows the flow fields around the single cylinder configuration at $U_r = 6$. At this reduced velocity, the single cylinder reaches the peak in transverse oscillation amplitude response. A characteristic feature, compared to the low Reynolds number flow, is the significantly increased vortex formation length. The separation points in the cylinder's boundary layer are shifted backward compared to the flow visualizations at $Re = 200$ presented in Chapter 4 (e.g. Fig. 4.14). The shedding mode is clearly of a 2P type, where two vortex pairs are shed per oscillation cycle from the upper (A1 and

**(a)** $\phi_{C_L-Y}$ at $U_r = 6$      **(b)** Trajectory at $U_r = 6$

**Figure 6.17:** Phase picture ($\phi_{C_L-Y}$) of $C_L$ and $y/D$ and $X - Y$ trajectory; coupled cylinders $\alpha = 90°$; $e/D = 2.0$; $Re = 3.6 \times 10^6$; $U_r = 6$.



**(a)** $\phi_{C_L-Y}$ at $U_r = 4$      **(b)** Trajectory at $U_r = 4$

**Figure 6.19:** Phase picture ($\phi_{C_L-Y}$) of $C_L$ and $y/D$ and $X - Y$ trajectory; coupled cylinders $\alpha = 180°$; $e/D = 2.0$; $Re = 3.6 \times 10^6$; $U_r = 4$.

A2 in Fig. 6.23) and lower surfaces of the cylinder (B1 and B2 in Fig. 6.23). This is the source of the lift coefficient fluctuations within one oscillation period which can be seen in Fig. 6.24. At present gap ratio $e/D = 2$, the cylinder is not submerging into the boundary layer. The bottom shear layer roll up can be observed in Fig. 6.23(a) where the anti-clockwise vortex (C) forces the boundary layer to rollup (D). This action takes place further away from the cylinder compared to the low Reynolds number flow (see Fig. 4.14).

Flow fields in the $\alpha = 0°$ configuration at $U_r = 5$ are shown in Fig. 6.26. Here the shedding mode can be identified as a 2S mode. Clockwise and anti-clockwise vortices form the wake in an alternating way. However, the vortex formation in the shear layers of the large cylinder is affected by the small cylinder presence. The gap flow between

**(a)** $\phi_{C_L-Y}$ at $U_r = 10$        **(b)** Trajectory at $U_r = 10$

**Figure 6.21:** Phase picture ($\phi_{C_L-Y}$) of $C_L$ and $y/D$ and $X - Y$ trajectory; coupled cylinders $\alpha = 180°$; $e/D = 2.0$; $Re = 3.6 \times 10^6$; $U_r = 10$.

the cylinder is present which is indicated by the streamlines passing through the gap as shown in Fig. 6.26. It can be observed that in the first half cycle of one oscillation period vortices are formed around the small cylinder (S1,S2 in Fig. 6.26(a)) and merge with the vortices shed from the large cylinder (L3 and L4 in Fig. 6.26(b)). This sequence is repeated in the second half cycle where vortices from the small cylinder (S3 and S4 in Fig. 6.26(c)) merge with the newly formed vortices on the large cylinder (Fig. 6.26(d)).
  Effect of the wake interference due to the small cylinder presence can be found in the drag coefficient time trace presented in Fig. 6.27, in the form of random fluctuations of the $C_D$.

Flow around the side-by-side configuration in which the small cylinder is placed on top of the large cylinder ($\alpha = 90°$) is shown in Fig. 6.29. In this case, the formation of the vortex street behind the small cylinder (E) can be observed in Fig. 6.29. It can be seen that the vortex shedding frequency from the small cylinder is five times the vortex shedding frequency of the large cylinder. This is in agreement with the diameter ratio of the cylinders $d/D = 0.2$ and follows from the Strouhal's law. The vortices from the small cylinder (E) merge with the clockwise vortex shed from the upper surface of the large cylinder (F1) destabilizing the upper shear layer. In consequence, the formation of the clockwise vortex (F1) is disrupted. This leads to the fluctuations in the lift coefficient when the cylinder is moving from the trough to the peak position as shown in Fig. 6.30. Here in each cycle, five small oscillations can be spotted. Merging of the vortices from the small cylinder with the clockwise vortex from the large cylinder reinforces the anti-clockwise vortex developed on the bottom surface of the large cylinder (F2). This anti-clockwise vortex (F2) remains coherent as it is convected away down the wake. In case of the clockwise vortex (F1), the interaction with the vortex street from the small cylinder
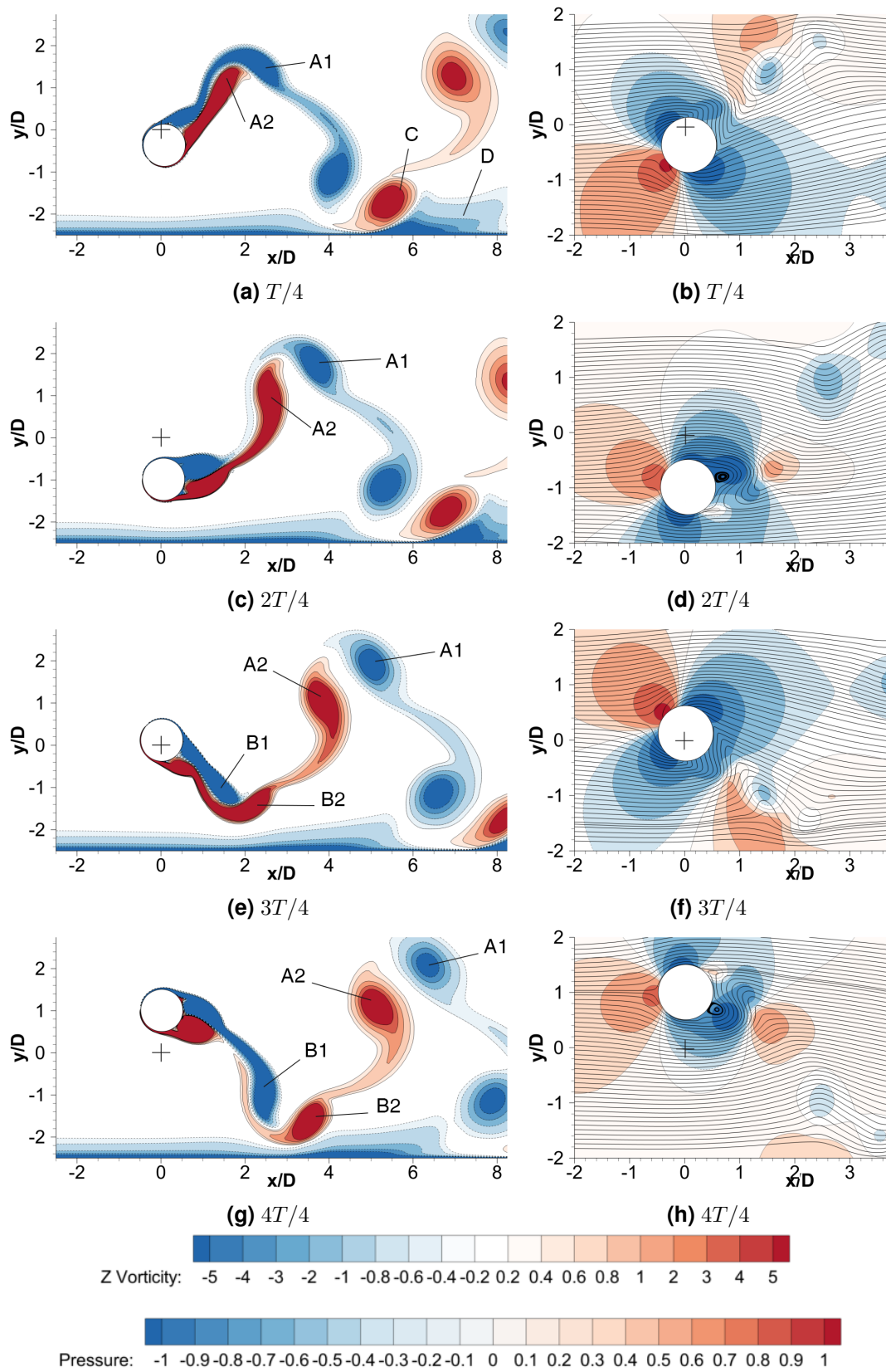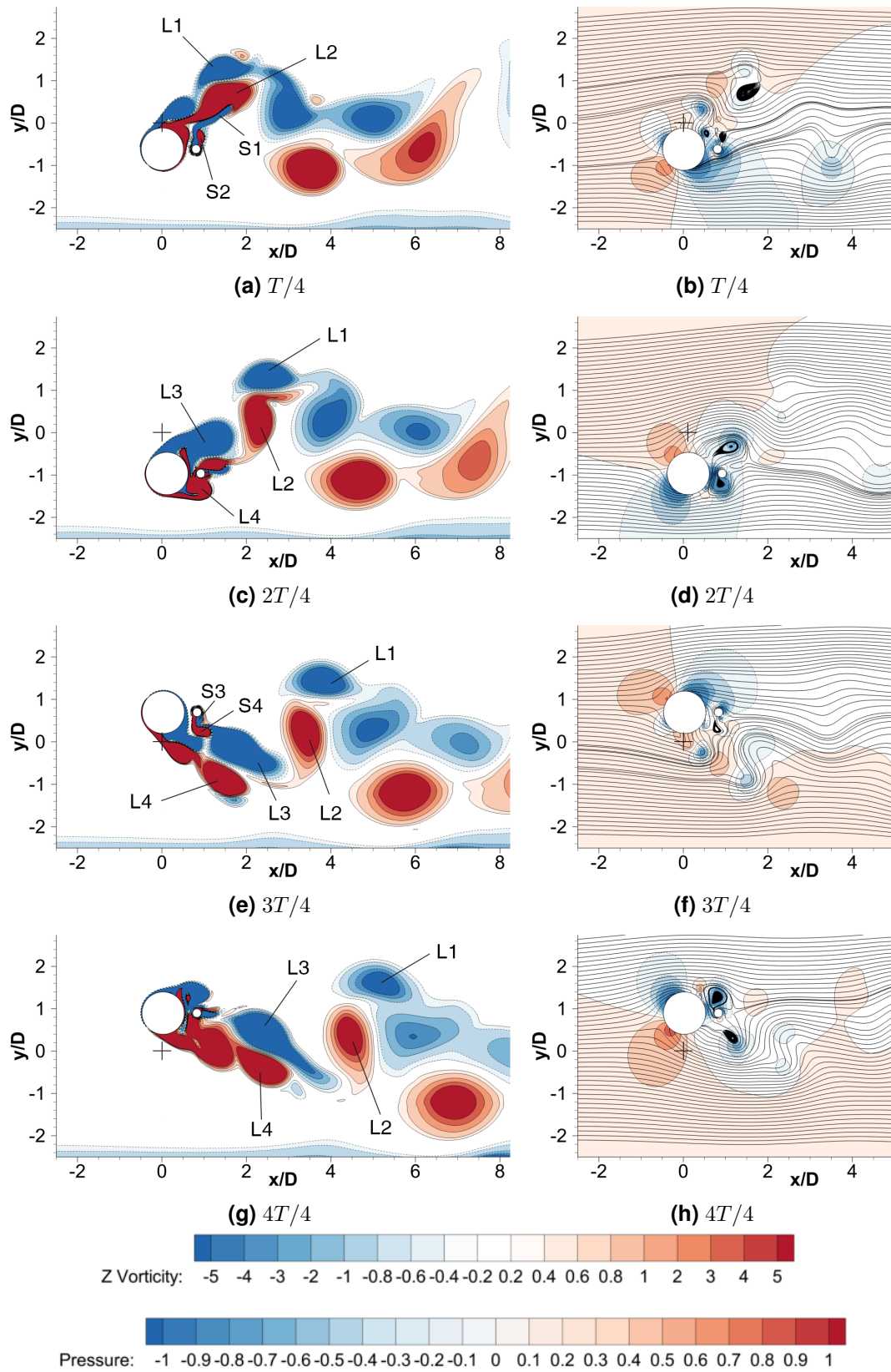
**Figure 6.23:** Vorticity contours (left) and streamlines with normalized pressure contours (right) at selected time instances of one shedding cycle for a single cylinder at $U_r = 6$.
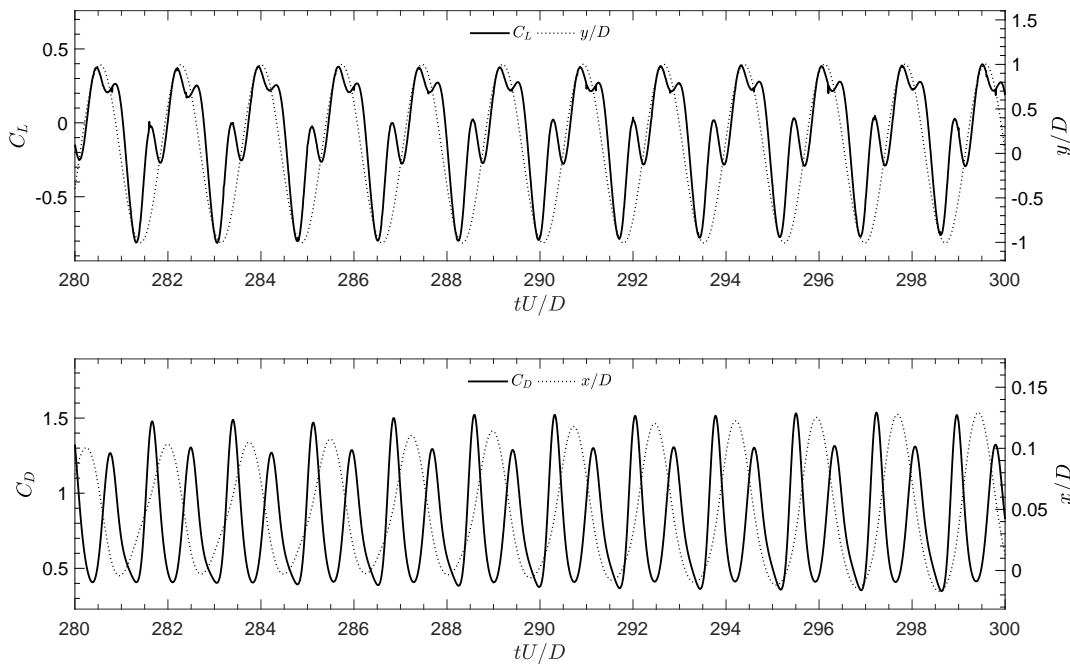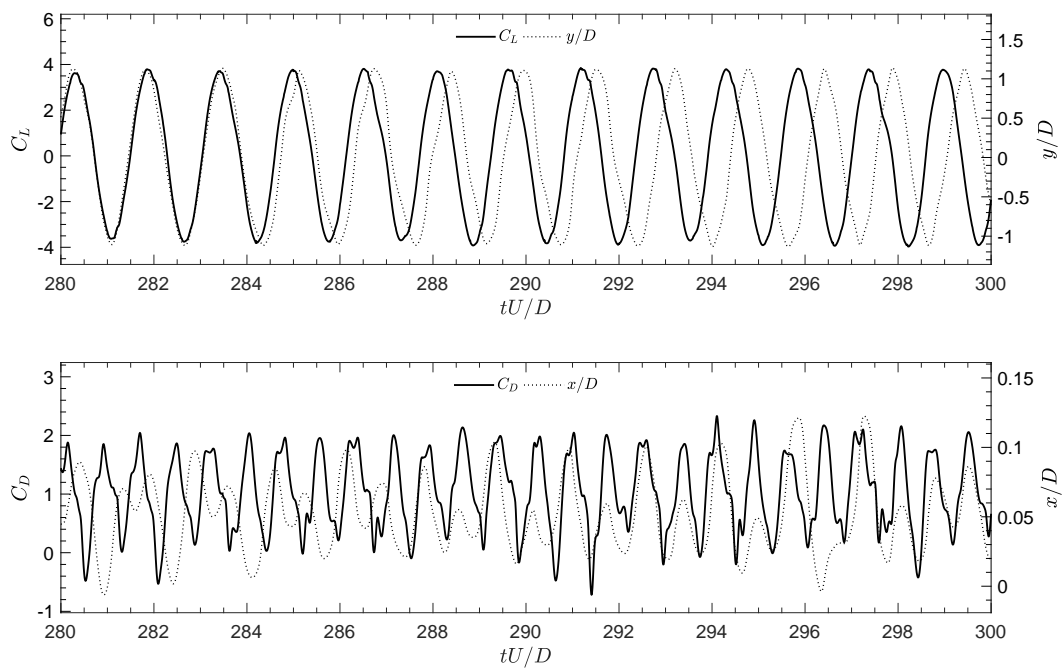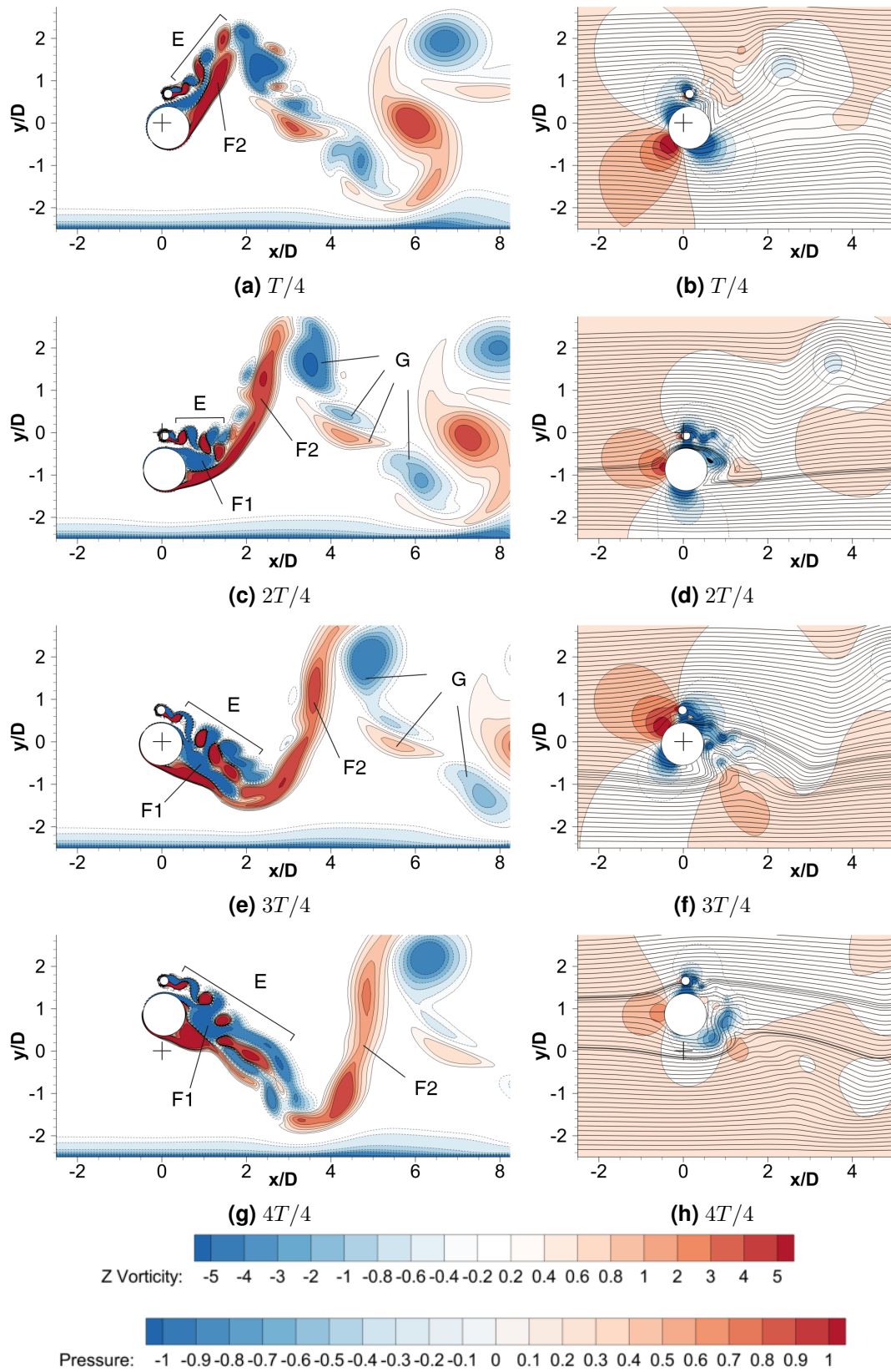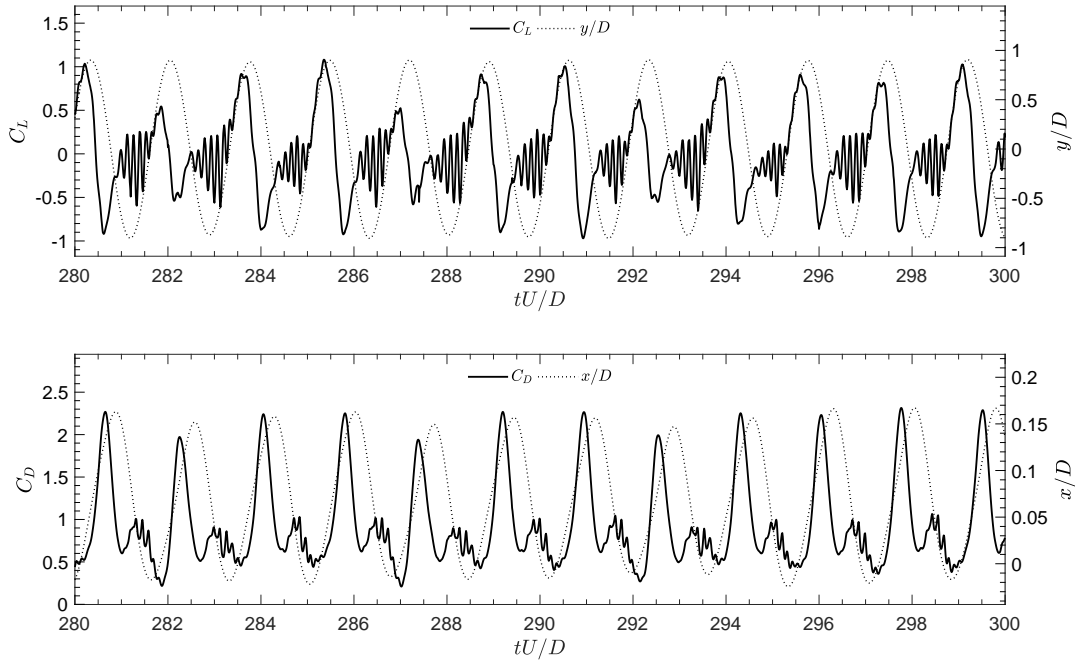
**Figure 6.24:** Time histories of $C_D$, $C_L$, $x/D$ and $y/D$; single cylinder at $U_r = 6$, $Re = 3.6 \times 10^6$.

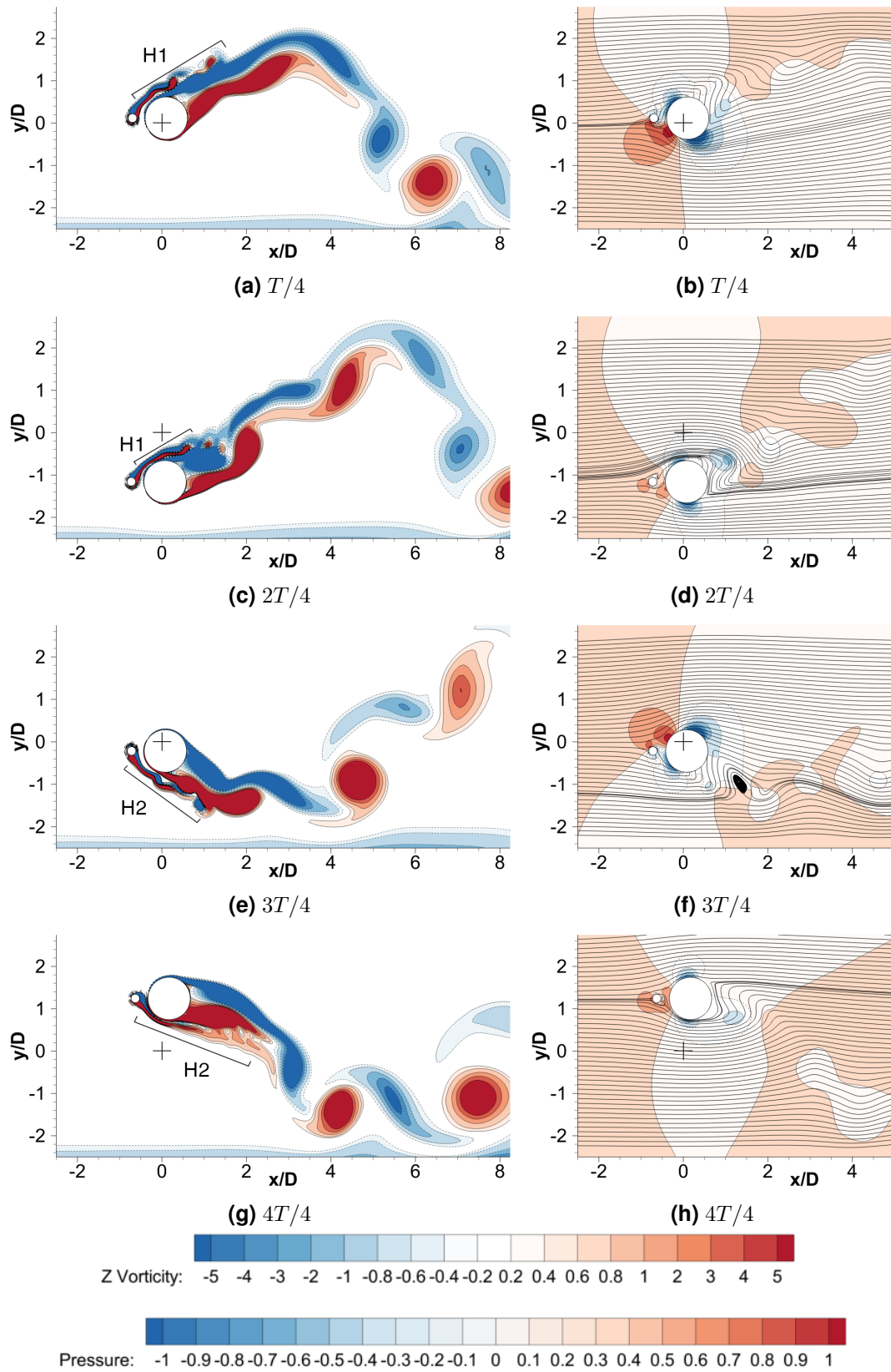leads to a break down of the clockwise vortex (F1) into few smaller vortical structures (G) which can be seen in Fig. 6.30(a) and (c).

The vorticity contours and the pressure contours with streamlines in the $\alpha = 180°$ configuration are presented in Fig. 6.33. In this case, the regular vortex street behind the small cylinder is not formed. Instead, a jet flow in the gap between the cylinders is developed. The jet flow from the gap merges into the top shear layer from the large cylinder (H1 in Fig. 6.33(a) and (c)) in the first half-cycle of the oscillation period and into the bottom shear layer in the second half-cycle of the oscillation period (H2 in Fig. 6.33(e) and (g)). This enhances the shear layers from the large cylinder. From the vorticity contours presented in Fig. 6.33 it is clearly visible that formation length is increased by that mechanism. The time histories of hydrodynamic force coefficients and displacements (Fig. 6.31) show that at $U_r = 10$ the $C_L$ is still in phase with the $y/D$ resulting in the frequency lock-in and large amplitude oscillations. It can be concluded that placement of the small cylinder upstream the large cylinder widens the reduced velocity lock-in regime significantly at this spacing ratio $G/D = 0.2$ and cylinders' diameter ratio $d/D = 0.2$.

**(a)** $T/4$

**(b)** $T/4$

**(c)** $2T/4$

**(d)** $2T/4$

**(e)** $3T/4$

**(f)** $3T/4$

**(g)** $4T/4$

**(h)** $4T/4$

**Figure 6.26:** Vorticity contours (left) and streamlines with normalized pressure contours (right) at selected time instances of one shedding cycle for a coupled cylinders $\alpha = 0°$ at $U_r = 5$.

**Figure 6.27:** Time histories of $C_D$, $C_L$, $x/D$ and $y/D$; coupled cylinders $\alpha = 0°$ at $U_r = 5$, $Re = 3.6 \times 10^6$.

**Figure 6.29:** Vorticity contours (left) and streamlines with normalized pressure contours (right) at selected time instances of one shedding cycle for a coupled cylinders $\alpha = 90°$ at $U_r = 6$.

**Figure 6.30:** Time histories of $C_D$, $C_L$, $x/D$ and $y/D$; coupled cylinders $\alpha = 90°$ at $U_r = 6$, $Re = 3.6 \times 10^6$.
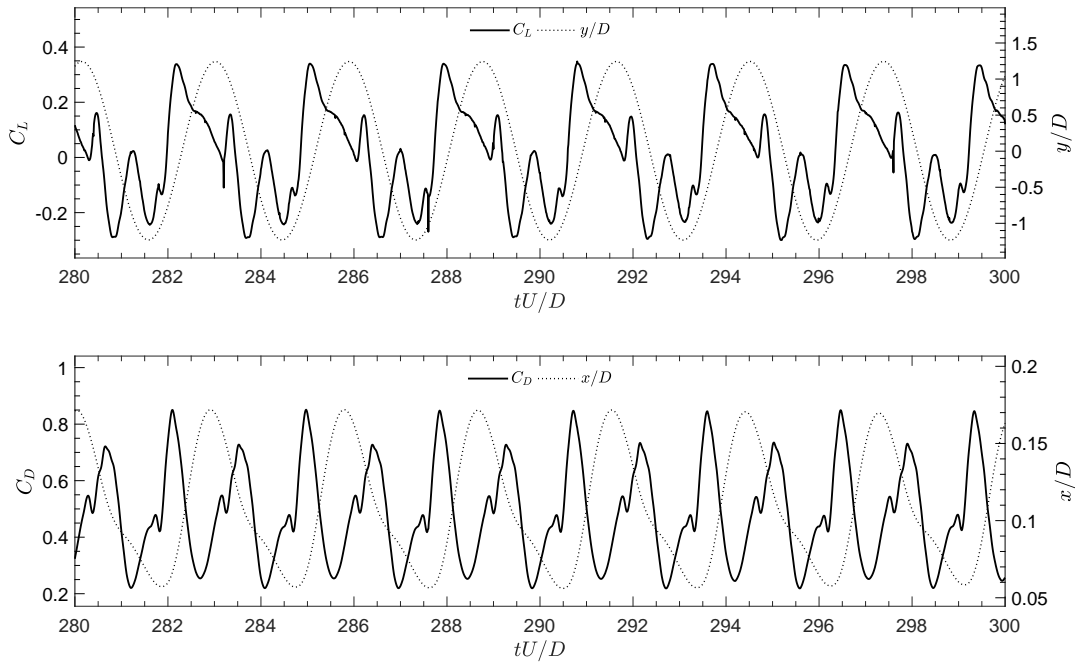


**Figure 6.31:** Time histories of $C_D$, $C_L$, $x/D$ and $y/D$; coupled cylinders $\alpha = 180°$ at $U_r = 10$, $Re = 3.6 \times 10^6$.

**(a)** $T/4$

**(b)** $T/4$

**(c)** $2T/4$

**(d)** $2T/4$

**(e)** $3T/4$

**(f)** $3T/4$

**(g)** $4T/4$

**(h)** $4T/4$

Z Vorticity:  -5  -4  -3  -2  -1  -0.8 -0.6 -0.4 -0.2 0.2 0.4 0.6 0.8 1  2  3  4  5

Pressure:  -1 -0.9 -0.8 -0.7 -0.6 -0.5 -0.4 -0.3 -0.2 -0.1  0  0.1 0.2 0.3 0.4 0.5 0.6 0.7 0.8 0.9 1

**Figure 6.33:** Vorticity contours (left) and streamlines with normalized pressure contours (right) at selected time instances of one shedding cycle for a coupled cylinders $\alpha = 180°$ at $U_r = 10$.

## 6.3  Summary

A series of two-dimensional numerical simulations of vortex-induced vibrations of two circular cylinders with uneven diameters at a Reynolds number of $Re = 3.6 \times 10^6$ near a horizontal plane wall is performed. The k-$\omega$ SST model with a wall function approach is used in the study to predict the effects of the turbulence. Constant mass ratio $m^*$ = 10, gap ratio $e/D = 2$ and spacing ratio between the cylinders $G/D = 0.2$ are kept constant. Position of the small cylinder is varied between the three angles relative to the main cylinder center line ($\alpha = 0°, \alpha = 90°$, and $\alpha = 180°$). The cylinders diameter ratio equals $d/D = 0.2$. The summary of the findings outlined in the present chapter is following:

1. The k-$\omega$ SST model appears to perform reasonably well at $Re = 3.6 \times 10^6$ compared to the experimental and numerical results available in the literature. The $\overline{C}_D$ and $-C_{Pb}$ values show very good agreement with the other numerical studies and fall well within the experimental results range. The $C_L^{rms}$ and $St$ values are at the upper limit of the uncertainty band of the experimental data.

2. At the gap ratio $e/D = 2$ the interaction of the vortices shed from the bottom surface of the large cylinder with the bottom boundary layer leads to the bottom boundary layer roll-up. In the high Reynolds regime, this interaction is shifted away further downstream of the cylinder/coupled cylinders system. The suppression mechanism of the vortex shedding from the bottom surface of the cylinder is present which is confirmed by the streamwise oscillation lock-in and the skewed oval vibration trajectories observed in most of the analyzed cases.

3. The lock-in regime in the case of the single near-wall cylinder is identified approximately at $3 \leq U_r \leq 8$. In the $\alpha = 0°$ configuration the lock-in regime is significantly smaller and is found at $3 \leq U_r \leq 6$. In the $\alpha = 90°$ configuration the lock-in regime is wider than in the single cylinder configuration and is identified at $4 \leq U_r \leq 12$. When the small cylinder is in the $\alpha = 180°$ position, the lock-in regime is the widest among all analyzed configurations and extends beyond the range of reduced velocities considered in the present study: $3 \leq U_r > 12$.

4. The maximum transverse amplitude response $A_{Y,max}/D$ of the single cylinder is recorded at $U_r = 6$ and equals $A_{Y,max}/D = 1.01$. The transverse amplitude response $A_{Y,max}/D$ of coupled cylinders in the $\alpha = 0°$ configuration is larger than that of the single cylinder and is equal $A_{Y,max}/D = 1.15$. The transverse amplitude response $A_{Y,max}/D$ of coupled cylinders in the $\alpha = 180°$ configuration is the largest among

analyzed configurations and is equal $A_{Y,max}/D = 1.23$. The $\alpha = 90°$ configuration shows the smallest transverse amplitude response at $A_{Y,max}/D = 0.92$.

# References

Achenbach, E. (1968). Distribution of local pressure and skin friction around a circular cylinder in cross-flow up to $Re = 5 \times 10^6$. *Journal of Fluid Mechanics 34*, 625 – 639.

Catalano, P., M. Wang, G. Iaccarino, and M. P. (2003). Numerical simulation of the flow around a circular cylinder at high Reynolds numbers. *International Journal of Heat and Fluid Flow 24*, 463 – 469.

Jones, G. W., J. J. Cincotta, and W. W. Robert (1969). Aerodynamic forces on a stationary and oscillating circular cylinder at high Reynolds numbers. Technical Report TR R-300, NASA.

Menter, F. (1994). Two-equation eddy-viscosity turbulence models for engineering applications. *AIAA Journal 32*, 1598 – 1605.

Ong, M. C., T. Utnes, L. E. Holmedal, D. Myrhaug, and B. Pettersen (2010). Numerical simulation of flow around a circular cylinder close to a flat seabed at high Reynolds numbers using a k-$\epsilon$ model. *Coastal Engineering 57*(10), 931 – 947.

Ong, M. C., T. Utnes, L. E. Holmedal, D. Myrhaug, and B. Pettersen (2012). Near-bed flow mechanisms around a circular marine pipeline close to a flat seabed in the subcritical flow regime using a k-$\epsilon$ model. *Journal of Offshore Mechanics and Arctic Engineering 134*, 021803–1 – 021803–11.

Porteous, A., R. Habbit, J. Colmenares, and S. Poroseva (2015, 06). Simulations of incompressible separated turbulent flows around two-dimensional bodies with urans models in openfoam. In *Proc. 22nd AIAA Computational Fluid Dynamics Conference,* pp. 1 – 15. AIAA.

Roshko, A. (1961). Experiments on the flow past a circular cylinder at very high Reynolds number. *Journal of Fluid Mechanics 10*, 345 – 356.

Schewe, G. (1983). On the force fluctuations acting on a circular cylinder in crossflow from subcritical up to transcritical Reynolds numbers. *Journal of Fluid Mechanics 133*, 265 – 285.

Schmidt, L. V. (1966, Jun). Fluctuating force measurements upon a circular cylinder at Reynolds numbers up to $5 \times 10^6$. Technical report, Langley Research Center.

Shih, W. C. L., C. Wang, D. Coles, and A. Roshko (1993). Experiments on flow past rough circular cylinders at large Reynolds numbers. *Journal of Wind Engineering and Industrial Aerodynamics 49*, 351 – 368.

Wen, P. and W. Qiu (2017). Investigation of drag crisis phenomenon using CFD methods. *Applied Ocean Research 67*, 306 – 321.

Zang, Z. and F. Gao (2014). Steady current induced vibration of near-bed piggyback pipelines: Configuration effects on viv suppression. *Applied Ocean Research 46*, 62 – 69.

# CHAPTER 7

# CONCLUSIONS AND RECOMMENDATIONS

In this thesis, a numerical study using CFD package OPENFOAM is performed and validated to predict the vortex-induced vibrations of a single cylinder and three different configurations of coupled cylinders with uneven diameters placed in the proximity of a horizontal plane wall. Suitability of computational models for practical engineering tasks is assessed by considering the computational cost. Two-dimensional computational models are used for the purpose of extensive parametric studies. Numerical studies are conducted in two flow regimes, a laminar vortex street regime at Reynolds number $Re = 200$ and an upper transition regime at $Re = 3.6 \times 10^6$. The unsteady RANS method with k-$\omega$ SST turbulence model is selected to solve for the flow fields in the upper transition regime study.

## 7.1   Conclusions

The conclusions based on the findings presented in Chapters 4, Chapter 5 and Chapter 6 can be formulated as follows:

1. Convergence studies and grid resolution:

   A convergence studies regarding the grid resolution and domain size are conducted in order to set a baseline for the simulations carried out in this thesis. In the laminar study, the wall integration grids resolving the boundary layer are adopted. The first grid spacing is refined so that the wall unit $y^+$ is $\mathcal{O}(1)$ or less. Selected meshes have a density of approximately 70.000 cells. In the high Reynolds number study, the wall functions are used resulting in the $y^+$ requirement of $30 < y^+ < 100$. The meshes selected for the simulations have a similar density to those in the laminar study, approximately 76.000 cells. Such mesh requirement is found to be adequate for the common engineering design tasks and can be used on a modern workstation with multicore CPU within reasonable computation time.

2. Two degree-of-freedom near wall VIV in laminar vortex street regime:

   - The results show that the wall proximity enlarges the mean lift force but the influence on the mean drag force is minimal.

   - Proximity of the wall strongly enhances the streamwise response of a cylinder. Analysis of the phase relations between the drag force and the streamwise displacement reveals two distinct phases in the lock-in regime. The phase of the positive net energy transfer from the fluid to the structure and phase of the negative energy transfer when the energy is dissipated by the fluid. The first phase is found to coincide with the pre-lock-in regime and the initial branch of the lock-in. The second phase is identified in the lower branch of the lock-in regime.

   - Study of the vortex shedding mechanism shows that the bottom shear layer vorticity counteracts the vortices shed from the bottom surface of the cylinder leading to the asymmetry of the wake. This, in turn, reduces the streamwise oscillation frequency by half and is the reason for the streamwise frequency lock-in.

   - The lock-in regime in the case of the single near-wall cylinder is observed at $3.6 \leq U_r \leq 6$. In the $\alpha = 180°$ configuration of coupled cylinders the lock-in regime is comparable to that of the single cylinder and is observed at $3 \leq U_r \leq 6$. In the $\alpha = 90°$ configuration the lock-in regime is wider than in the single cylinder configuration and is observed at $3 \leq U_r \leq 7$. In the $\alpha = 0°$ configuration the lock-

in regime is the widest among all analyzed configurations and extends beyond the range of reduced velocities considered in this numerical study: $3 \leq U_r > 12$.

- The maximum transverse amplitude response $A_{Y,max}/D$ of the single cylinder is observed at $U_r = 4$ and is equal $A_{Y,max}/D = 0.58$. The transverse amplitude responses $A_{Y,max}/D$ of coupled cylinders are smaller than that of the single cylinder. In the $\alpha = 0°$ configuration the transverse amplitude response is equal $A_{Y,max}/D = 0.55$. In the $\alpha = 90°$ configuration the transverse amplitude response is equal $A_{Y,max}/D = 0.53$. When the small cylinder is placed at $\alpha = 180°$ position the maximum transverse amplitude response is equal $A_{Y,max}/D = 0.43$.

3. Two degree-of-freedom near wall VIV in upper transition regime:

- The k-$\omega$ SST model appears to perform reasonably well at $Re = 3.6 \times 10^6$ compared to the experimental and numerical results available in the literature. The $\overline{C}_D$ and $-C_{Pb}$ values show very good agreement with the other numerical studies and fall well within the experimental results range. The $C_L^{rms}$ and $St$ values are at the upper limit of the uncertainty band of the experimental data.

- At a gap ratio $e/D = 2$ the interaction of the vortices shed from the bottom surface of the large cylinder with the bottom boundary layer leads to the bottom boundary layer roll-up. In the high Reynolds regime, this interaction is shifted away further downstream of the cylinder/coupled cylinders system. The suppression mechanism of the vortex shedding from the bottom surface of the cylinder is present which is confirmed by the streamwise oscillation lock-in and the skewed oval vibration trajectories observed in most of the analyzed cases.

- The lock-in regime in the case of the single near-wall cylinder is observed approximately at $3 \leq U_r \leq 8$. In the $\alpha = 0°$ configuration the lock-in regime is significantly smaller and is found at $3 \leq U_r \leq 6$. In the $\alpha = 90°$ configuration the lock-in regime is wider than in the single cylinder configuration and is observed at $4 \leq U_r \leq 12$. When the small cylinder is in the $\alpha = 180°$ position the lock-in regime is the widest among all analyzed configurations and extends beyond the range of reduced velocities considered in the present study: $3 \leq U_r > 12$.

- The maximum transverse amplitude response $A_{Y,max}/D$ of the single cylinder is observed at $U_r = 6$ and is equal $A_{Y,max}/D = 1.01$. The transverse amplitude response $A_{Y,max}/D$ of coupled cylinders in the $\alpha = 0°$ configuration is larger than that of the single cylinder and is equal $A_{Y,max}/D = 1.15$. The transverse amplitude response $A_{Y,max}/D$ of coupled cylinders in the $\alpha = 180°$ configuration is the largest among analyzed configurations and is equal $A_{Y,max}/D = 1.23$.

The $\alpha = 90°$ configuration shows the smallest transverse amplitude response at $A_{Y,max}/D = 0.92$.

## 7.2  Recommendations for Future Work

The following list describes some ideas for future work:

1. Study on VIV of a near-wall cylinder using LES turbulence model at $Re = 3.6 \times 10^6$. More numerical studies, preferably with eddy resolving turbulence modeling focused on very high Reynolds number flows could decrease the knowledge gap on the near-wall VIV in this regime.

2. Study on the applicability of two-dimensional CFD model on VIV prediction in the critical regime using transitional turbulence modeling (e.g. k-kl-$\omega$ model by Walters and Cokljat(2008), $\gamma - Re - \theta$ model by Langtry and Menter(2009), $k - \omega - v^2$ model by Lopez and Walters(2016)). The ability to resolve the drag crisis phenomenon should be investigated.

3. Study on VIV of multiple bodies with uncoupled motion in two-degrees-of-freedom. This could include parametric studies on the spacing and different configurations and their influence on the vortex shedding.

# APPENDIX A

# RESULTS OF SIMULATIONS IN LAMINAR VORTEX STREET REGIME

This appendix provides the results of simulations of 2DoF VIV of a single cylinder in laminar vortex street regime at $Re = 200$. Details of the computational setup are provided in Chapter 4.

## A.1 Time histories of $C_D$, $C_L$, $X/D$ and $Y/D$ and power spectral analysis. Single cylinder at $Re = 200$, $e/D = 0.9$
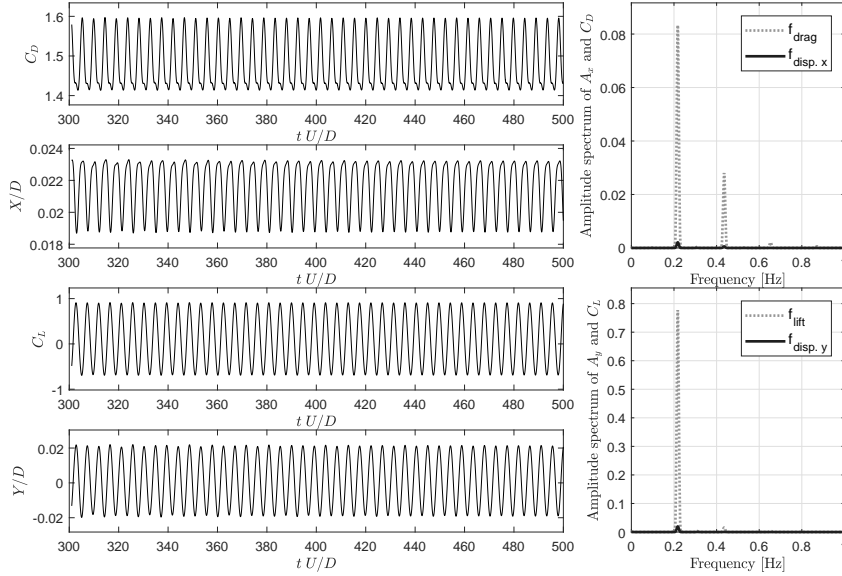


**Figure A.1:** Time histories ($tU/D = 250 - 500$) of $C_D$, $C_L$, $X/D$ and $Y/D$ and power spectral analysis. Near-wall cylinder ($e/D = 0.9$) at $U_r = 3.0$ and $Re = 200$.
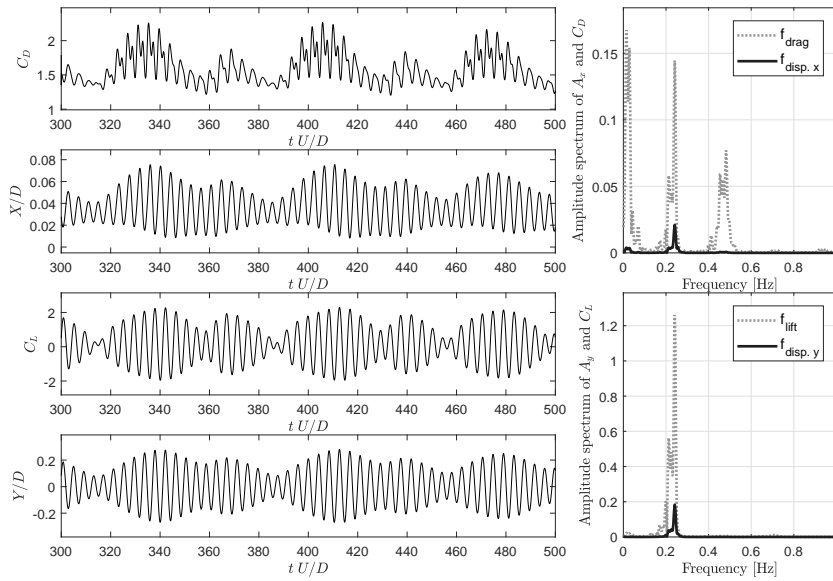


**Figure A.2:** Time histories ($tU/D = 250 - 500$) of $C_D$, $C_L$, $X/D$ and $Y/D$ and power spectral analysis. Near-wall cylinder ($e/D = 0.9$) at $U_r = 3.8$ and $Re = 200$.
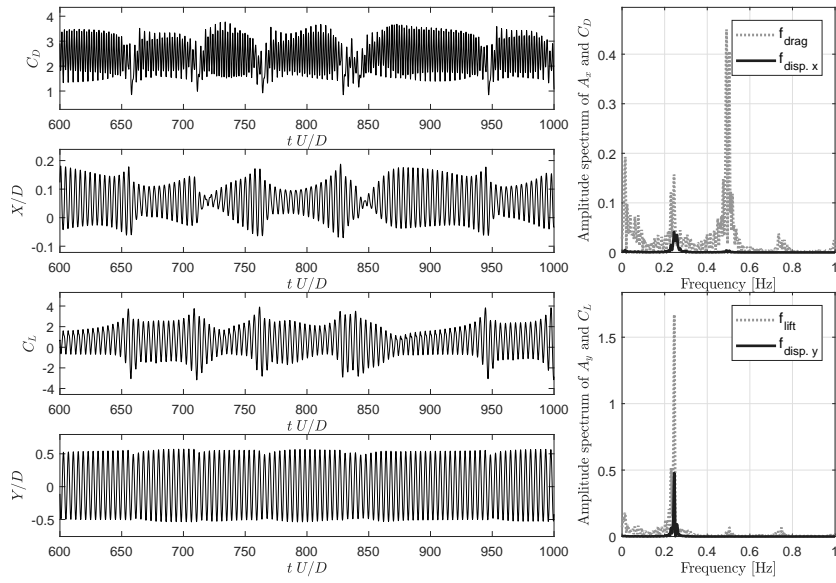
**Figure A.3:** Time histories ($tU/D = 250 - 500$) of $C_D$, $C_L$, $X/D$ and $Y/D$ and power spectral analysis. Near-wall cylinder ($e/D = 0.9$) at $U_r = 3.9$ and $Re = 200$.
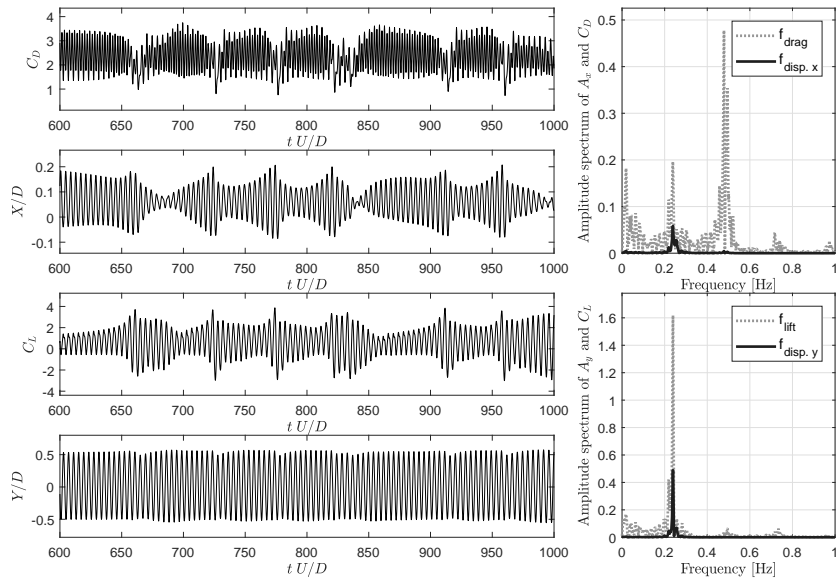


**Figure A.4:** Time histories ($tU/D = 250 - 500$) of $C_D$, $C_L$, $X/D$ and $Y/D$ and power spectral analysis. Near-wall cylinder ($e/D = 0.9$) at $U_r = 4.0$ and $Re = 200$.
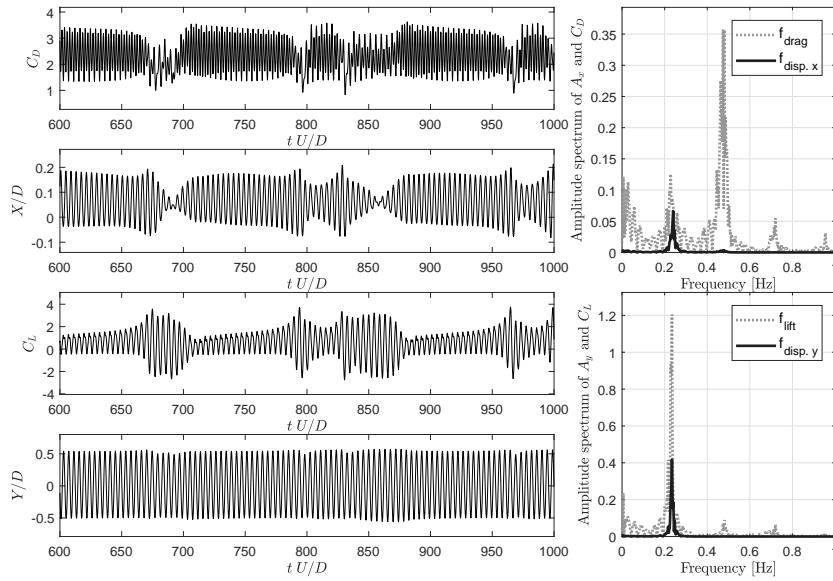
**Figure A.5:** Time histories ($tU/D = 250 - 500$) of $C_D$, $C_L$, $X/D$ and $Y/D$ and power spectral analysis. Near-wall cylinder ($e/D = 0.9$) at $U_r = 4.1$ and $Re = 200$.
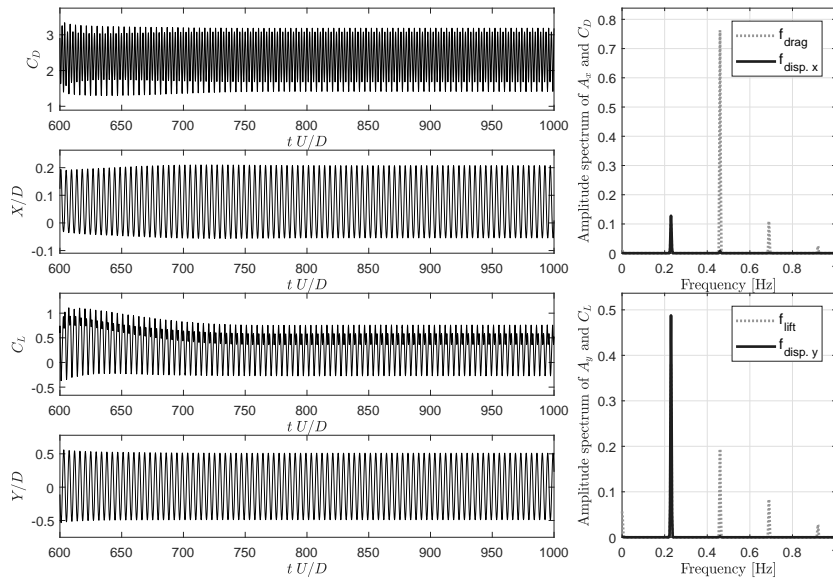


**Figure A.6:** Time histories ($tU/D = 250 - 500$) of $C_D$, $C_L$, $X/D$ and $Y/D$ and power spectral analysis. Near-wall cylinder ($e/D = 0.9$) at $U_r = 4.3$ and $Re = 200$.
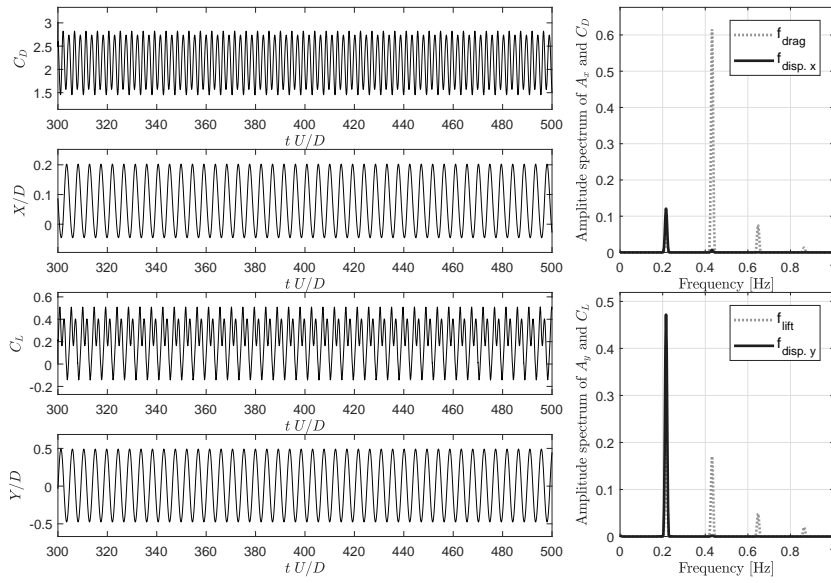
**Figure A.7:** Time histories ($tU/D = 250 - 500$) of $C_D$, $C_L$, $X/D$ and $Y/D$ and power spectral analysis. Near-wall cylinder ($e/D = 0.9$) at $U_r = 4.6$ and $Re = 200$.
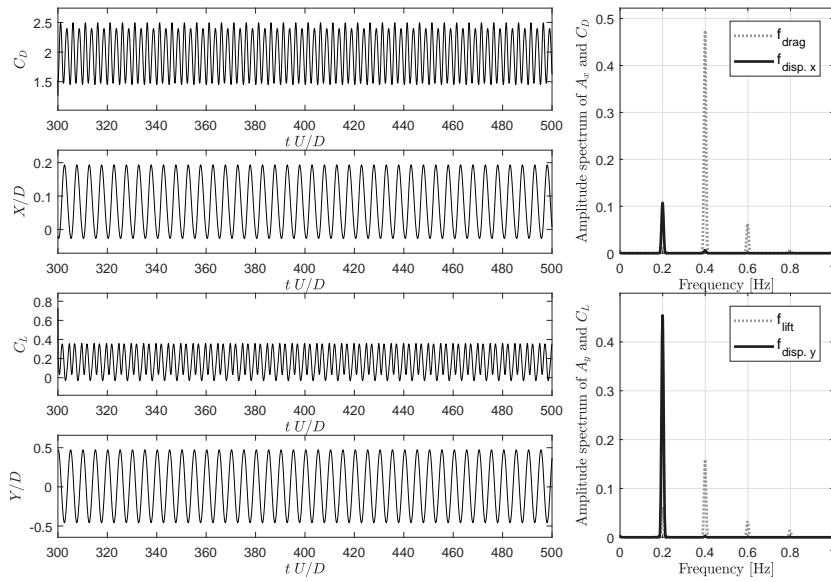


**Figure A.8:** Time histories ($tU/D = 250 - 500$) of $C_D$, $C_L$, $X/D$ and $Y/D$ and power spectral analysis. Near-wall cylinder ($e/D = 0.9$) at $U_r = 5.0$ and $Re = 200$.
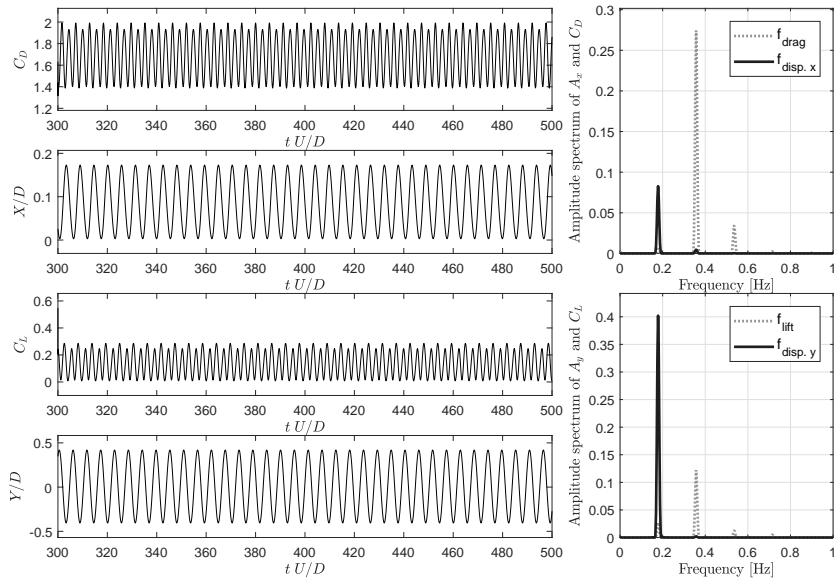
**Figure A.9:** Time histories ($tU/D = 250 - 500$) of $C_D$, $C_L$, $X/D$ and $Y/D$ and power spectral analysis. Near-wall cylinder ($e/D = 0.9$) at $U_r = 5.6$ and $Re = 200$.
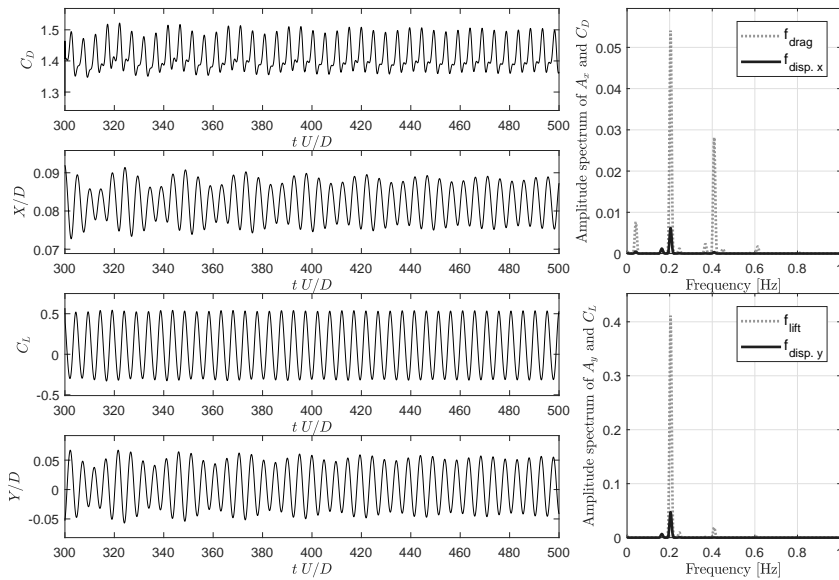


**Figure A.10:** Time histories ($tU/D = 250 - 500$) of $C_D$, $C_L$, $X/D$ and $Y/D$ and power spectral analysis. Near-wall cylinder ($e/D = 0.9$) at $U_r = 6.0$ and $Re = 200$.
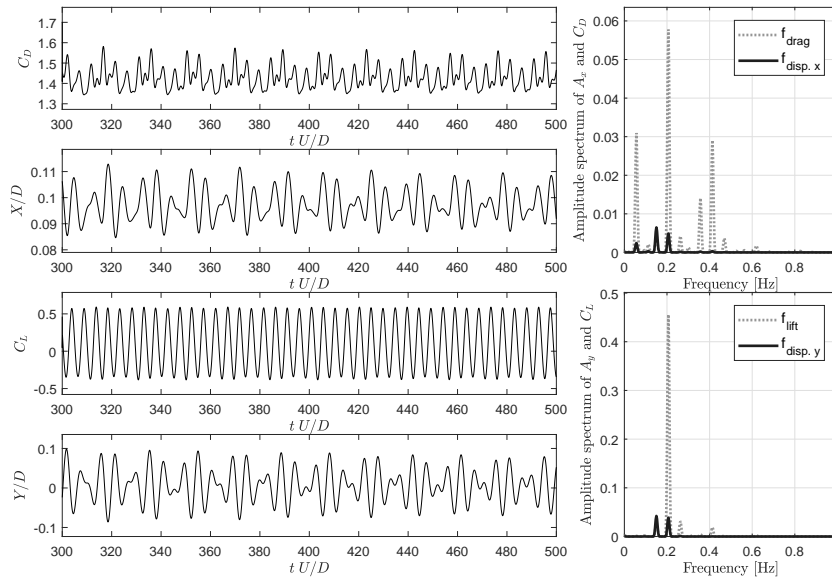
**Figure A.11:** Time histories ($tU/D = 250 - 500$) of $C_D$, $C_L$, $X/D$ and $Y/D$ and power spectral analysis. Near-wall cylinder ($e/D = 0.9$) at $U_r = 6.5$ and $Re = 200$.
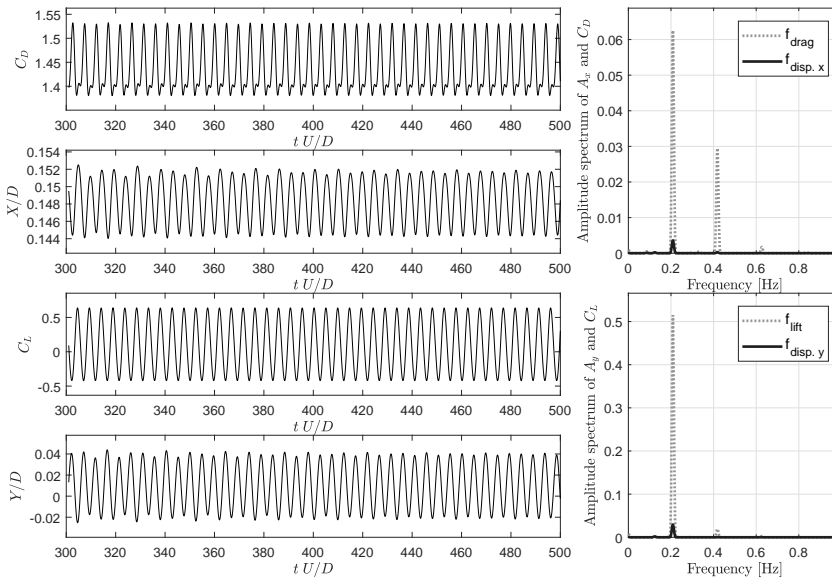


**Figure A.12:** Time histories ($tU/D = 250 - 500$) of $C_D$, $C_L$, $X/D$ and $Y/D$ and power spectral analysis. Near-wall cylinder ($e/D = 0.9$) at $U_r = 8.0$ and $Re = 200$.

# APPENDIX B

# RESULTS OF SIMULATIONS IN
# UPPER TRANSITION REGIME

This appendix provides the results of simulations of 2DoF VIV of a single cylinder and three considered configurations of coupled cylinders with uneven diameters in upper transition regime at $Re = 3.6 \times 10^6$. Details of the computational setup are provided in Chapter 6.

## B.1 Time histories of streamwise displacement $x/D$, cross-flow displacement $y/D$, drag coefficient $C_D$ and lift coefficient $C_L$ at investigated reduced velocities $U_r$



**(a)** $U_r = 3$

**(b)** $U_r = 4$
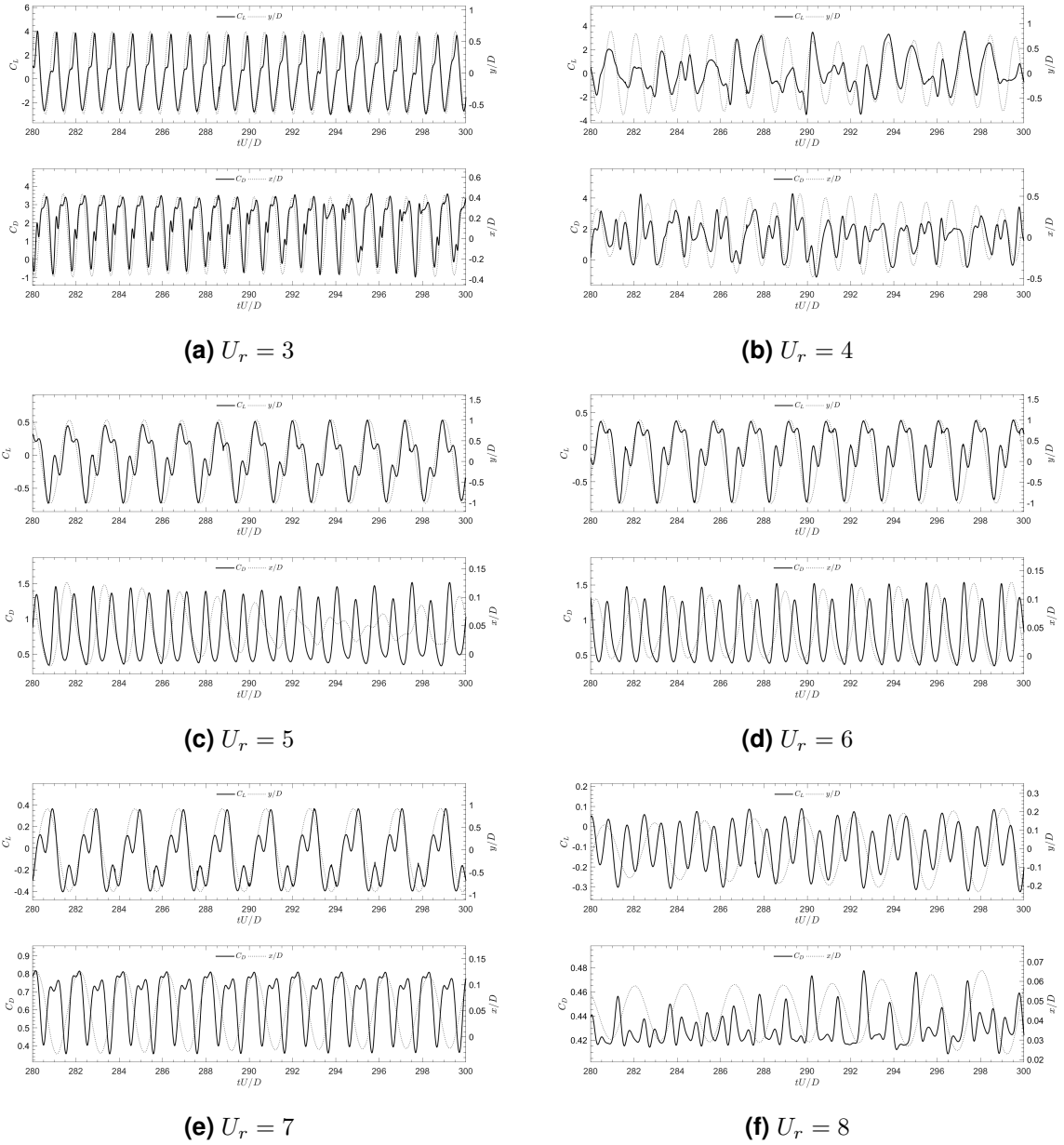
**(c)** $U_r = 5$

**(d)** $U_r = 6$

**(e)** $U_r = 7$

**(f)** $U_r = 8$

**Figure B.1:** Single cylinder; $e/D = 2.0$; $Re = 3.6 \times 10^6$; $U_r = 3 - 8$.
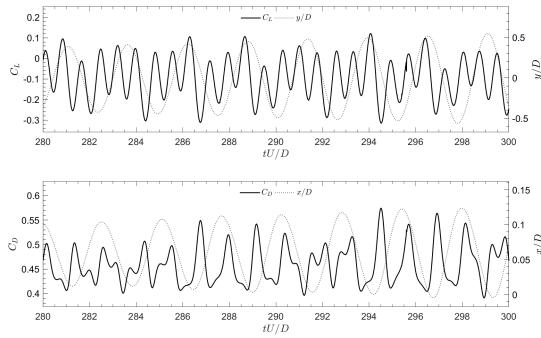
**(a)** $U_r = 9$
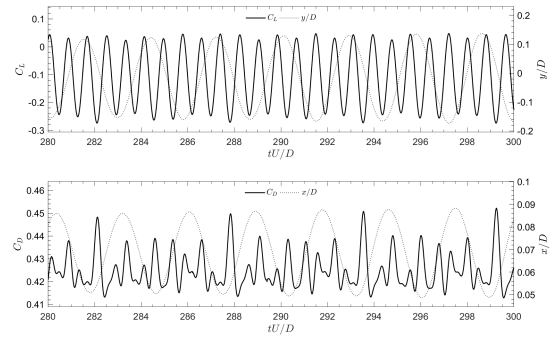
**(b)** $U_r = 10$
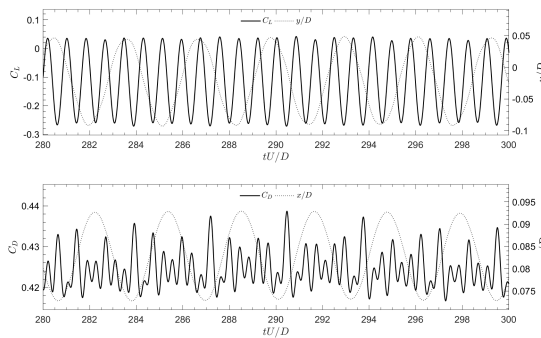
**(c)** $U_r = 11$
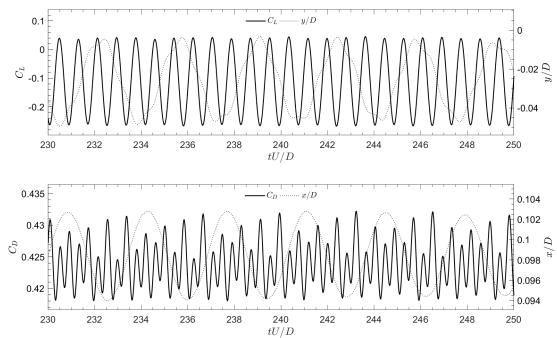
**(d)** $U_r = 12$

**Figure B.2:** Single cylinder; $e/D = 2.0$; $Re = 3.6 \times 10^6$; $U_r = 9 - 12$.
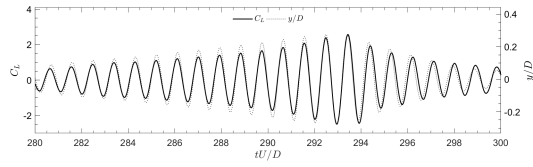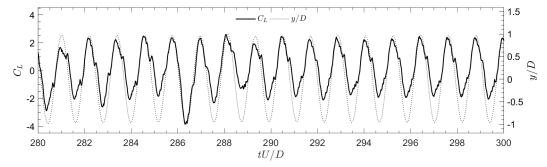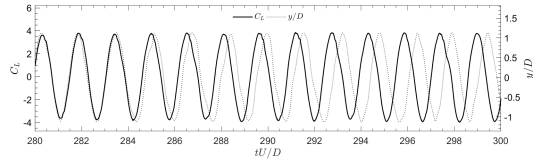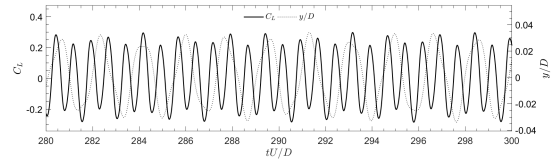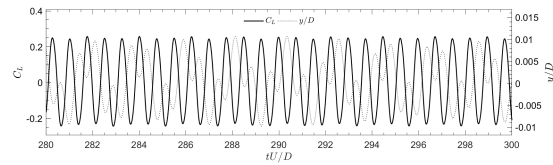
**(a)** $U_r = 3$
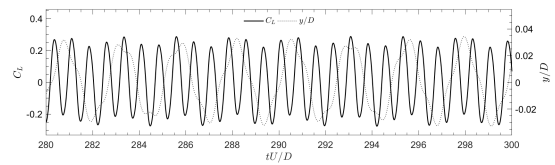
**(b)** $U_r = 4$

**(c)** $U_r = 5$

**(d)** $U_r = 6$

**(e)** $U_r = 7$

**(f)** $U_r = 8$

**Figure B.3:** Coupled cylinders $\alpha = 0°$; $e/D = 2.0$; $Re = 3.6 \times 10^6$; $U_r = 3 - 8$.

**(a)** $U_r = 3$

**(b)** $U_r = 4$
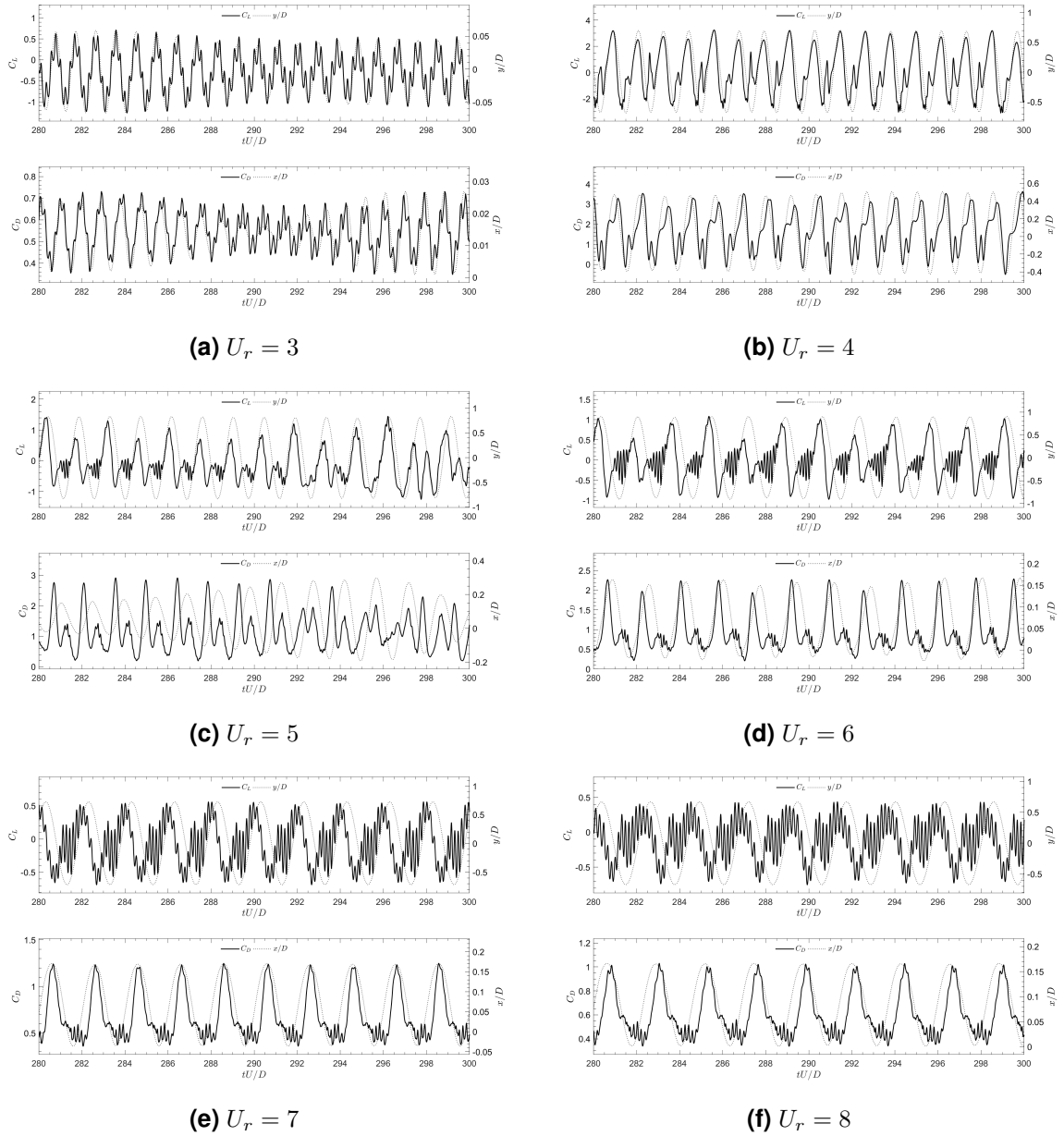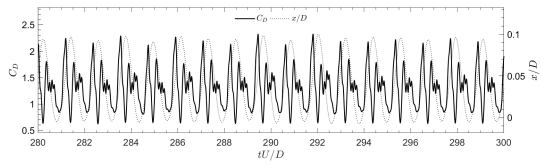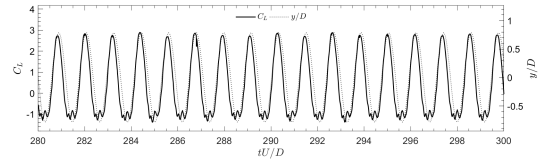
**(c)** $U_r = 5$

**(d)** $U_r = 6$

**(e)** $U_r = 7$

**(f)** $U_r = 8$

**Figure B.4:** Coupled cylinders $\alpha = 90°$; $e/D = 2.0$; $Re = 3.6 \times 10^6$; $U_r = 3 - 8$.

**(a)** $U_r = 9$



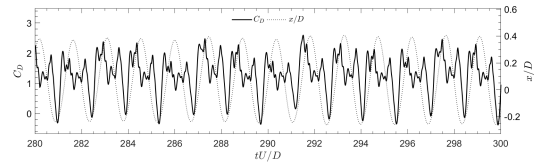**(b)** $U_r = 10$



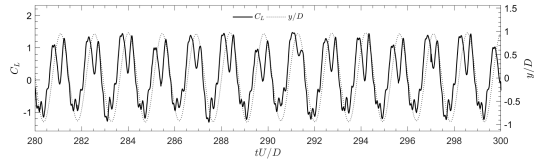**(c)** $U_r = 11$



**(d)** $U_r = 12$
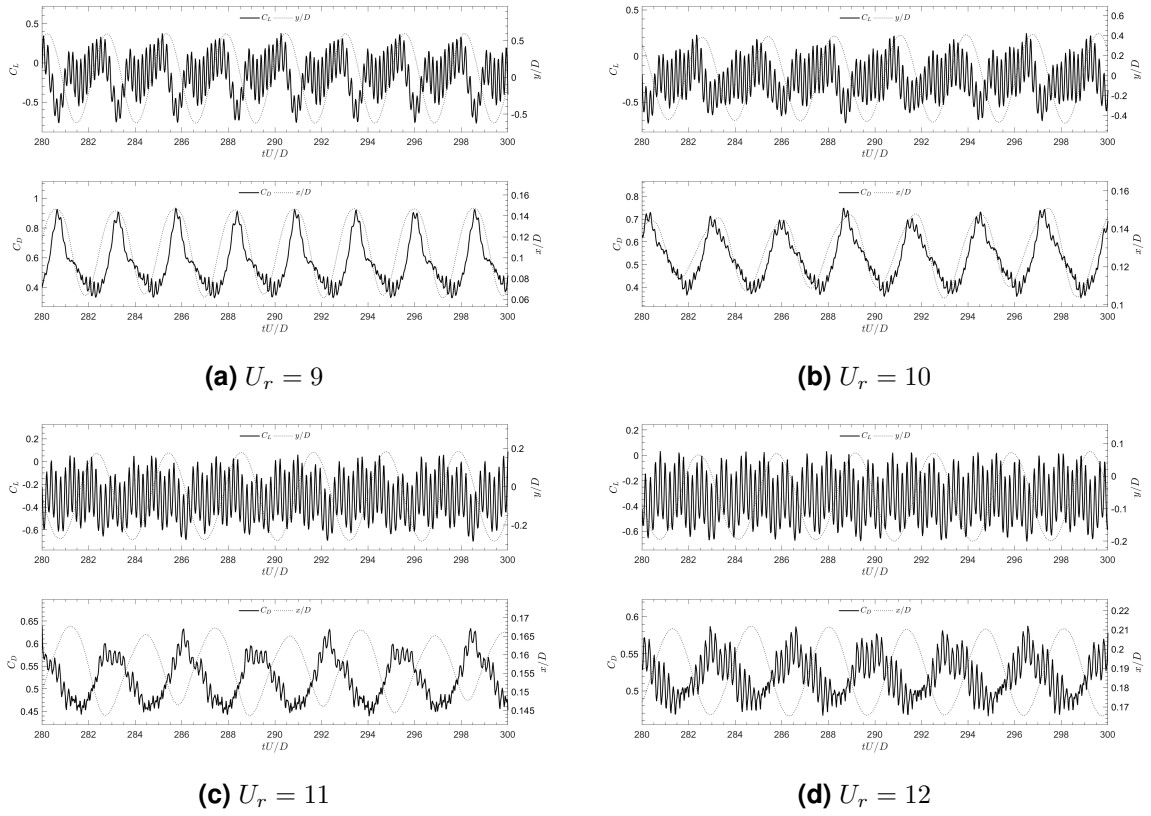
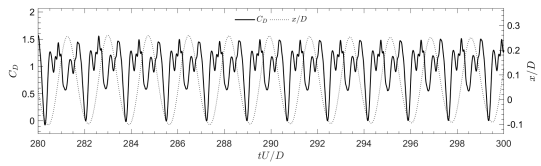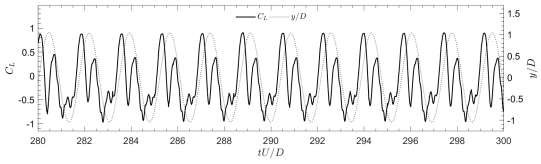**Figure B.5:** Coupled cylinders $\alpha = 90°$; $e/D = 2.0$; $Re = 3.6 \times 10^6$; $U_r = 9 - 12$.
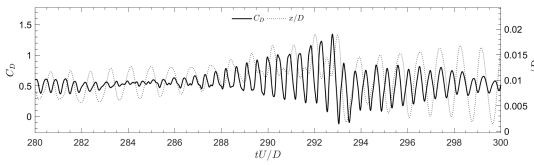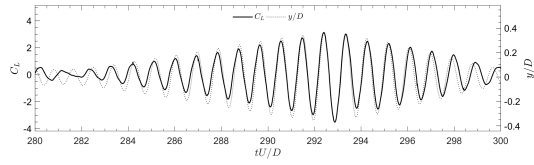
**(a)** $U_r = 3$

**(b)** $U_r = 4$

**(c)** $U_r = 5$

**(d)** $U_r = 6$
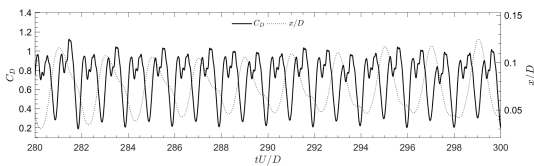
**(e)** $U_r = 7$
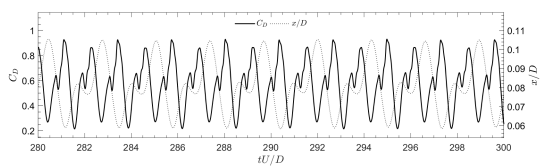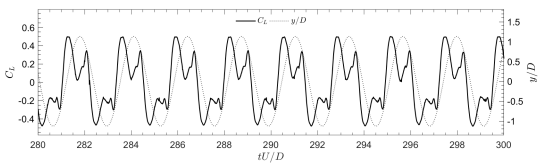
**(f)** $U_r = 8$

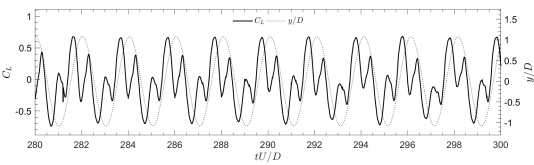**Figure B.6:** Coupled cylinders $\alpha = 180°$; $e/D = 2.0$; $Re = 3.6 \times 10^6$; $U_r = 3 - 8$.

**(a)** $U_r = 9$



**(b)** $U_r = 10$



**(c)** $U_r = 11$



**(d)** $U_r = 12$
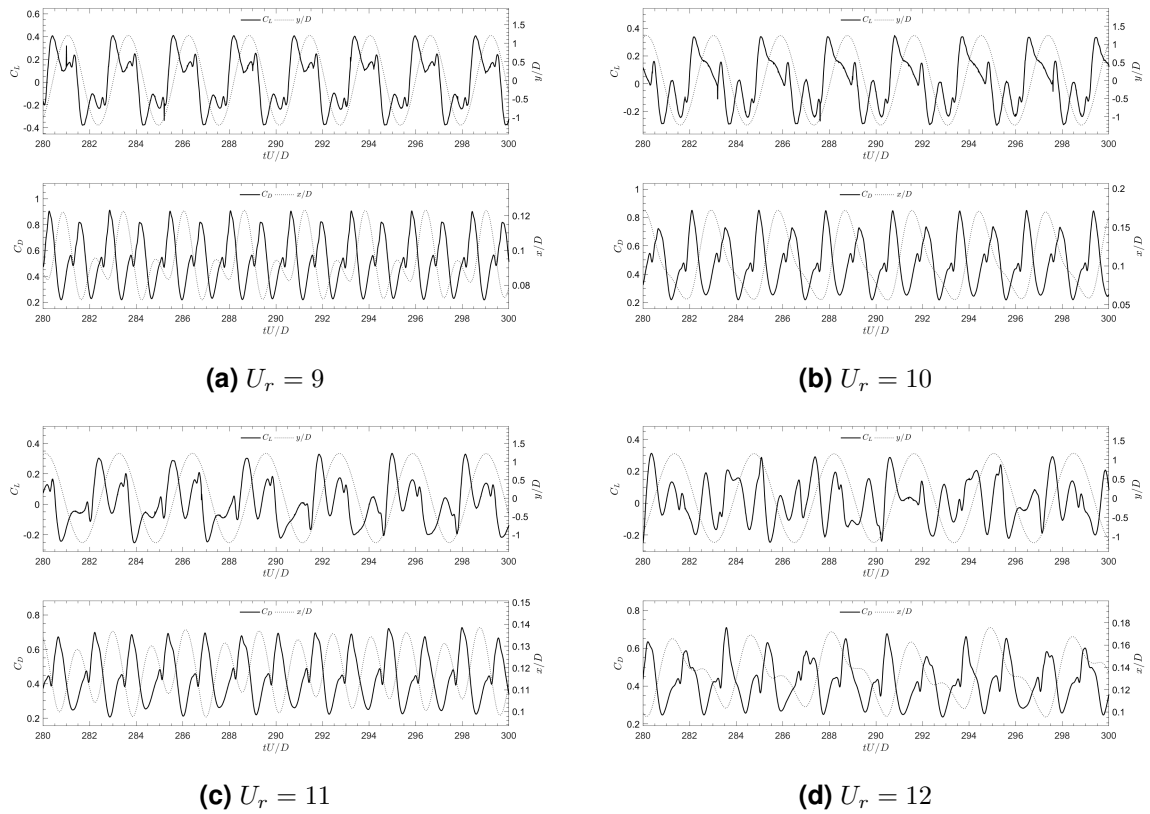
**Figure B.7:** Coupled cylinders $\alpha = 180°$; $e/D = 2.0$; $Re = 3.6 \times 10^6$; $U_r = 9 - 12$.

## B.2    Fast Fourier Transform of transverse displacement $y/D$ and lift coefficient $C_L$ at investigated reduced velocities $U_r$



**Figure B.8:** Single cylinder; $e/D = 2.0$; $Re = 3.6 \times 10^6$; $U_r = 3 - 12$.
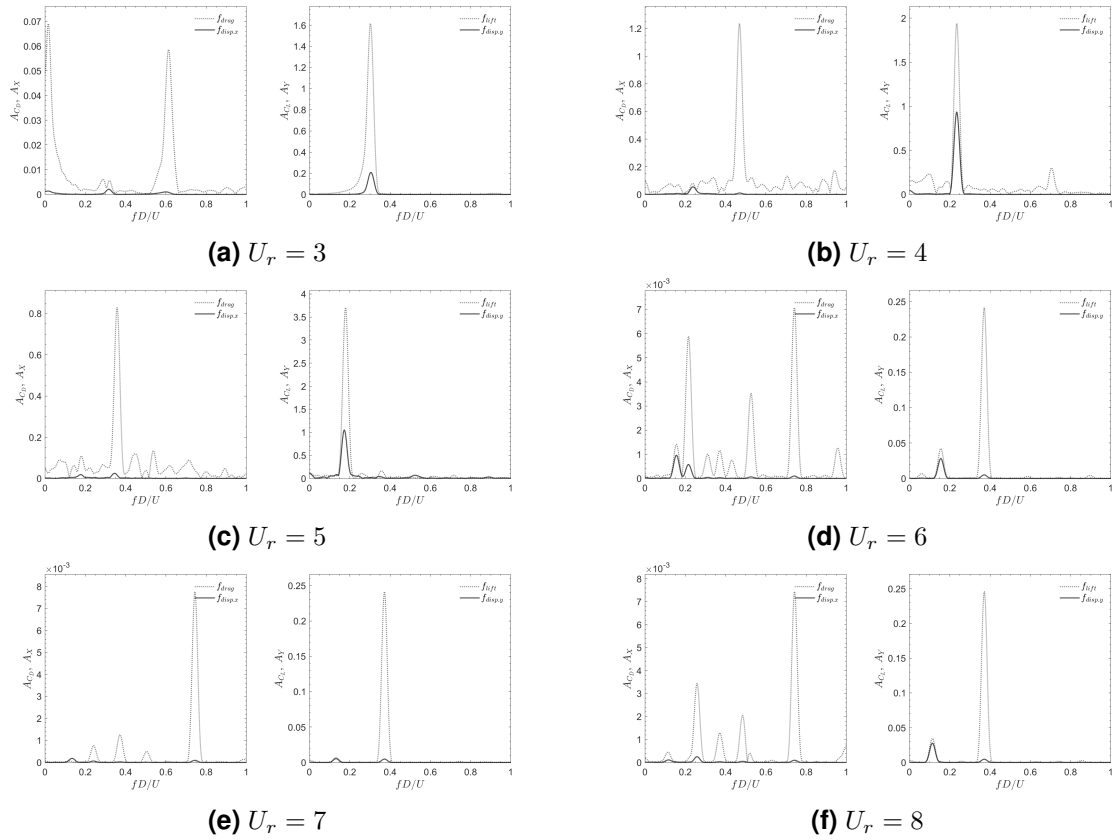
**Figure B.9:** Coupled cylinders $\alpha = 0°$; $e/D = 2.0$; $Re = 3.6 \times 10^6$; $U_r = 3 - 12$.

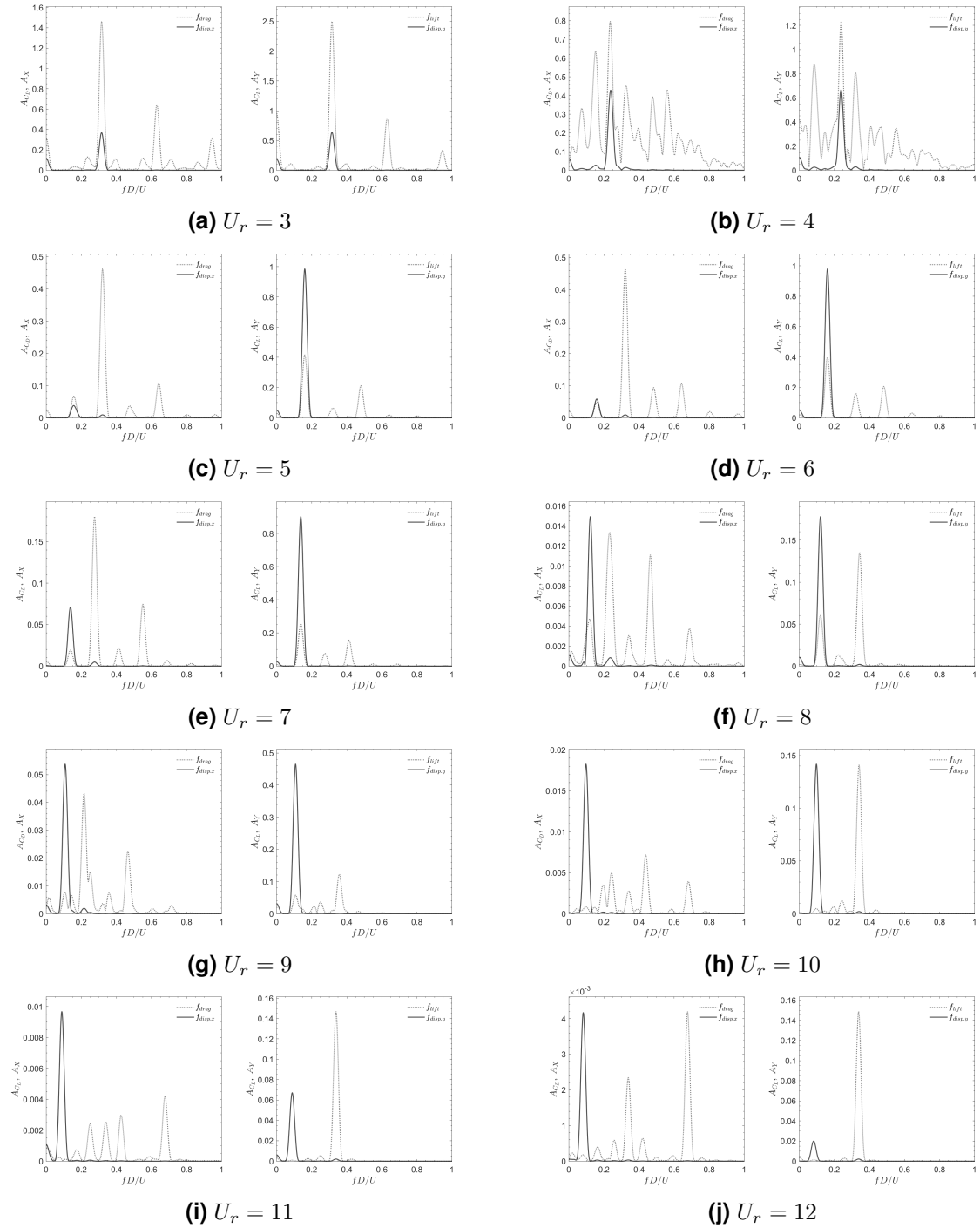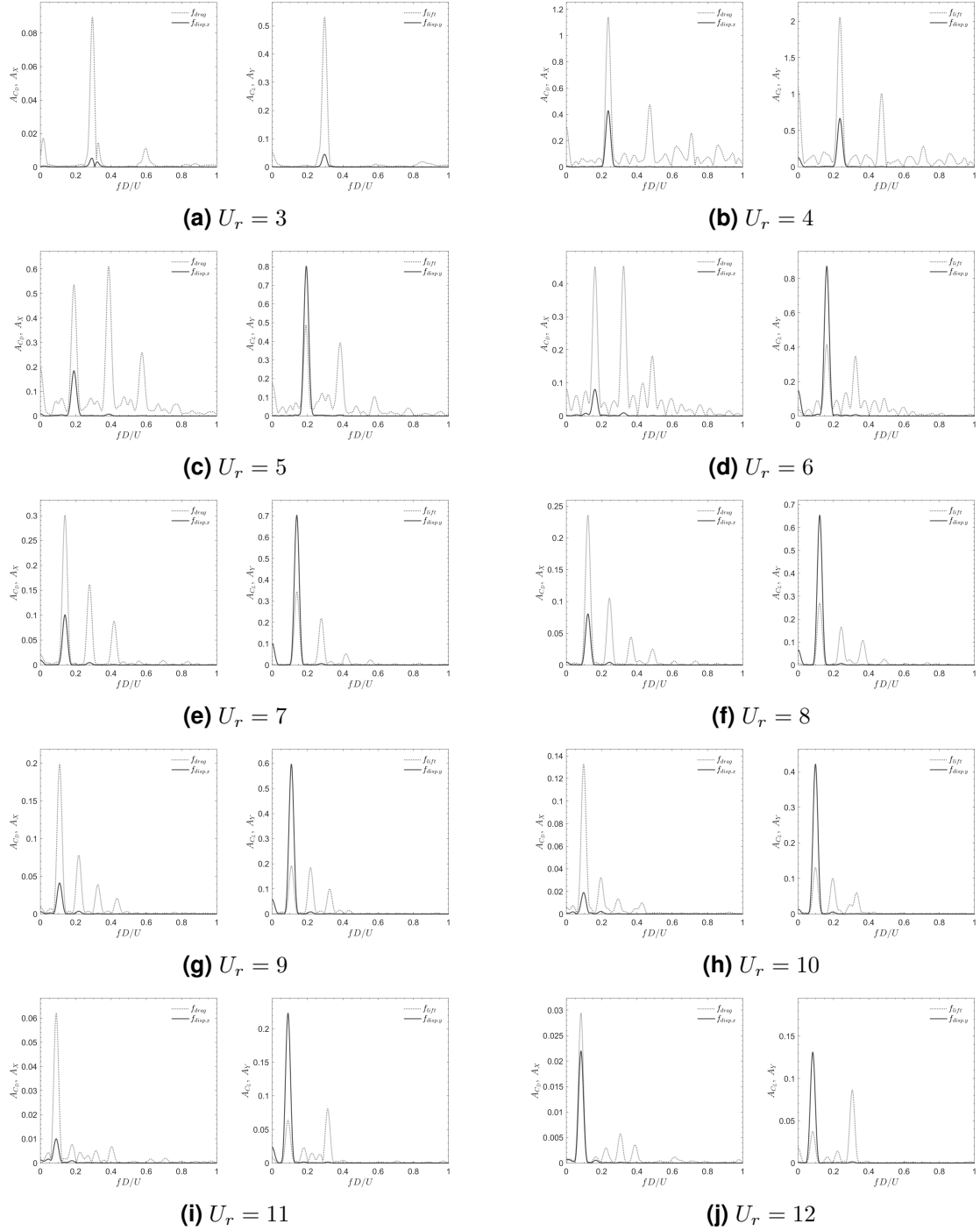**Figure B.10:** Coupled cylinders $\alpha = 90°$; $e/D = 2.0$; $Re = 3.6 \times 10^6$; $U_r = 3 - 12$.
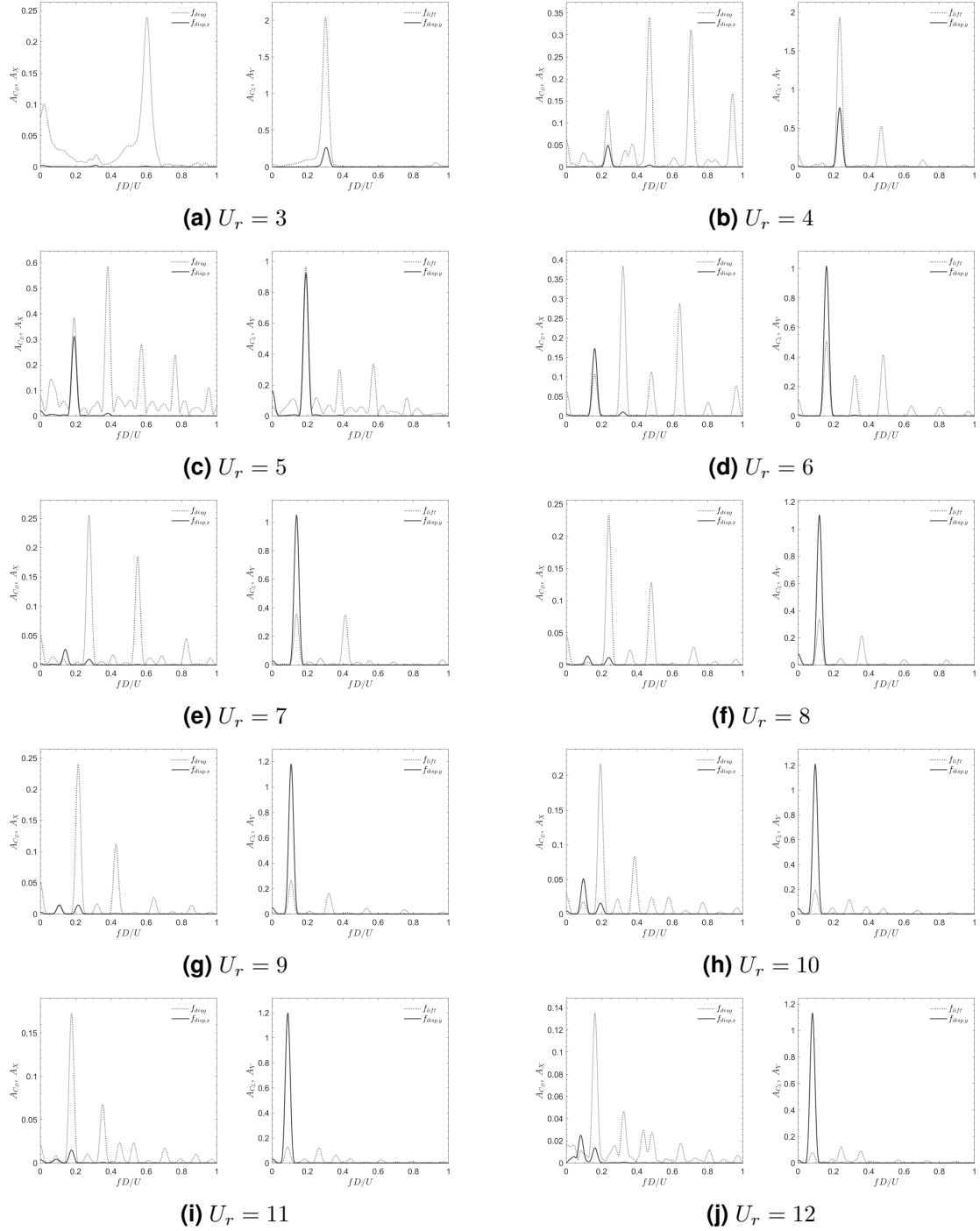
**Figure B.11:** Coupled cylinders $\alpha = 180°$; $e/D = 2.0$; $Re = 3.6 \times 10^6$; $U_r = 3 - 12$.

## B.3 Phase pictures of lift coefficient $C_L$ and transverse displacement $y/D$,and $X-Y$ trajectory plots at investigated reduced velocities $U_r$



**(a)** $\phi_{C_L-Y}$ at $U_r = 3$    **(b)** Trajectory at $U_r = 3$    **(c)** $\phi_{C_L-Y}$ at $U_r = 4$    **(d)** Trajectory at $U_r = 4$

**(e)** $\phi_{C_L-Y}$ at $U_r = 5$    **(f)** Trajectory at $U_r = 5$    **(g)** $\phi_{C_L-Y}$ at $U_r = 6$    **(h)** Trajectory at $U_r = 6$

**(i)** $\phi_{C_L-Y}$ at $U_r = 7$    **(j)** Trajectory at $U_r = 7$    **(k)** $\phi_{C_L-Y}$ at $U_r = 8$    **(l)** Trajectory at $U_r = 8$

**(m)** $\phi_{C_L-Y}$ at $U_r = 9$    **(n)** Trajectory at $U_r = 9$    **(o)** $\phi_{C_L-Y}$ at $U_r = 10$    **(p)** Trajectory at $U_r = 10$
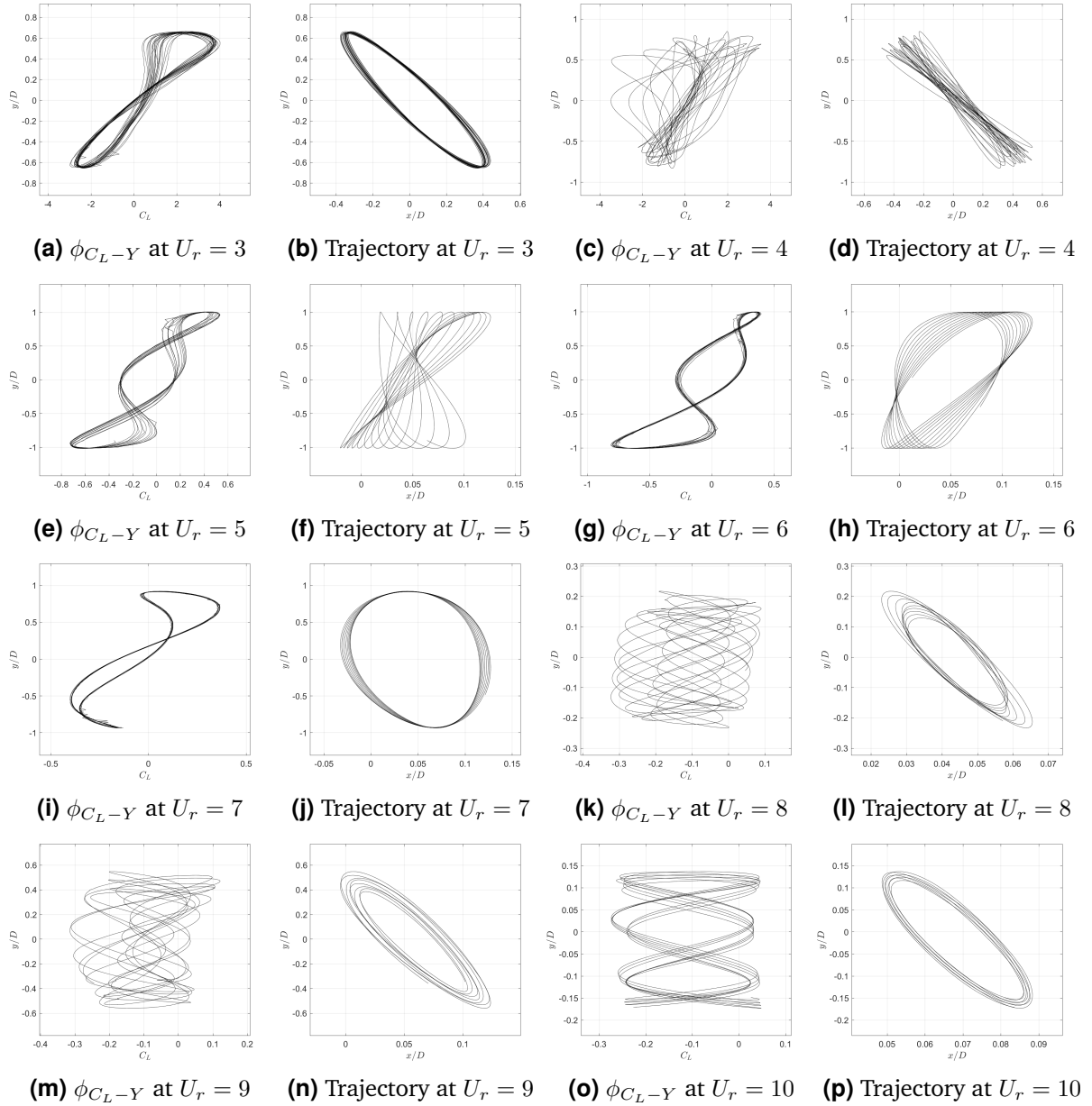
**Figure B.12:** $X-Y$ trajectories and phase pictures ($\phi_{C_L-Y}$) of $C_L$ and $y/D$; single cylinder $e/D = 2.0$; $Re = 3.6 \times 10^6$; $U_r = 3-10$.

**(a)** $\phi_{C_L-Y}$ at $U_r = 3$    **(b)** Trajectory at $U_r = 3$    **(c)** $\phi_{C_L-Y}$ at $U_r = 4$    **(d)** Trajectory at $U_r = 4$

**(e)** $\phi_{C_L-Y}$ at $U_r = 5$    **(f)** Trajectory at $U_r = 5$    **(g)** $\phi_{C_L-Y}$ at $U_r = 6$    **(h)** Trajectory at $U_r = 6$

**(i)** $\phi_{C_L-Y}$ at $U_r = 7$    **(j)** Trajectory at $U_r = 7$    **(k)** $\phi_{C_L-Y}$ at $U_r = 8$    **(l)** Trajectory at $U_r = 8$

**Figure B.13:** $X - Y$ trajectories and phase pictures ($\phi_{C_L-Y}$) of $C_L$ and $y/D$; coupled cylinders $\alpha = 0°$; $e/D = 2.0$; $Re = 3.6 \times 10^6$; $U_r = 3 - 10$.

**(a)** $\phi_{C_L-Y}$ at $U_r = 3$     **(b)** Trajectory at $U_r = 3$     **(c)** $\phi_{C_L-Y}$ at $U_r = 4$     **(d)** Trajectory at $U_r = 4$

**(e)** $\phi_{C_L-Y}$ at $U_r = 5$     **(f)** Trajectory at $U_r = 5$     **(g)** $\phi_{C_L-Y}$ at $U_r = 6$     **(h)** Trajectory at $U_r = 6$

**(i)** $\phi_{C_L-Y}$ at $U_r = 7$     **(j)** Trajectory at $U_r = 7$     **(k)** $\phi_{C_L-Y}$ at $U_r = 8$     **(l)** Trajectory at $U_r = 8$

**(m)** $\phi_{C_L-Y}$ at $U_r = 9$     **(n)** Trajectory at $U_r = 9$     **(o)** $\phi_{C_L-Y}$ at $U_r = 10$     **(p)** Trajectory at $U_r = 10$
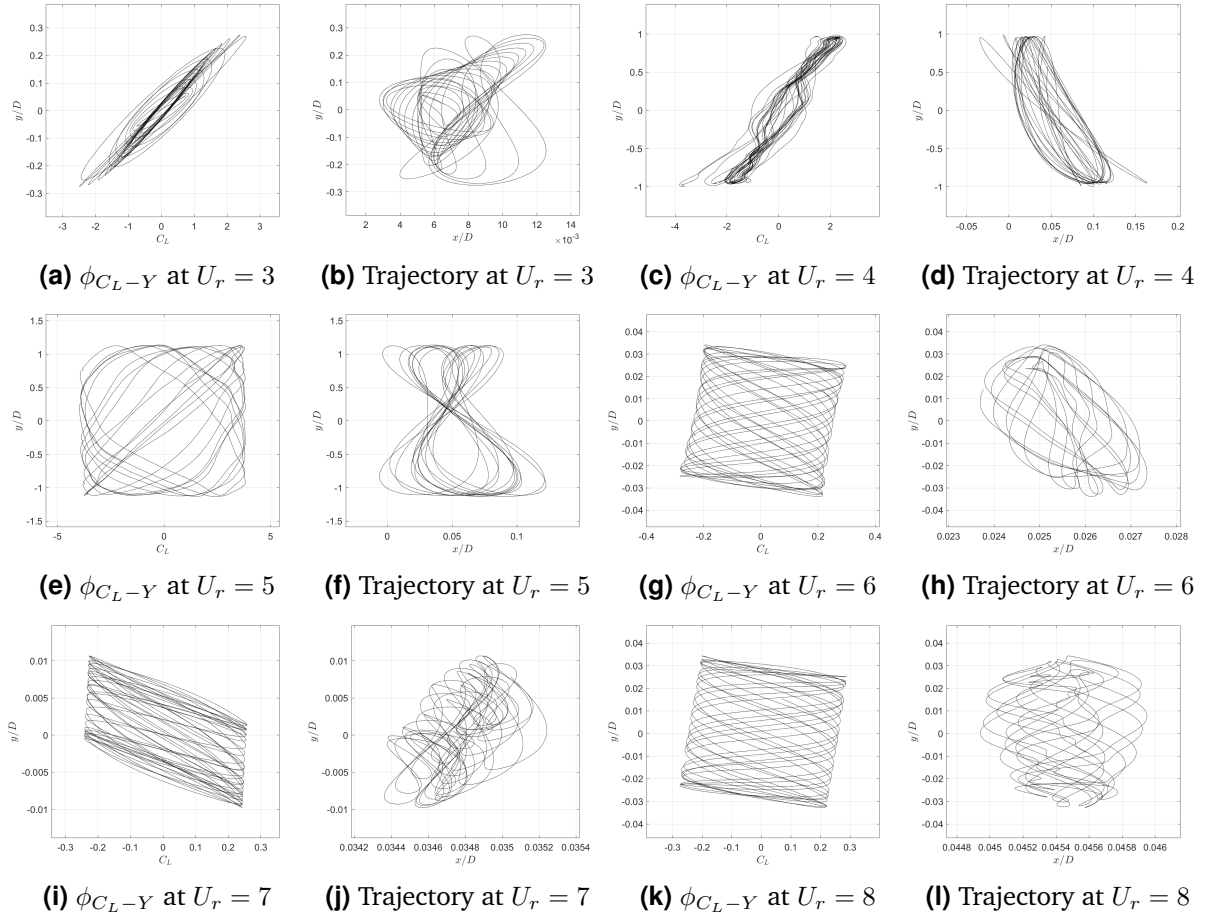
**Figure B.14:** $X-Y$ trajectories and phase pictures ($\phi_{C_L-Y}$) of $C_L$ and $y/D$; coupled cylinders $\alpha = 90°$; $e/D = 2.0$; $Re = 3.6 \times 10^6$; $U_r = 3-10$.
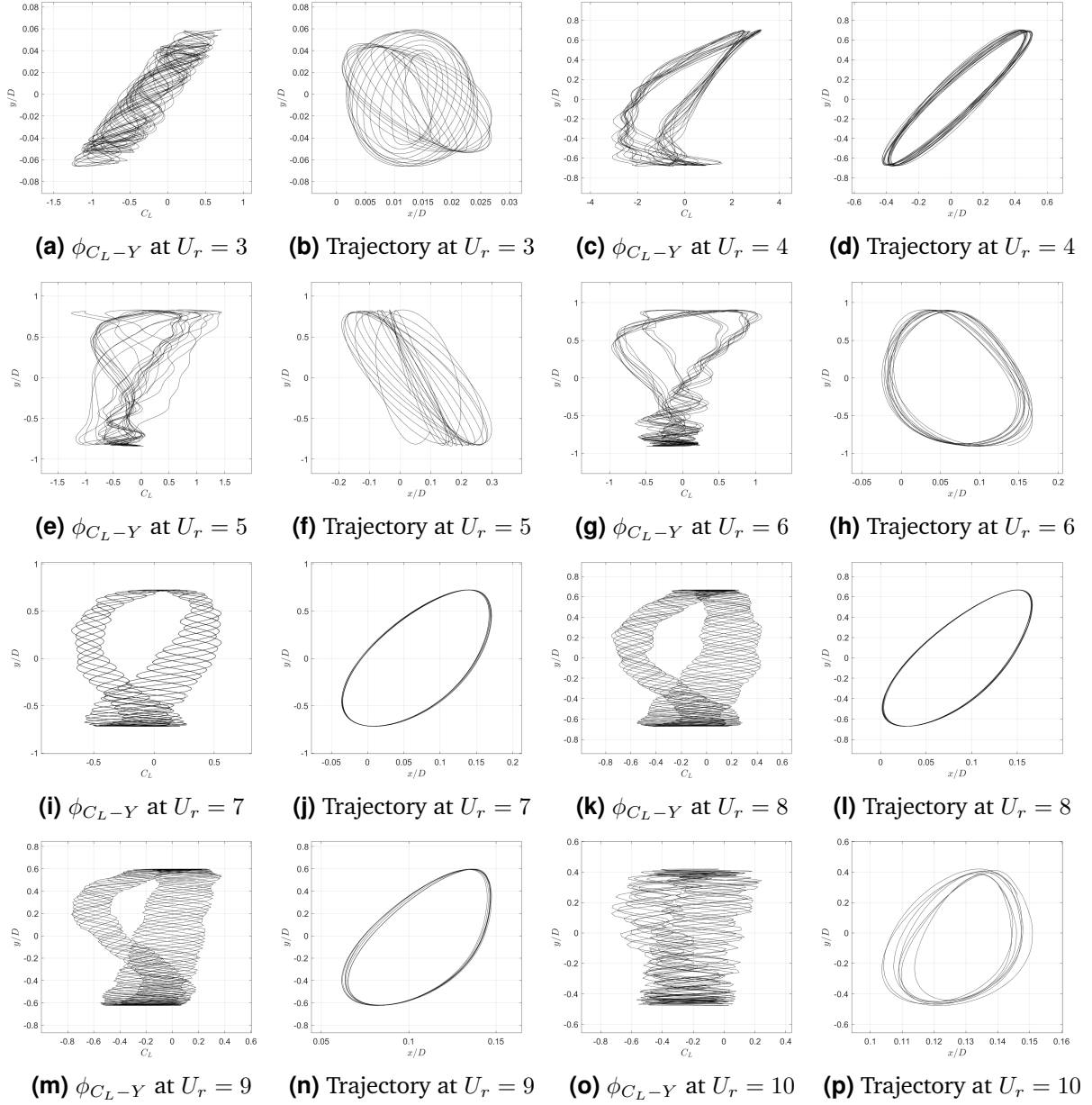
**(a)** $\phi_{C_L-Y}$ at $U_r = 3$     **(b)** Trajectory at $U_r = 3$     **(c)** $\phi_{C_L-Y}$ at $U_r = 4$     **(d)** Trajectory at $U_r = 4$

**(e)** $\phi_{C_L-Y}$ at $U_r = 5$     **(f)** Trajectory at $U_r = 5$     **(g)** $\phi_{C_L-Y}$ at $U_r = 6$     **(h)** Trajectory at $U_r = 6$

**(i)** $\phi_{C_L-Y}$ at $U_r = 7$     **(j)** Trajectory at $U_r = 7$     **(k)** $\phi_{C_L-Y}$ at $U_r = 8$     **(l)** Trajectory at $U_r = 8$

**(m)** $\phi_{C_L-Y}$ at $U_r = 9$     **(n)** Trajectory at $U_r = 9$     **(o)** $\phi_{C_L-Y}$ at $U_r = 10$     **(p)** Trajectory at $U_r = 10$
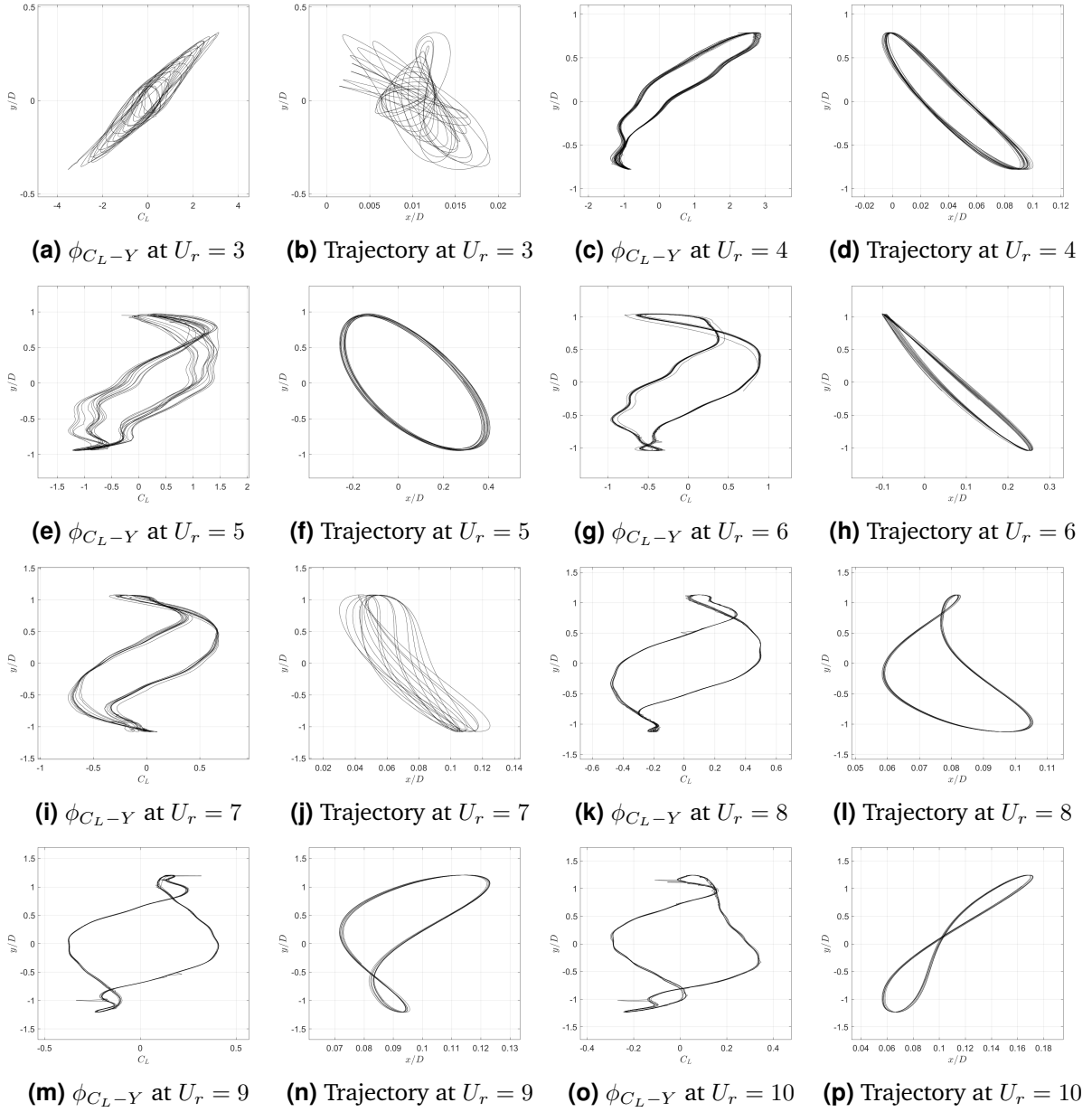
**Figure B.15:** $X - Y$ trajectories and phase pictures ($\phi_{C_L-Y}$) of $C_L$ and $y/D$; coupled cylinders $\alpha = 180°$; $e/D = 2.0$; $Re = 3.6 \times 10^6$; $U_r = 3 - 10$.